



This work is protected by copyright and other intellectual property rights and duplication or sale of all or part is not permitted, except that material may be duplicated by you for research, private study, criticism/review or educational purposes. Electronic or print copies are for your own personal, non-commercial use and shall not be passed to any other individual. No quotation may be published without proper acknowledgement. For any other use, or to quote extensively from the work, permission must be obtained from the copyright holder/s.

**Non-Newtonian and non-isothermal effects in the
gravity-driven draining of a vertically-aligned thin
liquid film**

Mr Hani Nami Alahmadi

Submitted in partial fulfilment of the requirements of the degree of

Doctor of Philosophy

October 2020

Keele University

School of Computing and Mathematics

Abstract

The drainage and thinning of liquid films are important in a variety of applications, such as in liquid and solid foam networks, relevant in the manufacture of metallic and ceramic foams, the food industry, processing in the petro-chemical industry, and the biological and life sciences. In a liquid foam network, there are gas bubbles separated by thin liquid lamellae. If one is interested in predicting the lifetime of a foam or its overall stability then, as a starting point, understanding the drainage within the lamella is important.

Motivated by the above, in this thesis, we consider a two-dimensional model system to investigate the draining and thinning of the lamella relevant to metallic and polymeric melts. Lubrication theory is employed to derive two master Partial Differential Equations (PDEs) for a generalised Newtonian liquid describing the evolution of the film thickness and the extensional flow speed. The PDEs include the effects due to gravity, extensional viscous and surface tension forces. We use the non-Newtonian (Power-law and Carreau) and viscoplastic (Bingham and Herschel-Bulkley) constitutive laws to describe the flow rheology.

We first describe the evolution of a Newtonian liquid film in the limit of large Capillary number, $Ca = \rho^* g^* L^{*2} / (\epsilon \gamma^*) \gg 1$. We derive early and late-time similarity solutions for the draining and thinning of the lamella. A new power law thinning rate of $t^{-2.25}$ in the lamella is identified at late times. This is in comparison to a thinning rate of

t^{-2} predicted for a Newtonian film without gravity, suggesting a weak-dependence on gravity.

Next, we perform numerical simulations to investigate the influence of non-Newtonian and viscoplastic effects by varying the power-law index and the yield stress. We observe that the power law index and the yield stress affects the time scale of the thinning, but has weak dependence on the late-time thinning rate relative to the Newtonian thinning rate. We identify the limitations of the power-law model when the shear rate is low and how these can be resolved using the Carreau model.

We extend the Newtonian model to include non-isothermal effects, such as temperature-dependent viscosity and surface tension. We perform numerical simulations to describe the evolution for a variety of parameter values, such as the reduced Péclet number and those related to the exponential viscosity-temperature model and the linear surface tension-temperature model.

Our results indicate that the resulting temperature drop in the film due to cooling from the free surface, particularly in the lamella, and the corresponding viscosity and surface tension contrast, significantly influence the draining and thinning of the film. Preliminary results show that the viscosity variation has greater influence compared to surface tension variations; however additional work is required to confirm this.

The new knowledge will enhance the current understanding to a wider class of thin liquid film draining flows associated with metallic and polymeric melts.

Acknowledgements

I would like to express my gratitude and sincerest thanks to my supervisor for his encouragement, comments, and guidance through this process. This work would not have been possible without his advice and patience.

I would like to take this opportunity and express my profound appreciation towards my dear parents and my brothers and my sisters. Likewise, I would like to thank my dear wife and my children for patience, encouragement and love to me to realize a doctoral degree.

In addition, I would like to thank from the bottom of my heart, my friends for help and friendship through the years. I want to thank Keele University for giving me the opportunity to pursue a PhD degree.

Last but not least, I would like to thank Aljouf University - Ministry of Education, Kingdom of Saudi Arabia and the Saudi Arabian Cultural Bureau in London (UKSACB) for believing in me and giving me full scholarship, and for their generous support for the completion of my doctoral degree.

Contents

1	Introduction	1
1.1	Motivation	1
1.2	Theoretical models related to the thinning, drainage and rupture of thin free liquid films	7
1.3	Preliminary background	19
1.3.1	Constitutive Laws	19
1.3.2	The heat energy equation	21
1.3.3	Temperature-dependent viscosity and surface tension constitu- tive relationships	23
1.4	Thesis aims and objectives	23
1.5	Thesis outline	25
2	Gravity-driven draining of a vertically-aligned thin liquid free film: The master PDEs	28
2.1	Introduction	28

2.2	Mathematical formulation	30
2.2.1	Governing equations	32
2.2.2	Boundary conditions	33
2.3	Nondimensionalization of the governing equations and boundary conditions	36
2.4	The lubrication (long-wavelength) approximation	40
3	Gravity-driven draining of a vertically-aligned thin Newtonian liquid free film	46
3.1	Introduction	46
3.2	Governing Equations	47
3.3	Numerical solution using the finite difference method	48
3.4	Numerical results	51
3.5	Early and late-time similarity solutions of the film evolution and extensional flow	57
3.5.1	Early-time similarity solution	57
3.5.2	Late-time similarity solution	61
3.6	Conclusions	85
4	Gravity-driven draining of a vertically-aligned thin non-Newtonian liquid free film	89
4.1	Introduction	89
4.2	Governing Equations	90

	iii
4.3 Non-Newtonian and viscoplastic constitutive models	91
4.4 Numerical results	97
4.5 Conclusions	115
5 Gravity-driven draining of a vertically-aligned thin Newtonian and non-isothermal liquid free film with temperature-dependent viscosity and surface tension	121
5.1 Introduction	121
5.2 Mathematical Formulation	122
5.3 Governing equations	123
5.4 Numerical results	131
5.5 Conclusions	153
6 Gravity-driven draining of a vertically-aligned thin Newtonian and non-isothermal liquid free film: the small reduced Péclet number limit	157
6.1 Introduction	157
6.2 Asymptotic limit of small reduced reduced Péclet number, $Pe_r = \epsilon^2 Pe \ll$ 1	158
6.3 Numerical results	161
6.4 Conclusions	177
7 Conclusions and future work	179

List of Figures

1.1	(a) snapshot of a soap foam, and (b) schematic showing gas bubbles, lamella and Plateau borders.	3
2.1	(A) Schematic of a vertically-aligned free liquid film draining under gravity between two rigid wire frames, and (B) late-time film shape after the liquid in the film drains under the influence of gravity.	31
3.1	The evolution of (a), (b) the film thickness $h(x, t)$ (b plots $h(x, t)$ on a logarithmic scale), and (c) the extensional flow speed $u(x, t)$, for varying $t = 0$ to $t = 10^3$. The Capillary number $Ca = 10^3$, and $\Delta x = 5 \times 10^{-4}$	52
3.2	The evolution of the film thickness $h(x, t)$, the extensional flow speed $u(x, t)$ and the stress balance given by Eq. (3.1b) (the solid black lines represent $\frac{1}{Ca}hh_{xxx}$ and the blue dashed lines represent $4(hu_x)_x$) near the bottom end (a, b and c, respectively) and the upper end (d, e and f, respectively), for $t = (5, 6, 7, 8, 9, 10) \times 10^2$. The Capillary number $Ca = 10^3$, and $\Delta x = 5 \times 10^{-4}$	54

- 3.3 (a) Film thickness $h(x, t = t_f)$, and (b) extensional flow speed $u(x, t_f)$, for varying Capillary number, $Ca = 10^2, 10^3, 10^4$, for $\Delta x = 5 \times 10^{-4}$ and $t_f = 10^3$ for $Ca = 10^2, 10^3$; $t_f = 339$ for $Ca = 10^4$ 56
- 3.4 The global minimum h_{min} as a function of time t , for $Ca = 10^3$. The corresponding thinning rates is estimated to be $t^{-2.25}$, for the range of times where h_{min} reaches 1 – 10% of its initial value. 56
- 3.5 Computed film thickness profiles, h , (a) and extensional flow speeds, u , (b) (solid lines) and the corresponding early-time similarity solution (dashed lines) given by Eqs. (3.19,3.21), for times, $t = 1, 2, 3, 4, 5, 6, 7$ 61
- 3.6 Late-time self-similar spatial structure of the film thickness h , showing Region I, the capillary meniscus, Region II, the almost flat draining section, Region III, the pendant drop and two transition regions, A and B. The characteristic variables, $x_{1,2}(t)$, $h_{1,2}$ and $h_{min}(t)$ are explained in the sections describing each region. 62
- 3.7 Evolution of the characteristic variables: (a) $x_{1,2}$ and $x_{\{1,2\}_1}$, and (b) $h_{1,2}$ and h_{min} , for time $t = 5 \times 10^2 - 10^3$ from the numerical solution (solid curves) and the asymptotic model (dashed curves). The parameter values are $Ca = 10^3$ and $Re = 0$ 65
- 3.8 Evolution of h in region I using data shown in Fig. for time $t = 5 \times 10^2 - 10^3$ (solid black curves) for $Ca = 10^3$. The red dashed line shows the corresponding late-time asymptotic solution given by Eq. (3.27), using $V_1 = 0.04$ (corresponding $x_{1\infty} = 0.13464$). 67

- 3.9 Evolution of u in region II using data shown in Fig. for time $t = 5 \times 10^2 - 10^3$. The blue, green and red dashed curves show the solution of Eq. (3.45) for $x_{1,2}$ evaluated from the numerical solution at $t = 5 \times 10^2, 8 \times 10^2, 10^3$, respectively. 72
- 3.10 Evolution of h in region III using data shown in Fig. for time $t = 5 \times 10^2 - 10^3$ (solid black curves) for $Ca = 10^3$. The red dashed line shows the corresponding late-time asymptotic solution given by Eq. (3.58), using $V_2 = 1 - 0.04 = 0.96$ (corresponding $x_{2\infty} = 0.511$). 75
- 3.11 Computed film thickness profiles, h , (a) plotted on a semi-logarithmic axis and the extensional flow speed, u , (b) (solid lines) using the similarity coordinate $\xi = Ca(x - x_{2_1}(t))$ for $t = (5, 6, 7, 8) \times 10^2$. The dashed lines show the corresponding late-time similarity solution given by Eqs. (3.60,3.62). The dotted curve in (a) shows the quasi-static solution of region III given by Eq. (3.58) in the similarity variable ξ for $0 \leq \xi \leq \xi^1$. The parameter values are $Ca = 10^3$, $Re = 0$ and $x_{2\infty} = 0.510583$ 78

- 3.12 Computed film thickness profiles, h , (a) plotted on a semi-logarithmic axis, and the extensional flow speed, u , (b) (solid lines) using the similarity coordinate $\xi = Ca(x - x_{1_1}(t))$ for $t = (5, 6, 7, 8) \times 10^2$. The dashed lines show the corresponding late-time similarity solution given by Eqs. (3.63,3.66). The dotted curve in (a) shows the quasi-static solution of region I given by Eq. (3.27) in the similarity variable ξ for $-Cax_{1_1} \leq \xi \leq 0$. The parameter values are $Ca = 10^3$, $Re = 0$ and $x_{1_\infty} = 0.13464$ 82
- 4.1 (a) Film thickness $h(x, t = 30)$, and (b) extensional flow speed $u(x, t = 30)$, and (c) the global minimum h_{min} as a function of time t , for varying consistency parameter K , for fixed Power Law index, $n = 0.9$ and $Ca = 10^3$ 99
- 4.2 The film thickness $h(x, t = 30)$ (black curve), the extensional flow speed $u(x, t = 30)$ (blue curve), the shear-rate $u_x(x, t = 30)$ (red curve) and the shear-rate dependent viscosity $\mu(|u_x|)$ (green curve) for (a) $K = 0.02$ (corresponding to a liquid of a very low consistency index), (b) $K = 0.1$ (corresponding to a liquid of a low consistency index), (c) $K = 1$ (corresponding to a liquid of an intermediate consistency index) and (d) $K = 10$ (corresponding to a liquid of a high consistency index), for fixed $n = 0.9$ and $Ca = 10^3$ 101

- 4.3 (a) Film thickness $h(x, t = 360)$, and (b) extensional flow speed $u(x, t = 360)$, and (c) the global minimum h_{min} as a function of time t , for varying Power Law index, $n = 0.6, 0.65, 0.75, 0.85, 1, 1.1, 1.2$, for fixed $K_0 = 1$ and $Ca = 10^3$. The corresponding thinning rates are t^{-2} for $n < 1$ and $t^{-2.25}$ for $n \geq 1$ 102
- 4.4 The film thickness $h(x, t = 360)$, the extensional flow speed $u(x, t)$ and the stress balance given by Eq. (4.1b) (the dashed lines represent $h(\frac{1}{Ca}hh_{xxx} + 1)$ and the solid lines represent $4(hu_x)_x$) near the bottom end (a, b and c, respectively) and the upper end (d, e and f, respectively), for $n = 0.75, 1, 1.2$, $K_0 = 1$, $Ca = 10^3$ and $\Delta x = 5 \times 10^{-4}$ 104
- 4.5 The film thickness $h(x, t = 360)$ (black curve), the extensional flow speed $u(x, t = 360)$ (blue curve), the shear-rate $u_x(x, t = 360)$ (red curve) and the shear-rate dependent viscosity $\mu(|u_x|)$ (green curve) for (a) $n = 0.75$ (corresponding to the shear-thinning fluid case), (b) $n = 1$ (corresponding to the Newtonian fluid case), and $n = 1.25$ (corresponding to the shear-thickening fluid case), and fixed $K_0 = 1$ and $Ca = 10^3$ 106
- 4.6 The global minimum h_{min} as a function of time t , for varying Power Law index, $n = 0.9, 1, 1.2$, for fixed $K_0 = 30$ and $Ca = 10^3$ 107
- 4.7 The absolute value of the initial extensional stress $|\tau_{xx}^x(x, t = 0)|$ for $n = 1.1$. 108

- 4.8 (a) Film thickness $h(x, t = 10^3)$, and (b) extensional flow speed $u(x, t = 10^3)$, and (c) the global minimum h_{min} as a function of time t , for varying yield stress $\tau_p = 10^{-4}, 5 \times 10^{-3}, 10^{-2}, 2 \times 10^{-2}, 4 \times 10^{-2}$, for $n = 0.75$, $K_0 = 1$ and $Ca = 10^3$. The corresponding thinning rates are t^{-2} for $\tau_p = 10^{-4}$ and $t^{-1.8}$ for $\tau_p = 2 \times 10^{-2}$ 109
- 4.9 (a) Film thickness $h(x, t = 1000)$, and (b) extensional flow speed $u(x, t = 1000)$, and (c) the global minimum h_{min} as a function of time t , for varying yield stress $\tau_p = 2 \times 10^{-2}, 10^{-2}, 5 \times 10^{-3}, 10^{-4}$, for $n = 1$, $K_0 = 1$ and $Ca = 10^3$. The corresponding thinning rates are $t^{-2.25}$ for $\tau_p = 10^{-4}$ and $t^{-1.7}$ for $\tau_p = 2 \times 10^{-2}$ 111
- 4.10 (a) Film thickness $h(x, t = 360)$, and (b) extensional flow speed $u(x, t = 360)$, and (c) the global minimum h_{min} as a function of time t , for varying yield stress $\tau_p = 1.6 \times 10^{-2}, 10^{-2}, 5 \times 10^{-3}, 10^{-4}$, for $n = 1.2$, $K_0 = 1$ and $Ca = 10^3$. The corresponding thinning rates are $t^{-2.35}$ for $\tau_p = 10^{-4}$ and t^{-2} for $\tau_p = 1.6 \times 10^{-2}$ 112
- 4.11 (a) Film thickness $h(x, t = 800)$, (b) extensional flow speed $u(x, t = 800)$ and (c) the global minimum h_{min} as a function of time t , for the Carreau model with $n = 0.6, 0.65, 0.75, 0.85, 1, 1.1, 1.2$, $\mu_1 = 1$, $Ca = 10^3$, $\lambda = 100$ ($\lambda^* = 10$ s) and $\mu_\infty = 0$ fixed. We estimate the thinning rate to be $t^{-2.25}$ for $n < 1$ and $n \geq 1$ 114

- 4.12 The film thickness $h(x, t = 800)$ (black curve), the extensional flow speed $u(x, t = 800)$ (blue curve), the shear-rate $u_x(x, t = 800)$ (red curve) and the shear-rate dependent viscosity $\mu(|u_x|)$ (green curve) for (a) $n = 0.75$ (corresponding to the shear-thinning fluid case), and (b) $n = 1.2$ (corresponding to the shear-thickening fluid case), for fixed $\mu_1 = 1$, $Ca = 10^3$, $\lambda = 100$ ($\lambda^* = 10$ s) and $\mu_\infty = 0$ 115
- 4.13 Comparison between the Power Law and Carreau models for two different liquids, (a) Polystyrene $(n, K, \lambda) = (0.8, 4, 0.001)$, and (b) Hydroxyethylcellulose $(n, K, \lambda) = (0.8, 0.51, 30)$ 119
- 5.1 The contour plot for (a) $\theta(x, z, t = 10)$, (b) $\theta(x, z, t = 20)$, (c) $\theta(x, z, t = 30)$, (d) $\theta(x, z, t = 40)$, (e) $\theta(x, z, t = 50)$, (f) $\theta(x, z, t = 60)$, (g) $\theta(x, z, t = 70)$, (h) $\theta(x, z, t = 80)$, (i) $\theta(x, z, t = 90)$, and (j) $\theta(x, z, t = 100)$ (the temperature profiles are superimposed on the corresponding free surface shape h), with $Pe_r = 0.1$, $a = 0.02$, $\alpha = 2$, $\theta_s = 0$ 134
- 5.2 The contour plot for (a) $\theta(x, z, t = 10)$, (b) $\theta(x, z, t = 20)$, (c) $\theta(x, z, t = 30)$, (d) $\theta(x, z, t = 40)$, (e) $\theta(x, z, t = 50)$, (f) $\theta(x, z, t = 60)$, (g) $\theta(x, z, t = 70)$, (h) $\theta(x, z, t = 80)$, (i) $\theta(x, z, t = 90)$, and (j) $\theta(x, z, t = 100)$ (the temperature profiles are superimposed on the corresponding free surface shape h), with $Pe_r = 1$, $a = 0.02$, $\alpha = 2$, $\theta_s = 0$ 135

- 5.3 The contour plot for (a) $\theta(x, z, t = 10)$, (b) $\theta(x, z, t = 20)$, (c) $\theta(x, z, t = 30)$, (d) $\theta(x, z, t = 40)$, (e) $\theta(x, z, t = 50)$, (f) $\theta(x, z, t = 60)$, (g) $\theta(x, z, t = 70)$, (h) $\theta(x, z, t = 80)$, (i) $\theta(x, z, t = 90)$, and (j) $\theta(x, z, t = 100)$ (the temperature profiles are superimposed on the corresponding free surface shape h), with $Pe_r = 10$, $a = 0.02$, $\alpha = 2$, $\theta_s = 0$ 136
- 5.4 The contour plot for (a) $\theta(x, z, t = 10)$, (b) $\theta(x, z, t = 20)$, (c) $\theta(x, z, t = 30)$, (d) $\theta(x, z, t = 40)$, (e) $\theta(x, z, t = 50)$, (f) $\theta(x, z, t = 60)$, (g) $\theta(x, z, t = 70)$, (h) $\theta(x, z, t = 80)$, (i) $\theta(x, z, t = 90)$, and (j) $\theta(x, z, t = 100)$ (the temperature profiles are superimposed on the corresponding free surface shape h), with $Pe_r = 10^2$, $a = 0.02$, $\alpha = 2$, $\theta_s = 0$ 138
- 5.5 The contour plot for (a) $\theta(x, z, t = 10)$, (b) $\theta(x, z, t = 20)$, (c) $\theta(x, z, t = 30)$, (d) $\theta(x, z, t = 40)$, (e) $\theta(x, z, t = 50)$, (f) $\theta(x, z, t = 60)$, (g) $\theta(x, z, t = 70)$, (h) $\theta(x, z, t = 80)$, (i) $\theta(x, z, t = 90)$, and (j) $\theta(x, z, t = 100)$ (the temperature profiles are superimposed on the corresponding free surface shape h), with $Pe_r = 10^3$, $a = 0.02$, $\alpha = 2$, $\theta_s = 0$ 139
- 5.6 (a) Film thickness $h(x, t = 50)$, (b) extensional flow speed $u(x, t = 50)$, and (c) the global minimum $h_{min}(t)$, for varying $Pe_r = 0.1, 1, 10, 10^2, 10^3$ the rupture time t_{rupt} as a function of Pe_r . The parameter values are: $\alpha = 2$, $a = 0.2$ and $\beta = 0$ 140

- 5.7 The contour plot for (a) $\theta(x, z, t = 10)$, (b) $\theta(x, z, t = 20)$, (c) $\theta(x, z, t = 30)$, (d) $\theta(x, z, t = 40)$, (e) $\theta(x, z, t = 50)$, (f) $\theta(x, z, t = 60)$, (g) $\theta(x, z, t = 70)$, (h) $\theta(x, z, t = 80)$, (i) $\theta(x, z, t = 90)$, and (j) $\theta(x, z, t = 100)$ (the temperature profiles are superimposed on the corresponding free surface shape h), with $Pe_r = 10^3$, $a = 0.2$, $\alpha = 2$, $\theta_s = 0$ 142
- 5.8 The contour plot for (a) $\theta(x, z, t = 10)$, (b) $\theta(x, z, t = 20)$, (c) $\theta(x, z, t = 30)$, (d) $\theta(x, z, t = 40)$, (e) $\theta(x, z, t = 50)$, (f) $\theta(x, z, t = 60)$, (g) $\theta(x, z, t = 70)$, (h) $\theta(x, z, t = 80)$, (i) $\theta(x, z, t = 90)$, and (j) $\theta(x, z, t = 100)$ (the temperature profiles are superimposed on the corresponding free surface shape h), with $Pe_r = 10^3$, $a = 1$, $\alpha = 2$, $\theta_s = 0$ 143
- 5.9 The contour plot for (a) $\theta(x, z, t = 10)$, (b) $\theta(x, z, t = 20)$, (c) $\theta(x, z, t = 30)$, (d) $\theta(x, z, t = 40)$, (e) $\theta(x, z, t = 50)$, (f) $\theta(x, z, t = 60)$, (g) $\theta(x, z, t = 70)$, (h) $\theta(x, z, t = 80)$, (i) $\theta(x, z, t = 90)$, and (j) $\theta(x, z, t = 100)$ (the temperature profiles are superimposed on the corresponding free surface shape h), with $Pe_r = 10^3$, $a = 2$, $\alpha = 2$, $\theta_s = 0$ 144
- 5.10 The contour plot for (a) $\theta(x, z, t = 10)$, (b) $\theta(x, z, t = 20)$, (c) $\theta(x, z, t = 30)$, (d) $\theta(x, z, t = 40)$, (e) $\theta(x, z, t = 50)$, (f) $\theta(x, z, t = 60)$, (g) $\theta(x, z, t = 70)$, (h) $\theta(x, z, t = 80)$, (i) $\theta(x, z, t = 90)$, and (j) $\theta(x, z, t = 100)$ (the temperature profiles are superimposed on the corresponding free surface shape h), with $Pe_r = 10^3$, $a = 5$, $\alpha = 2$, $\theta_s = 0$ 145

- 5.11 (a) Film thickness $h(x, t = 48)$, (b) extensional flow speed $u(x, t = 48)$, and (c) the global minimum $h_{min}(t)$, for varying $a = 0.02, 0.2, 1, 2, 5$ the rupture time t_{rupt} as a function of a . The parameter values are: $\alpha = 2$, $Pe_r = 10^3$ and $\beta = 0$ 146
- 5.12 The contour plot for (a) $\theta(x, z, t = 10)$, (b) $\theta(x, z, t = 20)$, (c) $\theta(x, z, t = 30)$, (d) $\theta(x, z, t = 40)$, (e) $\theta(x, z, t = 50)$, (f) $\theta(x, z, t = 60)$, (g) $\theta(x, z, t = 70)$, (h) $\theta(x, z, t = 80)$, (i) $\theta(x, z, t = 90)$, and (j) $\theta(x, z, t = 100)$ (the temperature profiles are superimposed on the corresponding free surface shape h), with $Pe_r = 10^3$, $a = 0.02$, $\alpha = 1$, $\theta_s = 0$). 148
- 5.13 The contour plot for (a) $\theta(x, z, t = 10)$, (b) $\theta(x, z, t = 20)$, (c) $\theta(x, z, t = 30)$, (d) $\theta(x, z, t = 40)$, (e) $\theta(x, z, t = 50)$, (f) $\theta(x, z, t = 60)$, (g) $\theta(x, z, t = 70)$, (h) $\theta(x, z, t = 80)$, (i) $\theta(x, z, t = 90)$, and (j) $\theta(x, z, t = 100)$ (the temperature profiles are superimposed on the corresponding free surface shape h), with $Pe_r = 10^3$, $a = 0.02$, $\alpha = 3$, $\theta_s = 0$ 149
- 5.14 The contour plot for (a) $\theta(x, z, t = 10)$, (b) $\theta(x, z, t = 20)$, (c) $\theta(x, z, t = 30)$, (d) $\theta(x, z, t = 40)$, (e) $\theta(x, z, t = 50)$, (f) $\theta(x, z, t = 60)$, (g) $\theta(x, z, t = 70)$, (h) $\theta(x, z, t = 80)$, (i) $\theta(x, z, t = 90)$, and (j) $\theta(x, z, t = 100)$ (the temperature profiles are superimposed on the corresponding free surface shape h), with $Pe_r = 10^3$, $a = 0.02$, $\alpha = 5$, $\theta_s = 0$ 150

5.15 (a) Film thickness $h(x, t = 43)$, (b) extensional flow speed $u(x, t = 43)$, and (c) the global minimum $h_{min}(t)$, for varying $\alpha = 1, 2, 3, 5$ the rupture time t_{rupt} as a function of α . The parameter values are: $Pe_r = 10^3$, $a = 0.02$, $\beta = 0$ 151

5.16 (a) Film thickness $h(x, t = 43)$, (b) extensional flow speed $u(x, t = 43)$, and (c) the global minimum $h_{min}(t)$, for varying $Pe_r = 10^{-1}, 1, 10, 10^2, 10^3$ the rupture time t_{rupt} as a function of Pe_r . The parameter values are: $\beta = 0.5$, $a = 0.02$ and $\alpha = 0$ 152

6.1 (a) The film thickness $h(x, t)$, (b) extensional flow speed $u(x, t)$, and (c) temperature $\theta(x, t)$ for $t = 0 - 10^3$, with $Pe = 10^{-2}$ ($Pe_r = 10^{-4}$), $\alpha = 2$, $a = 0.2$ and $\beta = 0$ 163

6.2 The temperature profile $\theta(x, t)$ for varying $Pe(Pe_r) = (a)0.1(10^{-3})$, (b) $1(10^{-2})$, (c) $10(10^{-1})$ and $t = 0 - 500$, except (e) where $t = 0 - 340$. The parameter values are: $\alpha = 2$, $a = 0.2$ and $\beta = 0$ 164

6.3 (a) Film thickness $h(x, t = 300)$, (b) extensional flow speed $u(x, t = 300)$, and (c) the global minimum $h_{min}(t)$, for varying $Pe(Pe_r) = 0.1(10^{-3})$, $1(10^{-2})$, $10(10^{-1})$, 10 and (d) the rupture time t_{rupt} as a function of Pe . The parameter values are: $\alpha = 2$, $a = 0.2$ and $\beta = 0$ 166

6.4 The temperature profile $\theta(x, t)$ for varying $a = 0.1, 0.5, 1.5, 2, 5$ and $t = 0 - 300$, respectively. The parameter values are: $Pe = 10^3$ ($Pe_r = 10$), $\alpha = 2$ and $\beta = 0$ 168

- 6.5 (a) Film thickness $h(x, t = 50)$, (b) extensional flow speed $u(x, t = 50)$, and (c) the global minimum $h_{min}(t)$, for varying $a = 0.1, 0.5, 1.5, 2, 5$, and (d) the rupture time t_{rupt} as a function of a . The parameter values are: $Pe(Pe_r) = 10^3(10)$, $\alpha = 2$ and $\beta = 0$ 169
- 6.6 (a) Film thickness $h(x, t = 45)$, (b) extensional flow speed $u(x, t = 45)$, and (c) the global minimum $h_{min}(t)$, for varying $\alpha = 0.1, 3, 5, 10$, and (d) the rupture time t_{rupt} as a function of α . The parameter values are: $Pe(Pe_r) = 10(10^{-1})$, $a = 0.2$ and $\beta = 0$ 170
- 6.7 (a) Film thickness $h(x, t = 68)$, (b) extensional flow speed $u(x, t = 68)$, and (c) the global minimum $h_{min}(t)$, for varying $Pe(Pe_r) = 10^{-1}(10^{-3}), 1(10^{-2}), 10(10^{-1})$, and (d) the rupture time t_{rupt} as a function of Pe . The parameter values are: $\alpha = 0$, $a = 0.2$ and $\beta = 0.5$ 172
- 6.8 (a) Film thickness $h(x, t = 50)$, (b) extensional flow speed $u(x, t = 50)$, and (c) the global minimum $h_{min}(t)$, for varying $\beta = 0.1, 0.5, 0.9$, and (d) the rupture time t_{rupt} as a function of β . The parameter values are: $Pe(Pe_r) = 10^3(10)$, $a = 0.2$ and $\alpha = 0$ 174
- 6.9 (a) Film thickness $h(x, t = 40)$, (b) extensional flow speed $u(x, t = 40)$, and (c) the global minimum $h_{min}(t)$, for varying α and β . The parameters values are: $Pe = 10^3$ and $a = 0.2$ 175
- 6.10 Map of the rupture time t_{rupt} as a function of α and β , for $Pe(Pe_r)$ (a) $10^{-2}(10^{-4})$, (b) $1(10^{-2})$, (c) $10(10^{-1})$, and (d) $10^2(1)$. The parameter value $a = 0.2$ 176

Chapter 1

Introduction

1.1 Motivation

The draining, thinning and break-up of liquid films that intertwine a network of gas bubbles play an important role in the manufacturing and stability of foams, and in predicting their lifetime [11, 59, 76]. A foam is a two-phase system formed by trapping gas bubbles in a liquid or molten solid [75, 11]. Some examples of liquid foam are the head of a glass of beer and soap foam bubbles (see Fig. 1.1(*a*)). Foams are a common occurrence in everyday life, such as when applying shaving gel or foam to your face before shaving and when using washing-up liquid to wash and rinse dishes. It is fascinating to observe foams changing their shape and structure constantly throughout their lifetime, as if trying to reach a stable state or at least a metastable state [75]. A nice book detailing the beauty and physics of foams is by Denis Weaire and Stefan

Hutzler - *The Physics of Foams*.

Due to their dispersed nature, foams are used in a wide variety of important industrial processes and applications [66, 20]. The property of gas-liquid foams of having very high surface area is exploited in fire retardant foam, such as those produced by fire extinguishers to blanket fires, in chemical engineering processes of distillation and froth flotation used in recovering minerals, and in oil recovery. Foams made with aqueous surfactant solutions are widely used in cosmetic applications and for detergency purposes, such as in creams, soaps, shaving foam and washing-up liquids, while foams made with protein solutions are the base of many food products, such as in bread dough [74]. Solid foams made by foaming and solidifying melts, referred to as cellular solids [5], are used in the manufacturing industry due to their superior mechanical properties, e.g., lightweight and low thermal conductivity or heat resistivity. Solid foams include polymeric foams, such as polystyrene and polyurethane, with applications as insulation panels in the construction industry and as packing and cushioning materials, in metal foams used in the car and space industries [11, 6], and in ceramic foams used in thermal and acoustic insulation. Biomedical foams are a new class of materials, which are increasingly being used in bone tissue engineering applications [51].

What are foams?

A foam exists in the form of a dispersed two-phase medium consisting of gas bubbles (which may be of different sizes) separated by a network of liquid regions which can

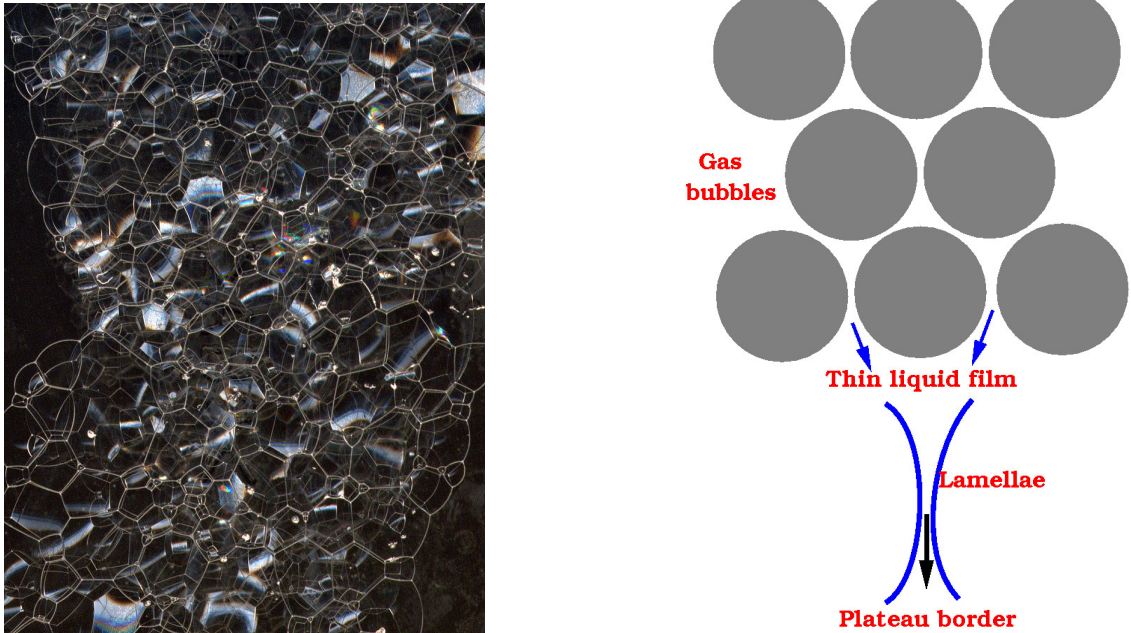


Figure 1.1: (a) snapshot of a soap foam, and (b) schematic showing gas bubbles, lamella and Plateau borders.

form thin films of variable orientation - referred to as *lamella* (see Fig. 1.1(b)). The lamella connect in groups of three and radiate outward from the connection points, known as *Plateau borders* [54] (see Fig. 1.1(b)).

Liquid foams can be either dry (when the liquid fraction is very low) or wet otherwise. The liquid fraction can vary between 0 (dry limit)-35% (wet limit) (Weaire *et al.* [76]). The bubbles are generally polygonal in structure in dry foams and more rounded in wet foams (Weaire & Hutzler [75]). The geometrical arrangement of dry foams can be described by mathematical problems related to minimal surfaces while Plateau's laws describe the structure of soap films based on the assumption that soap films are made of smooth surfaces and the geometrical laws governing the mean curvature of the surfaces and the angles at which the surfaces meet at a vertex and edge (Douglas *et*

al. [56]). The fluid dynamical effects in wet foams, particularly in the lamella, play an essential role in the overall behaviour of the foam (Weaire *et al.* [76]). This will form the basis of the PhD research.

A foam in general is a multi-scale system. It can be analysed as distinct inter-related structural elements - bubbles, thin liquid films (lamella), Plateau borders and junctions (Weaire *et al.* [59]) - see Fig. 1(a).

- (i) Bubbles: they consist of gas and can be of variable diameter and pressure. Their diameters are usually a few millimetres in length scale.
- (ii) Films: The bubbles which are pressed with each other to make thin films with different orientations separate the foam. Their length scales vary between a few nanometres (in dry foams) to a few micrometres (in wet foam). Foams can collapse because of film rupture.
- (iii) Plateau borders: Where the thin films meet along a line or curve, there is a liquid-filled channel called a Plateau border. Their length scale is bigger than that of the thin films but much smaller than the bubble size - usually a few hundred micrometres.
- (iv) Junctions: Where some Plateau borders join to make an interconnected network, they do so at a junction.

The stability of foams is crucial in order to keep the foam from collapsing. Liquid foams go through a series of transient states and change their shape and structure

constantly throughout their lifetime. They are hardly ever stable, usually metastable. While some of the rapid changes in a foam are an essential part of the process, others are damaging and limit the applicability of foam technology. The forces acting on a foam are: gravity, external atmospheric and internal gas pressures, mechanical forces, surface tension and their gradients, etc. Any change in the balance of these forces will lead to motion within the foam. Changes in foam shape and structure can be due to:

- (i) The movement of bubbles concerning each other caused either by external forces or changes in the internal gas pressure, e.g., during the foam production process.
- (ii) Drainage is the fluid flow from the lamella into the Plateau borders due to the change in curvature of the gas-liquid interface moving from the flat lamellar region into a curved Plateau border region, and also due to gravity. The fluid flowing from the lamella into the Plateau borders results in thinning of the lamella.
- (iii) Rupture (or coalescence) is a sudden instability in a film leading to its disappearance. This might be caused by the rupture of the thin liquid films resulting in the bubbles coalescing and the foam collapsing. Long-range attractive and repulsive molecular forces, such as van der Waals attractions (Sheludko [64]) and repulsive forces between surfactant molecules become important when the film is ultra-thin and close to rupture. Competition between the two can result in stable *black* films. The film is so thin that it does not reflect light so is black in colour in interferometric images.
- (iii) Coarsening (or Ostwald ripening) is slow diffusion of gas from smaller bubbles to

bigger ones driven by a pressure difference.

We note that the effects described are not independent. Bubble flow during growth of a foam can result in rupture. Thinning of the lamella due to drainage of fluid into the Plateau borders can lead to lamellar rupture and the coalescence of neighbouring bubbles.

The process of liquid drainage and thinning of the lamella is well-studied in aqueous foams, e.g., (Weaire *et al.* [76]). In aqueous foams, surface active chemicals, such as surfactants, are required to stabilize foams. They not only lower the surface tension but also create surface tension gradients that can counteract the downward flow due to gravity and curvature effects (the so-called Marangoni effect). Surfactants can significantly reduce the drainage or film thinning rate and surfactant-stabilized foams have very long lifetimes in the order of several hours, e.g., soap foam bubbles in the bathtub last for several hours.

In pure molten metal and polymeric foams, the drainage and thinning of the lamella is rapid and rupture can happen in the order of milliseconds. Surfactants are not available to affect the surface tension of metallic foams. Therefore, particles are often added to metallic foam to increase the effective liquid viscosity and to slow down the drainage, thinning and rupture time [11, 80]. Safouane *et al.* [57] have performed forced drainage experiments in shear-thinning (non-Newtonian behaviour) foam solutions. Their results showed that the dynamics of liquid drainage in a foam with a shear-thinning liquid solution is identical to the drainage of foam having a Newtonian liquid

if an effective viscosity based on an estimated shear rate within the foam is used. This implies that the drainage dynamics in foams appears to occur in a narrow range of shear rates.

Most solid foams, such as metal and ceramic foams, originate from a liquid (e.g., metal foams originate from molten liquid metal and ceramic foams from polymer melts), so that a solid foam is usually the frozen or solidified form of the liquid foam. One would then require the solidification or cooling timescale of the lamella to be much faster than its draining and thinning timescale so as to delay or even prevent rupture and maintaining the overall stability of the solid foam. Studies in solid foams are difficult due to their high temperature [11, 6]. Such films display non-Newtonian and viscoplastic behaviour, such as shear-thinning and yield stress. Therefore, theoretical investigations on the fluid dynamics in the lamella of molten metal and polymeric melts are important under both isothermal and non-isothermal conditions in order to better understand their thinning behaviour and its overall influence on foam stability.

1.2 Theoretical models related to the thinning, drainage and rupture of thin free liquid films

There are numerous theoretical investigations focussing on the thinning and rupture of thin liquid films on a *substrate*. These studies take advantage of the slender geometry, i.e., the ratio of the film thickness to its length - its aspect ratio - is small. Lubrication

or long-wavelength theory is then used to simplify the Navier-Stokes equations and the boundary conditions at the free surface to an evolution equation for the film thickness (or free surface shape). The underlying shear flow and the free surface evolution equation includes the physics considered relevant to the problem at leading order in the aspect ratio, e.g., Newtonian, non-Newtonian and viscoelastic effects, surface tension, surface tension gradients due to surfactants, gravity, intermolecular forces, van der Waals forces and other physical effects due to electric field, for example. A nice review of these can be found in the review papers by Oron, Davis & Bankoff [53] and Craster & Matar [24].

In contrast to the above, there are relatively fewer studies of thin *free* films, relevant to the drainage, thinning and rupture of soap films and foams. Unlike films on a substrate, for free films, however, the leading-order evolution equation is not completely determined from the linearised Navier-Stokes equations using the lubrication approximation. For example, consider a two-dimensional flow in a Cartesian coordinate system (x, z) . At leading order, the flow speed u (say) in the longitudinal direction x satisfies $u_{zz} = 0$, with zero shear stress boundary conditions, $u_z = 0$, at the two free surfaces (or at $z = 0$, if centreline symmetry is assumed). Hence, $u = u(x)$, implying a purely extensional or plug flow through the film at leading order. An equation for u is derived at the next order through a compatibility condition and physically represents the balance of forces at the free surface (see Erneux & Davis [29]). The kinematic boundary condition at the free surface along with the continuity equation, then provides the

evolution equation of the free surface due the liquid flux of the extensional flow u . We note the difference with the above scenario of a shear flow between the free surface and the substrate; the zero shear at the free surface along with the no-slip boundary condition at the substrate allow for u to be determined at leading order.

Many researchers have made assumptions, such as assuming the interface to act as a no-slip but deformable interface valid in the presence of surfactants or any other physical effect resulting in a nonzero shear stress at the free surface, which makes the flow a combination of plug and shear flow. This allows a complete description of the flow, and hence the evolution of the free surface, at leading order (see Schwartz & Roy [62]).

The purely extensional flow and the combination of extensional and shear flow framework have been used by several researchers to investigate the draining, thinning and rupture of thin free liquid films, including Newtonian and non-Newtonian rheology, viscoelastic effects, under both isothermal and non-isothermal conditions. These studies are described below, with the focus on the ones relevant to the drainage, thinning and rupture of liquid and aqueous or soap films.

The model system used to mimic the draining of liquid films is based on two configurations: either a liquid film supported within a wire frame or between two rigid supports [47, 62], or a liquid film partially drawn out of a bath of liquid using a wire frame, so it is supported on three sides by the wire frame or by a rigid support at the top and connects directly onto the surface of the liquid bath [22, 49, 48, 50, 14]. These two

configurations mimic the fluid dynamics associated with the draining of a lamella into a Plateau border. The latter configuration also allows investigation of the speed at which the wire frame is drawn out of the bath, and its influence on the stability of the draining film [22]. Other related configurations considered in the literature depending on the application being investigated include, the thinning and break-up of free-falling liquid jets [70, 2, 3], viscous threads [23] and sheets [35, 72, 13].

The now classical experimental investigation by Mysels, Shinoda & Frankel [47] using soap films attached to wire frames gave the first comprehensive description of the draining and thinning of soap films. Subsequently, this has spurred several theoretical studies investigating the thinning and drainage of liquid films using the model systems described above for Newtonian liquids under isothermal conditions. Schwartz and Princen [61] assumed that the interfaces contain sufficient surfactant to become immobile and used quasi-static asymptotic analysis to predict the flow rate to and from films and Plateau borders within a foam that is in periodic deformation. Koehler *et al.* [39] modelled the interaction between gravity, viscous forces and surface tension analytically using a one-dimensional nonlinear PDE called the foam drainage equation. Similarity solutions are described in every case and compared with numerical solutions and available experimental data. Schwartz & Roy [62] present a simplified mathematical model of two-dimensional vertical soap films with an insoluble surfactant bounded between stationary wire frames that captures many of the physical features observed in the experiments of Mysels *et al* [47]. They showed that the drainage rate related to film

thinning was reduced when surfactants are present due to a combination of lowering surface tension and the Marangoni effect. The limit of an immobile interface was observed when the surfactant concentration was large and the thinning rate of the lamella scales like $t^{1/2}$, where t is time. Breward [15] and Breward & Howell [16] have developed and analysed models describing surfactant free and surfactant-stabilized drainage of a foam lamella. Their solution procedure involves dividing the liquid domain into a capillary-static Plateau border, a time-dependent thinning film and a quasi-steady transition region between the two. They use matched asymptotic analysis to describe the evolution of each region, which is then used to derive the thinning rates with and without surfactant. They determined that the lamella drains or the film thins as t^{-2} for a surfactant-free film. They found that surfactants can reduce the draining of the lamella and greatly increase its lifetime. Naire and co-workers [48, 49, 50, 14] introduce surface shear viscosity (surface analogue of the bulk shear viscosity) due to an insoluble surfactant and consider the lamella draining into the Plateau borders in both one and two dimensions. They show that in the limit of large surface viscosity, the immobile $t^{1/2}$ thinning rate is recovered; in the limit of low surface viscosity, the mobile thinning rate of t^{-1} is calculated. Brush & Davis [17] derive the thinning rate of a surfactant-free lamella in a gas-liquid foam using matched asymptotic analysis, in the spirit of Breward [15] and Breward & Howell [16]. Two limiting cases were identified at small Capillary number (dimensionless number comparing viscous and surface tension forces): the wet and the dry foam. They found that the lamellar thinning rates in both cases to be t^{-2} power-law behaviour at long times even though the foam liquid area

fractions have different orders of magnitude in Capillary number; the dynamics and rupture times, though, were distinct for both foam types.

The influence of gravitational forces on the drainage of surfactant-stabilised aqueous foams has been widely studied, in particular its influence in the drainage, thinning and rupture of the lamella (see for example the studies by Schwartz & Roy [62] and Naire and co-workers [48, 49, 50, 14]). However, the gravitational drainage of surfactant-free foams is relatively understudied. To the best of our knowledge, the only study to have examined the role of gravity in the drainage and thinning of flow from the lamella into the Plateau border is by Davis *et al.* [26]. They combine numerical simulations and asymptotic analysis (based on the domain decomposition procedure proposed by Breward & Howell [16] and also used by Brush & Davis [17]) to demonstrate how gravitational effects strongly modify the shape of the Plateau border interfaces and enhance the drainage flow in the liquid films. The lamella thins non-uniformly with exponential decay of the minimum film thickness, which is significantly faster than the t^{-2} power-law thinning predicted when gravitational effects are negligible [15, 16, 17]. Motivated by this study, we focus on the scenario when the liquid films are initially thick (on the order of microns) so that the liquid flow driven by gravitational forces is non-negligible, and could significantly influence the overall foam stability.

There have been numerous studies investigating the rupture of the lamella alone for a Newtonian fluid under isothermal conditions. Prevost & Gallez [55] derived a nonlinear PDE based on the assumption that the interfaces are immobilized or *tangentially*

immobile (that is the component of the fluid velocity tangential to the interface is zero), making them no-slip but deformable interfaces. This model was used to study the rupture of the lamella. Erneux & Davis [29] derive asymptotically the governing equations without making the above assumption. Two evolution equations for the free surface evolution and the longitudinal extensional or plug flow speed were derived and the rupture of the free film is analysed. These studies have been extended to include long-range attractive and repulsive molecular forces via a *disjoining pressure* (Deryagin [28]). Repulsive forces, e.g., between surfactant molecules, can result in a disjoining pressure (repulsive force between the two faces of a film) which opposes further thinning. The film thickness at which equilibrium is achieved is determined by the balance between the disjoining pressure and the bulk pressure gradient of the liquid. Surfactant effects mentioned previously have also been included for mobile films (where the film is no longer considered to be tangentially immobile). De Wit *et al.* [27] consider the dynamics of a free-liquid film with insoluble surfactants and consider film rupture using a model based on three nonlinear evolution equations for the film thickness, the surfactant concentration and the tangential velocity of the fluid in the film. They show that rupture times can be significantly reduced in the presence of surfactants. More recently, Thete *et al.* [71] described the self-similar behaviour during rupture of a free film under the competing influences of inertia, viscous stress, van der Waals pressure, and capillary pressure.

Anderson *et al.* [4] investigate the spontaneous rupture of a free film in two dimensions

due to an instability associated with van der Waals forces. A linear stability analysis of the thinning film shows that the rupture occurs once the film has thinned to tens of nanometres, while for a static film with a constant and uniform thickness, rupture happens when the thickness is hundreds of nanometres. Plateau borders and flow are shown to be involved in the stabilization for the former case. Champougny *et al.* [22] derive a lubrication model to describe the non-stationary free liquid film that is created when a vertical film is pulled out of a liquid bath at a given speed, Including extensional flow and van der Waals interaction between the interfaces, they were able to predict the time and location of rupture, which are shown to compare favourably with their film draining experiments.

There are also a few models that consider the overall behaviour of the foam as a network. Stewart *et al.* [67] formulate a large-scale network model for the dynamics and stability of a planar (gas - liquid) foam with low liquid fraction and composed of approximately polygonal gas bubbles. The model explicitly combines the coupling between the pressure of bubbles and its area, surface tension forces on the gas-liquid interfaces and extensional flows in the liquid films. The model also accounts for van der Waals instabilities that lead to rupture of the liquid film, once it is sufficiently thin, leading to bubble coalescence and hence coarsening of the foam. Initially, the foam is made up of regular polygonal bubbles with the same pressure, but the first film rupture initiates a dynamic coalescence process where the mean bubble area increases rapidly. Numerical simulations explain the large-scale topological rearrangement as the foam

coarsens. This work has been extended to include the accumulation of liquid at the bubble vertices (Plateau borders) as dynamic nodes and the liquid bridges separating the bubbles as uniformly thinning free films (Stewart *et al.* [68]) and fracturing of a surfactant-laden aqueous foam under an applied driving pressure (Stewart *et al.* [69]).

Few models have considered the influence of non-Newtonian rheology, such as shear-thinning and viscoplastic behaviour, relevant in metallic, polymeric and ceramic foams. Brush & Roper [18] extend their two-dimensional small Capillary number matched asymptotic analysis for Newtonian liquids [17] to determine the thinning rates of liquid films in surfactant-free, non-Newtonian gas-liquid foams. The liquid viscosity is modelled as a power-law function of the shear rate and by the Ellis law [45]. They observed that the Ellis model is more realistic than the power law model at a low shear rate, where the viscosity is well behaved in the Ellis model while it diverges to infinity in the power law model. They observed the thinning rate to be t^{-2} for both models, which is the same as that for a Newtonian liquid. They reasoned that the non-Newtonian behaviour influences the time to rupture without affecting the thinning rate. Many researchers have also investigated non-Newtonian behaviour in other contexts, such as in the thinning and rupture of viscous liquid threads and sheets [42, 10]. Studies have also investigated the influence of viscoelastic effects in liquid jets, threads and sheets [2, 3, 12, 82]. In this thesis, we only investigate non-Newtonian behaviour and viscoelastic effects are not considered. This will be considered as future work.

All of the above studies assume isothermal (constant temperature) conditions, and do

not explicitly consider the liquid properties, such as viscosity and surface tension, varying with temperature. Non-isothermal effects are important when there exists a strong coupling between the flow and the temperature field due to a strong dependence of the liquid properties on the temperature. The viscosity of most materials decreases with temperature. Some materials, such as glass, metallic and polymeric melts, can exhibit dramatic changes in their viscosity due to variations in temperature, e.g., cooling and solidification of silicate (or glass-like) lava flows [33]. For glasses and polymers, the surface tension can also vary with temperature (surface tension in most liquids decreases with increase in temperature), perhaps not as dramatic as the variation in viscosity.

In the context of liquid foams, the heat transfer between the hot liquid within the lamella and Plateau borders and the cooler surrounding gas bubbles via the free surface, could result in the lamella cooling down considerably and rapidly in some situations. The resulting thermoviscous (viscosity variations with temperature) and thermocapillary effects (surface tension variations with temperature) could have a significant influence on film drainage and thinning.

Most non-isothermal mathematical models for thin liquid films assume that, within the lubrication approximation, the diffusion of heat across the film thickness is much faster than heat transfer due to convection along the film length. This results in the temperature being uniform across the film thickness in the asymptotic limit of the reduced Péclet number, $Pe_r = \epsilon^2 Pe \ll 1$, where ϵ is the aspect ratio and Pe is Péclet number which is the ratio of the convective to the diffusive heat transport.

This is referred to as the diffusion-dominated scenario of heat transport (also referred to as isothermal or well-mixed heat transport along the thickness of the film). That enables reduction of the temperature field to vary only along the length of the film and time, incorporating the boundary conditions at the free surfaces. Many researchers have employed the $Pe_r \ll 1$ limit to investigate various aspects of thin film flow due to thermocapillary and thermoviscous effects. It is worth noting here that most polymeric and metallic melts have very large Péclet numbers, so the small reduced Péclet number limit may not be applicable in these flows. One would need to consider the variation in temperature both along the length as well as the thickness of the film, coupled to the flow. Balmforth *et al.* [8] have investigated the spreading of molten liquid domes for $Pe_r = O(1)$ and larger, and show that variations in viscosity across the thickness of the dome could significantly affect the spreading dynamics of the flow.

There is a large body of work that have investigated surface wave instability associated with thin liquid film flows or falling films over a heated and inclined substrate, for both thermocapillary and thermoviscous effects (see, e.g., [37, 58, 43, 60, 32, 25, 30, 31, 36]). Several studies have investigated thermoviscous flows associated with spreading of viscous gravity currents, relevant to flow of lava and nuclear material [9, 7, 38, 77, 78], and with phase-transition due to solidification [19, 46, 81]. The role of thermoviscous and thermocapillary effects have also been investigated by several researchers in the extensional flow associated with the drawing of viscous threads, with focus on the stretching and pinching of the threads (see, e.g., [79, 34]). The rupture of thin viscous

fluid sheets has been studied by Tilley & Bowen [72]. They investigate the influence of thermocapillary effects on the evolution of a thin viscous sheet to show how the Marangoni-induced shear stresses (caused by surface tension gradients due to variations in temperature), if comparable to the inertial effects, can control the location and the time to rupture. In a subsequent study [13], they show how thermally induced van der Waals forces could rupture thin viscous fluid sheets. Recently, Shah *et al.* [63] have investigated the influence of thermal fluctuations on the drainage, thinning and rupture of liquid films. They show that thickness variations due to thermal fluctuations at the free surface (originating from random thermal motion of molecules) can compete with the curvature-induced drainage at the Plateau borders. In particular, if the drainage is weak, then the film ruptures at a random location due to spontaneous growth of fluctuations originating from thermal fluctuations. This is in contrast to a scenario where the drainage is strong, resulting in the film rupturing at a local depression - so-called *dimple* - between the lamella and the Plateau border.

We can conclude from the above literature review that the main emphasis of the research in this area has been primarily on aqueous or soap-like films that exhibit Newtonian rheological characteristics. Moreover, most of the studies are under isothermal conditions where the liquid properties, such as the liquid viscosity and surface tension, are held constant. Very few studies have investigated non-Newtonian and viscoplastic effects, and the coupling between the draining flow and cooling, and their influence on the draining characteristics. Investigating these effects will enhance the current under-

standing to a wider class of thin liquid film draining flows associated with metallic and polymeric melts.

1.3 Preliminary background

In this section, we will describe the Newtonian and non-Newtonian rheological models investigated in this thesis. We will also introduce the energy equation and the temperature-dependent models for the viscosity and surface tension that we will use in this thesis.

1.3.1 Constitutive Laws

We can write the constitutive equation for the viscosity as a function of the shear rate for a generalized Newtonian liquid as [44]:

$$\boldsymbol{\tau}^* = \mu(\dot{\boldsymbol{\gamma}}^*)\dot{\boldsymbol{\gamma}}^*, \quad (1.1)$$

where $\mu(\dot{\boldsymbol{\gamma}}^*)$ is the shear rate-dependent viscosity and $\dot{\boldsymbol{\gamma}}^* = \left[\frac{1}{2}\text{Trace}(\dot{\boldsymbol{\gamma}}^* \cdot \dot{\boldsymbol{\gamma}}^*)\right]^{1/2}$, is the second invariant of the shear rate tensor. $\dot{\boldsymbol{\gamma}}^*$ is the shear rate or rate of strain tensor.

Power law fluid

The Power-law model is the the most widely used model of a non-Newtonian liquid where the viscosity in the power-law model can be written in the form:

$$\mu(\dot{\gamma}^*) = K^*(\dot{\gamma}^{*2})^{\frac{n-1}{2}}, \quad (1.2)$$

where K^* is a consistency index and n is a power law index. When $n < 1$ the fluid classified as shear thinning; for $n = 1$ we recover the Newtonian fluid: $n > 1$ the fluid is shear thickening (see Myers [45]). The power-law model might not accurately reflect the dynamics of flows where the shear is low [45]. Moreover, the viscosity becomes infinite when the shear rate approaches zero, which is not physical.

Carreau model

The Carreau model is another model of a non-Newtonian liquid. The Carreau model of the viscosity is given by:

$$\mu(\dot{\gamma}^*) = \mu_{\infty}^* + (1 - \mu_{\infty}^*)[1 + (\lambda^{*2}\dot{\gamma}^{*2})]^{(n-1)/2}, \quad (1.3)$$

where μ_{∞}^* and μ_{∞}^* are the limiting viscosities at high and low shear rates, and λ^* is a relaxation time [45]. The Carreau model is well behaved at low shear rates, unlike the power-law model.

Herschel-Bulkley Model

This is a more general non-Newtonian model for liquids that have a yield stress, i.e., a threshold stress that needs to be exceeded for fluid motion to start. For this model, the viscosity related to the shear rate can be written as [10]:

$$\mu(\dot{\gamma}^*) = K^*(\dot{\gamma}^*)^{n-1} + \frac{\tau_p^*}{\dot{\gamma}^*}, \quad \text{if } \tau^* > \tau_p, \quad (1.4)$$

where $\tau^* = \left[\frac{1}{2}\text{Trace}(\boldsymbol{\tau}^* \cdot \boldsymbol{\tau}^*)\right]^{1/2}$, is the second invariant of the stress tensor and τ_p^* is the yield stress. If the power law index $n = 1$ and $\tau_p^* \neq 0$ then the fluid is referred to as a Bingham liquid, and if $\tau_p^* = 0$, then we recover the power-law model.

1.3.2 The heat energy equation

In non-isothermal problems, we require an additional equation to describe the transport of heat energy due to heat conduction and convection due to the flow. In some scenarios, if the shear rate is sufficiently large, this can result in significant heat generation due to the so-called viscous heating. Wylie *et al.* [79] have shown viscous heating to play a significant role during the stretching of viscous threads by an external force applied at one end of the thread. In this thesis, we do not consider viscous heating. If the density and specific heat of the material are both assumed constant, the heat energy equation

can be written in a Cartesian coordinate system as (see Carslaw & Jaeger [21]):

$$\rho^* c_p^* (T_{t^*}^* + u^* T_{x^*}^* + w^* T_{z^*}^*) = \kappa^* [T_{x^* x^*}^* + T_{z^* z^*}^*], \quad (1.5)$$

in a material with density, ρ^* , specific heat, c_p^* , thermal conductivity, κ^* and thermal diffusivity, $\kappa_d^* = \kappa^*/(\rho^* c_p^*)$. Here, T^* is the temperature.

We use the following type of heat transfer boundary condition for Eq.(1.5),

$$-\kappa^* \mathbf{n}^* \cdot \nabla T^* = F^*(T^*), \quad (1.6)$$

where \mathbf{n}^* is the outward pointing normal to the boundary, F^* is the heat flux. We use Newton's law of cooling to model F^* which can be written as:

$$a_m^* (T^* - T_a^*), \quad (1.7)$$

where a_m^* is a heat transfer coefficient (assumed constant) and T_a^* is the ambient temperature (assumed constant). This assumes that the heat flux is proportional to the temperature difference across this boundary (see, e.g., Balmforth *et al.* [9, 8]).

1.3.3 Temperature-dependent viscosity and surface tension constitutive relationships

We describe the relationship between the temperature and viscosity following the widely used exponential decay constitutive law written as [41, 40]:

$$\mu^*(T^*) = \mu_0^* e^{-\alpha^*(T^* - T_a^*)}, \quad (1.8)$$

where T^* is the temperature, T_a^* is a reference temperature, $\alpha^* > 0$ is a decay constant and μ_0^* is the viscosity at the reference temperature T_a^* . The temperature-dependent constitutive law for surface tension assumes a linear relation given by [72, 34]:

$$\gamma^*(T^*) = \gamma_0^* [1 - \beta^*(T^* - T_a^*)], \quad (1.9)$$

where γ_0^* is the surface tension at the reference temperature T_a^* and β^* is a positive constant.

1.4 Thesis aims and objectives

The main aim of this thesis is to develop a theoretical framework for the draining of a vertically-aligned free liquid film, incorporating gravity, extensional viscous and surface tension forces - the key physical effects that are essential in describing the drainage and evolution of the lamella and Plateau borders in liquid foam films.

Next, this underlying theoretical framework will be used to investigate the influence of non-Newtonian effects, such as shear thinning, and viscoplastic effects, such as yield stress. These are relevant in understanding the drainage and thinning of metallic and polymeric melt films.

The final aim of this thesis is to investigate the coupling between the fluid flow and cooling of the film due to heat transfer at the film's free surface. We incorporate non-isothermal effects, such as a temperature-dependent viscosity and surface tension to understand the influence of variation in viscosity and surface tension due to cooling on the draining and evolution of liquid films. We will only investigate the cooling of the film without any phase transition due to solidification.

The focus of the PhD project is in understanding the drainage and thinning of the lamella based on the above project aims. The main objective is to determine the thinning rates of the lamella which characterise the dynamics of this process. While the literature review highlights the main theoretical works that have investigated the drainage and thinning of the lamella, the role of gravity in influencing the dynamics remains largely unexplored. We believe that if the lamella is initially sufficiently thick (thickness in the order of a few tens of microns), then gravity will have a strong influence in the subsequent drainage and thinning process. The new contribution of this thesis is to include the effect of gravity in the theoretical framework and to investigate its influence combined with extensional viscous, surface tension, non-Newtonian and non-isothermal effects on the drainage and thinning of the lamellae. The influence of

non-Newtonian effects on the draining and thinning of sufficiently thin films (much less than the micron thickness) has been investigated by Brush and Roper [18]. To the best of our knowledge, our work will be the first to consider non-Newtonian effects in thicker films where the additional influence of gravity may result in larger shear rates contributing to more enhanced non-Newtonian behaviour displayed by the draining films. To the best of our knowledge, the influence of non-isothermal effects has never been investigated in the setting of draining and thinning films.

This new knowledge will enhance the current understanding to a wider class of thin liquid film draining flows associated with metallic and polymeric melts. This is relevant in a wide variety of important industrial processes and applications involving metallic, polymeric and ceramic foams.

1.5 Thesis outline

In chapter 2, we present a two-dimensional mathematical model of a vertically-aligned thin liquid film draining under gravity. We use lubrication theory to simplify the governing equations and boundary conditions. Focussing on the main physical balance between the extensional viscous stresses and gravity, we derive, at leading order, the master Partial Differential Equations (PDEs) for a generalised Newtonian liquid describing the time-evolution of the film's free surface and the extensional flow speed, represented by a coupled fourth-order and second-order parabolic PDE in the spatial

coordinate, respectively. The master equations incorporate the key physics, including gravity, surface tension, extensional viscous stresses and a shear-rate dependent viscosity.

In chapter 3, we explore the solutions to the master PDEs for a Newtonian liquid under isothermal conditions, both numerically and analytically. We focus our attention on solutions in the asymptotic limit when the rescaled Capillary number, $Ca = \frac{\rho^* g^* L^{*2}}{\epsilon \gamma^*} \gg 1$, where ρ^* and γ^* are the liquid density and surface tension, respectively, L^* is a characteristic film length and ϵ is the film's aspect ratio. For $Ca \gg 1$, we identify both early and late-time similarity solutions, and determine the film's thinning rate at late times. The similarity solutions are validated with the numerical solutions.

In chapter 4, we use the master PDEs to investigate the influence of non-Newtonian effects, such as a shear rate-dependent viscosity and yield stress. We use the Power-law and Carreau models to describe the shear-thinning and thickening behaviour, and the Herschel-Bulkley and Bingham model to describe the influence of the yield stress. We use numerical simulations to conduct a parameter study in order to determine the influence of the film's evolution, its drainage and its late-time thinning rate on key parameters, such as the consistency index, the power-law exponent and the yield stress. The validity of the power-law model is verified and comparisons made with the Carreau model.

In chapter 5, we extend the model for a Newtonian liquid to incorporate non-isothermal effects, in particular, a temperature-dependent viscosity and temperature-dependent

surface tension. For the reduced Péclet number, $Pe_r = O(1)$, the one-dimensional evolution equations for the film's free surface and the extensional flow speed are coupled to a two-dimensional (across the film's thickness and along its length) advection-diffusion equation for the temperature. We perform numerical simulations to describe the evolution of the free surface shapes, the extensional flow speeds, and temperature fields for a variety of parameter values, such as the reduced Péclet number, Pe_r , and those related to the exponential viscosity-temperature model and the linear surface tension-temperature model.

In chapter 6, we focus on the asymptotic limit of the reduced Péclet number $Pe_r = \epsilon^2 Pe \ll 1$ (ϵ is the aspect ratio and Pe is the Péclet number), which enables the two-dimensional temperature field to be reduced to a one-dimensional evolution equation for the temperature. We use numerical simulations to describe the evolution of the film's free surface, the extensional flow speed and the temperature, in different parameter regimes. We are able to show that the one-dimensional temperature solutions obtained in this chapter for small Pe_r are in good agreement with their corresponding parameter values in chapter 5.

Finally, in chapter 7, we make some final conclusions and describe the future work.

Chapter 2

Gravity-driven draining of a vertically-aligned thin liquid free film: The master PDEs

2.1 Introduction

This chapter investigates the evolution of a vertically-aligned liquid free film as it drains due to gravity and surface tension forces. The fluid flow configuration considered here (and in the rest of the thesis) involves a thin liquid film supported between wire frames (Figure 2.1 shows a cross-sectional view of this configuration). This configuration has been considered by Schwartz & Roy [62] for investigating the draining of mobile and immobile soap films supported within a wire frame in the presence of surfactants.

Another configuration investigated by several researchers involves lifting the wire frame out of a bath of liquid resulting in a liquid film that connects onto the bath at its lower end (for example, see Champougny *et al.* [22] and Naire *et al* [49, 48, 50, 14]). The former configuration is the simplest model of a draining free liquid film, and it is relatively straightforward to prescribe the no flux boundary conditions at both ends of the film. This is in comparison to the latter configuration where one needs to approximate the boundary conditions for the film to match onto the bath [49, 48, 50, 14, 22].

The focus of this chapter is in deriving the master PDEs for a generalised Newtonian liquid under isothermal conditions. Chapters 3 and 4 investigate the flow behaviour for specific fluid rheologies representing a Newtonian, and generalised non-Newtonian, and visco-plastic liquid, respectively. In §2.2, we formulate the two-dimensional mathematical problem in a Cartesian coordinate system, which provides the governing equations and boundary conditions for the flow. We then non-dimensionalise the governing equations and boundary conditions in §2.3, focussing on the scenario where gravity and extensional viscous effects dominate, and surface tension is comparatively smaller. The lubrication approximation is used in §2.4 to simplify the non-dimensional governing equations and boundary conditions to two PDEs for the evolution of the one-dimensional film's free surface shape and the speed of the extensional draining flow. Eqs. (2.42) and (2.44) represent the master PDEs for a generalised Newtonian liquid, which along with the boundary conditions given in Eqs.(2.45) and (2.46) describe the

flow configuration shown in Figure 2.1.

2.2 Mathematical formulation

We consider the two-dimensional flow due to the draining of a liquid in a vertically-aligned thin film with two free surfaces (see Figure 2.1). The draining flow evolves due to the effects of gravity, viscous forces and surface tension. We make the following assumptions: The liquid is assumed to be a generalised Newtonian liquid with a shear rate-dependent viscosity. The liquid is assumed incompressible, so its density is constant. We assume isothermal conditions, so the liquid properties are independent of variations in temperature. Temperature-dependent variation of liquid properties will be considered in chapter 5. The liquid film is supported by solid frames at the top and bottom (see Figure 2.1). This is a simple idealisation of the physical situation, but it should not influence the drainage in the middle section of the film which is our main focus. We assume symmetry about the film's centre line. We assume the film to be vertically aligned with gravity acting downwards (see Figure 2.1).

We consider a liquid film suspended between two horizontal frames, as shown in Figure 2.1. We consider a two-dimensional Cartesian coordinate system (x^*, z^*) with the z^* -axis in the horizontal direction and along the film's thickness and the x^* -axis in the vertical direction pointing downwards in the direction of the film length. The horizontal frames are separated by a distance L^* and are of width $2H_0^*$. Gravity is acting vertically

downwards. The two free surfaces of the film are represented by $z^* = \pm h^*(x^*, t^*)$ with centre line at $z^* = 0$. Using left-right symmetry, we only consider half of the film between $z^* = 0$ and $z^* = h^*(x^*, t^*)$. Figure 2.1 shows a schematic of the geometry considered.

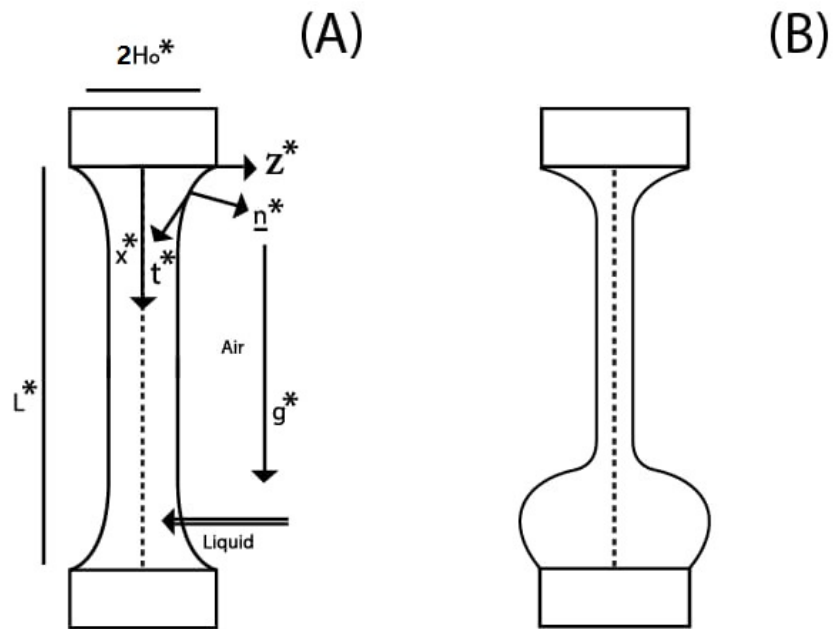


Figure 2.1: (A) Schematic of a vertically-aligned free liquid film draining under gravity between two rigid wire frames, and (B) late-time film shape after the liquid in the film drains under the influence of gravity.

2.2.1 Governing equations

The flow is described by the Navier-Stokes equations (Ascheson[1] and Ockendon [52]). The density ρ^* is constant (due to the incompressibility assumption), so reduces the continuity equation to

$$u_{x^*}^* + w_{z^*}^* = 0. \quad (2.1)$$

In the above, $\mathbf{v}^* = (u^*, w^*)$ are the flow speeds in the x^* and z^* directions, respectively, and the subscript denotes differentiation with respect to the subscript variable. The momentum equations can be written as

$$\rho^* (u_{t^*}^* + u^* u_{x^*}^* + w^* u_{z^*}^*) = -p_{x^*}^* + \tau_{x^*}^{*x^*x^*} + \tau_{z^*}^{*xz^*} + \rho^* g^*, \quad (2.2a)$$

$$\rho^* (w_{t^*}^* + u^* w_{x^*}^* + w^* w_{z^*}^*) = -p_{z^*}^* + \tau_{x^*}^{*x^*z^*} + \tau_{z^*}^{*z^*z^*}. \quad (2.2b)$$

Here p^* is the liquid pressure, $\tau^{*x^*x^*}$ and $\tau^{*z^*z^*}$ are the extensional viscous stresses in the x^* and z^* directions, respectively, $\tau^{*x^*z^*}$ is the viscous shear stress and g^* is the acceleration due to the gravity.

We require a constitutive law relating the viscous stress $\boldsymbol{\tau}$ with the shear rate $\dot{\boldsymbol{\gamma}}^*$, where

$$\boldsymbol{\tau}^* = \begin{pmatrix} \tau^{*x^*x^*} & \tau^{*x^*z^*} \\ \tau^{*x^*z^*} & \tau^{*z^*z^*} \end{pmatrix}, \quad (2.3)$$

and

$$\dot{\boldsymbol{\gamma}}^* = \begin{pmatrix} \gamma^{*x^*x^*} & \gamma^{*x^*z^*} \\ \gamma^{*x^*z^*} & \gamma^{*z^*z^*} \end{pmatrix} = \begin{pmatrix} 2u_{x^*}^* & u_{z^*}^* + w_{x^*}^* \\ u_{z^*}^* + w_{x^*}^* & 2w_{z^*}^* \end{pmatrix}. \quad (2.4)$$

We use a constitutive law for a generalised Newtonian liquid of the form

$$\boldsymbol{\tau}^* = \mu^*(\dot{\boldsymbol{\gamma}}^*)\dot{\boldsymbol{\gamma}}^*, \quad (2.5)$$

where $\mu^*(\dot{\boldsymbol{\gamma}}^*)$ is the shear rate-dependent viscosity and

$\dot{\boldsymbol{\gamma}}^* = [\frac{1}{2}\text{Trace}(\dot{\boldsymbol{\gamma}}^* \cdot \dot{\boldsymbol{\gamma}}^*)]^{1/2} = [2(u_{x^*}^{*2} + w_{z^*}^{*2}) + (u_{z^*}^* + w_{x^*}^*)^2]^{1/2}$, is the second invariant of the shear rate tensor.

2.2.2 Boundary conditions

Symmetry along the center line $z^* = 0$ is imposed through the boundary conditions:

$$w^* = u_{z^*}^* = \tau^{*x^*z^*} = 0, \text{ at } z^* = 0. \quad (2.6)$$

At the free surface, $z^* = h^*(x^*, t^*)$, we have the following boundary conditions. The normal stress boundary condition balances the jump in the total normal stress (between the outside air and the liquid) with the product of the surface tension times the

curvature of the free surface,

$$\mathbf{n}^* \cdot [\boldsymbol{\sigma}_{air}^* - \boldsymbol{\sigma}^*] \cdot \mathbf{n}^* = -\frac{\gamma^* h_{x^* x^*}^*}{(1 + h_{x^*}^{*2})^{\frac{3}{2}}} \text{ at } z^* = h^*(x^*, t^*),$$

$$\boldsymbol{\sigma}^* = \begin{pmatrix} -p^* + \tau^* x^* x^* & \tau^* x^* z^* \\ \tau^* x^* z^* & -p^* + \tau^* z^* z^* \end{pmatrix}, \quad \boldsymbol{\sigma}_{air}^* = -p_{air}^* \mathbf{I}, \quad (2.7)$$

where $\boldsymbol{\sigma}^*$ and $\boldsymbol{\sigma}_{air}^*$ are the stress tensors in the fluid and air, respectively, \mathbf{I} is the 2×2 identity matrix, γ^* is the surface tension (assumed constant), $\frac{h_{x^* x^*}^*}{(1 + h_{x^*}^{*2})^{\frac{3}{2}}}$ is the surface curvature, p_{air}^* is the atmospheric pressure (assumed constant). $\mathbf{n}^* = \frac{1}{\sqrt{1 + h_{x^*}^{*2}}}(-h_{x^*}^*, 1)$ and $\mathbf{t}^* = \frac{1}{\sqrt{1 + h_{x^*}^{*2}}}(1, h_{x^*}^*)$ are the unit outward-facing normal and tangent to the free surface, respectively (see Figure 2.1). Without loss of generality, we take $p_{air}^* = 0$ and the liquid pressure p^* is now relative to the atmospheric pressure.

The normal stress boundary condition can be written as

$$-p^* + \frac{1}{1 + h_{x^*}^{*2}} [h_{x^*}^{*2} \tau^* x^* x^* - 2h_{x^*}^* \tau^* x^* z^* + \tau^* z^* z^*] = \frac{\gamma^* h_{x^* x^*}^*}{(1 + h_{x^*}^{*2})^{\frac{3}{2}}}. \quad (2.8)$$

The tangential stress boundary condition imposes continuity of stress at the free surface, $\mathbf{t}^* \cdot \boldsymbol{\sigma}^* \cdot \mathbf{n}^* = \tau^*(x^*, t^*)$, where τ^* is the stress applied in the outside air phase. Since there are no physical effects due to surfactants, electric field, temperature variations, etc., $\tau^* = 0$. This equation can then be written as

$$(1 - h_{x^*}^{*2}) \tau^* x^* z^* + h_{x^*}^* (\tau^* z^* z^* - \tau^* x^* x^*) = 0, \text{ at } z^* = h^*(x^*, t^*). \quad (2.9)$$

Finally, the kinematic boundary condition at the free surface is given by

$$h_{t^*}^* = w^* - u^* h_{x^*}^*, \text{ at } z^* = h^*(x^*, t^*). \quad (2.10)$$

At the top and bottom boundary, $x = 0, L$, respectively, we fix the film thickness and impose no slip,

$$h^* = H_0^* \text{ and } \mathbf{v}^* = 0, \text{ at } x^* = 0, L. \quad (2.11)$$

Here, H_0^* is a prescribed film thickness.

Using the continuity equation, Eq. (2.1), and Leibniz's rule, one can re-write the kinematic boundary condition, Eq. (2.10), as

$$h_{t^*}^* + Q_{x^*}^* = 0, \quad Q^* = \int_0^{h^*} u^*(x^*, z^*, t^*) dz^*, \quad (2.12)$$

where $Q^*(x^*, t^*)$ is the liquid flux at any location x^* along the length of the film. This partial differential equation represents the evolution of the film thickness, $h^*(x^*, t^*)$.

2.3 Nondimensionalization of the governing equations and boundary conditions

The governing equations, Eqs. (2.1)-(2.2b), (2.12) and boundary conditions, Eqs. (2.6)-(2.11), are nondimensionalised using

$$\begin{aligned}
 x^* &= L^* x, \quad (z^*, h^*) = H_0^*(z, h^*), \quad u^* = U^* u, \quad w^* = W^* w, \\
 (p^*, \tau^{*x^*x^*}, \tau^{*z^*z^*}, \tau^{*x^*z^*}) &= (P^* p, T^* \tau^{xx}, T^* \tau^{zz}, \frac{T^*}{\epsilon} \tau^{xz}), \\
 (\gamma^{*x^*x^*}, \gamma^{*z^*z^*}, \gamma^{*x^*z^*}) &= \mu_0 \left(\frac{U^*}{L^*} \gamma^{xx}, \frac{U^*}{L^*} \gamma^{zz}, \frac{U^*}{\epsilon L^*} \gamma^{xz} \right), \quad t^* = \frac{L^*}{U^*} t, \quad Q^* = U^* H_0^* Q, \quad (2.13)
 \end{aligned}$$

where H_0^* and L^* are length scales associated with the width and length of the film, μ_0^* is a reference viscosity of the liquid and U^* , W^* , P^* and T^* are characteristic speeds, pressure and stress, respectively. The ratio of the two length scales is denoted by $\epsilon = \frac{H_0^*}{L^*}$, which is typically much less than one. We are interested in deriving the thin film equations in the asymptotic limit $\epsilon \rightarrow 0$. Here we focus on the scenario where the flow is primarily extensional (or plug flow) with a uniform velocity in the direction transverse to the film [35]. Extensional film flow corresponds mathematically to a distinguished limit, as described by Breward [15] and Breward & Howell [16], in which extensional viscous stresses balance all other forces along the film such as inertia, surface tension, gravity and van der Waals forces. Our focus here is on a balance between extensional viscous stresses and gravity to describe the draining regime of film thinning. In this case, the downward pressure gradient ($p_{x^*}^*$) is comparable to the

gradient of the extensional viscous stress ($\tau_{x^*x^*}^{*x^*x^*}$) in the x^* component of the momentum equation, Eq. (2.2a). So, $p_{x^*}^* \sim \tau_{x^*}^{*x^*x^*}$ which implies that the stress scale $T^* = P^*$. Now, from the x^* component of the momentum equation, Eq. (2.2a), we also demand that the downward pressure gradient (p_x) is comparable to the force due to gravity (ρ^*g^*), hence the characteristic pressure scale $P^* = \rho^*g^*L^*$, so the characteristic stress scale $T^* = \rho^*g^*L^*$. The extensional flow speed U^* will be determined later on based on a distinguished limit. The continuity equation, Eq. (2.1), implies $u_x \sim w_z$ which gives $W = \epsilon U$.

Table 2.1 provides the values of the dimensional quantities which are based on those reported for polymeric liquids, such as Polystyrene, Aluminium soap and Hydroxyethylcellulose (see Table 1 in Myers [45]). Their viscosities at zero shear rate (μ_0^*) show a wide variation, from 4×10^6 for Polystyrene, 89.6 Pa s for Aluminium soap to 0.2 Pa s for Hydroxyethylcellulose. A typical lengthscale is about 1cm and film thickness scale is about 50 micrometres. We consider relatively thicker films and far away from rupture. Substituting the non-dimensional variables in Eq. (2.13) into the governing equations, Eqs. (2.1)-(2.2a)-(2.2b), boundary conditions, Eqs. (2.6)-(2.11) and Eq.

Dimensional quantities	Values
density, ρ^*	10^3kg/m^3
viscosity, μ_0^*	10Pa s
surface tension, σ^*	42mN/m
length, L^*	10^{-2}m
width, H_0^*	50 μm
characteristic speed, $U^* = \frac{\rho^* g^* L^{*2}}{\mu_0^*}$	0.1m/s
characteristic pressure, $p^* = \rho^* g^* L^*$	10^3N/m^2
characteristic time, $t^* = \frac{L^*}{U^*}$	0.1s

Table 2.1: Values of the dimensional quantities, assuming that the liquid is representative of a polymeric liquid.

(2.12), gives the following non-dimensionalized system:

$$u_x + w_z = 0, \quad (2.14)$$

$$\epsilon^2 Re (u_t + uu_x + wu_z) = -\epsilon^2 p_x + \epsilon^2 \tau_x^{xx} + \tau_z^{xz} + \epsilon^2 B, \quad (2.15)$$

$$\epsilon^2 Re (w_t + uw_x + ww_z) = -p_z + \tau_x^{xz} + \tau_z^{zz}, \quad (2.16)$$

$$w = u_z = \tau^{xz} = 0, \quad \text{at } z = 0, \quad (2.17)$$

$$\frac{\epsilon}{\hat{C}a} \frac{h_{xx}}{(1 + \epsilon^2 h_x^2)^{\frac{3}{2}}} = -p + \frac{1}{1 + \epsilon^2 h_x^2} [\epsilon^2 h_x^2 \tau^{xx} - 2h_x \tau^{xz} + \tau^{zz}],$$

$$\text{at } z = h(x, t), \quad (2.18)$$

$$(1 - \epsilon^2 h_x^2) \tau^{xz} + \epsilon^2 h_x (\tau^{zz} - \tau^{xx}) = 0, \quad \text{at } z = h(x, t), \quad (2.19)$$

$$h = 1 \text{ and } u = w = 0, \quad \text{at } x = 0, 1, \quad (2.20)$$

$$h_t + Q_x = 0, \quad Q = \int_0^h u(x, z, t) dz. \quad (2.21)$$

The nondimensional constitutive law, Eq. (2.5), can be written as

$$\begin{pmatrix} \tau^{xx} & \tau^{xz} \\ \tau^{xz} & \tau^{zz} \end{pmatrix} = \mu(\dot{\gamma}) \begin{pmatrix} 2u_x & u_z + \epsilon^2 w_x \\ u_z + \epsilon^2 w_x & 2w_z \end{pmatrix}, \quad (2.22)$$

where the dimensionless form of the function $\mu(\dot{\gamma})$ depends on the constitutive law used, e.g., for a Newtonian liquid, $\mu(\dot{\gamma}) = 1$. In the above, the dimensionless number $B = \frac{\rho^* g^* L^{*2}}{\mu_0^* U^*}$ compares gravity and extensional viscous forces, $Re = \frac{\rho^* U^{*2}/L^*}{\mu_0^* U^*/L^{*2}}$ is the Reynolds number (compares inertial and extensional viscous forces) and $\hat{Ca} = \frac{\mu_0^* U^*}{\gamma^*}$ is the Capillary number (compares extensional viscous and surface tension forces). There are 2 distinguished limits to be considered here based mainly on the order of magnitude of B and Re . We also note a third distinguished limit which is not the focus of this work.

- (i) Balancing extensional viscous forces and gravity, $B \sim 1$. This gives a characteristic speed $U^* \sim \frac{\rho^* g^* L^{*2}}{\mu_0^*} \sim 0.1\text{m/s}$. The inertial forces are smaller in comparison, with corresponding $Re \sim 0.1$. This balance has been investigated by Schwartz & Roy [62] and Champougny *et al.* [22].
- (ii) Balancing extensional viscous forces and inertia, $Re \sim 1$. This gives a characteristic speed $U^* \sim \frac{\mu^*}{\rho^* L^*} \sim 1\text{m/s}$. The force due to gravity is smaller in comparison, with corresponding $B \sim 0.1$. This balance has been investigated by Erneux & Davis [29].
- (iii) If $B \sim 1/\epsilon^2$, i.e., corresponding $U^* \sim \epsilon^2$, then the leading order balance is between

viscous shear forces and gravity (see, for example, Naire *et al* [49, 48, 50, 14]).

Our work focusses on the balance between extensional viscous forces and gravity, hence we set $B = 1$, which sets the characteristic speed $U = \frac{\rho^* g^* L^{*2}}{\mu_0^*} \sim 0.1\text{m/s}$. The corresponding Reynolds number $Re = 0.1$. We assume that the Capillary number, $\hat{Ca} = O(1)$. We will see later on, that surface tension effects will be important over smaller lengthscales, so in anticipation of this we define a rescaled Capillary number, $Ca = \frac{\mu_0^* U^*}{\epsilon \gamma^*}$, and retain the surface tension term at leading order in Eq. (2.18).

Estimates of the dimensionless parameters are provided in Table 1.2.

Dimensional quantities	Values
$\epsilon = H_0^*/L^*$	10^{-2}
$B = \frac{\rho^* g^* L^{*2}}{\mu_0^* U^*}$	1
$Re = \frac{\rho^* U^* L^*}{\mu_0^*}$	0.1
$\hat{Ca} = \frac{\mu_0^* U^*}{\gamma^*}$	25
$Ca = \frac{\hat{Ca}}{\epsilon}$	2.5×10^3

Table 2.2: Estimates of the dimensionless parameters.

2.4 The lubrication (long-wavelength) approximation

We can now exploit the fact that $\epsilon = \frac{H_0^*}{L^*} \ll 1$ and expand each of the unknowns variables $(u, w, p, \tau^{xx}, \tau^{zz}, \tau^{xz}, h)$ as a power series in ϵ^2 since the terms appearing in

the equations and boundary conditions are all powers of ϵ^2 . We write:

$$\begin{aligned} (u, w, p, \tau^{xx}, \tau^{zz}, \tau^{xz}, h) &= (u, w, p, \tau^{xx}, \tau^{zz}, \tau^{xz}, h)_0(x, z, t) \\ &+ \epsilon^2(u, w, p, \tau^{xx}, \tau^{zz}, \tau^{xz}, h)_1(x, z, t) + O(\epsilon^4). \end{aligned} \quad (2.23)$$

Substituting the above into Eqs. (2.14)-(2.21), we obtain at leading order:

$$u_{0x} + w_{0z} = 0, \quad (2.24)$$

$$\tau_{0z}^{xz} = 0, \quad (2.25)$$

$$-p_{0z} + \tau_{0x}^{xz} + \tau_{0z}^{zz} = 0, \quad (2.26)$$

$$w_0 = u_{0z} = \tau_0^{xz} = 0, \text{ at } z = 0, \quad (2.27)$$

$$-p_0 + \tau_0^{zz} - 2h_{0x}\tau_0^{xz} = \frac{1}{Ca} \frac{h_{0xx}}{(1 + \epsilon^2 h_{0x}^2)^{3/2}}, \text{ at } z = h_0 \quad (2.28)$$

$$\tau_0^{xz} = 0, \text{ at } z = h_0. \quad (2.29)$$

Eqs. (2.25), (2.27), (2.29) implies that

$$\tau_0^{xz}(x, z, t) = 0. \quad (2.30)$$

Now, we can integrate Eq.(2.26) with respect to z and using Eqs. (2.27) and (2.28), we obtain

$$p_0 = \tau_0^{zz} - \frac{1}{Ca} h_{0xx}. \quad (2.31)$$

To determine $\tau_0^{xx,zz}$, we need to analyse the $O(\epsilon^2)$ equations. Before we do this, we note the following: $u_{0z} = 0$, so $u_0 = u_0(x, t)$ (i.e., the leading order extensional flow speed is independent of the transverse coordinate z ; see Howell [35]), using $\tau_0^{xz} = 0$ and the constitutive law, Eq. (2.22), at leading order. In addition, $\tau_0^{zz} = -\tau_0^{xx}$, using the continuity equation, Eq. (2.24) in the constitutive law, Eq. (2.22). Eq. (2.24) also gives $w_{0z} = -u_{0x}$, which on intergrating with respect to z and using $w_0 = 0$ at $z = 0$, gives $w_0(x, z, t) = -u_{0x}z$. At $O(\epsilon^2)$, we have

$$Re(u_{0t} + u_0 u_{0x} + w_0 u_{0z}) = -p_{0x} + \tau_{0x}^{xx} + \tau_{1z}^{xz} + 1, \quad (2.32)$$

$$Re(w_{0t} + u_0 w_{0x} + w_0 w_{0z}) = -p_{1z} + \tau_{1x}^{xz} + \tau_{1z}^{zz}, \quad (2.33)$$

$$w_1 = u_{1z} = \tau_{1z}^{xz} = 0, \text{ at } z = 0, \quad (2.34)$$

$$-p_1 + h_{0x}^2 \tau_0^{xx} + 2h_{0x}^3 \tau_0^{xz} - \tau_0^{zz} h_{0x}^2 - 2h_{0x} \tau_1^{xz} + \tau_1^{zz} = -\frac{3}{2} \frac{1}{Ca} h_{0x}^2 h_{0xx}, \text{ at } z = h_0, \quad (2.35)$$

$$\tau_1^{xz} + h_{0x}^2 \tau_0^{xz} + h_{0x}(\tau_0^{zz} - \tau_0^{xx}) = 0, \text{ at } z = h_0. \quad (2.36)$$

Integrating Eq. (2.32) with respect to z and using Eq. (2.34), we obtain

$$\tau_1^{xz} = - \left[2\tau_{0x}^{xx} + \frac{1}{Ca} h_{0xxx} + 1 - Re(u_{0t} + u_0 u_{0x}) \right] z. \quad (2.37)$$

Substituting this into Eq. (2.36) gives

$$2(h_0 \tau_0^{xx})_x + h_0 \left[\frac{1}{Ca} h_{0xxx} + 1 \right] - Re h_0 (u_{0t} + u_0 u_{0x}) = 0. \quad (2.38)$$

Eq. (2.38) represents the force balance at the free surface of the extensional stress (represented by the first term), surface tension (represented by the second term), gravity (represented by the third term) and inertia (represented by the last term).

To determine the evolution equation of h_0 using Eq. (2.21), we also need to determine u_0 and the $O(\epsilon^2)$ correction u_1 . We use the constitutive law to determine these. From Eq. (2.22), we obtain

$$u_{0x} = \frac{1}{2\mu(\dot{\gamma}_0)}\tau_0^{xx}, \quad (2.39)$$

$$u_{1z} + w_{0x} = \frac{1}{\mu(\dot{\gamma}_0)}\tau_1^{xz}, \Rightarrow u_{1z} = \frac{1}{\mu(\dot{\gamma}_0)}\tau_1^{xz} - w_{0x} = \frac{1}{\mu(\dot{\gamma}_0)}\tau_1^{xz} + u_{0xx}z, \quad (2.40)$$

where $\dot{\gamma}_0 = |u_{0x}|$, is the leading order second invariant of the shear rate tensor. Integrating Eq. (2.37) and using the boundary condition $u_1 = 0$ at $z = h_0$ gives

$$u_1(x, z, t) = \frac{1}{2} \left[-\frac{1}{\mu(|u_{0x}|)} \left(2\tau_{0x}^{xx} + \frac{1}{Ca} h_{0xxx} + 1 - Re(u_{0t} + u_0 u_{0x}) \right) + u_{0xx} \right] (z^2 - h_0^2). \quad (2.41)$$

We note here that Champougny *et al.* [22] have used the boundary condition $\int_0^h u_1 dz = 0$.

Finally, the evolution equation for h_0 can be obtained from Eq. (2.21) as

$$h_{0t} + Q_{0x} + \epsilon^2 Q_{1x} = 0, \quad (2.42)$$

$$Q_0 = u_0 h_0, \quad Q_1 = \frac{1}{3} h_0^3 \left[\frac{1}{\mu(|u_{0x}|)} \left(2\tau_{0x}^{xx} + \frac{1}{Ca} h_{0xxx} + 1 - Re(u_{0t} + u_0 u_{0x}) \right) - u_{0xx} \right]. \quad (2.43)$$

Hence, Eqs. (2.42), (2.43), (2.38) and (2.39) provide a coupled system of three PDEs for the film's free surface evolution, $h_0(x, t)$, the extensional stress, $\tau_0^{xx}(x, t)$ and the extensional flow speed $u_0(x, t)$. In practise, it is more instructive to combine Eqs. (2.38) and (2.39) to write a single evolution equation for u_0 . This can be written as:

$$-Re h(u_{0t} + u_0 u_{0x}) + 4(h_0 \mu(|u_{0x}|) u_{0x})_x + h_0 \left[\frac{1}{Ca} h_{0xxx} + 1 \right] = 0. \quad (2.44)$$

The factor of 4 in the extensional viscosity term in Eq. (2.44) is the so-called *Trouton* viscosity [73]. The boundary conditions for Eqs. (2.42) and (2.44) are prescribed as follows:

$$h_0(0, t) = h_0(1, t) = 1, \quad Q(0, t) = Q(1, t) = 0; \quad (2.45)$$

the film is pinned at the top and bottom, and there is no flux through the boundaries.

$$Q(0, t) = Q(1, t) = 0 \Rightarrow u_0(0, t) = u_0(1, t) = 0, \quad \frac{1}{Ca} h_{0xxx}(0, t) = \frac{1}{Ca} h_{0xxx}(1, t) = -1. \quad (2.46)$$

The third and fourth boundary conditions describe no-slip at the ends while the last two describe the balance between capillary flow (represented by the third derivative) and gravity. Eqs. (2.45) and (2.46) provide the six boundary conditions required in total for Eqs. (2.42) and (2.44). In the film thickness equation, the contribution from the shear flow is $O(\epsilon^2)$ smaller than the extensional component. Hence, to leading order in ϵ , the PDE is hyperbolic. We include the $O(\epsilon^2)$ terms since they are important near the upper and lower boundary and for the boundary conditions in Eq. (2.46) to be

satisfied.

The master system of PDEs and boundary conditions for the evolution of the film's free surface $h(x, t)$ and the extensional flow speed $u(x, t)$ (dropping the subscript 0) for the configuration shown in Fig. 2.1 are given by:

$$h_t + Q_x = 0, \quad Q = uh + \epsilon^2 \frac{h^3}{3} \left[\frac{1}{\mu(|u_x|)} \left(4(\mu(|u_x|)u_x)_x + \frac{1}{Ca} h_{xxx} + 1 - Re(u_t + uu_x) \right) - u_{0xx} \right], \quad (2.47a)$$

$$- Re h(u_t + uu_x) + 4(h\mu(|u_x|)u_x)_x + h \left[\frac{1}{Ca} h_{xxx} + 1 \right] = 0, \quad (2.47b)$$

$$h(0, t) = h(1, t) = 1, \quad h_{xxx}(0, t) = h_{xxx}(1, t) = -Ca, \quad u(0, t) = u(1, t) = 0. \quad (2.47c)$$

Similar equations have been derived by Brush & Roper [18], without the $O(\epsilon^2)$ regularisation terms, and not including the effect of gravity. Eq. (2.47) is parametrised by the parameters Re and Ca . Our focus is on investigating the draining flow for $Re \ll 1$ and $Ca \gg 1$. In the subsequent chapters, we consider various functional forms of $\mu(|u_x|)$ corresponding to a Newtonian liquid (in chapter 3) and liquids displaying generalised non-Newtonian and visco-plastic behaviour (in chapter 4).

Chapter 3

Gravity-driven draining of a vertically-aligned thin Newtonian liquid free film

3.1 Introduction

This chapter investigates the evolution of a vertically aligned Newtonian liquid free film as it drains due to gravity and surface tension between two rigid supports (Figure 2.1 shows this configuration). This problem is the simplest model of a draining free liquid film. We use similarity and numerical solutions to characterise the early and late-time evolution of the free surface for a scenario where gravity and viscous effects dominate, and surface tension is comparatively smaller.

The outline of this chapter is as follows. In §3.2, we write down the evolution equations for the film's free surface $h(x, t)$ and the extensional flow speed $u(x, t)$ for a Newtonian liquid. §3.3 describes the spatial discretisation using the finite-difference scheme and the Method of Lines to solve the discretised system of PDEs. In §3.4, we perform numerical simulations of the evolution equations to determine the free surface shapes and extensional flow speeds, varying the parameter values. In §3.5 we derive early and late-time similarity solutions for the evolution of the free surface and the extensional flow speed. In §3.6 we discuss the main results.

3.2 Governing Equations

For a Newtonian liquid $\mu(|u_x|) = 1$. Substituting this in Eqs. (2.47), we obtain the evolution equations for the film's free surface $h(x, t)$ and the extensional flow speed $u(x, t)$ for a Newtonian liquid, given by:

$$h_t + Q_x = 0, \quad Q = uh + \epsilon^2 \frac{h^3}{3} \left[3u_{xx} + \frac{1}{Ca} h_{xxx} + 1 - Re(u_t + uu_x) \right], \quad (3.1a)$$

$$- Re h(u_t + uu_x) + 4(hu_x)_x + h \left[\frac{1}{Ca} h_{xxx} + 1 \right] = 0, \quad (3.1b)$$

$$h(0, t) = h(1, t) = 1, \quad h_{xxx}(0, t) = h_{xxx}(1, t) = -Ca, \quad u(0, t) = u(1, t) = 0. \quad (3.1c)$$

The above equations and boundary conditions are parametrised by the Capillary number Ca and the Reynold's number Re . We seek solutions of Eq. (3.1) for $Ca \gg 1$ and $Re \ll 1$, which corresponds to much weaker surface tension and inertial effects in

comparison to gravity, respectively. Eq. 3.1, including the boundary conditions are the same as those derived Schwartz & Roy [62], except that the free films investigated in this thesis do not include surfactants or surfactant-related effects. Similar evolution equations have also been derived focussing on particular balance of physical effects, e.g., Erneux & Davis [29] (extensional flow balancing inertia, not including gravity), Champougny *et al.* [22] (extensional flow balancing gravity and van der Waals forces) and Breward [15, 16], Brush & Davis [17] (balancing extensional flow with surface tension effects, not including gravity) and Davis *et al.* [26] (balancing extensional flow with surface tension effects, including gravity).

We first seek a numerical solution of Eq. (3.1) for varying Ca and Re using the finite difference method and the method of lines, outlined in §3.3.

3.3 Numerical solution using the finite difference method

We discretize the spatial derivatives in Eq. (3.1) using the finite difference method, but keep the time derivative continuous. The domain $[0, 1]$ is split into $N + 1$ discrete points, $0 = x_1 < x_2 < x_3, \dots < x_N < x_{N+1} = 1$, such that $x_{i+1} - x_i = \Delta x$ and the corresponding $(h, u)_i = (h, u)(x_i, t)$. We approximate a first, second and third

derivatives for an arbitrary function $f(x)$ as follows:

$$f_x(x) \approx f_{x,i} = \frac{f_{i+1} - f_i}{\Delta x} + O(\Delta x), \quad f_x(x) \approx f_{\bar{x},i} = \frac{f_i - f_{i-1}}{\Delta x} + O(\Delta x),$$

$$f_x(x) \approx \frac{f_{i+1} - f_{i-1}}{2\Delta x} + O(\Delta x^2), \quad (3.2a)$$

$$f_{xx}(x) \approx f_{\bar{x}\bar{x},i} = \frac{f_{i+1} - 2f_i + f_{i-1}}{\Delta x^2} + O(\Delta x^2), \quad (3.2b)$$

$$f_{xxx}(x) \approx f_{xxx,i} = \frac{f_{i+2} - 2f_{i+1} + 2f_{i-1} - f_{i-2}}{2\Delta x^3} + O(\Delta x^2). \quad (3.2c)$$

Using the above approximations, Eq. (3.1) is discretised as follows (keeping the time derivative continuous):

$$h_{t,i} + \frac{Q_{i+1} - Q_{i-1}}{2\Delta x} = 0, \quad Q_i = (uh)_i + \epsilon^2 \frac{h_i^3}{3} \left[3u_{xx,i} + \frac{1}{Ca} h_{xxx,i} + 1 - Re(u_{t,i} + u_i(\frac{u_i - u_{i-1}}{\Delta x})) \right], \quad (3.3a)$$

$$- Reh_i(u_{t,i} + u_i(\frac{u_i - u_{i-1}}{\Delta x})) + 4(\frac{h_{i+1} - h_{i-1}}{2\Delta x})(\frac{u_{i+1} - u_{i-1}}{2\Delta x}) + 4h_i(\frac{u_{i+1} - 2u_i + u_{i-1}}{\Delta x^2})$$

$$+ h_i[\frac{1}{Ca} h_{xxx,i} + 1] = 0, \quad (3.3b)$$

$$h_1 = h_{N+1} = 1, \quad u_1 = u_{N+1} = 0, \quad Q_1 = Q_{N+1} = 0. \quad (3.3c)$$

The second term in equation (3.1b) was obtained by applying the product rule,

$$(hu_x)_x = h_x u_x + h u_{xx} \approx (\frac{h_{i+1} - h_{i-1}}{2\Delta x})(\frac{u_{i+1} - u_{i-1}}{2\Delta x}) + h_i(\frac{u_{i+1} - 2u_i + u_{i-1}}{\Delta x^2}). \quad (3.4)$$

To evaluate $h_{xxx,i}$ at $i = 2, N$ we used the following finite difference approximations

$$h_{xxx,i} = \frac{h_{i+2} - 2h_{i+1} + 2h_{i-1} - h_{i-2}}{2\Delta x^3}. \quad (3.5)$$

Expressions for the fictitious endpoints h_0 and h_{N+2} , which are outside the domain, are found using one-sided finite differences, and the boundary conditions at $x = 0, 1$ given by $h_{xxx,1} = h_{xxx,N+1} = -Ca$. These can be written as:

$$h_0 = \frac{1}{3}(2Ca\Delta x^3 + 10h_1 - 12h_2 + 6h_3 - h_4) \quad (3.6)$$

$$h_{N+2} = \frac{1}{3}(-2Ca\Delta x^3 + 10h_{N+1} - 12h_N + 6h_{N-1} - h_{N-2}). \quad (3.7)$$

Eq. (3.3) represents a system of differential-algebraic equations (DAEs) which are solved using the method of lines [65]. We use the implicit solver *ode15i* in MATLAB (MATLAB 6.1, The MathWorks Inc., Natick, MA, 2000) for our numerical simulations. This solves a system of equations of the form $f(t, y, y') = 0$, for the dependent variable y . The unknowns h_i and u_i are numbered according to $y = (h_1, u_1, h_2, u_2, \dots, h_{N+1}, u_{N+1})$. This enables the Jacobian matrix to have a much smaller bandwidth which accelerates the computations, compared to a numbering system, for example, $y = (h_1, h_2, \dots, h_{N+1}, u_1, u_2, \dots, u_{N+1})$, which has a much bigger bandwidth.

3.4 Numerical results

In the numerical results to follow we investigate the evolution of varying the Capillary number $Ca \gg 1$ on the evolution of the film thickness $h(x, t)$ and extensional flow speed $u(x, t)$. Results not reported here have shown that varying the Reynolds number $Re \ll 1$ has no significant influence on the evolution of the film and the extensional speed, hence for all the results to follow we choose $Re = 0$. The initial condition is $h(x, 0) = 1$, and the corresponding initial condition for the extensional flow speed is $u(x, 0) = \frac{x(1-x)}{8}$ (by solving Eq. (3.1b) with $h = 1$). In all the results to follow we choose $\Delta x = 5 \times 10^{-4}$ for convergence to be achieved and the solutions to be accurate.

Figure 3.1(a, b, c) show the evolution of $h(x, t)$ ($h(x, t)$ is plotted on a logarithmic scale in (b)) and $u(x, t)$, respectively, for varying $t = 0$ to $t = 10^3$, with $Ca = 10^3$. At early times, the fluid has begun to flow vertically downwards (Fig. 3.1(c)) leading to thinning of the film in the upper region and a thickening in the lower region, and the film shape is concave-out (Fig. 3.1(a)). At late times, the fluid has drained significantly towards the lower end of the domain forming a quasi-static pendant drop there, leaving a very thin and almost flat film in the middle region, and a quasi-static capillary meniscus at the upper end (Fig. 3.1(a)). This late-time behaviour can be clearly observed using a logarithmic scale for $h(x, t)$ shown in Fig. 3.1(b). This shows the thinning middle section of the film connecting onto quasi-static curves at the top and bottom represented by the capillary meniscus and the pendant drop, respectively. In §3.5, we develop asymptotic solutions describing the late-time behaviour of the above

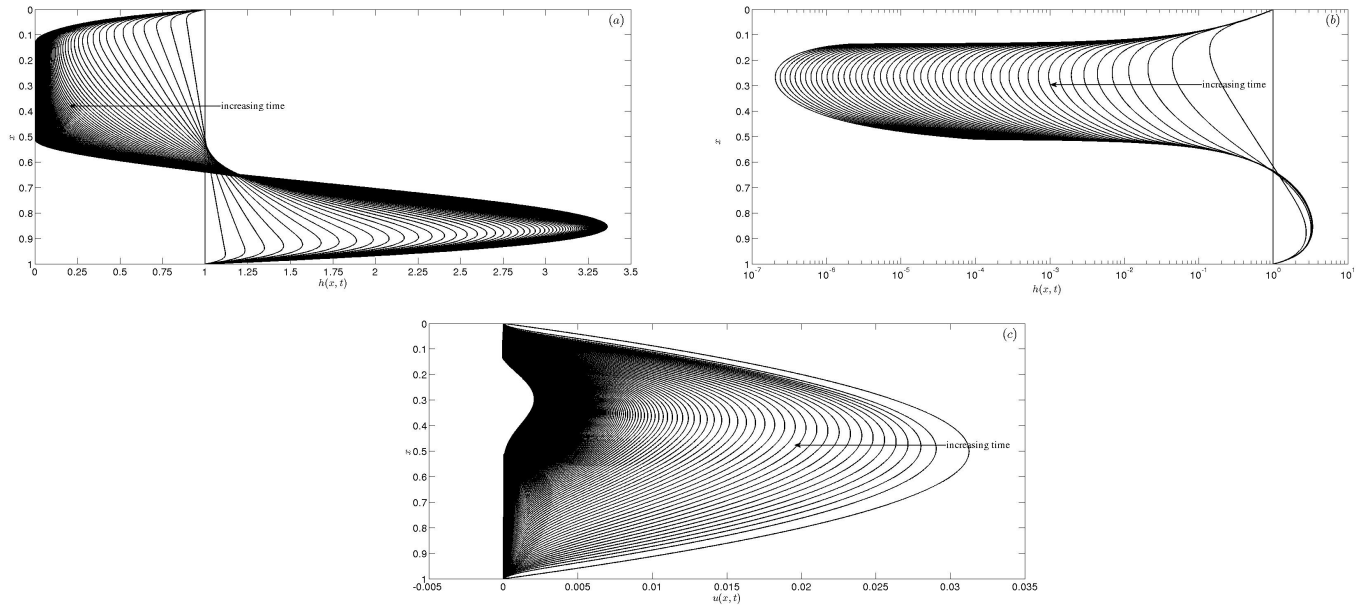


Figure 3.1: The evolution of (a), (b) the film thickness $h(x,t)$ (b plots $h(x,t)$ on a logarithmic scale), and (c) the extensional flow speed $u(x,t)$, for varying $t = 0$ to $t = 10^3$. The Capillary number $Ca = 10^3$, and $\Delta x = 5 \times 10^{-4}$.

long lengthscale structures, namely, the capillary meniscus, the middle section and the pendant drop, for $Ca \gg 1$. The maximum flow speeds are in the middle section of the film (Fig. 3.1(c)) which causes the film thickness to decrease severely there. It appears that the extensional flow approaches a steady profile for very large times (see Fig. 3.1(c)). The flow speed is zero near the top in the capillary meniscus region, and at the bottom in the pendant drop region.

We now describe the characteristic late-time flow behaviour and film evolution in regions of very small width of $O(1/Ca)$ near the top (where the upper meniscus meets the thin film section) and bottom ends (where the thin film meets the pendant drop) of the film. Figure 3.2(a – c) show the evolution of the film thickness $h(x,t)$, the extensional flow speed $u(x,t)$ and the stress balance given by Eq. (3.1b) near the bottom

end, respectively, for $t = (5, 6, 7, 8, 9, 10) \times 10^2$ and $Ca = 10^3$. We observe a similarity solution behaviour in the evolution of h and u . The similarity solution behaviour of h (see Fig. 3.2(a)) shows a family of solutions gradually thinning in time at its upstream end; at the downstream end, each solution connects onto a single quasi-static curve (represented by the pendant drop) at different locations (see Fig. 3.2(a)). The similarity solution behaviour of u shows a characteristic jump (or shock-like behaviour) in u at its downstream end (see Fig. 3.2(b)). This sudden deceleration of the flow is due to the sudden increase in film curvature (from almost zero in the flat draining film to $Ca \gg 1$ as the film connects onto the pendant drop). Indeed, the stress balance shown in Fig. 3.2(c) shows that the dominant contribution to the downward flow is due to the surface tension-related term, $\frac{1}{Ca}hh_{xxx}$ shown by the black solid lines (dominant compared to the contribution to the downward flow due to gravity in this region) which is balanced by the resistive (in this scenario) extensional stress term, $4(hu_x)_x$, shown by the blue dashed lines. The resistive extensional stress results in the sudden deceleration of the flow. Figure 3.2(d – f) show the evolution of the film thickness $h(x, t)$, the extensional flow speed $u(x, t)$ and the stress balance given by Eq. (3.1b) near the upper end, respectively, for $t = (5, 6, 7, 8, 9, 10) \times 10^2$ and $Ca = 10^3$. We also observe a similarity solution behaviour in the evolution of h and u . The similarity solution behaviour of h (see Fig. 3.2(d)) shows a family of solutions gradually thinning in time at its downstream end (much more severe thinning compared to that shown in Fig. 3.2(a)); at the upstream end, each solution connects onto a single quasi-static curve (represented by the capillary meniscus) at different locations. The similarity solution

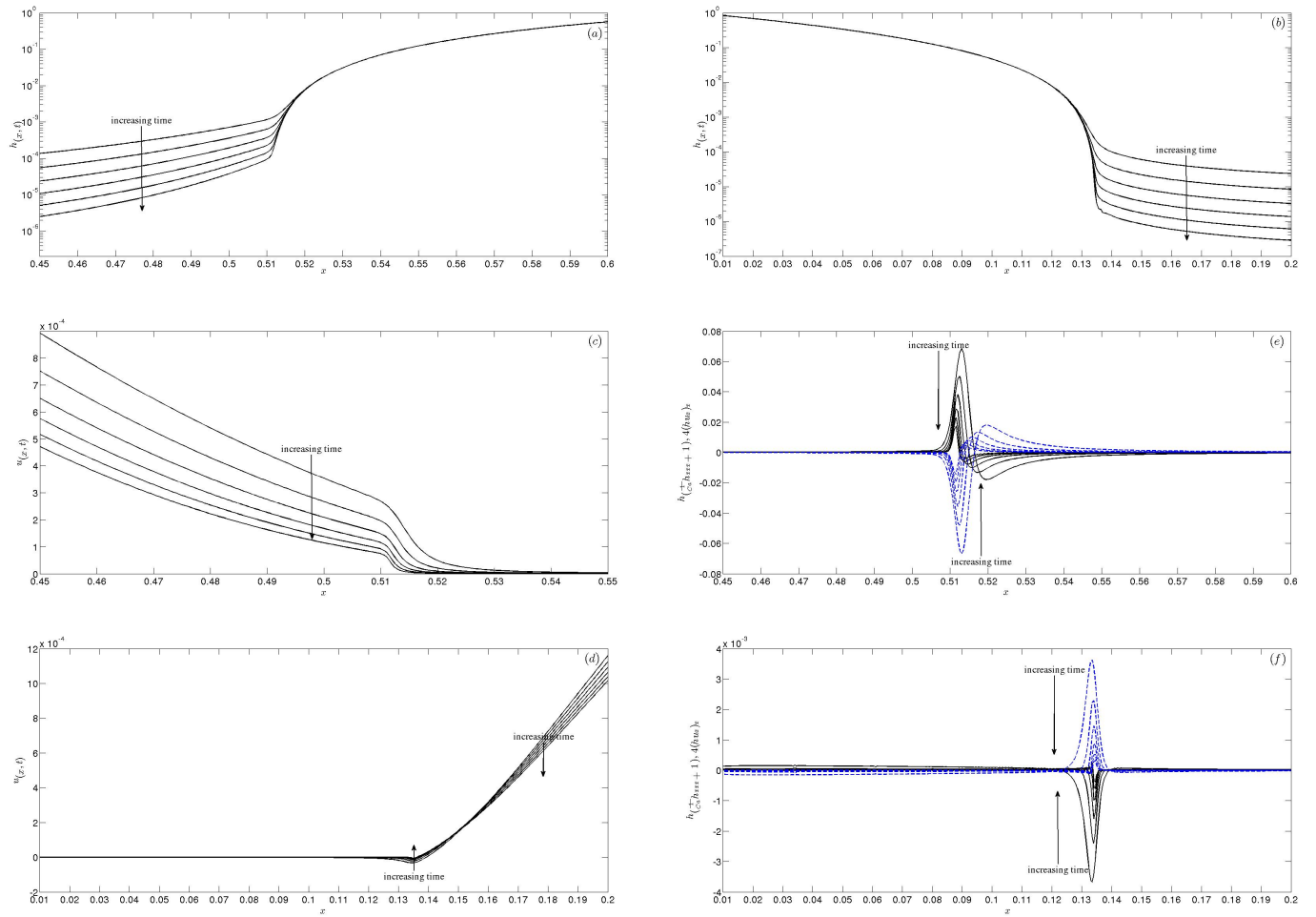


Figure 3.2: The evolution of the film thickness $h(x, t)$, the extensional flow speed $u(x, t)$ and the stress balance given by Eq. (3.1b) (the solid black lines represent $\frac{1}{Ca} h h_{xxx}$ and the blue dashed lines represent $4(hu_x)_x$) near the bottom end (a, b and c, respectively) and the upper end (d, e and f, respectively), for $t = (5, 6, 7, 8, 9, 10) \times 10^2$. The Capillary number $Ca = 10^3$, and $\Delta x = 5 \times 10^{-4}$.

behaviour of u shows a region where the flow is in the upward direction (see Fig. 3.2(e)) where $u < 0$). This reversal of the flow is due to the sudden increase in film curvature (from almost zero in the flat draining film to $Ca \gg 1$ as the film connects onto the upper capillary meniscus). Indeed, the stress balance shown in Fig. 3.2(f) shows that the contribution due to the surface tension-related term, $\frac{1}{Ca}hh_{xxx}$ (shown by the black solid lines) dominates that due to gravity in this region. Moreover, $\frac{1}{Ca}hh_{xxx}$ is negative resulting in flow being sucked into the capillary meniscus leading to the reversal in flow, however, the extensional stress term, $4(hu_x)_x$ (shown by the blue dashed lines) is positive, and resists this upward flow. However, at the downstream end of this region the contribution of $\frac{1}{Ca}hh_{xxx}$ is negligible in comparison to gravity, resulting in downward flow (see Fig. 3.2(e)). In §3.5, we develop asymptotic solutions describing the late-time behaviour of the above structures of $O(1/Ca)$ lengthscale where surface tension or curvature effects influence the evolution characteristics, for $Ca \gg 1$.

Figure 3.3(a, b) show the effect of increasing the Capillary number, $Ca = 10^2, 10^3, 10^4$, on $h(x, t_f)$ and $u(x, t)$, respectively. Here t_f is a fixed time for purposes of comparison, which is taken to be 10^3 for $Ca = 10^2, 10^3$; $t_f = 339$ for $Ca = 10^4$, as the film thins rapidly for very large values of Ca . We observe from Fig. 3.3(a) that as the Ca increases the film thins more rapidly and the middle section becomes much longer with a corresponding increase in the liquid collecting in the pendant drop at the bottom. As Ca increases, the effect of surface tension decreases in relation to gravity, thereby draining the film further. We also observe that the flow speed is much higher for larger

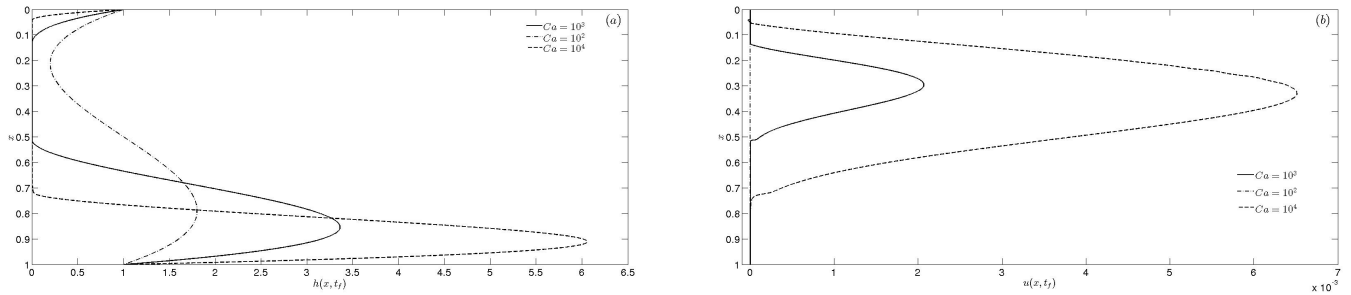


Figure 3.3: (a) Film thickness $h(x, t = t_f)$, and (b) extensional flow speed $u(x, t_f)$, for varying Capillary number, $Ca = 10^2, 10^3, 10^4$, for $\Delta x = 5 \times 10^{-4}$ and $t_f = 10^3$ for $Ca = 10^2, 10^3$; $t_f = 339$ for $Ca = 10^4$.

values of Ca (Fig. 3.3(b)), resulting in faster drainage, and hence the film thins rapidly.

Figure 3.4 tracks h_{min} , the global minimum in $h(x, t)$, as a function of time t , for fixed $Ca = 10^3$. $h_{min}(t)$ is attained precisely where $u(x, t)$ has a global maximum, and

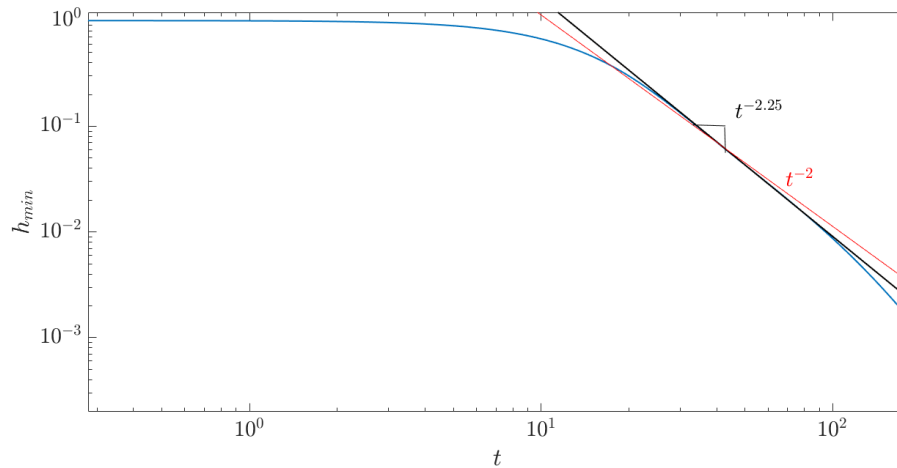


Figure 3.4: The global minimum h_{min} as a function of time t , for $Ca = 10^3$. The corresponding thinning rate is estimated to be $t^{-2.25}$, for the range of times where h_{min} reaches 1 – 10% of its initial value.

this is in the middle section of the film. After an initial transient, the film evolution displays power-law behaviour at large times. We estimate the film's thinning rate to be $t^{-2.25}$, for the range of times where h_{min} reaches 1 – 10% of its initial value. One

would expect this power-law behaviour to continue until the film becomes sufficiently thin and close to rupture, where other physical effects, such as van der Waals forces, need to be taken into account. We observe from Fig. 3.4, that for h_{min} much less than 1% of its initial value, the thinning rate appears to diverge from this estimated power-law thinning behaviour. The numerical solution when the film thickness reaches such small values may not be reliable for the value of $\Delta x = 5 \times 10^{-4}$ used. One would need smaller values of Δx for the solution to be reliable in its accuracy and convergence at these values, which is not considered here. We have also confirmed that the same power-law behaviour is observed as long as the $Ca \gg 1$; in our numerical solutions, this is observed for $Ca > 10^2$.

In the next section, we investigate the early and late-time self-similar evolution behaviour displayed by the film and the extensional flow speed as seen in the numerical simulations shown in Fig. 3.1.

3.5 Early and late-time similarity solutions of the film evolution and extensional flow

3.5.1 Early-time similarity solution

At early times, the majority of the film exhibits a characteristic concave-out form. This is due to the dominating extensional viscous flow, with the effect of surface tension

confined to boundary layers near the ends (see Fig. 3.5(a)). The early-time similarity solution was identified by Schwartz & Roy [62].

The early-time similarity solution for this section of the film is determined primarily by the simplified equations for the film thickness, h , and extensional flow speed, u , namely,

$$h_t + (uh)_x = 0, \quad (3.8)$$

$$(hu_x)_x = -\frac{1}{4}h. \quad (3.9)$$

Integrating Eq. (3.9) with respect to x , we obtain

$$hu_x|_{x_1(t)}^x = hu_x = -\frac{1}{4} \int_{x_1(t)}^x h \, dx, \quad (3.10)$$

where $x_1(t)$ is the location at which $u_x(x_1(t)) = 0$. Applying the method of characteristics to Eq. (3.8), we obtain

$$\frac{dh}{dt} = -u_x h = \frac{1}{4} \int_{x_1(t)}^x h \, dx, \quad (3.11)$$

$$\frac{dx}{dt} = u(x, t), \quad (3.12)$$

along the characteristics given by $x = x(\xi, t)$.

Conservation of liquid mass along the characteristics (which is valid at least at early times), implies $h \, dx = h_0 \, d\xi$, where $h_0 = h(\xi, t = 0)$. We take h_0 equal to a constant

which in our simulations is $h_0 = 1$. Using this, we have $\int_{x_1(t)}^x h dx = h_0 \int_{\xi_1(t)}^{\xi} d\xi = h_0(\xi - \xi_1(t))$, where $x_1(t) = x(\xi_1(t))$. Hence,

$$\frac{dh}{dt} = \frac{1}{4}h_0(\xi - \xi_1(t)). \quad (3.13)$$

Integrating with respect to t and using the initial condition, $h(\xi, t = 0) = h_0$, we obtain

$$h(x(\xi, t), t) = h_0 \left[1 + \frac{1}{4}(\xi t - \int_0^t \xi_1 dt) \right]. \quad (3.14)$$

Now, we have $h(x(\xi, t), t) = h_0 \frac{d\xi}{dx}$ (using mass conservation along a characteristic).

Hence,

$$\frac{d\xi}{dx} = 1 + \frac{1}{4}(\xi t - \int_0^t \xi_1 dt), \quad \text{or} \quad \frac{d\xi}{dx} - \frac{1}{4}\xi t = 1 - \frac{1}{4} \int_0^t \xi_1 dt. \quad (3.15)$$

The solution for this using the boundary condition, $x(\xi = 0, t) = 0$ (or $\xi(x = 0, t) = 0$),

is

$$\xi(x, t) = -4 \frac{[1 - e^{xt/4}]}{t} \left[1 - \frac{1}{4} \int_0^t \xi_1 dt \right]. \quad (3.16)$$

Using this, Eq. (3.14) can be written as

$$h(x(\xi, t), t) = h_0 e^{xt/4} \left[1 - \frac{1}{4} \int_0^t \xi_1 dt \right]. \quad (3.17)$$

Using Eq. (3.10) and the above relations, we obtain

$$u_x = -\frac{[1 - e^{-xt/4}]}{t}. \quad (3.18)$$

Integrating this and using the boundary condition, $u(x = 0, t) = 0$, gives

$$u(x, t) = -\frac{x}{t} - \frac{4}{t^2} [e^{(x_1-x)t/4} - e^{x_1t/4}]. \quad (3.19)$$

Using the boundary condition, $x(\xi = 1, t) = 1$ (or $\xi(x = 1, t) = 1$), in Eq. (3.16) gives

$$1 - \frac{1}{4} \int_0^t \xi_1 dt = \frac{1}{4} \frac{t}{[e^{t/4} - 1]}. \quad (3.20)$$

Hence,

$$h(x(\xi, t), t) = \frac{1}{4} h_0 \frac{te^{xt/4}}{[e^{t/4} - 1]}. \quad (3.21)$$

Using the boundary condition, $u(x = 1, t) = 0$, we can solve for $x_1(t)$ as:

$$x_1(t) = \frac{4}{t} \log \left(\frac{t}{4[1 - e^{-t/4}]} \right). \quad (3.22)$$

Figure 3.5(a, b) show a comparison between the numerical solution and the early-time similarity solution for h and u , respectively, for times $t = 1, 2, 3, 4, 5, 6, 7$. Good agreement is observed at early time for h , except for the surface tension boundary layers near the top and bottom supports. As t increases, the agreement is not so good. Good agreement is also observed at early time for u , except that the similarity solution slightly overestimates the corresponding numerical solution. This might be due to the influence of the boundary layers near the top and the bottom supports.

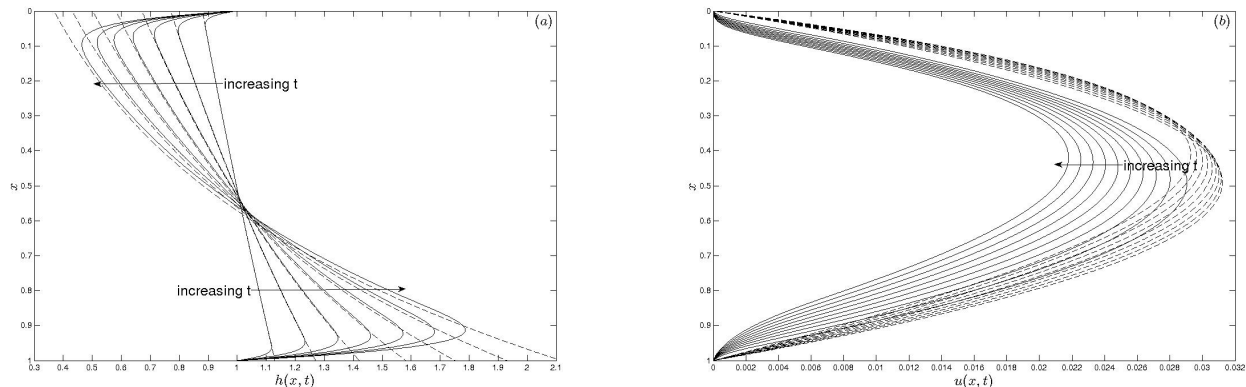


Figure 3.5: Computed film thickness profiles, h , (a) and extensional flow speeds, u , (b) (solid lines) and the corresponding early-time similarity solution (dashed lines) given by Eqs. (3.19,3.21), for times, $t = 1, 2, 3, 4, 5, 6, 7$.

3.5.2 Late-time similarity solution

Based on the observation from the numerical solutions shown previously for Capillary number, $Ca \gg 1$, we postulate a self-similar structure of the late-time evolution which can be divided into 5 regions (see Fig. 3.6), namely,

- (i) Region I: a quasi-static capillary meniscus in $0 \leq x \leq x_1(t)$ where gravity and surface tension forces balance.
- (ii) Region II: an almost flat draining section of the film between $x_1(t) \leq x \leq x_2(t)$, where gravity and extensional viscous forces balance, and surface tension is negligible.
- (iii) Region III: a quasi-static pendant drop in $x_2(t) \leq x \leq 1$ where gravity and surface tension forces balance.
- (iv) Region A: a short transition region of width $O(1/Ca)$ between regions I and II,

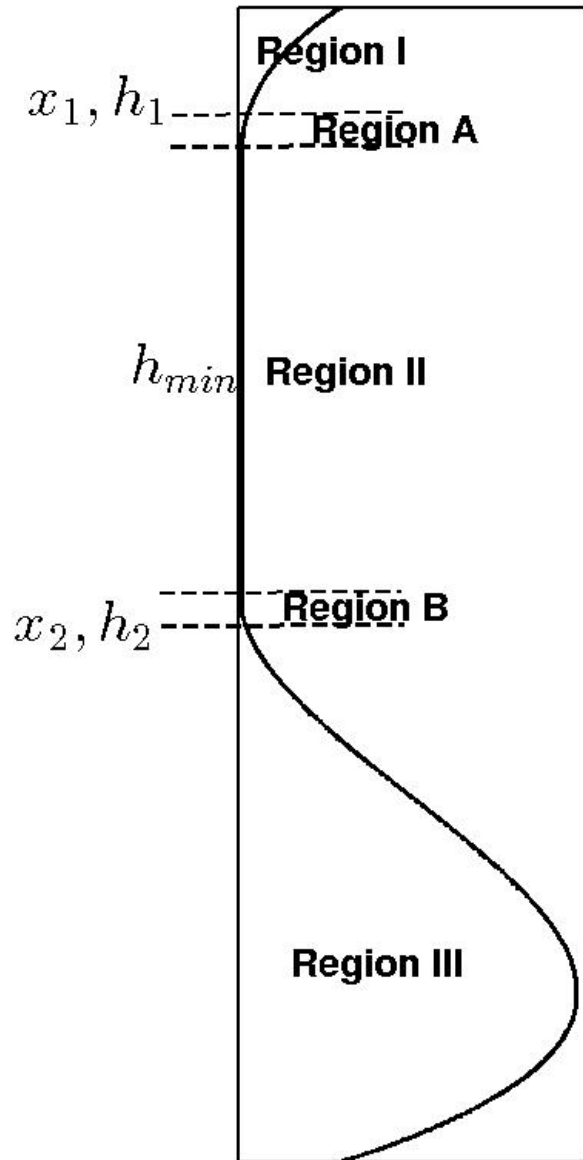


Figure 3.6: Late-time self-similar spatial structure of the film thickness h , showing Region I, the capillary meniscus, Region II, the almost flat draining section, Region III, the pendant drop and two transition regions, A and B. The characteristic variables, $x_{1,2}(t)$, $h_{1,2}$ and $h_{min}(t)$ are explained in the sections describing each region.

where extensional viscous and surface tension forces balance.

(iv) Region B: a short transition region of width $O(1/Ca)$ between regions II and III

where extensional viscous and surface tension forces balance.

The film evolution process is characterised by the key variables: $x_1(t)$, representing the location of the leading edge of the capillary meniscus in Region I; $h_1(t)$ the film thickness at $x_1(t)$; $x_2(t)$, representing the location of the leading edge of the pendant drop in Region III; $h_2(t)$ the film thickness at $x_2(t)$, and $h_{min}(t)$, the minimum film thickness in Region II. We also define $x_{\{1,2\}_1}(t)$, representing the location corresponding to the minimum and maximum in the change in curvature $h_{xxx}(t)$ in the transition regions A and B , respectively, and $x_{\{1,2\}_\infty} = \lim_{t \rightarrow \infty} x_{\{1,2\}_1}$ to be their limiting values. The quantities $x_{\{1,2\}_\infty}$ characterise the final state (say) separating Region I, with volume V_1 , and Region III, with volume $V_2 = 1 - V_1$ by a film of negligible thickness in Region II. We will show below that the closure conditions, that will enable us to fully describe the asymptotics of the evolution, assumes that the locus of points $(x_{1,2}, h_{1,2})$ will lie along the final state of Regions I and III, respectively. Their evolution will be determined by the change in volume in each of these regions due to flux entering or leaving the thin film in Region II.

Figure 3.7 (solid lines) shows the time evolution of $x_{1,2}$ and $x_{\{1,2\}_1}$ (Fig. 3.7(a)), and $h_{1,2,min}$ (Fig. 3.7(b)) determined from the numerical solution of the PDEs for time $t = 5 \times 10^2 - 10^3$, with $Ca = 10^3$ and $Re = 0$. These are computed from the numerical solution as follows: x_1 is the location corresponding to the endpoint of the interval

near the top of the film where $h_{xxx} + Ca$ differs from zero for the first time ($> 10^{-6}$, in practice; these quantities are necessarily equal to zero for $x < x_1$ and non-zero for $x > x_1$), with corresponding film thickness h_1 ; x_2 is the location corresponding to the starting point of the interval near the bottom of the film where $h_{xxx} + Ca$ is equal to zero for the first time ($< 10^{-6}$, in practice; these quantities are necessarily equal to zero for $x > x_2$ and non-zero for $x < x_2$), with corresponding film thickness h_2 ; x_{1_1} is the location corresponding to the minimum value of h_{xxx} near the top of the film where $h_{xxx} < 0$ (note that $x_1 < x_{1_1}$); x_{2_1} is the location corresponding to the maximum value of h_{xxx} near the bottom of the film where $h_{xxx} > 0$ (note that $x_2 > x_{2_1}$); h_{min} is the minimum film thickness in Region II, corresponding to the location where the extensional flow speed u is maximum.

We note from Fig. 3.7(a) that $x_{\{1,2\}_1}$ are almost constant in time, with $x_{1_\infty} = \lim_{t \rightarrow \infty} x_1 \approx 0.13464$ (corresponding to $V_1 \approx 0.04$) and $x_{2_\infty} = \lim_{t \rightarrow \infty} x_2 \approx 0.511$ (corresponding to $V_2 \approx 0.96$). The evolution of the characteristic variables shown in Fig. 3.7(a) suggests that the late-time evolution is characterised by two quasi-static regions, regions I and III, and region II connects onto these two regions via a family of solutions representing the transition regions A and B. The family of solutions in the transition regions emanate from the two quasi-static regions at $x_{1,2}(t)$. Figure 3.7(b) shows that the late-time thinning is severest in the film's middle section followed by less severe thinning near the top and then near the bottom.

We now describe each region in turn.

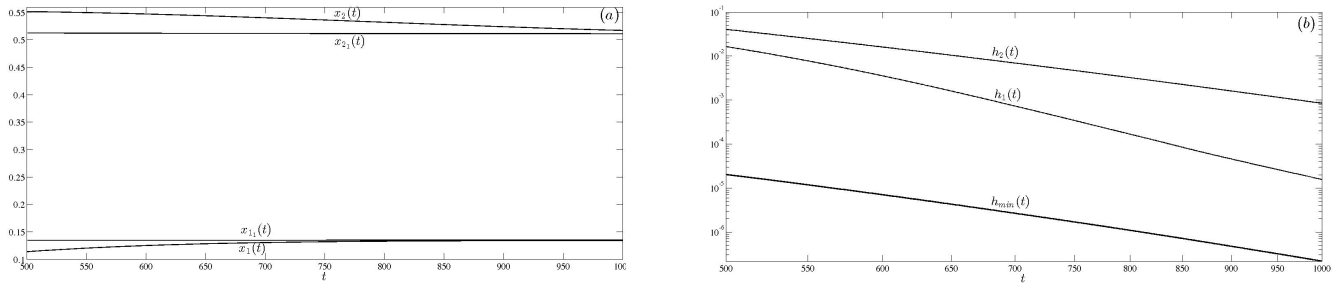


Figure 3.7: Evolution of the characteristic variables: (a) $x_{1,2}$ and $x_{\{1,2\}1}$, and (b) $h_{1,2}$ and h_{min} , for time $t = 5 \times 10^2 - 10^3$ from the numerical solution (solid curves) and the asymptotic model (dashed curves). The parameter values are $Ca = 10^3$ and $Re = 0$.

Region I: the capillary meniscus

This region lies between $0 \leq x \leq x_1$, and is quasi static with $u = 0$. The evolution is determined by balancing gravity and surface tension.

$$h_{xxx} = -Ca. \quad (3.23)$$

Integrating thrice with respect to x and applying the boundary condition, $h(x = 0) = 1$, the solution is given by

$$h(x) = -\frac{Ca}{6}x^3 + \frac{Cx^2}{2} + Dx + 1, \quad (3.24)$$

where C and D are constants of integration that need to be determined. To determine C and D we assume that the long-time behaviour of the meniscus is such that it meets the centreline $z = 0$ at the location $x = x_{1\infty}$ with zero effective contact angle, i.e., with zero slope, $h_x = 0$. So, we prescribe $h(x_{1\infty}) = h_x(x_{1\infty}) = 0$. Applying these

two boundary conditions at $x = x_{1\infty}$ gives two simultaneous equations for C and D , namely,

$$\begin{aligned} h(x = x_{1\infty}) &= -\frac{Ca}{6}x_{1\infty}^3 + \frac{Cx_{1\infty}^2}{2} + Dx_{1\infty} + 1 = 0, \\ h_x(x = x_{1\infty}) &= -\frac{Ca}{2}x_{1\infty}^2 + Cx_{1\infty} + D = 0. \end{aligned} \quad (3.25)$$

Solving the above equations simultaneously, we obtain

$$\begin{aligned} C &= \frac{2}{x_{1\infty}^2} + \frac{2Cax_{1\infty}}{3}, \\ D &= -\left(\frac{2}{x_{1\infty}} + \frac{Cax_{1\infty}^2}{6}\right). \end{aligned} \quad (3.26)$$

Hence,

$$h(x, t) = -\frac{Ca}{6}x^3 + \frac{Cx^2}{2} + Dx + 1, \quad (3.27)$$

with C and D given by the above expressions depending on the capillary number Ca and $x_{1\infty}$. The unknown quantity $x_{1\infty}$ is determined by imposing that the volume of this region is V_1 . Hence, $\int_0^{x_{1\infty}} h \, dx = V_1$. Using this, we obtain:

$$Cax_{1\infty}^4 - 8\left[\frac{1}{x_{1\infty}^2} + \frac{Cax_{1\infty}}{3}\right]x_{1\infty}^3 + 12\left[\frac{2}{x_{1\infty}} + \frac{Cax_{1\infty}^2}{6}\right]Cax_{1\infty}^2 + 24(V_1 - x_{1\infty}) = 0. \quad (3.28)$$

Equation (3.28) is a quartic equation for $x_{1\infty}$ for a given value of Ca and V_1 .

Figure 3.8 plots h versus $x - x_{1\infty}$ (black curves) for $t = 5 \times 10^2 - 10^3$ using the numerical solution shown in Fig, for $Ca = 10^3$. The red dashed line shows the corresponding

late-time asymptotic solution given by Eq. (3.27), using $V_1 = 0.04$ (corresponding $x_{1\infty} = 0.13464$). We observe that the asymptotic solution agrees very well with the scaled numerical solution.

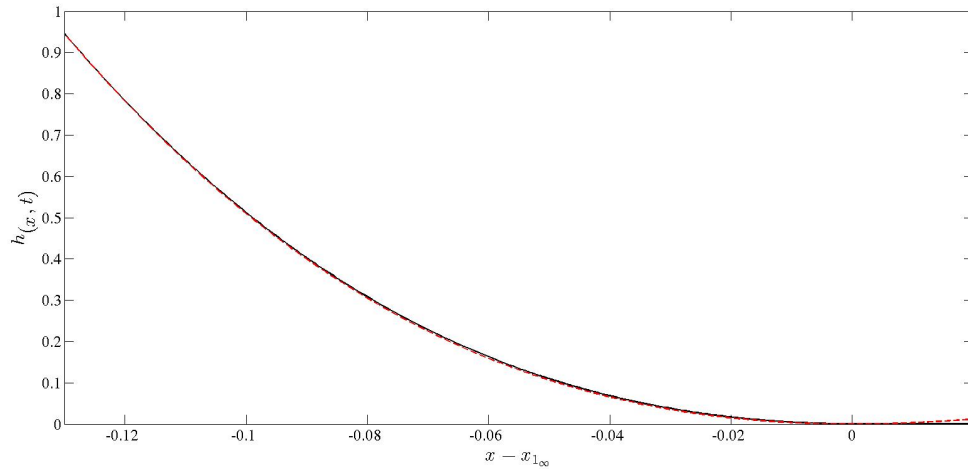


Figure 3.8: Evolution of h in region I using data shown in Fig. for time $t = 5 \times 10^2 - 10^3$ (solid black curves) for $Ca = 10^3$. The red dashed line shows the corresponding late-time asymptotic solution given by Eq. (3.27), using $V_1 = 0.04$ (corresponding $x_{1\infty} = 0.13464$).

Region II - the middle draining section

Extensional viscous forces control the film evolution in this region between $x_1 \leq x \leq x_2$.

The film is almost flat, so surface tension effects are negligible. The flow in this region is controlled by competing extensional viscous forces and gravity.

$$h_t + (uh)_x = 0, \quad (3.29)$$

$$(hu_x)_x = -\frac{1}{4}h. \quad (3.30)$$

Integrating Eq. (3.29) with respect to x , we obtain

$$(uh)(x, t) = (uh)(x_1) - \int_{x_1}^x h_t dx, \quad \text{or} \quad Q = Q_1(t) - \int_{x_1}^x h_t dx, \quad (3.31)$$

where $Q = uh$ and $Q_1(t) = (uh)(x = x_1(t))$. Hence,

$$h(x, t) = \frac{Q_1(t) - \int_{x_1}^x h_t dx}{u(x, t)}. \quad (3.32)$$

Also, using Eq. (3.31), we can write

$$Q_2(t) = Q_1(t) - \int_{x_1}^{x_2} h_t dx, \quad (3.33)$$

where $Q_2(t) = (uh)(x = x_2(t))$. Using Eq. (3.32), we can rewrite Eq. (3.30) in terms of u as:

$$\left(\left[Q_1(t) - \int_{x_1}^x h_t dx \right] \frac{u_x}{u} \right)_x = -\frac{1}{4} \frac{\left[Q_1(t) - \int_{x_1}^x h_t dx \right]}{u}. \quad (3.34)$$

We are unable to determine the solution of Eqs. (3.32,3.34) analytically. However, it will be useful to determine the behaviour of h and u near $x_{1,2}$ to match with regions A and B, respectively. We rewrite Eq. (3.34) as

$$Q(x, t)[uu_{xx} - u_x^2] + Q_x(x, t)uu_x + \frac{1}{4}Qu = 0, \quad (3.35)$$

where $Q(x, t)$ is defined in Eq. (3.31). We seek the behaviour of u subject to the boundary conditions, $u(x_{1,2}, t) = u_x(x_{1,2}, t) = 0$. We expand u in a Taylor's series

about $x = x_{1,2}$:

$$u(x, t) = u^{(2)}(x_{1,2}, t) \frac{(x - x_{1,2})^2}{2} + u^{(3)}(x_{1,2}, t) \frac{(x - x_{1,2})^3}{6} + u^{(4)}(x_{1,2}, t) \frac{(x - x_{1,2})^4}{24} + \dots$$

Here the superscript represents a higher order derivative with respect to x . We also expand

$Q(x, t)$ in a Taylor's series about $x = x_{1,2}$:

$$Q(x, t) = Q_{1,2}(t) + Q^{(1)}(x_{1,2}, t)(x - x_{1,2}) + Q^{(2)}(x_{1,2}, t) \frac{(x - x_{1,2})^2}{2} + \dots$$

Substituting the above in Eq. (3.35), we obtain the following sequence of problems. At $O((x - x_{1,2})^2)$,

we have $u^{(2)}(x_{1,2}, t) = \frac{1}{4}$. At $O((x - x_{1,2})^3)$, we obtain:

$$\begin{aligned} & -Q_{1,2}u^{(2)}(x_{1,2})u^{(3)}(x_{1,2}) - Q^{(1)}(x_{1,2}, t)[u^{(2)}(x_{1,2})]^2 + \frac{2}{3}Q_{1,2}u^{(2)}(x_{1,2})u^{(3)}(x_{1,2}) \\ & + Q^{(1)}(x_{1,2}, t)[u^{(2)}(x_{1,2})]^2 + \\ & \left[\frac{1}{24}Q_{1,2}u^{(3)}(x_{1,2}) + \frac{1}{8}Q^{(1)}(x_{1,2}, t)u^{(2)}(x_{1,2}) \right] = 0. \end{aligned} \quad (3.36)$$

Using $u^{(2)}(x_{1,2}) = 1/4$, we obtain $u^{(3)}(x_{1,2}) = \frac{3Q^{(1)}(x_{1,2}, t)}{4Q_{1,2}}$. The solutions for u and h

about $x = x_{1,2}$ are then given by

$$u(x, t) = \frac{1}{8}[x - x_{1,2}(t)]^2 \left[1 + \frac{Q^{(1)}(x_{1,2}, t)}{Q_{1,2}}(x - x_{1,2}) \right] + O((x - x_{1,2})^4), \quad (3.37)$$

$$h(x, t) = \frac{8Q_{1,2}(t)}{[x - x_{1,2}(t)]^2}, \quad (3.38)$$

near $x = x_{1,2}$, respectively. We approximate $Q^{(1)}(x_1, t)$ as follows. We approximate

$Q = Q_1(t) - \int_{x_1}^x h_t dx$ near $x = x_1$ as $Q = Q_1(t) - h_{1_t}(t)(x - x_1) + O((x - x_1)^2)$.

Hence, $Q^{(1)}(x_1, t) \approx -h_{1_t}(t)$, so the solution of u and h near $x = x_1$ can be written as

$$u(x, t) = \frac{1}{8}[x - x_1(t)]^2 \left[1 - \frac{h_{1_t}(t)}{Q_1}(x - x_1) \right] + O((x - x_1)^4), \quad (3.39)$$

$$h(x, t) = \frac{8Q_1(t)}{[x - x_1(t)]^2}, \quad (3.40)$$

respectively. Similarly, we approximate $Q = Q_1(t) - \int_{x_1}^x h_t dx = Q_2(t) + \int_x^{x_2} h_t dx$ near $x = x_2$ as $Q = Q_2(t) - h_{2_t}(t)(x - x_2) + O((x - x_2)^2)$. Hence, $Q^{(1)}(x_2, t) \approx -h_{2_t}(t)$, so the solution of u and h near $x = x_2$ can be written as

$$u(x, t) = \frac{1}{8}[x - x_2(t)]^2 \left[1 - \frac{h_{2_t}(t)}{Q_2}(x - x_2) \right] + O((x - x_2)^4), \quad (3.41)$$

$$h(x, t) = \frac{8Q_2(t)}{[x - x_2(t)]^2}, \quad (3.42)$$

respectively.

In order to make analytical progress we resort to making some meaningful approximations, particularly, to the unsteady term h_t . The accuracy of the solution based on these approximations will be tested against corresponding numerical solutions.

Quasi-steady approximation $h_t \approx 0$ ($Q_1 = Q_2 = Q$)

Eq. (3.34) can then be written as:

$$\left(\frac{u_x}{u}\right)_x = -\frac{1}{4u}, \quad \text{or} \quad uu_{xx} - u_x^2 + \frac{1}{4}u = 0, \quad (3.43)$$

subject to the boundary conditions, $u(x_1(t)) = u(x_2(t)) = 0$. This has solution

$$u(x) = \left[\frac{(x_2(t) - x_1(t))^2}{8\pi^2} \right] \sin^2 \left(\pi \left[\frac{x - x_1(t)}{x_2(t) - x_1(t)} \right] \right). \text{ Hence, the approximate solution}$$

in this region is given by:

$$h(x, t) = \left[\frac{8\pi^2 Q(t)}{(x_2(t) - x_1(t))^2} \right] \frac{1}{\sin^2 \left(\pi \left[\frac{x - x_1(t)}{x_2(t) - x_1(t)} \right] \right)}, \quad (3.44)$$

$$u(x, t) = \left[\frac{(x_2(t) - x_1(t))^2}{8\pi^2} \right] \sin^2 \left(\pi \left[\frac{x - x_1(t)}{x_2(t) - x_1(t)} \right] \right), \quad (3.45)$$

where $Q(t)$ is a constant flux in this region. The maximum extensional flow speed, $u_{max}(t)$ and minimum film thickness, $h_{min}(t)$, in this region is at $x = x_1(t) + (x_2(t) - x_1(t))/2$ and is given by

$$h_{min}(t) = \frac{8\pi^2 Q(t)}{[x_2(t) - x_1(t)]^2}, \quad (3.46)$$

$$u_{max}(t) = \frac{[x_2(t) - x_1(t)]^2}{8\pi^2}. \quad (3.47)$$

The unknown flux $Q(t)$ and the evolution of $x_1(t)$ and $x_2(t)$ will be determined from the transition regions A and B . Figure 3.9 shows the family of solutions characterised by $x_{1,2}$ for the extensional flow speed $u(x, t)$ versus $(x - x_1(t))/(x_2(t) - x_1(t))$ for $t = 5 \times 10^2 - 10^3$ using the numerical solution shown in Fig. The blue, green and red dashed curves show particular solutions of Eq. (3.45) for $x_{1,2}$ evaluated from the numerical solution at $t = 5 \times 10^2, 8 \times 10^2, 10^3$, respectively. We observe that although the quasi-steady approximation captures the general trends, assuming a constant flux of liquid through this region does not work very well in describing its evolution. This

suggests the important contribution of the unsteady term h_t in this region.

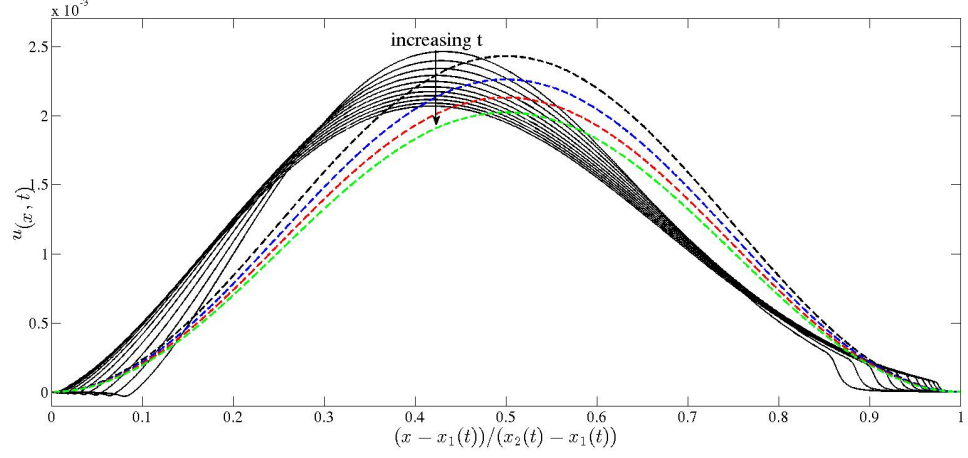


Figure 3.9: Evolution of u in region II using data shown in Fig. for time $t = 5 \times 10^2 - 10^3$. The blue, green and red dashed curves show the solution of Eq. (3.45) for $x_{1,2}$ evaluated from the numerical solution at $t = 5 \times 10^2, 8 \times 10^2, 10^3$, respectively.

Approximation $h_t \approx h_{min,t}$

A simple approximation of the unsteady term h_t is to assume it to be constant, $h_t \approx h_{min,t}$ (say), where h_{min} is the minimum film thickness of the middle section of the film.

Using this approximation, Eqs. (3.32,3.34) can be simplified to

$$h(x, t) = \frac{Q_1(t) - h_{min,t}(x - x_1)}{u(x, t)}, \quad (3.48)$$

$$\left([Q_1(t) - h_{min,t}(x - x_1)] \frac{u_x}{u} \right)_x = -\frac{1}{4} \frac{[Q_1(t) - h_{min,t}(x - x_1)]}{u}. \quad (3.49)$$

We are unable to solve Eq. (3.49) for the solution of u analytically. Using the approximation $h_t \approx h_{min,t}$ in Eq. (3.33), we obtain

$$Q_2(t) = Q_1(t) - h_{min,t}(x_2 - x_1), \Rightarrow h_{min,t} = \frac{[Q_1(t) - Q_2(t)]}{[x_2(t) - x_1(t)]}, \quad (3.50)$$

which provides an evolution equation for h_{min} . Also, using this approximation, $h_{1,2t} \approx h_{min,t}$, hence u and h near $x = x_{1,2}$ can be written as:

$$u(x, t) = \frac{1}{8}[x - x_1(t)]^2 \left[1 - \frac{h_{min,t}(t)}{Q_1}(x - x_1) \right] + O((x - x_1)^4), \quad (3.51)$$

$$h(x, t) = \frac{8Q_1(t)}{[x - x_1(t)]^2}, \quad (3.52)$$

$$u(x, t) = \frac{1}{8}[x - x_2(t)]^2 \left[1 - \frac{h_{min,t}(t)}{Q_2}(x - x_2) \right] + O((x - x_2)^4), \quad (3.53)$$

$$h(x, t) = \frac{8Q_2(t)}{[x - x_2(t)]^2}, \quad (3.54)$$

respectively.

Comparison with numerical solutions.

Region III - the pendant drop

This region lies between $x_2 \leq x \leq 1$, and is quasi static with $u = 0$. The evolution is determined by balancing gravity and surface tension.

$$h_{xxx} = -Ca, \quad (3.55)$$

which on integrating thrice with respect to x and using the boundary condition, $h(1) = 1$, gives

$$h(x) = -\frac{Ca}{6}(x-1)^3 + C\frac{(x-1)^2}{2} + D(x-1) + 1, \quad (3.56)$$

where C and D are constants of integration that need to be determined. To determine C and D we assume that the long-time behaviour of the pendant drop is such that it meets the centreline $z = 0$ at the location $x = x_{2\infty}$ with zero effective contact angle, i.e., with zero slope, $h_x = 0$. So, we prescribe $h(x_{2\infty}) = h_x(x_{2\infty}) = 0$. Applying these two boundary conditions at $x = x_{2\infty}$ gives two simultaneous equations for C and D , namely,

$$\begin{aligned} C &= \frac{2}{(x_{2\infty}-1)^2} + \frac{2Ca(x_{2\infty}-1)}{3}, \\ D &= -\left(\frac{2}{(x_{2\infty}-1)} + \frac{Ca(x_{2\infty}-1)^2}{6}\right), \end{aligned} \quad (3.57)$$

to give

$$h(x, t) = -\frac{Ca}{6}(x-1)^3 + \frac{C(x-1)^2}{2} + D(x-1) + 1, \quad (3.58)$$

with C and D given by the above expressions, depending on the capillary number Ca and $x_{2\infty}$. The unknown quantity $x_{2\infty}$ is determined by imposing that the volume of

this region is $V_2 = 1 - V_1$. Hence, $\int_{x_{2\infty}}^1 h \, dx = V_2$. Using this, we obtain:

$$\begin{aligned} & Ca(x_{2\infty} - 1)^4 - 8 \left[\frac{1}{(x_{2\infty} - 1)^2} + \frac{Ca(x_{2\infty} - 1)}{3} \right] (x_{2\infty} - 1)^3 \\ & + 12 \left[\frac{2}{(x_{2\infty} - 1)} + \frac{Ca(x_{2\infty} - 1)^2}{6} \right] (x_{2\infty} - 1)^2 + 24(V_2 - x_{2\infty} + 1) = 0. \end{aligned} \quad (3.59)$$

Equation (3.59) is a quartic equation for $x_{2\infty}$ for a given value of Ca and V_2 .

Figure 3.10 plots h versus $x - x_{2\infty}$ (black curves) for $t = 5 \times 10^2 - 10^3$ using the numerical solution shown in Fig, for $Ca = 10^3$. The red dashed line shows the corresponding late-time asymptotic solution given by Eq. (3.58), using $V_2 = 1 - 0.04 = 0.96$ (corresponding $x_{2\infty} = 0.511$). We observe that the asymptotic solution agrees very well with the scaled numerical solution.

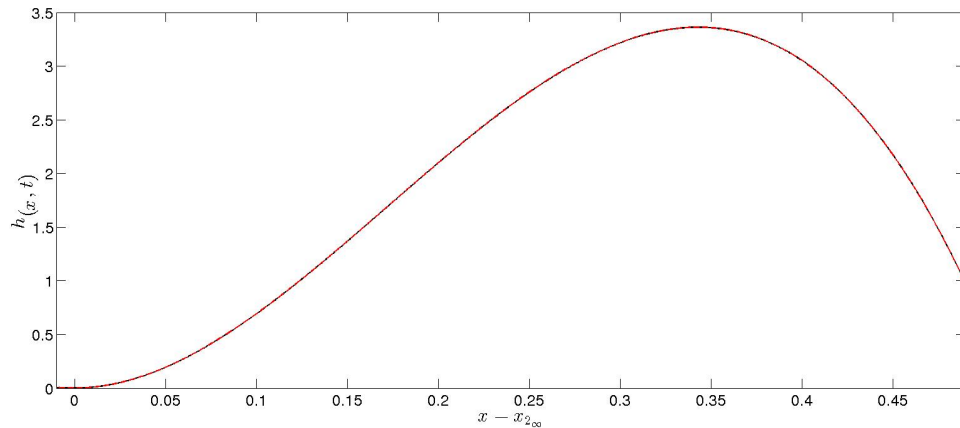


Figure 3.10: Evolution of h in region III using data shown in Fig. for time $t = 5 \times 10^2 - 10^3$ (solid black curves) for $Ca = 10^3$. The red dashed line shows the corresponding late-time asymptotic solution given by Eq. (3.58), using $V_2 = 1 - 0.04 = 0.96$ (corresponding $x_{2\infty} = 0.511$).

Region B: the transition region between regions II and III

This region around $x = x_{2_1}$ is characterised by a large change in the curvature h_{xxx} (see Fig. 3.2(c)). Hence, surface tension due to changes in curvature is the primary mechanism driving a downward flow into the pendant drop in region III with gravity playing a secondary role further contributing to the downward flow; this flow is resisted by the extensional viscous forces. The lengthscale of this region based on balancing surface tension and extensional viscous forces is of $O(1/Ca)$. Letting $x = x_{2_1} + (1/Ca)\xi$, we can write the evolution equations for h and u as:

$$\frac{1}{Ca}h_t - x_{2_{1t}}h_\xi + (uh)_\xi = 0, \quad (3.60)$$

$$4(hu_\xi)_\xi + h(h_{\xi\xi\xi} + \frac{1}{Ca^2}) = 0. \quad (3.61)$$

For $Ca \gg 1$, Eq. (3.60) can be written at leading order in $1/Ca$ as: $-x_{2_{1t}}h_\xi + (uh)_\xi = 0$.

We assume that any changes to the flux in the moving frame of reference are negligible, hence Eq. (3.60) simplifies to $(uh)_\xi = 0$. Integrating gives $uh = Q_2(t)$, where $Q_2(t)$ is the flux out of this region into region III. Substituting $u = Q_2(t)/h$ into Eq. (3.61)

gives the following boundary-value problem for h :

$$-4Q_2(t) \left[\frac{1}{h} h_\xi \right]_\xi + h(h_{\xi\xi\xi} + \frac{1}{Ca^2}) = 0, \quad (3.62a)$$

subject to the boundary conditions

$$h \rightarrow \frac{8Q_2Ca^2}{(\xi - \xi_2)^2}, \quad \xi \rightarrow -\infty, \quad \xi_2 = Ca(x_2 - x_{2_1}) > 0, \quad (3.62b)$$

$$h \rightarrow -\frac{1}{6Ca^2}(\xi - \xi^1)^3 + \frac{C(\xi - \xi^1)^2}{2Ca^2} + \frac{D}{Ca}(\xi - \xi^1) + 1, \quad \xi \rightarrow \infty,$$

$$\text{where } \xi^1 = Ca(1 - x_{2_1}) > 0, \quad (3.62c)$$

with C and D defined in region III above. Note that we leave the $\frac{1}{Ca^2}h$ term in Eq. (3.62a) so that we can match with regions II and III. The boundary conditions in Eqs. (3.62b, c) are obtained by taking the limit as $x \rightarrow x_2^-$ in Eq. (3.38) and $x \rightarrow x_2^+$ in Eq. (3.58), respectively.

In principle, we can use a shooting method to solve for the eigenvalue Q_2 in order to determine the numerical solution for the boundary value problem in Eq. (3.62). For a given $Ca \gg 1$, x_2 , x_{2_∞} and V_2 (these quantities are evaluated at some time t), we start with the boundary condition at the downstream end, Eq. (3.62c) (evaluated at $\xi = \xi_2 = Ca(x_2 - x_{2_1})$, where $\xi_2 \gg 1$ and $\xi_2 < \xi^1$), choosing Q_2 as the shooting parameter until the boundary condition at the upstream end, Eq. (3.62b), is satisfied (evaluated at $\xi = -\xi_{2_2}$, where $\xi_{2_2} \gg 1$). In practice, we shoot with Q_2 to satisfy $u_{\xi\xi} = Q_2 \left[2\frac{h_\xi^2}{h^3} - \frac{h_{\xi\xi}}{h^2} \right] \rightarrow \frac{1}{4Ca^2}$ as $\xi \rightarrow -\infty$.

Figure 3.11 compares the computed solution of h and u (solid lines) with the sim-

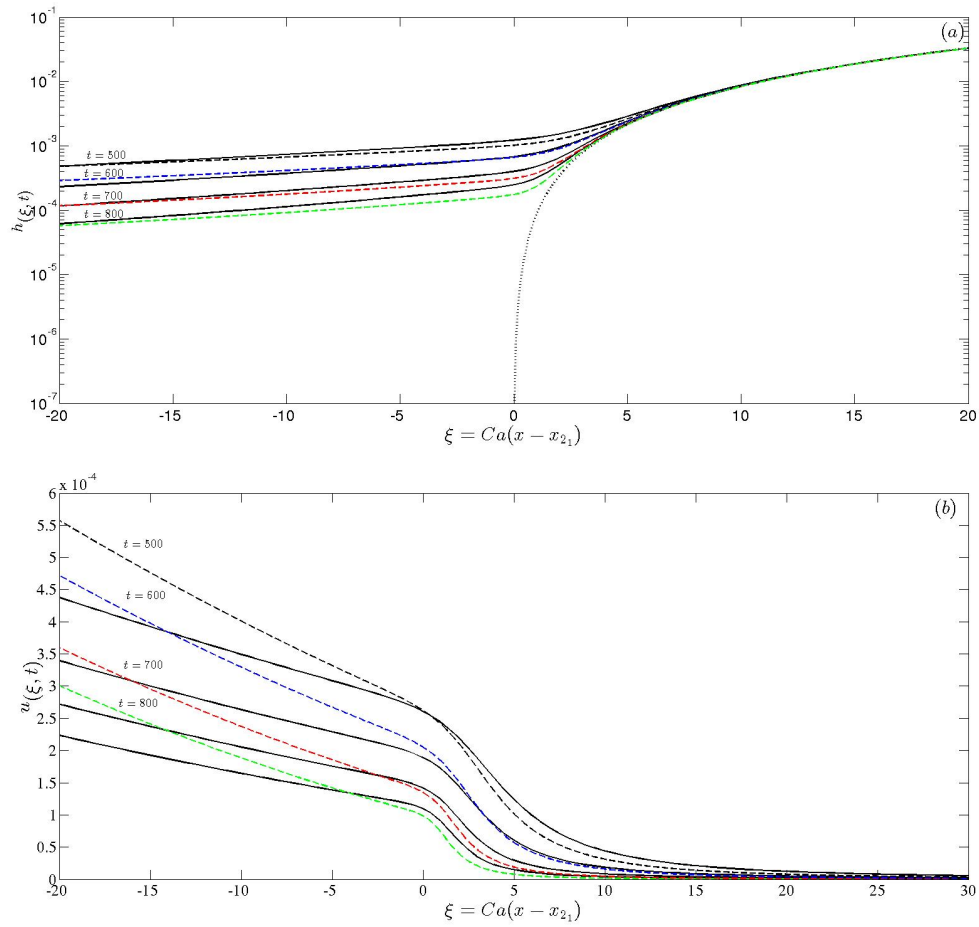


Figure 3.11: Computed film thickness profiles, h , (a) plotted on a semi-logarithmic axis and the extensional flow speed, u , (b) (solid lines) using the similarity coordinate $\xi = Ca(x - x_{2_1}(t))$ for $t = (5, 6, 7, 8) \times 10^2$. The dashed lines show the corresponding late-time similarity solution given by Eqs. (3.60,3.62). The dotted curve in (a) shows the quasi-static solution of region III given by Eq. (3.58) in the similarity variable ξ for $0 \leq \xi \leq \xi^1$. The parameter values are $Ca = 10^3$, $Re = 0$ and $x_{2_\infty} = 0.510583$.

ilarity solution given by Eqs. (3.60,3.62), using the similarity coordinate ξ for $t = (5, 6, 7, 8) \times 10^2$. The values of Q_2 computed using the shooting method are $Q_2 = (2.70, 1.38, 0.426, 0.174) \times 10^{-7}$, for $t = (5, 6, 7, 8) \times 10^2$, respectively. We use values of x_2 computed from the numerical solution shown in Fig. 3.7(a) at the given times, and $x_{2_1}(t) = x_{2_\infty} = 0.510583$. We observe that the similarity solution clearly captures the qualitative characteristics of the quasi-static evolution, namely, the family of solutions of h (see solid lines (numerical solution) and dashed lines (similarity solution) in Fig. 3.11(a)) emanating from the quasi-static solution of region III given by Eq. (3.58) in the similarity variable ξ for $0 \leq \xi \leq \xi^1$ (see dotted line in Fig. 3.11(a)), and the sudden deceleration of the flow u resulting in a shock-like discontinuity near $\xi = 0$ (Fig. 3.11(b)). Although the quantitative match is not perfect, the similarity solution given by Eqs. (3.62,3.60) capture very well the dynamics in this transition region.

Region A: the transition region between regions I and II

This region lies around x_{1_1} , and is also characterised by a large change in the curvature h_{xxx} (see Fig. 3.2(f)). Hence, surface tension due to changes in curvature is the primary mechanism driving an upward flow against gravity (see Fig. 3.2(e) for u in this region). In the upstream part of this region, although, changes in curvature are negligible in comparison to gravity, and the flow changes direction to a downward gravity-driven flow (see Fig. 3.2(e) for u in the upstream part of this region). Below we describe the evolution of h and u this region based on the above observations. The lengthscale of

this region by balancing surface tension and extensional viscous forces is of $O(1/Ca)$.

Letting $x = x_{1_1} + (1/Ca)\xi$, we can write the evolution equations for h and u as:

$$\frac{1}{Ca}h_t - x_{1_{1t}}h_\xi + (uh)_\xi = 0, \quad (3.63)$$

$$4(hu_\xi)_\xi + h(h_{\xi\xi\xi} + \frac{1}{Ca^2}) = 0. \quad (3.64)$$

For $Ca \gg 1$, Eq. (3.63) at leading order in $O(1/Ca)$ can be written as:

$-x_{1_{1t}}h_\xi + (uh)_\xi = 0$. We assume that any changes to the flux in the moving frame of reference are negligible, hence Eq. (3.63) simplifies to $(uh)_\xi = 0$. Integrating gives $uh = -Q_1(t)$ for $\xi < 0^-$ and $uh = Q_1(t)$ for $\xi > 0^+$. We assume that the flux changes sign over a much smaller lengthscale, and the flux is of the same magnitude but opposite sign on either side of $\xi = 0$. The numerical solutions suggest this, and also that Q_1 is small ($Q_1 \ll Q_2$), so this approximation is reasonable. Using this, we obtain

$$u = \frac{-Q_1}{h}, \text{ if } \xi < 0; u = \frac{Q_1}{h}, \text{ if } \xi > 0. \quad (3.65)$$

Substituting Eq. (3.65) into Eq. (3.64) gives the following boundary-value problem for h :

$$-4 \left[\mathcal{H}(Q) \frac{1}{h} h_\xi \right]_\xi + h(h_{\xi\xi\xi} + \frac{1}{Ca^2}) = 0, \quad (3.66a)$$

subject to the boundary conditions

$$h \rightarrow -\frac{1}{6Ca^2}(\xi^1 + \xi)^3 + \frac{C(\xi^1 + \xi)^2}{2Ca^2} + \frac{D}{Ca}(\xi^1 + \xi) + 1, \quad \xi \rightarrow -\infty,$$

$$\text{where } \xi^1 = Ca x_{1_1} > 0, \quad (3.66b)$$

$$h \rightarrow \frac{8Q_1 Ca^2}{(\xi - \xi_1)^2}, \quad \xi \rightarrow \infty, \quad \xi_1 = Ca(x_1 - x_{1_1}) < 0, \quad (3.66c)$$

where the piecewise constant function $\mathcal{H}(Q) = -Q_1$ if $\xi < 0$ and Q_1 if $\xi > 0$; C and D are defined in region I above. The boundary conditions in Eqs. (3.66b, c) are obtained by taking the limit as $x \rightarrow x_1^-$ in Eq. (3.27) and $x \rightarrow x_1^+$ in Eq. (3.38), respectively. Similar to region B, we use a shooting method to determine the numerical solution of the boundary value problem in Eq. (3.66) using Q_1 as the shooting parameter. In practice, we use a regularised form of the function $\mathcal{H} = Q_1 \tanh[A\xi]$, where $A > 0$ ($A = 1$ in the solutions shown in Fig. 3.12). For a given Ca , x_1 , x_{1_∞} and V_1 (these quantities are evaluated at some time t), we start with the boundary condition at the upstream end, Eq. (3.66b) (evaluated at $\xi = \xi_1 = Ca(x_1 - x_{1_1}) < 0$, where $|\xi_1| \gg 1$ and $|\xi_1| < \xi^1$), choosing Q_1 as the shooting parameter until the boundary condition at the downstream end, Eq. (3.66c), is satisfied (evaluated at $\xi = \xi_{1_2}$, where $\xi_{1_2} \gg 1$). In practice, we shoot with Q_1 to satisfy $u_{\xi\xi} = Q_1 \left[2\frac{h_\xi^2}{h^3} - \frac{h_{\xi\xi\xi}}{h^2} \right] \rightarrow \frac{1}{4Ca^2}$ as $\xi \rightarrow \infty$.

Figure 3.12 compares the computed solution of h and u (solid lines) with the similarity solution given by Eqs. (3.63,3.66), using the similarity coordinate ξ for $t = (5, 6, 7, 8) \times 10^2$. The values of Q_1 computed using the shooting method are $Q_1 = (2, 0.05, 0.001, 0.0001) \times 10^{-9}$, for $t = (5, 6, 7, 8) \times 10^2$, respectively (Note that $Q_2 \ll Q_1$, as observed from the numerical solutions). We use values of x_1 computed from the nu-

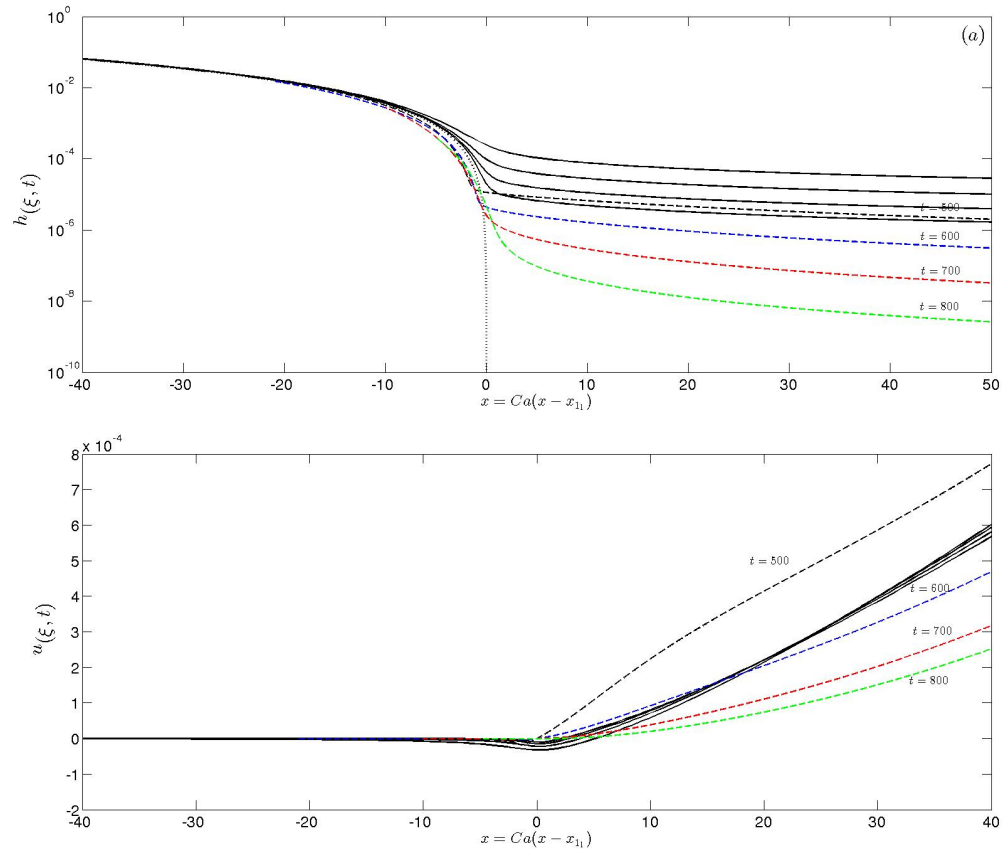


Figure 3.12: Computed film thickness profiles, h , (a) plotted on a semi-logarithmic axis, and the extensional flow speed, u , (b) (solid lines) using the similarity coordinate $\xi = Ca(x - x_{1_1}(t))$ for $t = (5, 6, 7, 8) \times 10^2$. The dashed lines show the corresponding late-time similarity solution given by Eqs. (3.63,3.66). The dotted curve in (a) shows the quasi-static solution of region I given by Eq. (3.27) in the similarity variable ξ for $-Cax_{1_1} \leq \xi \leq 0$. The parameter values are $Ca = 10^3$, $Re = 0$ and $x_{1_\infty} = 0.13464$.

merical solution shown in Fig. 3.7(a) at the given times, and $x_{1_1}(t) = x_{1_\infty} = 0.13464$.

We observe that the similarity solution clearly captures the qualitative characteristics of the quasi-static evolution, namely, the family of solutions of h (see solid lines (numerical solution) and dashed lines (similarity solution) in Fig. 3.12(a)) emanating from the quasi-static solution of region I given by Eq. (3.27) in the similarity variable ξ for $-Cax_{1_1} \leq \xi \leq 0$ (see dotted line in Fig. 3.11(a)), and the reversal of the flow u near $\xi = 0$ (Fig. 3.12(b)). Although the quantitative match is not perfect, the similarity solution given by Eqs. (3.62,3.60) capture very well the dynamics in this transition region.

Closure relationships to determine evolution of characteristic variables

The solution of the boundary value problems given by Eqs. (3.62,3.66) depend on the values of Ca and the characteristic quantities, $x_{1,2}$ and $Q_{1,2}$, at any instant of time starting from some initial conditions $x_{1,2}^{(0)}$. Note that $x_{\{1,2\}_1}(t)$ is almost constant (see Fig. 3.12(a)), and we assume that $x_{1_1}(t) = x_{1_\infty} = 0.13464$ and $x_{2_1}(t) = x_{2_\infty} = 0.511$. The solution to the boundary value problem in Eq. (3.62) provides the flux Q_2 as a function of x_2 , at any instant of time. Similarly, the solution to the boundary value problem in Eq. (3.66) provides the flux Q_1 as a function of x_1 , at any instant of time. We determine the late-time evolution of $x_{1,2}$ using volume conservation in regions I and II, $\frac{dV_1}{dt} = Q_1$ and $\frac{dV_2}{dt} = Q_2$, respectively. The algorithm to obtain the time evolution of $x_{1,2}$, and the corresponding family of solutions of Eqs. (3.62,3.66) is as follows:

1. Start with initial conditions $x_{1,2}^{(0)}$ at some time $t = t^{(0)}$. Compute the correspond-

ing volume $V_1^{(0)} = \int_0^{x_1^{(0)}} h dx$ and $V_2^{(0)} = \int_{x_2^{(0)}}^1 h dx$.

2. Solve the boundary value problems in Eqs. (3.62,3.66) to obtain the initial flux, $Q_{1,2}^{(0)}$.
3. Determine the values of $x_{1,2}^{(1)}$ at some time $t = t^{(0)} + \Delta t$ (where Δt is a small increment in time), using the updated volume $V_1^{(1)} \approx V_1^{(0)} + Q_1^{(0)} \Delta t = \int_0^{x_1^{(1)}} h dx$ and $V_2^{(1)} \approx V_2^{(0)} + Q_2^{(0)} \Delta t = \int_{x_2^{(1)}}^1 h dx$. Using the expressions for h in region I (given by Eq. (3.27)) and that in region II (given by Eq. (3.58)), these are quartic equations in $x_{1,2}^{(1)}$ which need to be solved to get the updated values of $x_{1,2}$ (similar to Eqs. (3.28,3.59) for $x_{\{1,2\}\infty}$, respectively).
4. Use $x_{1,2}^{(1)}$ to solve the boundary value problem in Eq. (3.62,3.66) to obtain the flux, $Q_{1,2}^{(1)}$ at time $t^{(1)}$.
5. Now repeat steps 3 and 4 to obtain the solution and characteristic variables at time $t^{(n)} = t^{(0)} + n\Delta t$.
6. Use Eq. (3.50) to numerically solve for h_{min} , e.g., using a forward Euler time-stepping scheme, $h_{min}(t^{(n)}) = h_{min}(t^{(n-1)}) + \Delta t \frac{[Q_1^{(n-1)}(t) - Q_2^{(n-1)}(t)]}{[x_2^{(n-1)}(t) - x_1^{(n-1)}(t)]}$.
7. Plot the characteristic variables and the family of solutions as a function of time.

3.6 Conclusions

In this chapter, we investigated the draining of a vertically-aligned free Newtonian liquid film between two rigid supports due to the combined effects of extensional viscous, gravity and surface tension forces. Our numerical simulations and asymptotic analysis have focussed on the case when the rescaled Capillary number $Ca = \hat{C}a/\epsilon \gg 1$, where the Capillary number $\hat{C}a = \mu^*U^*/\gamma^* = O(1)$. This limit recreated the decomposition of the liquid domain into a thin lamella connecting onto Plateau borders, which replicates the drainage due to gravity in liquid foams [15, 16, 17].

We focussed on the dominant balance between the extensional viscous and gravity forces, which is shown to control the drainage and thinning within the long, flat middle section of the film (Figs. 3.1(*a, c*) and Region II in §3.5.2). The balance of surface tension forces and gravity resulted in the development of a Plateau border (or a capillary-static meniscus) region near the top support (Figs. 3.1(*a, c*) and Region I in §3.5.2), while the liquid collects near the bottom support, forming a pendant drop region (Figs. 3.1(*a, c*) and Region III in §3.5.2). The middle region is shown to connect to the upper and lower regions via short-lengthscale transition regions, where extensional viscous, surface tension and gravity all balance to control the flux out or into the middle region (Figs. 3.2(*a – f*) and Regions A and B in §3.5.2).

We performed numerical simulations to reveal the influence of varying the Capillary number on the evolution of the film's free surface, its long-time thinning rate and the draining of liquid from the film. Larger the value of Ca , the faster was the extensional

flow speed, resulting in faster drainage of liquid out of the film, consequently leading to severe thinning of the film and its eventual rupture. For $Ca \gg 1$, we observed power-law behaviour in the thinning rate of the flat middle section of the film, which is estimated as $t^{-2.25}$. This is in comparison to previous studies by Breward [15, 16] and Brush & Davis [17] who derive a t^{-2} power-law behaviour. The new thinning rate reported here is due to the additional influence of gravity, which was not considered in these studies. This suggests the importance of gravity in enhancing the draining of the lamella, and accelerating its thinning rate, hence needs to be included in liquid foam models. Our predictions of power-law thinning behaviour is in contrast to a similar study by Davis *et al.* [26]. They demonstrated that the lamella thins non-uniformly with exponential decay of the minimum film thickness, which is significantly faster than the t^{-2} power-law thinning predicted when gravitational effects are negligible [15, 16, 17], and the $t^{-2.25}$ predicted here. This is due to their asymptotic analysis based on the assumption of capillary static Plateau Borders, the existence of which is restricted to liquid volume fractions that cannot exceed a threshold value. Moreover, this threshold liquid fraction decreases significantly as the Bond number (compares the force due to gravity relative to surface tension forces) of the system increases, indicating that gravitational effects reduce the stability of the Plateau Borders. Due to this, the analysis of Davis *et al.* [26] is restricted to initial film thicknesses that are much smaller than ours. We have no such restrictions on the liquid volume fraction since we do not assume that the Plateau Borders are capillary static and the initial film can be sufficiently thick. Therefore, their minimum film thickness decays exponentially for

long times, in accordance with our early-time solution behaviour described in Section 3.5.1 - there is a close resemblance in the form of both solutions.

The late-time self-similar solution structure in the limit $Ca \gg 1$ in §3.5.2 revealed the relationship between $Q_{1,2}$, the fluxes from the lamella (Region II) to the upper Plateau border (Region I) and the lower Plateau border region (upstream part of Region III), respectively, and $x_2 - x_1$, the width of the lamellar region. The fluxes $Q_{1,2}$ are shown to contribute to increasing the volume of the Plateau border regions; the increased volume reduces the width $x_2 - x_1$, which in turn influences $Q_{1,2}$ via the dynamics in the transition regions (Regions A and B). Indeed, an approximate analysis of the lamella showed that its minimum thickness $h_{min} \sim Q_2/(x_2 - x_1)^2$, while the corresponding maximum in extensional flow speed $u_{max} \sim (x_2 - x_1)^2$. We have developed an algorithm to determine the relationship between Q_2 and $x_2 - x_1$ numerically, however, we were unable to derive an analytical relationship to determine a power-law thinning rate analytically using the above relationships for $(h, u)_{min}$, and comparing with our numerical prediction of $t^{-2.25}$. It is worth noting here that the theoretical analysis by Breward [15, 16] and Brush & Davis [17] is based on determining the functional relationship $Q_2(h_{min})$. In their analysis, without including gravity, Eq. (3.61) in Region B can be integrated, and the relationship $Q_2(h_{min})$ is obtained using the boundary conditions. Moreover, without the inclusion of gravity, the extensional flow in the lamellar region (Region I) is linear, hence the film thickness h in this region is a time-dependent constant. One can then solve the differential equation in Eq. (3.29)

to obtain the t^{-2} thinning rate. However, the inclusion of gravity does not allow such analytical calculations.

We have also identified a novel boundary-value problem in §3.5.2 that captures the dynamics in Region A. A step function is employed to describe the spatial dependence of Q_1 such that it is negative upstream of this region (due to dominance of surface tension over gravity here that sucks liquid against the direction of gravity) and positive at its downstream end (surface tension is negligible here and the flow is due to gravity). The existence of a solution to this boundary-value problem is shown, which captures the qualitative features of the numerical solutions. Although Q_1 is negligible compared to Q_2 and does not affect the overall draining and thinning of the film, the analysis of this region is still essential to complete the overall understanding of the film's evolution. Figure 3.2(c) showed the strong deceleration of the flow as the lamella connects onto the lower plateau border region. The extensional shear rate u_x could be quite large in this region for non-Newtonian effects to play a significant role. In the next chapter, we investigate the influence of non-Newtonian effects, such as shear-thinning, and viscoplastic effects, such as yield stress, on the draining and thinning of the lamella.

Chapter 4

Gravity-driven draining of a vertically-aligned thin

non-Newtonian liquid free film

4.1 Introduction

Motivated by the observations in the previous chapter where the shear rate can be large, especially in the transition region, in this chapter, we extend the two-dimensional Newtonian liquid model to incorporate non-Newtonian effects, such as apparent or shear rate-dependent viscosity and yield stress, exhibited by the bulk liquid in the film. The constitutive relations between the liquid stress and its shear rate for a generalised Newtonian and viscoplastic liquid described in Chapter 1 are considered.

We use numerical solutions to characterise the evolution of the free surface for a range of parameter values associated with non-Newtonian and viscoplastic effects, along with the Capillary number, Ca .

The outline of this chapter is as follows. In §4.2, we write down the evolution equations for the film's free surface $h(x, t)$ and the extensional flow speed $u(x, t)$ for a generalised Newtonian liquid, whose apparent or effective viscosity is a function of its shear rate. In §4.3, we consider four commonly used non-Newtonian and viscoplastic constitutive relations for a Power Law and Carreau fluid (characterising generalised Newtonian rheology), and Bingham and Herschel-Bulkley fluid (representing viscoplastic rheology). We regularise the Power Law and Herschel-Bulkley constitutive models at low shear rates. These regularisations are also tested for their accuracy at shear rates close to zero and their practical implementation in solving the evolution equations. In §4.4, we perform numerical simulations of the evolution equations to determine the free surface shapes and extensional flow speeds, varying the parameter values, in particular, the Power Law index and the yield stress. In §4.5 we discuss the main results.

4.2 Governing Equations

The evolution equations for the film's free surface $h(x, t)$ and the extensional flow speed $u(x, t)$ for a generalised Newtonian liquid, is given by (Eq. (2.47) derived in Chapter

2):

$$h_t + Q_x = 0, \quad Q = uh + \epsilon^2 \frac{h^3}{3} \left[\frac{1}{\mu(|u_x|)} \left(4(\mu(|u_x|)u_x)_x + \frac{1}{Ca} h_{xxx} + 1 \right) - u_{0xx} \right], \quad (4.1a)$$

$$4(h\mu(|u_x|)u_x)_x + h \left[\frac{1}{Ca} h_{xxx} + 1 \right] = 0, \quad (4.1b)$$

$$h(0, t) = h(1, t) = 1, \quad h_{xxx}(0, t) = h_{xxx}(1, t) = -Ca, \quad u(0, t) = u(1, t) = 0. \quad (4.1c)$$

Note that we have assumed $Re = 0$ based on the results for the Newtonian liquid case. The above equations and boundary conditions are parametrised by the parameters describing the particular constitutive relationship for $\mu(|u_x|)$, and the Capillary number Ca . We seek solutions of Eq. (4.1) for $Ca \gg 1$, which corresponds to much weaker surface tension in comparison to gravity.

4.3 Non-Newtonian and viscoplastic constitutive models

We now consider different forms of the dimensionless function $\mu(|u_x|)$ in Eq. (4.1) corresponding to constitutive relationships for a Power Law, Herschel-Bulkley and Carreau

liquid.

$$\mu(|u_x|) = K|u_x|^{n-1}, \quad (\text{Power Law model}), \quad (4.2a)$$

$$\mu(|u_x|) = K|u_x|^{n-1} + \frac{\tau_p}{|u_x|}, \text{ if } \tau^{xx} > \tau_p, \text{ otherwise } u_x = 0, \quad (\text{Herschel-Bulkley model}), \quad (4.2b)$$

$$\mu(|u_x|) = \mu_\infty + (\mu_1 - \mu_\infty)[1 + (\lambda|u_x|)^2]^{(n-1)/2}, \quad (\text{Carreau model}), \quad (4.2c)$$

where $K = (K^*/\mu_0^*)(U^*/L^*)^{n-1}$, is a dimensionless liquid consistency index, n is the Power Law index (for $n < 1$, the fluid is shear thinning; $n > 1$ the fluid is shear thickening; $n = 1$ is the Newtonian case), $\tau_p = \frac{\tau_p^*}{\mu_0^*U^*/L^*}$ is the Bingham number which compares the liquid yield stress to the extensional viscous stress, $\mu_{1,\infty} = \mu_{1,\infty}^*/\mu_0^*$ are the viscosities in the limit of zero and large shear rate, respectively, and $\lambda = \lambda^*U^*/L^*$. We will make appropriate choices for the reference viscosity μ_0^* based on the parameter variation investigated in the results section.

We note that the first term in Eq. (4.1b) involving $\mu(u_x)$ has a singularity when $u_x = 0$ for $n < 1$, which occur near the top and bottom of the draining film, and where the flow attains its maximum value (see Fig. 3.1(b), for example). In practise, we relieve this singularity by regularising the Power Law and Herschel Bulkley models by adding

a sufficiently small positive number, δ , to u_x , namely,

$$\mu(|u_x|) = K[\sqrt{u_x^2 + \delta^2}]^{n-1}, \quad (\text{regularised Power Law model}), \quad (4.3a)$$

$$\mu(|u_x|) = K[\sqrt{u_x^2 + \delta^2}]^{n-1} + \frac{\tau_p}{\sqrt{u_x^2 + \delta^2}}. \quad (\text{regularised Herschel-Bulkley model}), \quad (4.3b)$$

The effect of regularisation on the Herschel-Bulkley model is that at low shear rates, the fluid becomes *weakly yielding* when $\tau^{xx} < \tau_p$ (Balmforth *et al.* [8]).

In practise, the appropriate value of δ is selected based on solving a simplified version of the governing equations in which $h = 1$. For this case, Eq. (4.1b) simplifies to

$$4(h\mu(|u_x|u_x))_x = -1. \quad (4.4)$$

This has an analytical solution for a Power Law constitutive model, as shown below. We then numerically solve this simplified equation using the regularised Power Law model, and choose the value of the regularisation parameter δ so that the error between the numerical and analytical solutions is less than a specified tolerance. In the case when $n = 1$, the analytical solution of Eq. (4.4) is

$$u(x, 0) = \frac{x}{8}(1 - x). \quad (4.5)$$

When $n \neq 1$, we split the domain into two regions defined by $u_x < 0$ and $u_x > 0$. We denote the x coordinate where $u_x = 0$ by L . For $u_x < 0$ ($L < x \leq 1$; see Fig. 3.1(b)),

Eq. (4.4) can be written as:

$$4 \left(K(-u_x)^{n-1} u_x \right)_x = -4 \left(K(-u_x)^n \right)_x = -1. \quad (4.6)$$

Integrating with respect to x yields

$$(-u_x)^n = \frac{x}{4K} + C, \quad (4.7)$$

where C is some constant. We ascertain the value of c using $u_x = 0$ at $x = L$, so

$$C = -\frac{L}{4K}. \quad (4.8)$$

With this value of C , the shear rate can be expressed as

$$(-u_x)^n = \frac{1}{4K} (x - L), \text{ or } u_x = - \left[\frac{1}{4K} (x - L) \right]^{1/n}. \quad (4.9)$$

A further integration results in

$$u(x) = -\frac{4Kn}{n+1} \left[\frac{1}{4K} (x - L) \right]^{\frac{n+1}{n}} + D, \quad (4.10)$$

and the constant of integration, D , can be obtained from the boundary condition on

$u(x = 1) = 0$, so

$$D = \frac{4Kn}{n+1} \left[\frac{1}{4K} (1-L) \right]^{\frac{n+1}{n}}. \quad (4.11)$$

Hence, we obtain

$$u(x) = \frac{4Kn}{n+1} \left[\left[\frac{1}{4K} (1-L) \right]^{\frac{n+1}{n}} - \left[\frac{1}{4K} (x-L) \right]^{\frac{n+1}{n}} \right], \text{ for } L \leq x \leq 1. \quad (4.12)$$

For $u_x > 0$ ($0 \leq x < L$; see Fig. 3.1(b)), Eq. (4.4) can be written as:

$$4 \left(K(u_x)^{n-1} u_x \right)_x = 4 \left(K(u_x)^n \right)_x = -1. \quad (4.13)$$

Integrating with respect to x yields

$$(u_x)^n = -\frac{x}{4K} + C, \quad (4.14)$$

where C is some constant. We ascertain the value of c using $u_x = 0$ at $x = L$, so

$$C = \frac{L}{4K}. \quad (4.15)$$

With this value of C , the shear rate can be expressed as

$$(u_x)^n = \frac{1}{4K} (L-x), \text{ or } u_x = \left[\frac{1}{4K} (L-x) \right]^{1/n}. \quad (4.16)$$

A further integration results in

$$u(x) = -\frac{4Kn}{n+1} \left[\frac{1}{4K} (L-x) \right]^{\frac{n+1}{n}} + D, \quad (4.17)$$

and the constant of integration, D , can be obtained from the boundary condition on $u(x=0) = 0$, so

$$D = \frac{4Kn}{n+1} \left[\frac{1}{4K} L \right]^{\frac{n+1}{n}}. \quad (4.18)$$

Hence, we obtain

$$u(x) = \frac{4Kn}{n+1} \left[\left[\frac{1}{4K} L \right]^{\frac{n+1}{n}} - \left[\frac{1}{4K} (L-x) \right]^{\frac{n+1}{n}} \right], \text{ for } 0 \leq x \leq L. \quad (4.19)$$

Finally, the position of the turning point in the velocity field, $x = L$, can be obtained by continuity of the above 2 solutions at $x = L$,

$$\frac{4Kn}{n+1} \left[\frac{1}{4K} (1-L) \right]^{\frac{n+1}{n}} = \frac{4Kn}{n+1} \left[\frac{L}{4K} \right]^{\frac{n+1}{n}}, \quad (4.20)$$

resulting in $L = \frac{1}{2}$. The value of δ can be obtained by comparing the numerical solution of Eq. (4.4) using the regularised Power Law model and the analytical solution given by Eqs. (4.12,4.19). The table below shows the resulting error (measured in the max norm) as the value of δ decreases, and allows us to pick an appropriate δ to restrict the error to a desired range. As n decreases, the singularity in $\mu(|u_x|)$ becomes more severe

δ	n	Error
10^{-1}	0.75	10^{-1}
	1.2	7×10^{-2}
10^{-2}	0.75	5×10^{-3}
	1.2	10^{-3}
10^{-3}	0.75	1×10^{-4}
	1.2	5×10^{-6}

Table 4.1: The error measured in the max norm of the numerical solution of Eq. (4.4) using the regularised Power Law model and the analytical solution given by Eqs. (4.12,4.19), as a function of the regularization parameter δ .

near $u_x = 0$, and a larger value of δ is required to regularise the solution. However, the accuracy of the solution is compromised. Due to this, we are unable to compute solutions for $n < 0.6$.

4.4 Numerical results

We discretize the spatial derivatives in Eq. (4.1) using the finite difference method, but keep the time derivative continuous. The spatial discretization is the same as for the Newtonian case, except for the functional form of $\mu(|u_x|)$ (described by the regularised Power Law and Herschel Bulkley, and the Carreau models), and is described in §3.3, in Chapter 3. The resulting system of system of differential-algebraic equations (DAEs) are again solved using the method of lines [65]. We use the implicit solver *ode15i* in MATLAB (MATLAB 6.1, The MathWorks Inc., Natick, MA, 2000) for our numerical simulations.

In the numerical results to follow we mainly focus on investigating the influence of the

liquid consistency parameter, K , the Power Law index, n , and the yield stress, τ_p , on the evolution of the film thickness $h(x, t)$ and extensional flow speed $u(x, t)$. We also investigate the influence of the more realistic Carreau model and the corresponding index n . The parameter values used are based on those reported for polymeric liquids, Polystyrene, Aluminium soap and Hydroxylethycellulose, in Table 1 in Myers [45]. For Polystyrene, $n = 0.39$ (power law model), $K^* = 3.5 \times 10^5 \text{ Pa s}^n$, $n = 0.4$ (Carreau model), $\mu_1^* = 4 \times 10^6 \text{ Pa s}$ and $\lambda^* = 46.4 \text{ s}^{-1}$. This corresponds to $K = 12$ and $\lambda = 10^{-3}$, assuming the reference viscosity $\mu_0^* = \mu_1^*$. For Aluminium soap, $n = 0.2$ (power law model), $K^* = 68.07 \text{ Pa s}^n$, $n = 0.2$ (Carreau model), $\mu_1^* = 89.6 \text{ Pa s}$ and $\lambda^* = 1.41 \text{ s}^{-1}$. This corresponds to $K = 0.7$ and $\lambda = 1$, assuming the reference viscosity $\mu_0^* = \mu_1^*$. For Hydroxylethycellulose, $n \approx 0.51$ (power law model), $K^* = 0.84 \text{ Pa s}^n$, $n \approx 0.51$ (Carreau model), $\mu_1^* = 0.22 \text{ Pa s}$ and $\lambda^* \approx 0.067 \text{ s}^{-1}$. This corresponds to $K \approx 0.1$ and $\lambda \approx 30$, assuming the reference viscosity $\mu_0^* = \mu_1^*$. We were unable to compute the solutions for $n < 0.6$, as mentioned previously. The regularization parameter, $\delta = 10^{-3}$, is chosen based on Table 4.1. The Capillary number, $Ca = 10^3$, is fixed for all simulations to follow, based on the results in chapter 3. In all the results to follow we choose $\Delta x = 5 \times 10^{-4}$ for convergence to be achieved and the solutions to be accurate. The initial condition is $h(x, 0) = 1$, and the corresponding initial condition for the extensional flow speed, $u(x, 0)$, is given by Eqs. (4.12,4.19), with $L = 1/2$, for the value of n chosen.

In the first set of results, we show the influence of varying the consistency parameter

K (or dimensional K^*), for fixed Power Law index n . This can also be obtained by choosing $\mu_0^* = K^* \left(\frac{U^*}{L^*} \right)^{n-1}$, so $K = 1$. The characteristic speed and time of draining of the flow and thinning of the film can then be shown to scale with K^* as $U^* \sim \frac{1}{K^{*1/n}}$ and $t^* \sim K^{*1/n}$, respectively. Figure 4.1(a, b, c) show the effect of varying the consistency parameter K , for fixed $n = 0.9$ and fixed $Ca = 10^3$ on $h(x, t = 30)$, $u(x, t = 30)$ and h_{min} , the global minimum in $h(x, t)$, as a function of time t , respectively. We

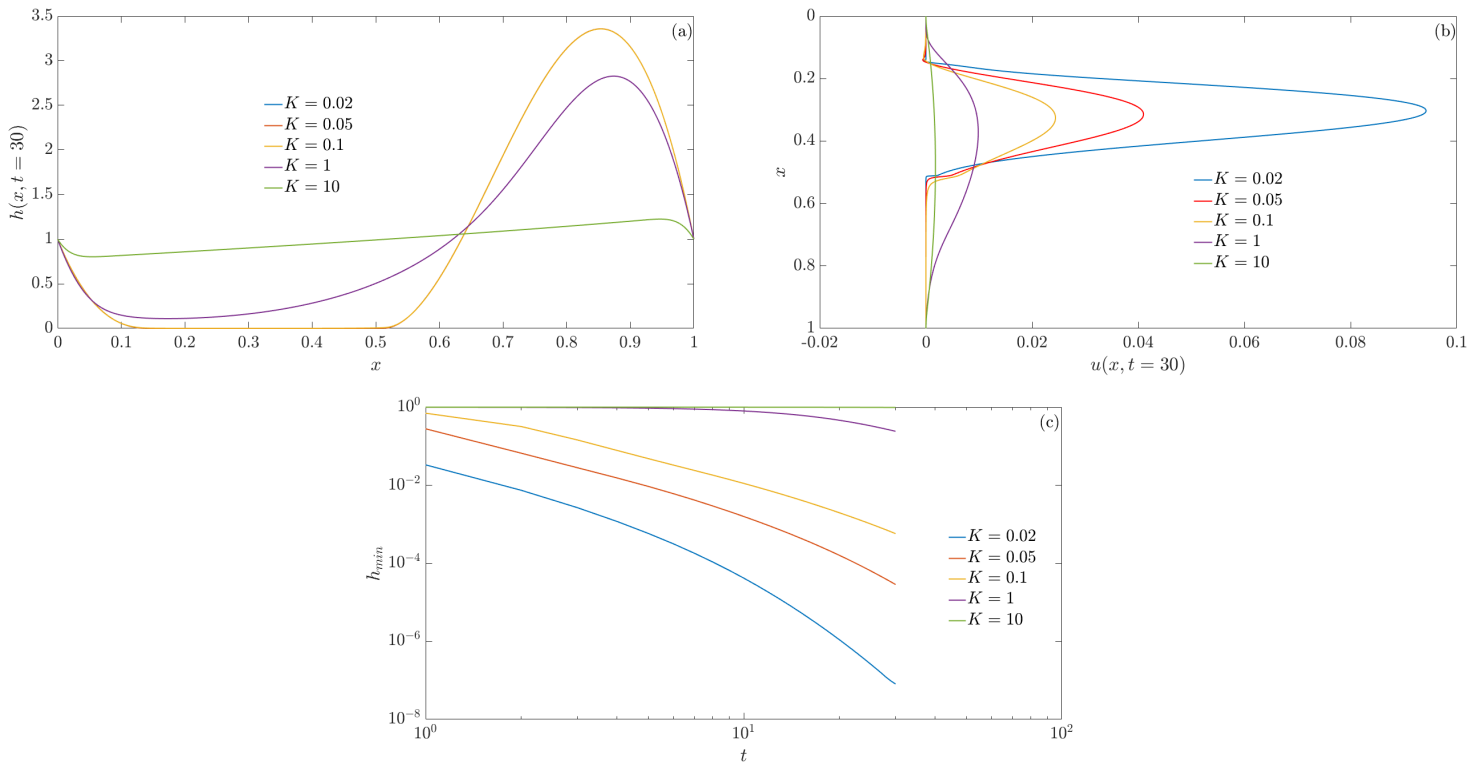


Figure 4.1: (a) Film thickness $h(x, t = 30)$, and (b) extensional flow speed $u(x, t = 30)$, and (c) the global minimum h_{min} as a function of time t , for varying consistency parameter K , for fixed Power Law index, $n = 0.9$ and $Ca = 10^3$.

observe that the film thins more rapidly as K decreases (Fig. 4.1(a)) due to the faster extensional flow speed as K decreases (Fig. 4.1(b)). Reducing K leads to lower viscosities, resulting in much faster drainage (note that $u \sim 1/K^{1/n}$). Figure 4.1(c)

tracks h_{min} , the global minimum in $h(x, t)$, as a function of time t . We observe that the film thins more rapidly as K decreases, in line with the observations in Fig. 4.1(a, b). We also note that the time scale for thinning scales like $t \sim K^{1/n}$. We chose not to scale K out of the results shown here by using the scalings $(u, t) \sim (1/K^{1/n}, K^{1/n})$ in order to explicitly investigate its influence. This will be useful in the results to follow. To better understand the above described variations in K , we plot key outputs, $h(x, t = 30)$, $u(x, t = 30)$, the shear-rate $u_x(x, t = 30)$ and the shear-rate dependent viscosity $\mu(|u_x|)$ for $K = 0.02$ (corresponding to a liquid of a very low consistency index) in Fig. 4.2(a), $K = 0.1$ (corresponding to a liquid of a low consistency index) in Fig. 4.2(b), $K = 1$ (corresponding to a liquid of an intermediate consistency index) in Fig. 4.2(c) and $K = 10$ (corresponding to a liquid of a high consistency index) in Fig. 4.2(d), for fixed $n = 0.9$ and $Ca = 10^3$. We observe that the magnitude of shear rate $|u_x|$ is larger for the lower values of K (Fig. 4.2(a, b)), in comparison to the higher values of K (Fig. 4.2(c, d)). We also observe a sharp peak in u_x for $K = 0.02$ concentrated in the transition region where the thin middle section of the film connects onto the pendant drop region near the bottom (Fig. 4.2(a)), which progressively becomes smaller as K increases (Fig. 4.2(b–e)). This results in lower viscosities for smaller K (Fig. 4.2(a, b)) and higher viscosities as K increases (Fig. 4.2(c, d)).

Next, we show the influence of varying the Power Law index n , for fixed consistency parameter K^* . We choose $\mu_0^* = K^*$ (choosing $n = 1$ or a Newtonian liquid reference viscosity). Then $K(n) = \left(\frac{U^*}{L^*}\right)^{n-1} = \left(\frac{\rho^* g^* L^*}{K^*}\right)^{n-1} = K_0^{n-1}$. Figure 4.3(a, b, c) show

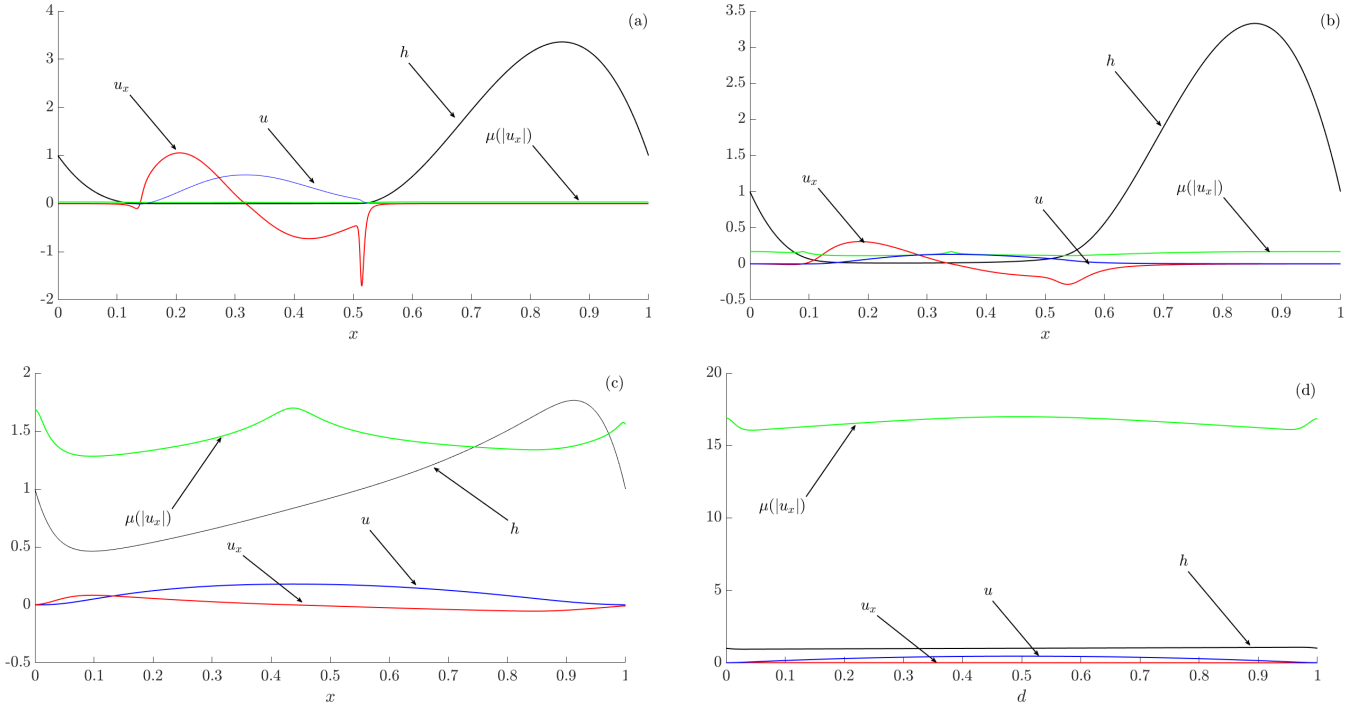


Figure 4.2: The film thickness $h(x, t = 30)$ (black curve), the extensional flow speed $u(x, t = 30)$ (blue curve), the shear-rate $u_x(x, t = 30)$ (red curve) and the shear-rate dependent viscosity $\mu(|u_x|)$ (green curve) for (a) $K = 0.02$ (corresponding to a liquid of a very low consistency index), (b) $K = 0.1$ (corresponding to a liquid of a low consistency index), (c) $K = 1$ (corresponding to a liquid of an intermediate consistency index) and (d) $K = 10$ (corresponding to a liquid of a high consistency index), for fixed $n = 0.9$ and $Ca = 10^3$.

the effect of varying the Power Law index, $n = 0.75, 1, 1.2$, for fixed $K_0 = 1$ and $Ca = 10^3$ on $h(x, t = 360)$, $u(x, t = 360)$ and h_{min} , the global minimum in $h(x, t)$, as a function of time t , respectively. We observe that the film thins more rapidly as n increases (Fig. 4.3(a)) due to the faster extensional flow speed as n increases (Fig. 4.3(b)). Figure 4.3(c) tracks h_{min} , the global minimum in $h(x, t)$, as a function

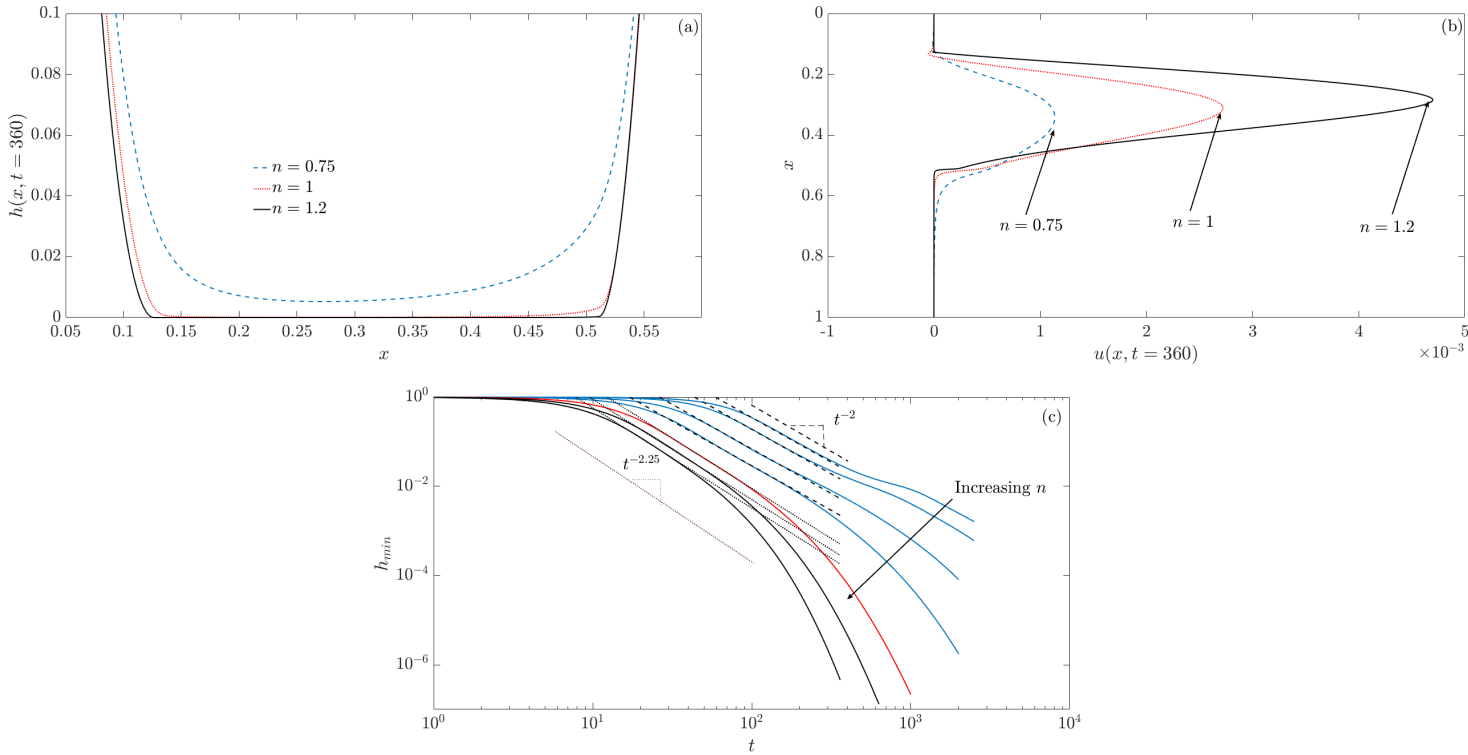


Figure 4.3: (a) Film thickness $h(x, t = 360)$, and (b) extensional flow speed $u(x, t = 360)$, and (c) the global minimum h_{min} as a function of time t , for varying Power Law index, $n = 0.6, 0.65, 0.75, 0.85, 1, 1.1, 1.2$, for fixed $K_0 = 1$ and $Ca = 10^3$. The corresponding thinning rates are t^{-2} for $n < 1$ and $t^{-2.25}$ for $n \geq 1$.

of time t , for $n = 0.6, 0.65, 0.75, 0.85, 1, 1.1, 1.2$. We observe that the film thins more rapidly as n increases, in line with the observations in Fig. 4.3(a, b). We estimate the thinning rates to be t^{-2} when $n < 1$, $t^{-2.25}$ when $n \geq 1$, suggesting a weak dependence of the thinning rate on n . This Power Law estimate is at best valid near $n = 1$ as

shown in Fig. 4.3(c), where the range of Power Law behaviour reduces as n moves further away from one. We now describe the characteristic late-time flow behaviour and film evolution in regions of very small width of $O(1/Ca)$ near the top (where the upper meniscus meets the thin film section) and bottom ends (where the thin film meets the pendant drop) of the film. Figure 4.4(d – f) show the evolution of the film thickness $h(x, t = 360)$, the extensional flow speed $u(x, t = 360)$ and the stress balance given by Eq. (4.1b) near the bottom end, respectively, for $n = 0.75, 1, 1.2$, $K_0 = 1$ and $Ca = 10^3$. We observe similar behaviour to that of a Newtonian liquid, as described in chapter 3, except that for the larger value of $n = 1.2$, the flow is much more mobile (Fig. 4.4(b)) and the film thickness is relatively thinner (Fig. 4.4(a)) in comparison to $n = 0.75$. This is due to the fact that the shear rates are less than unity (not only in this region, but also over the entire flow domain - see Fig. 4.5 for the shear-rates at these values of the Power Law index n), so at $n = 1.2$ the effective viscosity is much less than that at $n = 1$ (see Fig. 4.5(a, b) for comparison between the effective viscosities). Figure 4.4(a – c) show the evolution of the film thickness $h(x, t = 360)$, the extensional flow speed $u(x, t = 360)$ and the stress balance given by Eq. (4.1b) near the upper end, respectively, for $n = 0.75, 1, 1.2$ and $Ca = 10^3$. Again the qualitative behaviour is similar to the Newtonian case, except that the flow is more mobile and the film is thicker for $n = 0.75$ in comparison to $n = 0.75, 1$ due to the lower effective viscosity. To better understand the above described variations in n , we plot key outputs, $h(x, t = 360)$, $u(x, t = 360)$, the shear-rate $u_x(x, t = 360)$ and the shear-rate dependent viscosity $\mu(|u_x|)$ for $n = 0.75$ (corresponding to the shear-

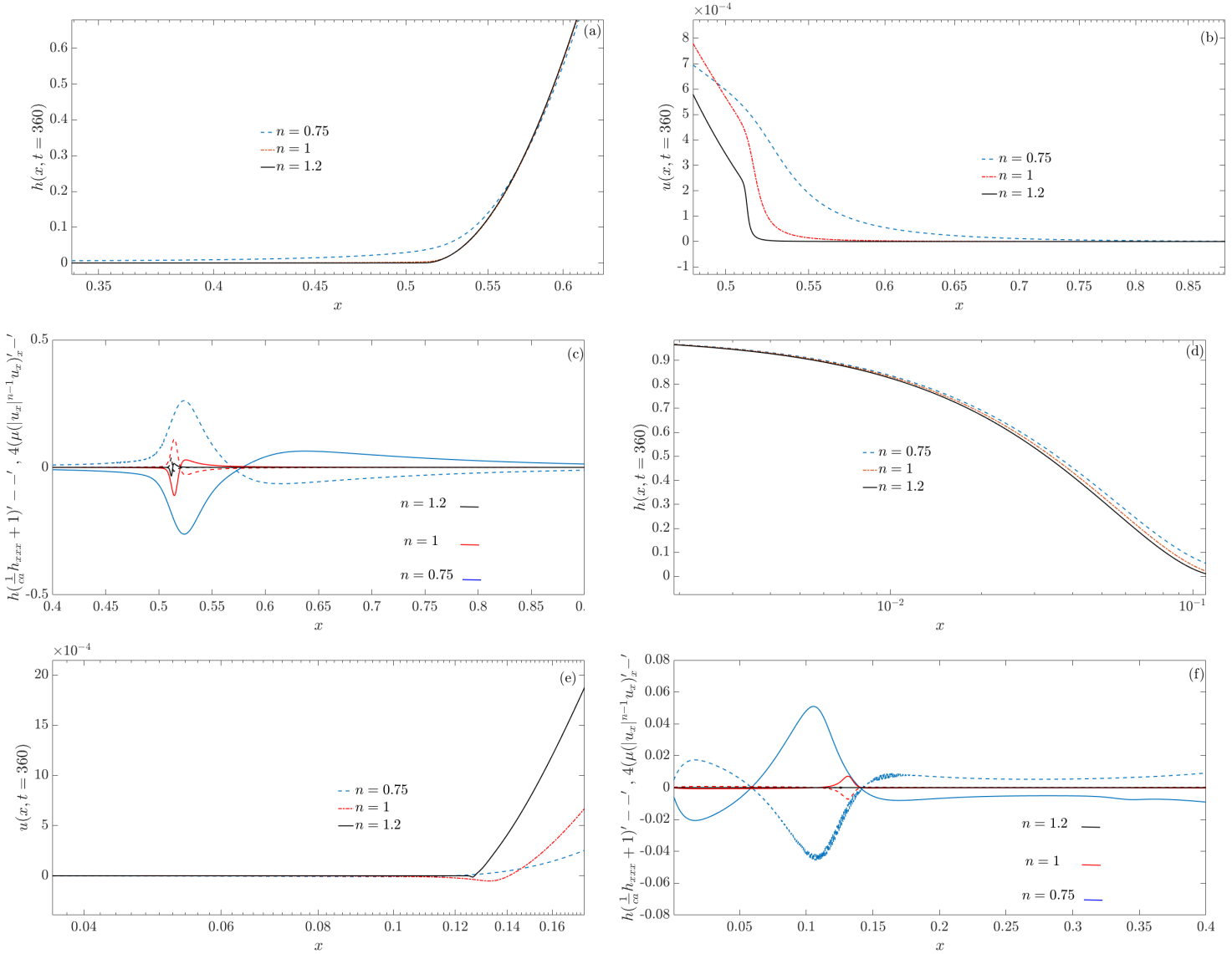


Figure 4.4: The film thickness $h(x, t = 360)$, the extensional flow speed $u(x, t)$ and the stress balance given by Eq. (4.1b) (the dashed lines represent $h(\frac{1}{Ca} h_{xxx} + 1)$ and the solid lines represent $4(hu_x)_x$ near the bottom end (a, b and c, respectively) and the upper end (d, e and f, respectively), for $n = 0.75, 1, 1.2$, $K_0 = 1$, $Ca = 10^3$ and $\Delta x = 5 \times 10^{-4}$.

thinning fluid case) in Fig. 4.5(a), $n = 1$ (corresponding to the Newtonian fluid case) in Fig. 4.5(b) and $n = 1.25$ (corresponding to the shear thickening fluid case) in Fig. 4.5(c), for fixed $Ca = 10^3$. We observe that the shear rate $u_x \ll 1$ across the entire film, and throughout the evolution process, for the value of K_0 (K^*) investigated here. This results in higher viscosities for $n < 1$ (Fig. 4.5(a)) and lower viscosities for $n \geq 1$ (Fig. 4.5(b, c)). Moreover, we observe from Fig. 4.5(a) that the spatial profile of viscosity for $n < 1$ is maximum near the top, bottom and central region of the film where the shear rate $u_x = 0$. The opposite happens for $n > 1$ (Fig. 4.5(c)), with a spike in viscosity corresponding to a change in shear rate observed where the flat middle region of the film connects onto the pendant drop near the bottom of the film (see Fig. 4.4(b)). We note here that Power Law model is not accurate at very low shear rates (see Myers [45]) as observed here, hence we need to be careful in interpreting the above results. We will compare the results here with that obtained from the Carreau model below. In order to further investigate the influence of varying n , we consider a much higher value of $K_0 = 30$ (which corresponds to smaller consistency index K^*). The resulting flow is of similar mobility and the shear rates are also similar to the previous case with $K_0=1$. Moreover, $K(n) = K_0^{n-1}$, depends on n , which was not the case before for $K_0 = 1$. So, the influence on n will now come from $\mu(|u_x|) = K_0^{n-1}|u_x|^{n-1}$. So, if the shear rates are low and $n < 1$, then the higher value of $|u_x|^{n-1}$ could be offset by the lower value of K_0^{n-1} (which is approximately 0.5 for $n = 0.9$), resulting in a lower viscosity $\mu(|u_x|)$. In contrast for $n > 1$, then $|u_x|^{n-1}$ is small, but K_0^{n-1} is large (which is approximately 2 for $n = 1.2$), which could result in a higher viscosity $\mu(|u_x|)$.

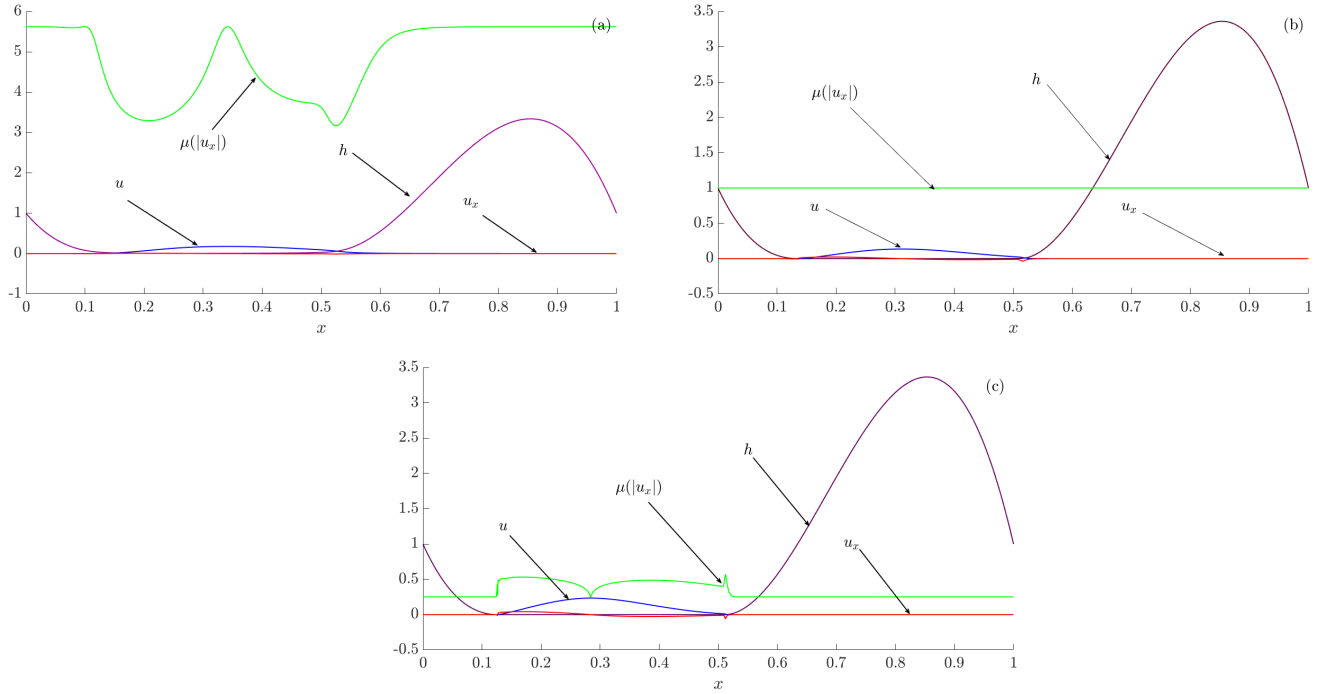


Figure 4.5: The film thickness $h(x, t = 360)$ (black curve), the extensional flow speed $u(x, t = 360)$ (blue curve), the shear-rate $u_x(x, t = 360)$ (red curve) and the shear-rate dependent viscosity $\mu(|u_x|)$ (green curve) for (a) $n = 0.75$ (corresponding to the shear-thinning fluid case), (b) $n = 1$ (corresponding to the Newtonian fluid case), and $n = 1.25$ (corresponding to the shear-thickening fluid case), and fixed $K_0 = 1$ and $Ca = 10^3$.

An illustration of this behaviour is observed in Fig. 4.6, which plots h_{min} versus t for $K_0 = 30$, and $n = 0.9, 1, 1.2$. We observe that at early to intermediate times during the

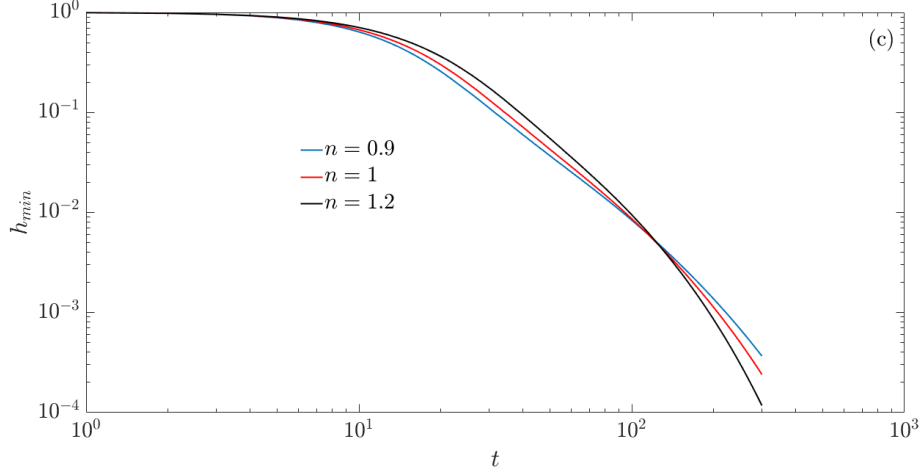


Figure 4.6: The global minimum h_{min} as a function of time t , for varying Power Law index, $n = 0.9, 1, 1.2$, for fixed $K_0 = 30$ and $Ca = 10^3$.

draining process, h_{min} thins faster for $n = 0.9$ compared to $n = 1.2$. This is due to the faster drainage for $n < 1$ at the given value of $K_0 = 30$, in comparison to a relatively slower drainage for $n > 1$ (results not shown). At later times, the roles are reversed and the thinning behaviour is similar to the case corresponding to $K_0 = 1$. This is due to the fact that the shear rates have become very small, so that the K_0^{n-1} can no longer offset the $|u_x|^{n-1}$ term, which is very large for $n < 1$ and very small for $n > 1$. If we were to further increase K_0 , then the thinning behaviour observed at early and intermediate times would persist for much longer times.

We now consider the effects of varying the yield stress τ_p on the evolution using the regularised Herschel-Bulkley constitutive model. The values of τ_p chosen are informed based on the absolute value of the extensional stress profile $|\tau_{xx}^x| = |u_x^n|$ determined

from the initial shear rate $u_x(x, t = 0)$ corresponding to the initial profile of u given by Eqs. (4.12,4.19), for the value of n chosen. An example is shown in Fig. 4.7, where we plot $|\tau_{xx}^x(x, t = 0)|$ for $n = 1$. The maximum value of the initial stress τ_{xx}^x then provides

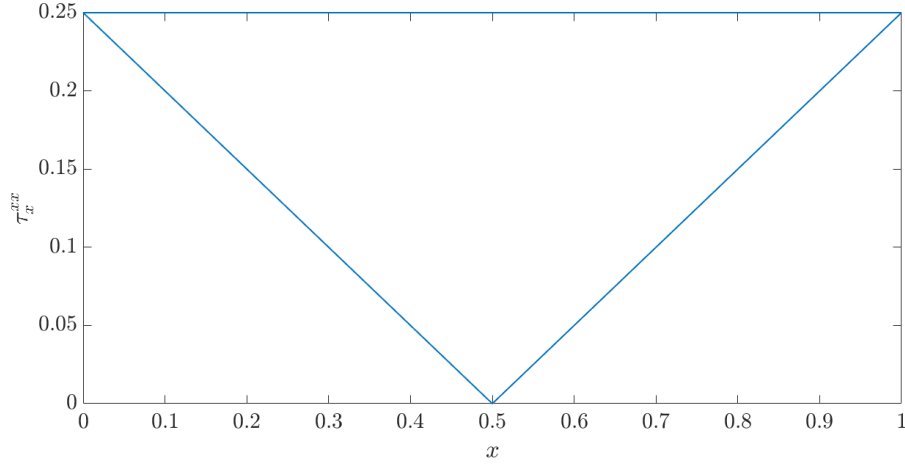


Figure 4.7: The absolute value of the initial extensional stress $|\tau_{xx}^x(x, t = 0)|$ for $n = 1$.

the maximum value of τ_p ; the flow will not yield from its initial state for any value of τ_p greater than this maximum value; any value of τ_p less than this maximum value will result in sections of the flow yielding while others do not yield (weakly yielding for the regularised form of the Herschel-Bulkley constitutive model). We explore this below for different Power Law index n . Figure 4.8(a, b, c) show the effect of varying the yield stress $\tau_p = 10^{-4}, 5 \times 10^{-3}, 10^{-2}, 2 \times 10^{-2}$, for $n = 0.75$, $K_0 = 1$ and $Ca = 10^3$, on $h(x, t = 10^3)$, $u(x, t = 10^3)$, and the global minimum h_{min} as a function of time t , respectively. We observe in Fig. 4.8(b) that increasing the yield stress τ_p slows u and exhibits weakly yielding behaviour for large τ_p . This results in the central region of the film to be much thicker near the top and the bottom as τ_p is increased, as observed in Fig. 4.8(a). There is a slight difference in the thickness of the film's middle section

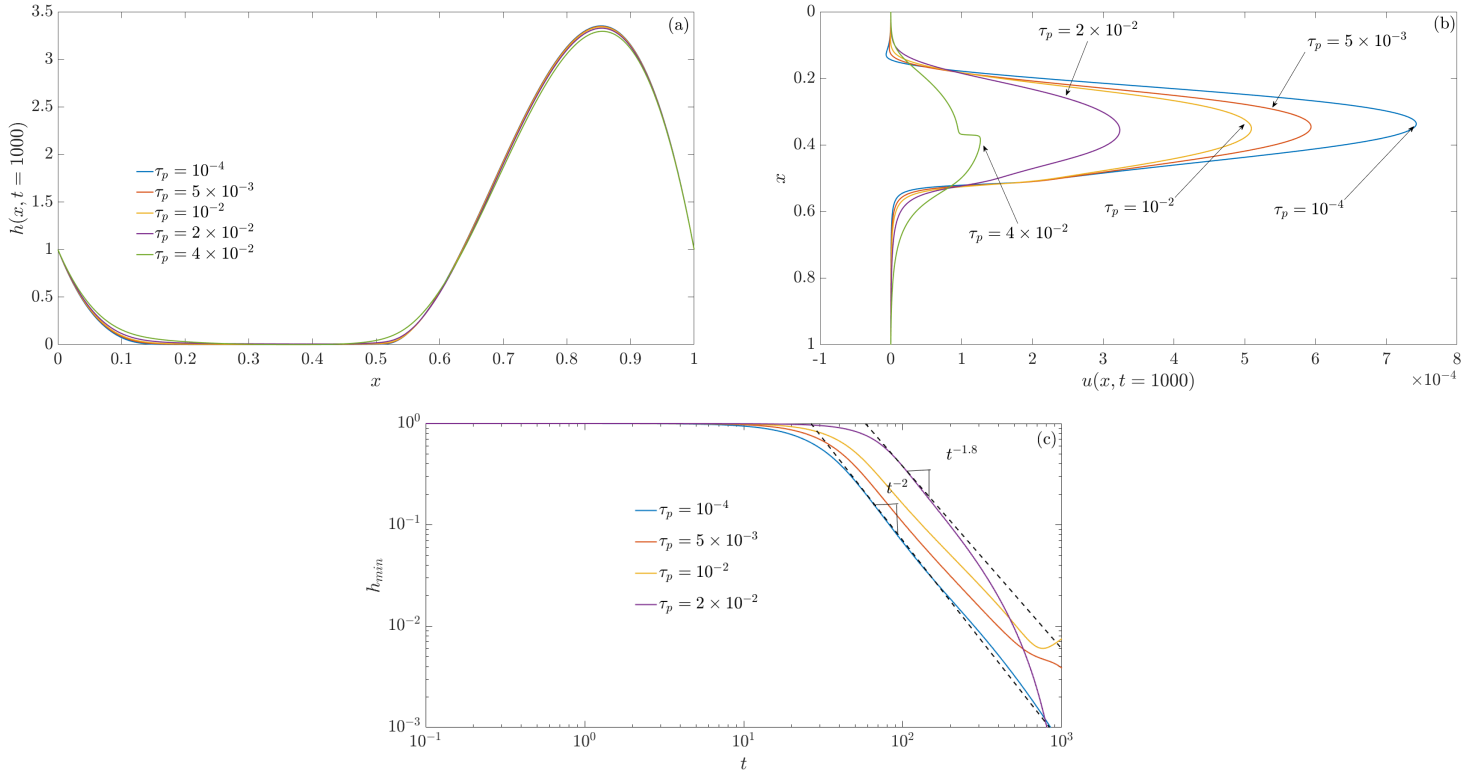


Figure 4.8: (a) Film thickness $h(x, t = 10^3)$, and (b) extensional flow speed $u(x, t = 10^3)$, and (c) the global minimum h_{min} as a function of time t , for varying yield stress $\tau_p = 10^{-4}, 5 \times 10^{-3}, 10^{-2}, 2 \times 10^{-2}, 4 \times 10^{-2}$, for $n = 0.75, K_0 = 1$ and $Ca = 10^3$. The corresponding thinning rates are t^{-2} for $\tau_p = 10^{-4}$ and $t^{-1.8}$ for $\tau_p = 2 \times 10^{-2}$.

as τ_p is increased, where u is maximum, and is not distinguishable from Fig. 4.8(a). Indeed, Fig. 4.8(c) shows that the film's minimum thickness h_{min} increases slightly as τ_p increases, for any given time t . We estimate the thinning rates to be t^{-2} for $\tau_p = 10^{-4}$ and $t^{-1.8}$ for $\tau_p = 2 \times 10^{-2}$. This suggests that the thinning rate decreases as τ_p increases.

A weak dependence of the yield stress on the thinning rate is observed when measured against the zero yield stress thinning rate of t^{-2} for $n = 0.75$. Figure 4.9(a, b, c) show the effect of varying the yield stress $\tau_p = 2 \times 10^{-2}, 10^{-2}, 5 \times 10^{-3}, 10^{-4}$, for $n = 1$, $K_0 = 1$ and $Ca = 10^3$, on $h(x, t = 10^3)$, $u(x, t = 10^3)$, and the global minimum h_{min} as a function of time t , respectively. Figures 4.9(a, b, c) show similar behaviour and trends as in the previous case for $n = 0.75$, except that u (and the corresponding shear rate u_x and stress τ) are larger as n increases (note that the maximum u is much higher than that for $n = 0.75$, and at later time). We estimate the thinning rates to be $t^{-2.25}$ for $\tau_p = 10^{-4}$ and $t^{-1.7}$ for $\tau_p = 2 \times 10^{-2}$. This suggests that the thinning rate decreases as τ_p increases. A weak dependence of the yield stress on the thinning rate is observed when measured against the zero yield stress thinning rate of $t^{-2.25}$ for $n = 1$. Figure 4.10(a, b, c) show the effect of varying the yield stress $\tau_p = 10^{-2}, 4 \times 10^{-3}, 10^{-4}, 10^{-5}$, for $n = 1.2$, $K_0 = 1$ and $Ca = 10^3$, on $h(x, t = 500)$, $u(x, t = 360)$, and the global minimum h_{min} as a function of time t , respectively. Figures 4.10(a, b, c) again show similar behaviour and trends as in the previous two cases for $n = 0.75, 1$, except that u (and the corresponding shear rate u_x and stress τ) are much larger as n increases. In figure 4.10 (c), we estimate the thinning rates to be $t^{-2.35}$ for $\tau_p = 10^{-4}$ and t^{-2} for $\tau_p = 1.6 \times 10^{-2}$. This suggests that the thinning rate decreases as τ_p increases. A weak

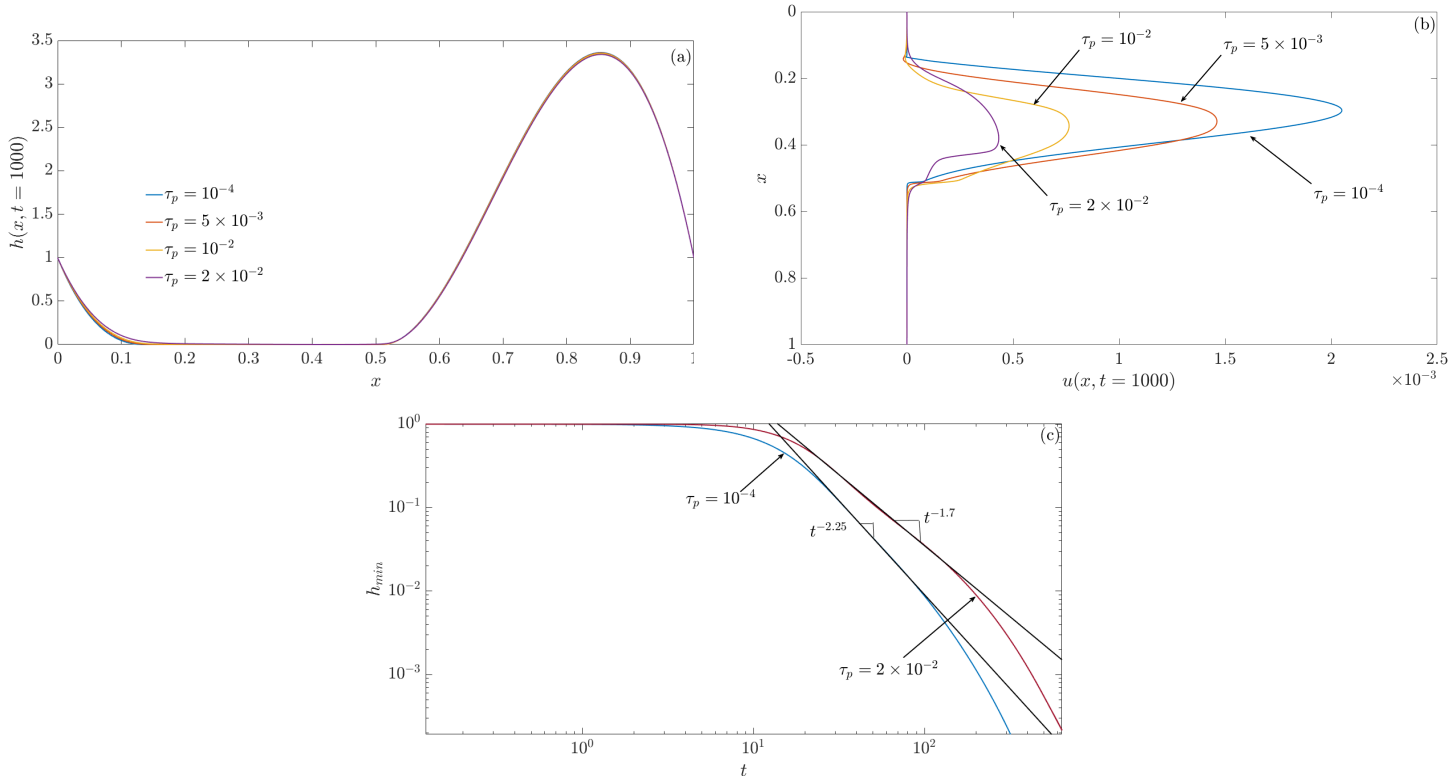


Figure 4.9: (a) Film thickness $h(x, t = 1000)$, and (b) extensional flow speed $u(x, t = 1000)$, and (c) the global minimum h_{min} as a function of time t , for varying yield stress $\tau_p = 2 \times 10^{-2}, 10^{-2}, 5 \times 10^{-3}, 10^{-4}$, for $n = 1, K_0 = 1$ and $Ca = 10^3$. The corresponding thinning rates are $t^{-2.25}$ for $\tau_p = 10^{-4}$ and $t^{-1.7}$ for $\tau_p = 2 \times 10^{-2}$.

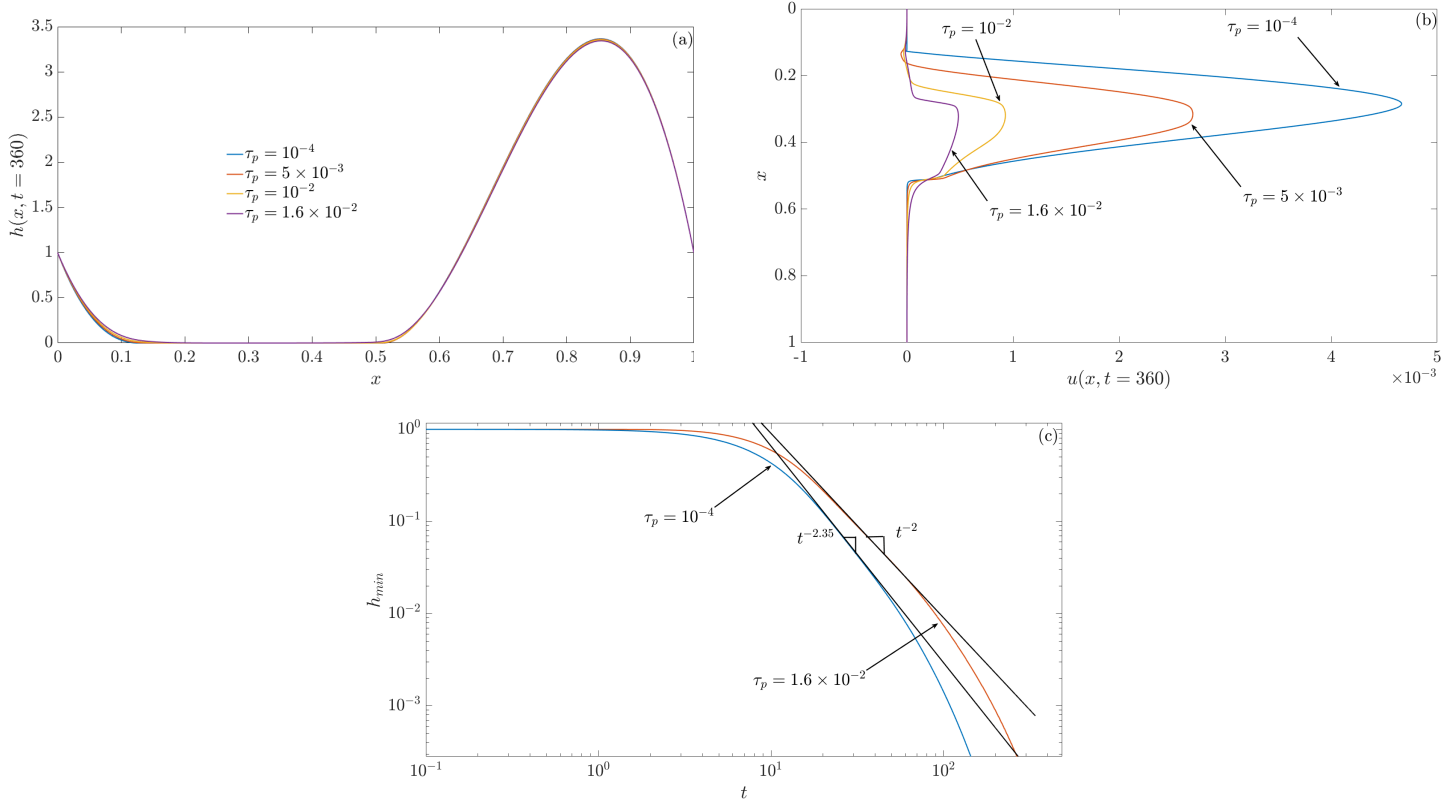


Figure 4.10: (a) Film thickness $h(x, t = 360)$, and (b) extensional flow speed $u(x, t = 360)$, and (c) the global minimum h_{min} as a function of time t , for varying yield stress $\tau_p = 1.6 \times 10^{-2}, 10^{-2}, 5 \times 10^{-3}, 10^{-4}$, for $n = 1.2$, $K_0 = 1$ and $Ca = 10^3$. The corresponding thinning rates are $t^{-2.35}$ for $\tau_p = 10^{-4}$ and t^{-2} for $\tau_p = 1.6 \times 10^{-2}$.

dependence of the yield stress on the thinning rate is observed when measured against the zero yield stress thinning rate of $t^{-2.35}$ for $n = 1.2$.

The Power Law model might not accurately reflect the dynamics of the low shear rate cases [45]. In this section, we investigate the Carreau model which is well behaved at low shear rates. Moreover, no regularisation is required at low shear rates for $n < 1$ either, unlike in the Power Law model. In the simulations to follow, we investigate the Carreau model for varying n , with $\mu_1 = 1$ (so the reference viscosity is chosen to be the zero shear rate viscosity), $Ca = 10^3$, $\lambda = 100$ ($\lambda^* = 10\text{s}$) and $\mu_\infty = 0$ fixed. (Note that $\mu_\infty \ll 1$.) Figure 4.11(a, b, c) show the effect of varying the Power Law index, $n = 0.75, 1, 1.2$, for $Ca = 10^3$, on $h(x, t = 800)$, $u(x, t = 800)$ and h_{min} , the global minimum in $h(x, t)$, as a function of time t , respectively. We observe that the film thins more rapidly as n decreases (Fig. 4.11(a)) due to the faster extensional flow speed as n decreases (Fig. 4.11(b)). Note Fig. 4.11(a) only shows the central regions as the upper and lower parts of the film are not significantly affected by varying n . The low flow shear rates during the evolution result in lower viscosities for $n < 1$ (shear thinning) and higher viscosities for $n > 1$ (shear thickening), resulting in much slower drainage for $n > 1$. Figure 4.11(c) tracks h_{min} , the global minimum in $h(x, t)$, as a function of time t , for $n = 0.6, 0.65, 0.75, 0.85, 1, 1.1, 1.2$. We observe that the film thins more rapidly as n decreases, in line with the observations in Fig. 4.11(a, b). We estimate the thinning rate to be $t^{-2.25}$ for $n \geq 1$ and $n < 1$. To better understand the variations in n , we plot key outputs, $h(x, t = 800)$, $u(x, t = 800)$, the shear-rate $u_x(x, t = 800)$ and

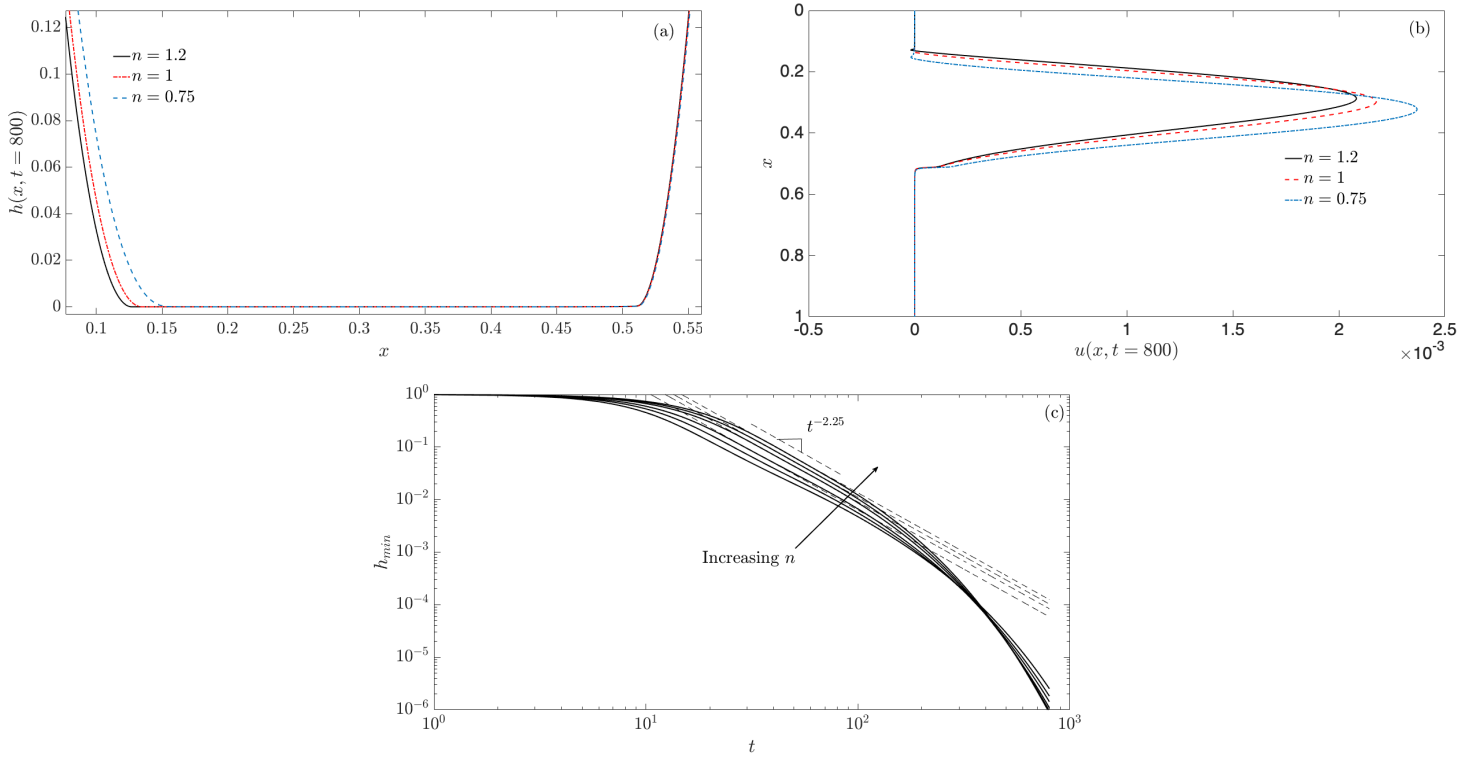


Figure 4.11: (a) Film thickness $h(x, t = 800)$, (b) extensional flow speed $u(x, t = 800)$ and (c) the global minimum h_{min} as a function of time t , for the Carreau model with $n = 0.6, 0.65, 0.75, 0.85, 1, 1.1, 1.2$, $\mu_1 = 1$, $Ca = 10^3$, $\lambda = 100$ ($\lambda^* = 10$ s) and $\mu_\infty = 0$ fixed. We estimate the thinning rate to be $t^{-2.25}$ for $n < 1$ and $n \geq 1$.

the shear-rate dependent viscosity $\mu(|u_x|)$ for $n = 0.75$ (corresponding to the shear-thinning fluid case) in Fig. 4.12(a), and $n = 1.2$ (corresponding to the shear thickening fluid case) in Fig. 4.12(b). We observe that the shear rate $u_x \ll 1$ across the entire

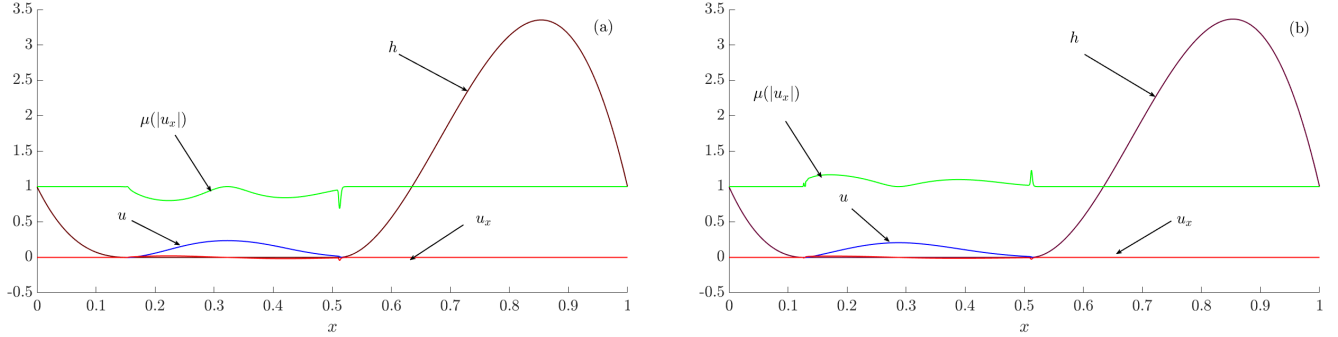


Figure 4.12: The film thickness $h(x, t = 800)$ (black curve), the extensional flow speed $u(x, t = 800)$ (blue curve), the shear rate $u_x(x, t = 800)$ (red curve) and the shear-rate dependent viscosity $\mu(|u_x|)$ (green curve) for (a) $n = 0.75$ (corresponding to the shear-thinning fluid case), and (b) $n = 1.2$ (corresponding to the shear-thickening fluid case), for fixed $\mu_1 = 1$, $Ca = 10^3$, $\lambda = 100$ ($\lambda^* = 10$ s) and $\mu_\infty = 0$.

film, and throughout the evolution process. This results in lower viscosities for $n < 1$ (Fig. 4.10(a)) and higher viscosities for $n \geq 1$ (Fig. 4.12(b)). Moreover, we observe from Fig. 4.12(a) that the spatial profile of viscosity for $n < 1$ is less than 1 near where the shear rate $u_x \neq 0$. The opposite happens for $n > 1$ (Fig. 4.12(b)), with a spike in viscosity corresponding to a change in shear rate observed where the flat middle region of the film connects onto the pendant drop near the bottom of the film.

4.5 Conclusions

In this chapter, we investigated the draining of a vertically-aligned free film containing a non-Newtonian liquid between two rigid supports due to the combined effects of

extensional viscous, gravity and surface tension forces. We assumed isothermal conditions, so the liquid properties are independent of variations in temperature. A study of the system parameters, mainly, the liquid consistency index K , the Power Law index, n , and the liquid yield stress, τ_p , was undertaken using a regularised Power Law model and regularised Herschel-Bulkley model of viscoplastic flow. The regularization was required since where the shear rate is zero, the Power Law model predicts infinite viscosity when $n < 1$, and the Power Law model predicts zero viscosity when $n > 1$ resulting in the stress balance equation becomes singular in this limit. Their influence on the evolution of the film's free surface, its long-time thinning rate and the draining of liquid from the film were investigated.

For fixed n , we observed that as K (K^*) was reduced (reducing liquid resistance), the film thinned more rapidly due to the faster extensional flow leading to severe thinning of the film and its eventual rupture (Fig. 4.1(c)). When n was varied for fixed K^* , we observed that the dynamics could depend on the relative magnitudes of the two terms in the Power Law model representing the dependence of K on n , $\left(\frac{\rho^* g^* L^*}{K^*}\right)^{n-1}$, and the shear-rate-dependent term, $|u_x|^{n-1}$. For large values of K^* , the two terms are of similar magnitude for the low shear rates observed in these cases. As a result, the effective fluid viscosity $\mu(|u_x|)$ was lower for $n > 1$ compared to $n < 1$, for $|u_x| < 1$. Due to this the film thinned more rapidly for $n > 1$ due to the faster extensional flow leading to severe thinning of the film and its eventual rupture. The opposite happened for $n < 1$, where an increase in viscosity at low shear rates results in an increase in

the liquid viscosity slowing down the drainage within the film and its thinning. We observed weak dependence of n on the Power Law thinning rate, with t^{-2} thinning rate for $n < 1$ and $t^{-2.25}$ for $n \geq 1$ (Fig. 4.3(c)). For low and intermediate values of K^* , the dependence of K on n dominates the shear rate dependence on n , for low shear rates, resulting in slower extensional flows and reduced thinning of the film for $n > 1$ compared to $n < 1$, at least for early and intermediate times (Fig. 4.6). This behaviour persists for much longer times if K^* is further reduced.

The draining and thinning behaviour was close to that of a Newtonian film for small values of τ_p . When τ_p was increased, the flow exhibited weakly yielding behaviour primarily in a region around the maximum in the extensional flow (corresponding to the minimum in the film thickness); the width of this weakly yielding region increased as the value of τ_p increases. The weakly yielding region slowed down the extensional flow speed in the lamellar region leading to a relatively thicker middle section in comparison to a film with zero yield stress at any given instant of time. We observed a noticeable decrease in the film's thinning rate as τ_p was increased, with a t^{-2} thinning rate for $n > 1$ (in comparison to $t^{-2.25}$ for $\tau_p = 0$) and $t^{-1.7}$ thinning rate for $n = 1$ (in comparison to $t^{-2.25}$ for $\tau_p = 0$). For $n < 1$, the dependence was weak with $t^{-1.8}$ thinning rate (in comparison to t^{-2} for $\tau_p = 0$).

It is known that Power Law fluids are inappropriate for certain low-shear rate flows (Myers [45]). Therefore, in the absence of any experimental evidence, our thinning rate predictions for the low shear rates are questionable. Our results identified the

parameter, $K = (K^*/\mu_0^*)(U^*/L^*)^{n-1}$ (a dimensionless liquid consistency index), to play a key role in the draining and thinning dynamics. Decreasing K for fixed n increased the extensional flow speed and corresponding shear rates (which scaled like $1/K^{1/n}$, resulting in the film thinning very rapidly on a timescale which scaled like $K^{1/n}$ (Fig. 4.1,4.2). Moreover, this also indicated that for small values of K , the highest shear rates and severest thinning rates would be for $n < 1$. For large values of K , the film drains and thins faster for $n > 1$ compared to $n < 1$. Experimental data for polymeric fluids show that $K \approx (10^{-2} - 20)$ (see Table 1 in Myers [45]). For the smaller range of values of K , the shear rate would be significantly larger and in the range of validity of the Power Law model for the film thinning rate predictions to be more reliable. However, for these values of K the thinning of the film is very rapid for any Power Law behaviour to be observed.

We also investigated the Carreau model which is well behaved at low shear rates [45]. We had to choose a large value of $\lambda^* \approx 10$ s (dimensionless $\lambda = 100$; although not unrealistic, e.g., experimental data for polystyrene liquid showed that $\lambda^* \approx 46$ [45]) to observe variation in the viscosity from the Newtonian case. We observed that the film drains and thins more rapidly for $n < 1$, compared to $n > 1$, unlike the Power Law model (compare Figs. 4.3 and 4.11 for Power Law and Carreau models, respectively). The thinning rates appeared to be less dependent on n , with a thinning rate estimated to be $t^{-2.25}$, similar to the Newtonian case. The disparity in the results between the Power Law models and the Carreau model highlights the inappropriateness of

applying the Power Law fluid model at low shear rates. At higher shear rates, one would need to compare both models by choosing appropriate values for K and λ . Such comparisons can be made, for example, in the shear thinning region by choosing $K^* = \mu_0^* \lambda^{*n-1}$ (or dimensionless $K = \lambda^{n-1}$). [45, 18]. Figure 4.13(a, b) shows h_{min} versus t for 2 different liquids, Polystyrene and Hydroxyethylcellulose, respectively, using the Power Law and Carreau models. The parameter values used are based on

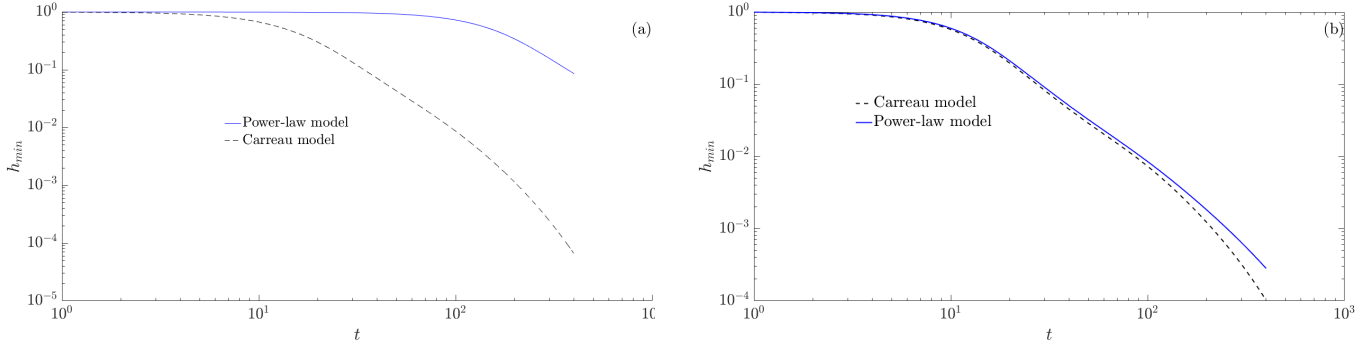


Figure 4.13: Comparison between the Power Law and Carreau models for two different liquids, (a) Polystyrene $(n, K, \lambda) = (0.8, 4, 0.001)$, and (b) Hydroxyethylcellulose $(n, K, \lambda) = (0.8, 0.51, 30)$.

those reported for these liquids in Table 1 in Myers [45], except the value of $n = 0.8$ is chosen for both liquids, while their reported values are $n = 0.4, 0.5$ for Polystyrene and Hydroxyethylcellulose, respectively [45]. We were unable to compute the solutions for low values of n , as mentioned previously. We note here that the comparison for Polystyrene was done using experimentally reported values for K and λ , while these values for Hydroxyethylcellulose were obtained by comparing the two models in the shear thinning region, as explained above. We observe from Fig. 4.13(a), that the comparison is not good for Polystyrene, but the two models are in good agreement for Hydroxyethylcellulose. This is consistent with the results shown in §4.4. The Power

Law model predicts low shear rates for large values of K resulting in a large effective viscosity and slower thinning of the film. For smaller values of K , even though the shear rates could be low, this is offset by the lower value of K , resulting in a lower effective viscosity and quicker thinning of the film.

We conclude by making some comparisons with a similar study done by Brush & Roper [18], who investigated the draining of a non-Newtonian liquid film without the influence of gravity. In the limit of $Ca \gg 1$, they were able to extend the asymptotic framework of Breward [15, 16] for a Newtonian liquid to a Power Law liquid. They analytically predicted the film's thinning rate to be t^{-2} and independent of the Power Law exponent n , which is the same as that for a Newtonian liquid. They concluded that the effect of n was to shift the h_{min} versus t curve, without affecting the thinning rate. Our numerical results shown in Fig. 4.3(c) are broadly similar to theirs, except for a weak dependence of the thinning rate on n . We were unable to validate our predictions using the asymptotic framework described in chapter 3 due to not being able to solve the equations analytically, although the asymptotic framework could be extended for a generalised Newtonian liquid (not done here).

In this chapter and chapters 2, 3, we investigated the draining and thinning of a Newtonian and generalised Newtonian liquid film under isothermal conditions. In the next two chapters, we will include the effects due to changes in temperature, in particular, temperature-dependent viscosity and surface tension. These are important in foams manufactured using polymeric melts [11].

Chapter 5

Gravity-driven draining of a vertically-aligned thin Newtonian and non-isothermal liquid free film with temperature-dependent viscosity and surface tension

5.1 Introduction

In the previous chapters, the draining problem was investigated under isothermal conditions. In this chapter, we extend the model for a Newtonian liquid to include non-

isothermal effects, in particular, a temperature-dependent viscosity and surface tension, which provides the coupling between the temperature field and the flow, and cooling effects due to heat transfer at the film's free surface, and the top and bottom surfaces of the wire frame.

The outline of this chapter is as follows. We formulate the two-dimensional mathematical problem in §5.2 which provides the governing equations and boundary conditions for the flow and the temperature field. The lubrication approximation, allows simplification of the governing equations and boundary conditions to a system of three coupled PDEs for the evolution of the one-dimensional free surface shape and the extensional flow speed, and the two-dimensional temperature field. In §5.4, we perform numerical simulations of the evolution equations to determine the free surface shapes, the extensional flow speeds and temperature fields for a variety of parameter values related to the exponential viscosity-temperature model and a linear surface tension-temperature model. In §5.5, we discuss the main results.

5.2 Mathematical Formulation

The fluid flow problem is the same as that described in §2.2. A vertically-aligned thin liquid film supported by two rigid supports at the top and the bottom drains under the influence of gravity (see Fig. 2.1 for a schematic). The liquid in the film is hot compared to its surroundings, and assumed to be Newtonian with constant properties,

except, the liquid viscosity and surface tension are dependent on the temperature. The liquid loses its heat via the cooler free surface at $z^* = h^*(x^*, t^*)$, and the top and bottom supports at $x^* = 0, L^*$.

5.3 Governing equations

The governing equations for the flow are given by the conservation of mass and momentum, Eqs. (2.1,2.2). The two-dimensional governing equation for the temperature, T^* in Cartesian coordinates, (x^*, z^*) is given by

$$\rho^* c_p^* (T_{t^*}^* + u^* T_{x^*}^* + w^* T_{z^*}^*) = \kappa^* [T_{x^* x^*}^* + T_{z^* z^*}^*], \quad (5.1)$$

in a material with density, ρ^* , specific heat, c_p^* , thermal conductivity, κ^* and thermal diffusivity, $\kappa_d^* = \kappa^*/(\rho^* c_p^*)$. We neglect the contribution from viscous dissipation. (u^*, w^*) are the flow speeds in the x^* and z^* directions, respectively. The constitutive relation between the liquid stress and its rate of strain for a Newtonian liquid with temperature-dependent viscosity is written as:

$$\boldsymbol{\tau}^* = \mu^*(T^*) \dot{\boldsymbol{\gamma}}^*, \quad (5.2)$$

where $\mu^*(T^*)$ is the temperature-dependent liquid viscosity and $\dot{\boldsymbol{\gamma}}^*$ is the rate of strain tensor given by Eq. (2.4).

The boundary conditions for the flow are given by Eqs. (2.6-2.11). The boundary conditions for the temperature, T^* are as follows. We impose the symmetry boundary condition along the center line $z^* = 0$ for the temperature:

$$T_{z^*}^* = 0. \quad (5.3)$$

At the free surface, $z^* = h^*(x^*, t^*)$, we impose a heat flux boundary condition:

$$-\kappa^* \mathbf{n}^* \cdot \nabla T^* = a_m^* (T^* - T_a^*), \quad (5.4)$$

where a_m^* is a heat transfer coefficient (assumed constant) and T_a^* is the ambient temperature (assumed constant), and $\mathbf{n}^* = \frac{1}{\sqrt{1 + h_{x^*}^{*2}}}(-h_{x^*}^*, 1)$ is the outward-pointing normal vector to the free surface. This assumes that the heat flux is proportional to the temperature difference across this boundary, referred to as Newton's law of cooling.

We can write Eq. (5.4) as:

$$\kappa^* (1 + h_{x^*}^{*2})^{-\frac{1}{2}} (T_{z^*}^* - h_{x^*}^* T_{x^*}^*) = -a_m^* (T^* - T_a^*). \quad (5.5)$$

At $x^* = 0, L^*$ we impose the following heat flux boundary condition:

$$-\kappa^* \mathbf{n}^* \cdot \nabla T^* = b_s^*(T^* - T_s^*), \quad (5.6)$$

$$\begin{cases} \kappa^* T_{x^*}^* = b_s^*(T^* - T_s^*), & \text{at } x^* = 0, \\ -\kappa^* T_{x^*}^* = b_s^*(T^* - T_s^*), & \text{at } x^* = L^*, \end{cases} \quad (5.7)$$

where b_s^* is a heat transfer coefficient at the wire frames (assumed constant) and T_s^* is the temperature there (assumed constant). In the above, we have used the fact that $\mathbf{n}^* = (-1, 0)$ at $x^* = 0$ and $\mathbf{n}^* = (1, 0)$ at $x^* = L^*$.

The non-dimensionalisation of the flow variables are the same as in §2.3 in chapter 2.

We define: $T^* = T_a^* + \Delta^* T^* \theta$ ($0 \leq \theta \leq 1$), $\Delta^* T^* = T_i^* - T_a^*$. Note: $\theta = 0$, implies $T^* = T_a^*$ and $\theta = 1$, implies $T^* = T_i^*$, where T_i^* is an initial temperature of the liquid within the film, and $T_i^* > T_a^*$. Using this, Eqs. (5.1,5.3,5.5,5.6) in dimensionless form are:

$$Pe_r[\theta_t + u\theta_x + w\theta_z] = [\epsilon^2\theta_{xx} + \theta_{zz}], \quad (5.8a)$$

$$\theta_z = 0, \text{ at } z = 0, \quad (5.8b)$$

$$\theta_z = \epsilon^2 h_x \theta_x - a\epsilon^2 \theta \sqrt{1 + \epsilon^2 h_x^2}, \text{ at } z = h(x, t), \quad (5.8c)$$

$$\theta_x = \epsilon^2 b(\theta - \theta_s), \text{ at } x = 0, \quad (5.8d)$$

$$\theta_x = -\epsilon^2 b(\theta - \theta_s), \text{ at } x = 1. \quad (5.8e)$$

Here the reduced Péclet number, $Pe_r = \epsilon^2 Pe$ (assumed to be $O(1)$), $Pe = (\rho^* c_p^* U^* L^*) / \kappa^* =$

U^*L^*/κ_d^* , is the Péclet number (compares convective to diffusive heat transport), $a = a_m^*H^*/(\epsilon^2\kappa^*)$ and $b = b_s^*H^*/(\epsilon^2\kappa^*)$ are the heat transfer coefficients at the free surface and substrate, respectively, and $\theta_s = (T_s^* - T_a^*)/(T_i^* - T_a^*)$.

Our starting point in deriving the evolution equation for h is from Eq. (2.32). Integrating Eq. (2.32) with respect to z and applying the boundary condition Eq. (2.34), we have

$$\tau_1^{xz} = -2 \int_0^z \tau_{0x}^{xx} dz - \frac{1}{Ca} \int_0^z (\gamma(\theta)h_{xx})_x dz - z[1 - Re(u_{0t} + u_0u_{0x})]. \quad (5.9)$$

Note that $\tau_0^{xx} = \mu(\theta(x, z, t))u_{0x}$. Unlike the isothermal case where there is no tangential stress at the free surface, the tangential stress at the free surface for the non-isothermal case is driven by gradients in surface tension due to variations in temperature (the so-called Marangoni stress). The tangential stress boundary condition at $z^* = h^*(x^*, t^*)$ is now written as $\mathbf{t}^* \cdot \boldsymbol{\sigma}^* \cdot \mathbf{n}^* = \nabla^* \gamma^* \cdot \mathbf{t}^*$. Hence, Eq.(2.9) becomes

$$(1 - h_{x^*}^{*2})\tau^{*xz^*} + h_{x^*}^* (\tau^{*z^*z^*} - \tau^{*x^*x^*}) = [\gamma_{x^*}^*(\theta^*) + h_{x^*}^* \gamma_{z^*}^*(\theta^*)] \sqrt{1 + h_{x^*}^{*2}}, \text{ at } z^* = h^*(x^*, t^*). \quad (5.10)$$

The nondimensionalised form of Eq. (5.10) can be written as:

$$(1 - \epsilon^2 h_x^2)\tau^{xz} + \epsilon^2 h_x (\tau^{zz} - \tau^{xx}) = \frac{1}{Ca} [\gamma_x(\theta) + h_x \gamma_z(\theta)] \sqrt{1 + \epsilon^2 h_x^2}, \text{ at } z = h(x, t), \quad (5.11)$$

Assuming that any gradients in surface tension arise only at $O(\epsilon^2)$, Eq.(2.36) can be written as:

$$\tau_1^{xz} + h_{0x}^2 \tau_0^{xz} + h_{0x}(\tau_0^{zz} - \tau_0^{xx}) = \frac{1}{Ca} [\gamma_x(\theta) + h_{0x} \gamma_z(\theta)], \text{ at } z = h_0. \quad (5.12)$$

On substituting Eq.(5.12) into Eq. (5.9), we obtain the stress balance equation at $z = h(x, t)$ (given by Eq. (2.38)), which can be written as:

$$\begin{aligned} & 4 \left[\mu(\theta) h_x u_{0x} + \int_0^h (\mu(\theta) u_{0x})_x dz \right] + \frac{1}{Ca} \int_0^h (\gamma(\theta) h_{xx})_x dz \\ & + h[1 - Re(u_{0t} + u_0 u_{0x})] = \frac{1}{Ca} [\gamma_x(\theta) + h_x \gamma_z(\theta)]. \end{aligned} \quad (5.13)$$

Using Eq. (2.40) and the expression for τ_1^{xz} in Eq. (5.9), we obtain

$$u_{1z} = -\frac{1}{\mu(\theta)} \left[4 \int_0^z (\mu(\theta) u_{0x})_x dz + \frac{1}{Ca} \int_0^z (\gamma(\theta) h_{xx})_x dz + z[1 - Re(u_{0t} + u_0 u_{0x})] \right] + u_{0xx} z. \quad (5.14)$$

Using the boundary condition $u_1 = 0$ at $z = h$, we can write the $O(\epsilon^2)$ correction to the flux Q as:

$$Q_1 = \int_0^h u_1 dz = - \int_0^h z u_{1z} dz, \quad (5.15)$$

which, using equation Eq. (5.14), gives

$$\begin{aligned}
Q_1 = & \int_0^h \frac{4z}{\mu(\theta)} \left[\int_0^z (\mu(\theta) u_{0x})_x dz' \right] dz + \frac{1}{Ca} \int_0^h \frac{z}{\mu(\theta)} \left[\int_0^z (\gamma(\theta) h_{xx})_x dz' \right] dz \\
& + [1 - Re(u_{0t} + u_0 u_{0x})] \int_0^h \frac{z^2}{\mu(\theta)} dz - \frac{h^3}{3} u_{0xx}. \tag{5.16}
\end{aligned}$$

Hence, using $Q_0 = u_0 h$ and the above expression for Q_1 , we can write the evolution equation for $h(x, t)$ as:

$$h_t + Q_{0x} + Q_{1x} = 0. \tag{5.17}$$

In order to solve Eqs. (5.8,5.13,5.17) numerically, it is instructive to map $(x, z) \in [0, 1] \times [0, h]$ to a rectangular domain $(x, z) \in [0, 1] \times [0, 1]$. We apply the following change of variables:

$$\bar{x} = x, \quad \bar{z} = \frac{z}{h(x, t)}, \quad \bar{t} = t. \tag{5.18}$$

Using the chain rule, we can write

$$\frac{\partial}{\partial x} = \frac{\partial}{\partial \bar{x}} - \frac{\bar{z} h_{\bar{x}}}{h} \frac{\partial}{\partial \bar{z}}, \quad \frac{\partial}{\partial z} = \frac{1}{h} \frac{\partial}{\partial \bar{z}}, \quad \frac{\partial}{\partial t} = \frac{\partial}{\partial \bar{t}} - \frac{\bar{z} h_{\bar{t}}}{h} \frac{\partial}{\partial \bar{z}}. \tag{5.19}$$

Applying the above change of variables to Eq. (5.8), we obtain the transformed evolu-

tion equation for $\theta(\bar{x}, \bar{z}, \bar{t})$ given by

$$Pe_r \left[\theta_{\bar{t}} + u_0 \theta_{\bar{x}} + (w_0 - \bar{z} u_0 h_{\bar{x}} - \bar{z} h_{\bar{t}}) \frac{1}{h} \theta_{\bar{z}} \right] = \frac{1}{h^2} \theta_{\bar{z}\bar{z}} \\ + \epsilon^2 \left[\theta_{\bar{x}\bar{x}} - \bar{z} \left(\frac{h_{\bar{x}}}{h} \right)_{\bar{x}} \theta_{\bar{z}} - \frac{\bar{z} h_{\bar{x}}}{h} \left(2\theta_{\bar{x}\bar{z}} - \left(\frac{\bar{z} h_{\bar{x}}}{h} \theta_{\bar{z}} \right)_{\bar{z}} \right) \right], \quad (\bar{x}, \bar{z}) \in [0, 1] \times [0, 1], \quad (5.20a)$$

$$\theta_{\bar{z}} = 0, \quad \text{at } \bar{z} = 0, \forall \bar{x}, \quad (5.20b)$$

$$\theta_{\bar{z}} = \frac{\epsilon^2 h h_{\bar{x}} \theta_{\bar{x}}}{1 + \epsilon^2 \bar{z} h_{\bar{x}^2}} - \frac{a h \theta}{1 + \epsilon^2 \bar{z} h_{\bar{x}^2}}, \quad \text{at } \bar{z} = 1, \forall \bar{x}, \quad (5.20c)$$

$$\theta_{\bar{x}} = \epsilon^2 b (\theta - \theta_s) + \frac{\bar{z} h_{\bar{x}}}{h} \theta_{\bar{z}}, \quad \text{at } \bar{x} = 0, \forall \bar{z} \quad (5.20d)$$

$$\theta_{\bar{x}} = -\epsilon^2 b (\theta - \theta_s) + \frac{\bar{z} h_{\bar{x}}}{h} \theta_{\bar{z}}, \quad \text{at } \bar{x} = 1, \forall \bar{z}. \quad (5.20e)$$

The film thickness evolution equation Eq. (5.17) in the transformed coordinates becomes,

$$h_{\bar{t}} + (Q_0 + \epsilon^2 Q_1)_{\bar{x}} = 0, \quad (5.21a)$$

$$Q_0 = u_0 h, \quad (5.21b)$$

$$Q_1 = 4 \int_0^1 \frac{h^3 \bar{z}}{\mu(\theta)} \left[\int_0^{\bar{z}} (\mu(\theta) u_{0\bar{x}})_{\bar{x}} d\bar{z}' \right] d\bar{z} - 4 \int_0^1 \frac{h^3 \bar{z}}{\mu(\theta)} \left[\int_0^{\bar{z}} \frac{\bar{z} h_{\bar{x}}}{h} (\mu(\theta) u_{0\bar{x}})_{\bar{z}} d\bar{z}' \right] d\bar{z} \\ + \frac{1}{Ca} \int_0^1 \frac{h^3 \bar{z}}{\mu(\theta)} \left[\int_0^{\bar{z}} (\gamma(\theta) h_{\bar{x}\bar{x}})_{\bar{x}} d\bar{z}' \right] d\bar{z} - \frac{1}{Ca} \int_0^1 \frac{h^3 \bar{z}}{\mu(\theta)} \left[\int_0^{\bar{z}} \frac{\bar{z} h_{\bar{x}}}{h} (\gamma(\theta) h_{\bar{x}\bar{x}})_{\bar{z}} d\bar{z}' \right] d\bar{z} \\ + \int_0^1 \frac{h^3 \bar{z}^2}{\mu(\theta)} d\bar{z} [1 - Re(u_{0t} + u_0 u_{0x})] - \frac{h^3}{3} u_{0\bar{x}\bar{x}}. \quad (5.21c)$$

The stress balance equation at $z = h(x, t)$, Eq. (5.13), in transformed variables can be

written as:

$$\begin{aligned}
& 4 \left[\mu(\theta) h_{\bar{x}} u_{0\bar{x}} + \int_0^1 (\mu(\theta) u_{0\bar{x}})_{\bar{x}} d\bar{z} - \int_0^1 \frac{\bar{z} h_{\bar{x}}}{h} (\mu(\theta) u_{0\bar{x}})_{\bar{z}} d\bar{z} \right] \\
& + \frac{1}{Ca} \left[\int_0^1 (\gamma(\theta) h_{\bar{x}\bar{x}})_{\bar{x}} d\bar{z} - \int_0^1 \frac{\bar{z} h_{\bar{x}}}{h} (\gamma(\theta) h_{\bar{x}\bar{x}})_{\bar{z}} d\bar{z} \right] + [1 - Re(u_{0t} + u_0 u_{0x})] h = \\
& \frac{1}{Ca} \left[\gamma_{\bar{x}} + \frac{h_{\bar{x}}}{h} (1 - h) \gamma_{\bar{z}} (z = h(x, t)) \right]. \tag{5.22}
\end{aligned}$$

Equations (5.21,5.22) are subject to the boundary conditions:

$$h(0, t) = h(1, t) = 1, \quad (\gamma(\theta) h_{\bar{x}\bar{x}})_{\bar{x}}(0, t) = (\gamma(\theta) h_{\bar{x}\bar{x}})_{\bar{x}}(1, t) = -Ca, \quad u(0, t) = u(1, t) = 0. \tag{5.23}$$

In the third and fourth boundary condition above, we assume that θ is uniform in z at $x = 0, 1$. The viscosity-temperature relationship, $\mu(\theta)$, is given by the non-dimensionalised form of Eqs. (1.8) in chapter 1,

$$\mu(\theta) = e^{-\alpha\theta}. \tag{5.24a}$$

Here, $\alpha = \alpha^*(T_i^* - T_a^*)$. The surface tension-temperature, $\gamma(\theta)$ is given by the non-dimensionalised form of Eq. (1.9) in chapter 1,

$$\gamma(\theta) = 1 - \beta\theta, \tag{5.25}$$

where $\beta = \beta^*(T_i^* - T_a^*) = O(\epsilon^2)$. This is to ensure that surface tension gradients arise

only at $O(\epsilon^2)$ as required in the above analysis.

5.4 Numerical results

In this section, we seek the numerical solution of Eqs. (5.20a,5.21,5.22) using the boundary conditions given in Eqs. (5.20b-5.20e,5.23). Equations (5.20a,5.21,5.22) are solved numerically using finite difference method on a two-dimensional rectangular mesh for $\theta(x, z, t)$ and one-dimensional mesh for $[h, u](x, t)$, and the method of lines. We use the implicit solver *ode15i* in MATLAB (MATLAB 6.1, The MathWorks Inc., Natick, MA, 2000) for our numerical simulations. The discretisation for the film's thickness (Eq. (5.21)) and the extensional flow speed (Eq. (5.22)) are the same as explained in Chapter 3. The only difference is the term $(\gamma(\theta)h_{xx})_x$, that appears in Eqs. (5.21,5.22,5.23). We write this term in the form $\gamma'(\theta)\theta_x h_{xx} + \gamma(\theta)h_{xxx}$, and use a second-order centered difference scheme to discretise $\gamma(\theta)_x$, θ_x and h_{xx} . We discretize h_{xxx} in the same way as shown in §3.3. All other terms in Eqs. (5.21,5.22) are discretized as previously discussed. The integrals that appear in Eq. (5.21) (in the flux terms) and Eq. (5.22) are approximated using the trapezium rule. For the inner indefinite integrals, we used MATLAB's inbuilt *cumtrapz* function and the outer definite integrals were evaluated using MATLAB's *trapz* function.

We discretize Eq. (5.20a) for $\theta(x, z, t)$ using second-order centered differences as follows

(keeping the time derivative continuous):

$$\begin{aligned}
& Pe_r \left[\theta_{t,i,j} + u_{0i} \left(\frac{\theta_{i+1,j} - \theta_{i-1,j}}{2\Delta x} \right) + (w_{0i} - j\Delta z u_{0i} \left(\frac{h_{i+1} - h_{i-1}}{2\Delta x} \right) - j\Delta z h_{t,i}) \frac{1}{h_i} \left(\frac{\theta_{i,j+1} - \theta_{i,j-1}}{2\Delta z} \right) \right] \\
& \hspace{15em} (5.26) \\
& = \frac{1}{h_i^2} \left(\frac{\theta_{i,j+1} - 2\theta_{i,j} + \theta_{i,j-1}}{\Delta z^2} \right) + \epsilon^2 \left(\frac{\theta_{i+1,j} - 2\theta_{i,j} + \theta_{i-1,j}}{\Delta x^2} \right), i = 1, \dots, N + 1, \quad j = 1, \dots, M + 1.
\end{aligned}$$

Note that we only retain the θ_{xx} term in the regularization of Eq. (5.20a). We use the boundary conditions at $x = 0, 1$, $\theta_x = 0$, Eqs. (5.20d,5.20e) to determine the fictitious points $\theta_{0,j} = \theta_{2,j}$, $\forall j = 1, \dots, M + 1$ and $\theta_{N+2,j} = \theta_{N,j}$, $\forall j = 1, \dots, M + 1$. We assume here that θ is uniform in z at $x = 0, 1$, so $\theta_z = 0$. Note $b = 0$ in all the results shown. Similarly, we use the boundary conditions at $z = 0, 1$ given by Eqs. (5.20b,5.20c) to determine the fictitious points $\theta_{i,0} = \theta_{i,2}$, $\forall i = 1, \dots, N + 1$ and $\theta_{i,M+2} = \theta_{i,M}$, $\forall i = 1, \dots, N + 1$. Here, $N + 1, M + 1$ are the number of mesh points in the x and z directions, respectively, and $\Delta(x, z)$ are the corresponding mesh widths.

The focus of this chapter is the evolution of the film's thickness $h(x, t)$, the extensional flow speed $u(x, t)$, and the temperature $\theta(x, z, t)$. We will vary the key parameters related to the non-isothermal conditions: the reduced Péclet number Pe_r , the heat transfer coefficient at the free surface a , the decay constant α in the exponential viscosity-temperature relationship, and β in the surface tension-temperature relationship. In all the results shown below, we choose the heat transfer coefficient at the substrate $b = 0$ and the Reynold's number $Re = 0$. The initial conditions for h , θ and u are chosen as: $h(x, 0) = \theta(x, z, 0) = 1$ and $u(x, 0) = x(1 - x)/8$. In all the results in

this chapter, we fix the Capillary number $Ca = 10^3$, $\Delta(x, z) = 10^{-3}$ in all the numerical simulations, to achieve convergence within a prescribed tolerance.

In the first set of results shown below, we investigate the influence of viscosity varying with temperature, and take the surface tension to be constant (so, $\beta = 0$). Figures 5.1(a – j) show the contour plot for $\theta(x, z, t)$ at times $t = 10, 20, 30, 40, 50, 60, 70, 80, 90, 100$, respectively, with $Pe_r = 0.1$, $a = 0.02$, $\alpha = 2$ and $\theta_s = 0$. The temperature profiles are superimposed on the corresponding free surface shape h . We clearly observe that the heat loss at the free surface results in the temperature dropping from its initial value $\theta = 1$ ($T = T_i$) to its equilibrium value, $\theta = 0$ ($T = T_a$), very quickly. At small values of Pe_r , the diffusion of temperature across the thickness of the film dominates, i.e., θ_{zz} , resulting in the film cooling uniformly.

Figures 5.2(a – j) show the contour plot for $\theta(x, z, t)$ at times $t = 10, 20, 30, 40, 50, 60, 70, 80, 90, 100$, respectively, with $Pe_r = 1$, $a = 0.02$, $\alpha = 2$ and $\theta_s = 0$. The temperature profiles are superimposed on the corresponding free surface shape h . The slower diffusion rate at $Pe_r = 1$ compared to the previous case with $Pe_r = 0.1$ results in less rapid cooling but still uniform along the free surface. Figures 5.3(a – j) show the contour plot for $\theta(x, z, t)$ at times $t = 10, 20, 30, 40, 50, 60, 70, 80, 90, 100$, respectively, with $Pe_r = 10$, $a = 0.02$, $\alpha = 2$ and $\theta_s = 0$. The temperature profiles are superimposed on the corresponding free surface shape h . We observe that at this value of Pe_r , the diffusion rate is even slower, and is less dominant in suppressing spatial variations in temperature due to non-uniform cooling both along the film as well as within

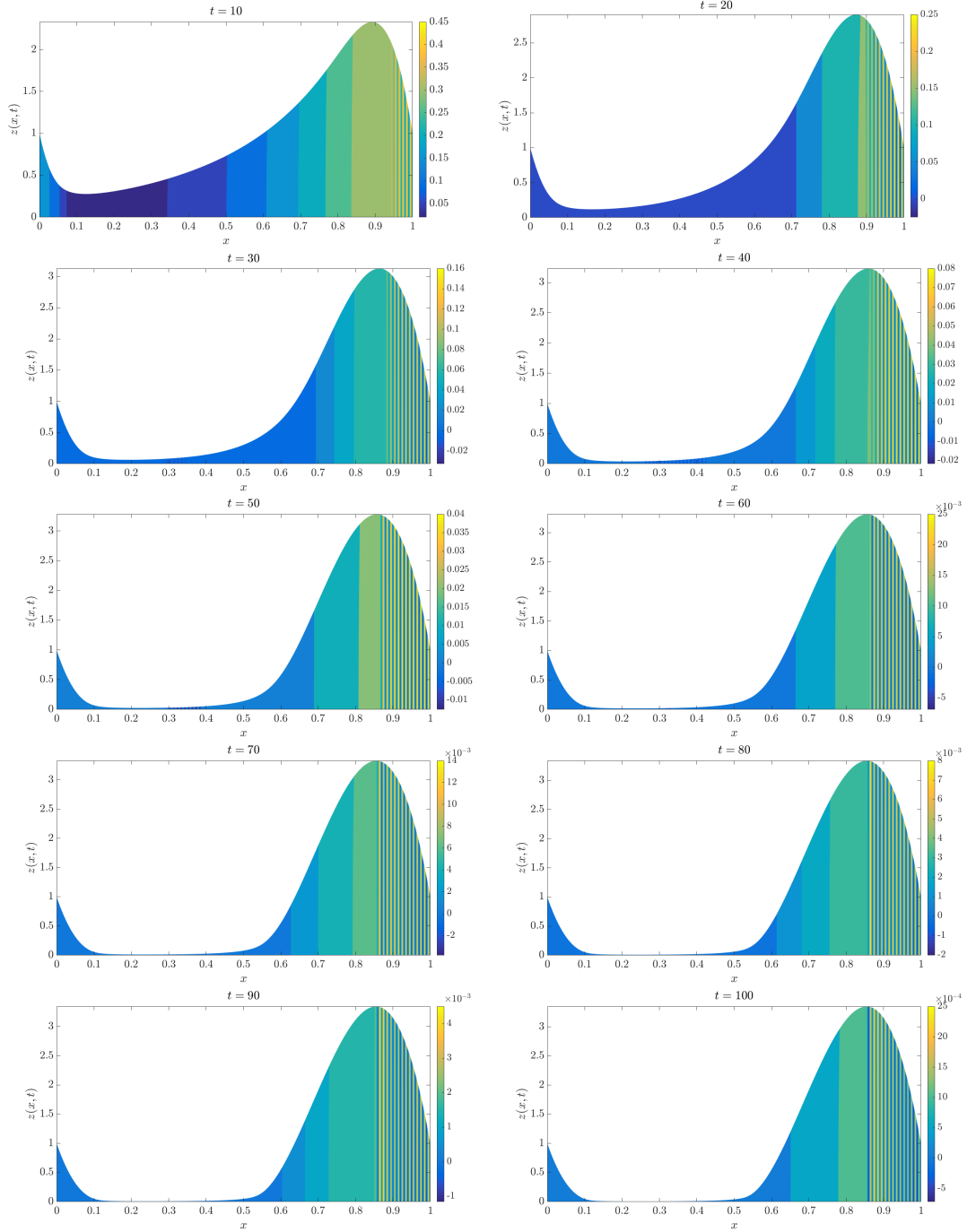


Figure 5.1: The contour plot for (a) $\theta(x, z, t = 10)$, (b) $\theta(x, z, t = 20)$, (c) $\theta(x, z, t = 30)$, (d) $\theta(x, z, t = 40)$, (e) $\theta(x, z, t = 50)$, (f) $\theta(x, z, t = 60)$, (g) $\theta(x, z, t = 70)$, (h) $\theta(x, z, t = 80)$, (i) $\theta(x, z, t = 90)$, and (j) $\theta(x, z, t = 100)$ (the temperature profiles are superimposed on the corresponding free surface shape h), with $Pe_r = 0.1$, $a = 0.02$, $\alpha = 2$, $\theta_s = 0$.

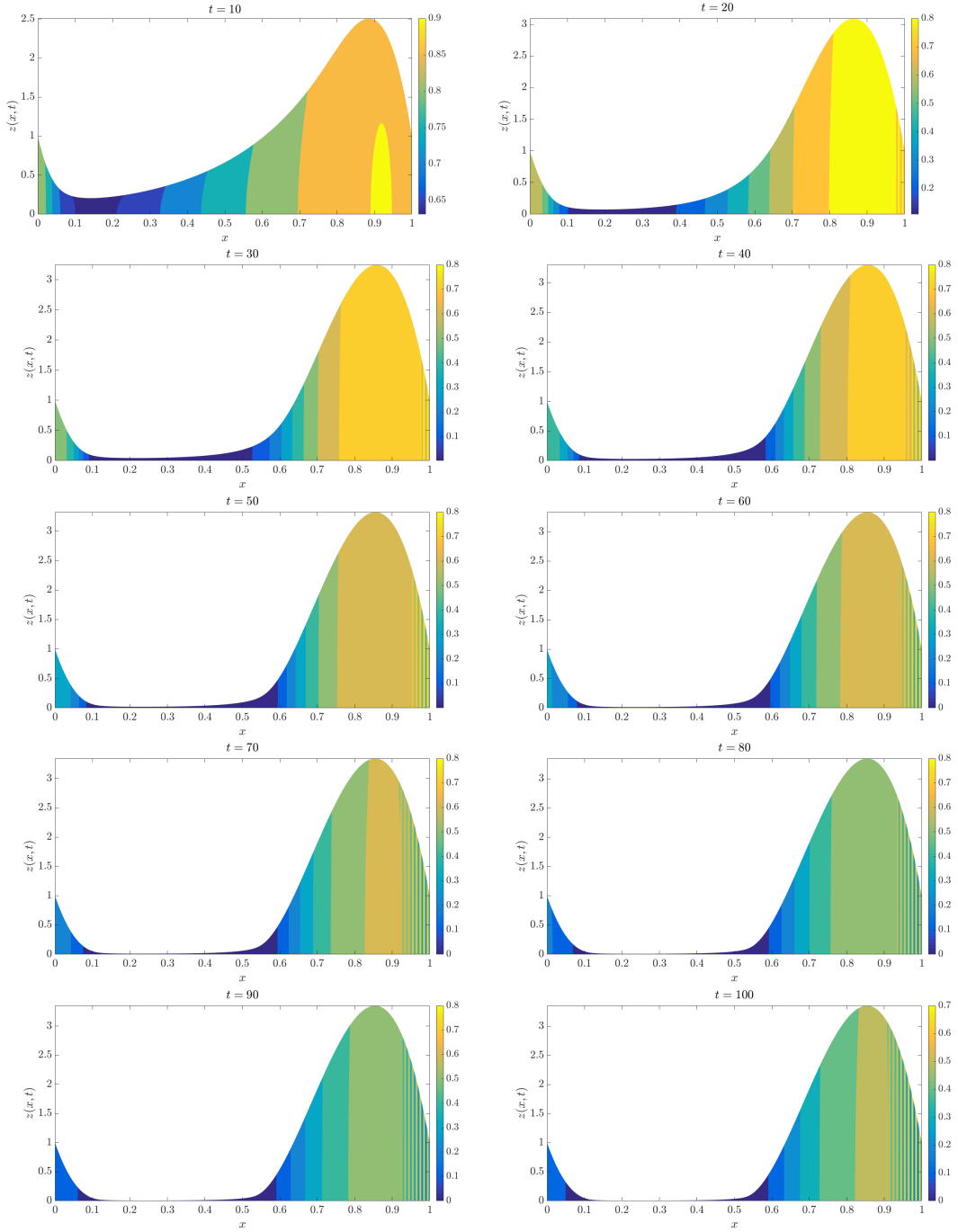


Figure 5.2: The contour plot for (a) $\theta(x, z, t = 10)$, (b) $\theta(x, z, t = 20)$, (c) $\theta(x, z, t = 30)$, (d) $\theta(x, z, t = 40)$, (e) $\theta(x, z, t = 50)$, (f) $\theta(x, z, t = 60)$, (g) $\theta(x, z, t = 70)$, (h) $\theta(x, z, t = 80)$, (i) $\theta(x, z, t = 90)$, and (j) $\theta(x, z, t = 100)$ (the temperature profiles are superimposed on the corresponding free surface shape h), with $Pe_r = 1$, $a = 0.02$, $\alpha = 2$, $\theta_s = 0$.

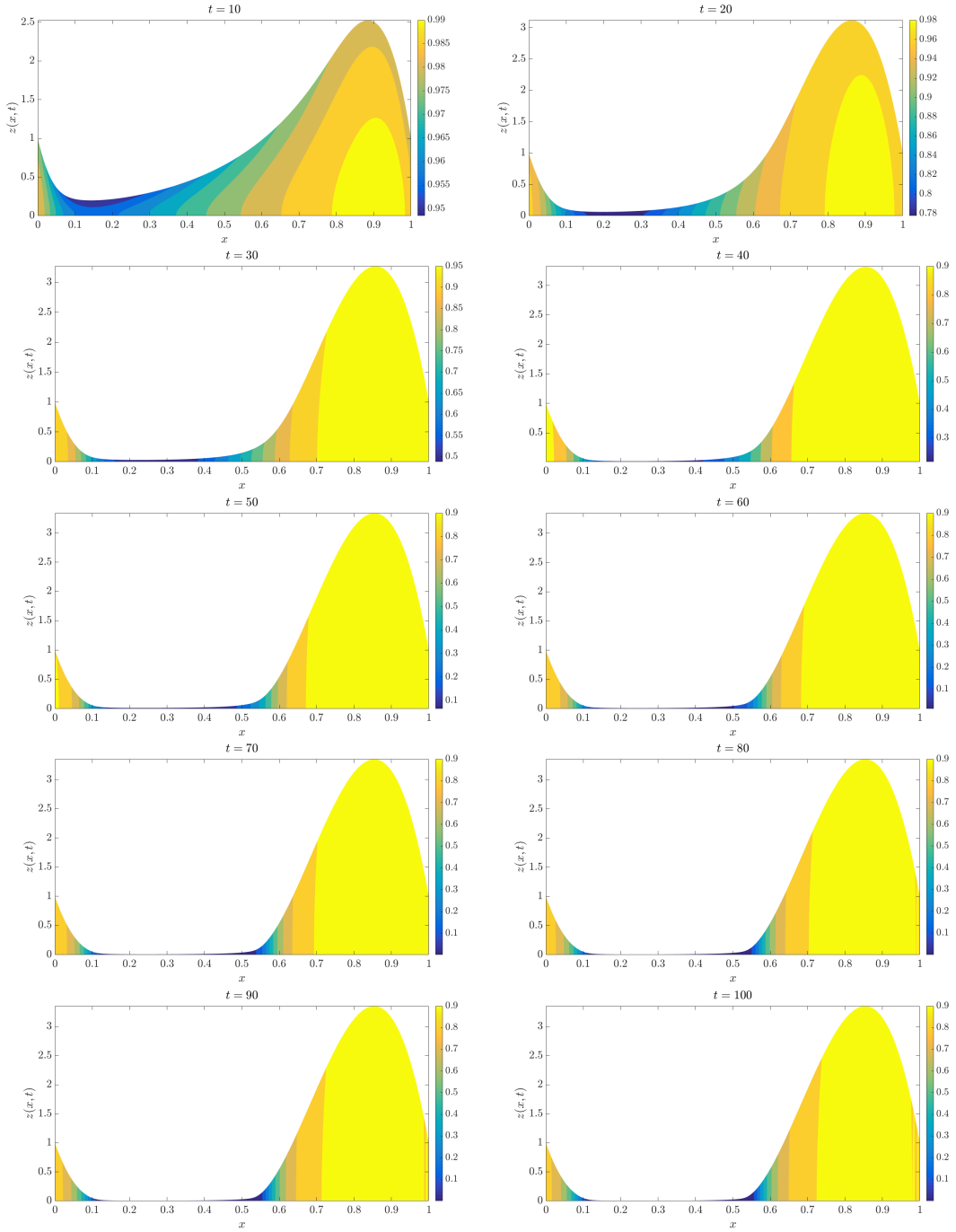


Figure 5.3: The contour plot for (a) $\theta(x, z, t = 10)$, (b) $\theta(x, z, t = 20)$, (c) $\theta(x, z, t = 30)$, (d) $\theta(x, z, t = 40)$, (e) $\theta(x, z, t = 50)$, (f) $\theta(x, z, t = 60)$, (g) $\theta(x, z, t = 70)$, (h) $\theta(x, z, t = 80)$, (i) $\theta(x, z, t = 90)$, and (j) $\theta(x, z, t = 100)$ (the temperature profiles are superimposed on the corresponding free surface shape h), with $Pe_r = 10$, $a = 0.02$, $\alpha = 2$, $\theta_s = 0$.

the film. This results in more pronounced cooling in the middle section of the film where h is much smaller, compared to near the ends where h is comparatively larger. This non-uniformity in the cooling is due to the rate of heat loss being inversely proportional to h - the thicker regions of the film retain their heat more compared to the thinner regions, which lose their heat and therefore cool relatively quickly. Figures 5.4($a - j$) show the contour plot for $\theta(x, z, t)$ at times $t = 10, 20, 30, 40, 50, 60, 70, 80, 90, 100$, respectively, with $Pe_r = 10^2$, $a = 0.02$, $\alpha = 2$ and $\theta_s = 0$. The temperature profiles are superimposed on the corresponding free surface shape h . For larger Pe_r , the spatial variations in θ are much more pronounced, with cooling in the middle section of the film where h is much smaller, compared to near the ends where h is comparatively larger. At the early times, we also observe variations in θ within the film (Fig. 5.4(a, b)), with the film slowly cooling from the free surface. At later times, it appears that θ is uniform across the film. Figures 5.5($a - j$) show the contour plot for $\theta(x, z, t)$ at times $t = 10, 20, 30, 40, 50, 60, 70, 80, 90, 100$, respectively, with $Pe_r = 10^3$, $a = 0.02$, $\alpha = 2$ and $\theta_s = 0$. The temperature profiles are superimposed on the corresponding free surface shape h . We clearly observe that the majority of the cooling is in the middle section of the film, where the film is very thin; the upper capillary meniscus and the pendant drop region at the bottom remain almost insulated at its initial temperature from the cooler middle section and a thin cooler boundary layer near the free surface (Fig. 5.5(a, b) where the boundary layer is clearly visible; in Fig. 5.3($c - j$) the boundary layer is very thin and not resolved here). Figure 5.6(a, b, c) show the effect of varying $Pe_r = 0.1, 1, 10, 10^2, 10^3$, on $h(x, t = 100)$, $u(x, t = 100)$ and $h_{min}(t)$ (the

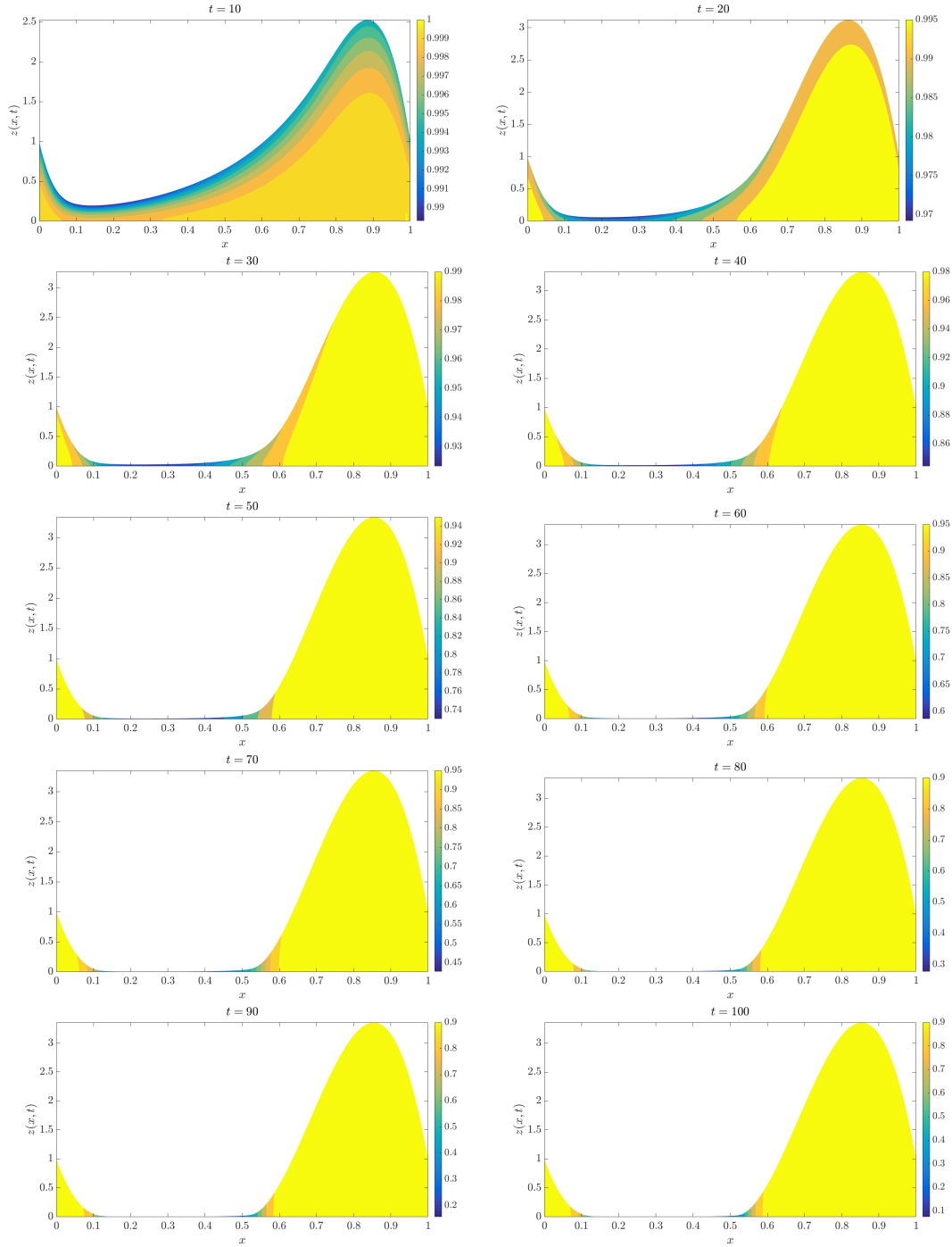


Figure 5.4: The contour plot for (a) $\theta(x, z, t = 10)$, (b) $\theta(x, z, t = 20)$, (c) $\theta(x, z, t = 30)$, (d) $\theta(x, z, t = 40)$, (e) $\theta(x, z, t = 50)$, (f) $\theta(x, z, t = 60)$, (g) $\theta(x, z, t = 70)$, (h) $\theta(x, z, t = 80)$, (i) $\theta(x, z, t = 90)$, and (j) $\theta(x, z, t = 100)$ (the temperature profiles are superimposed on the corresponding free surface shape h), with $Pe_r = 10^2$, $a = 0.02$, $\alpha = 2$, $\theta_s = 0$.

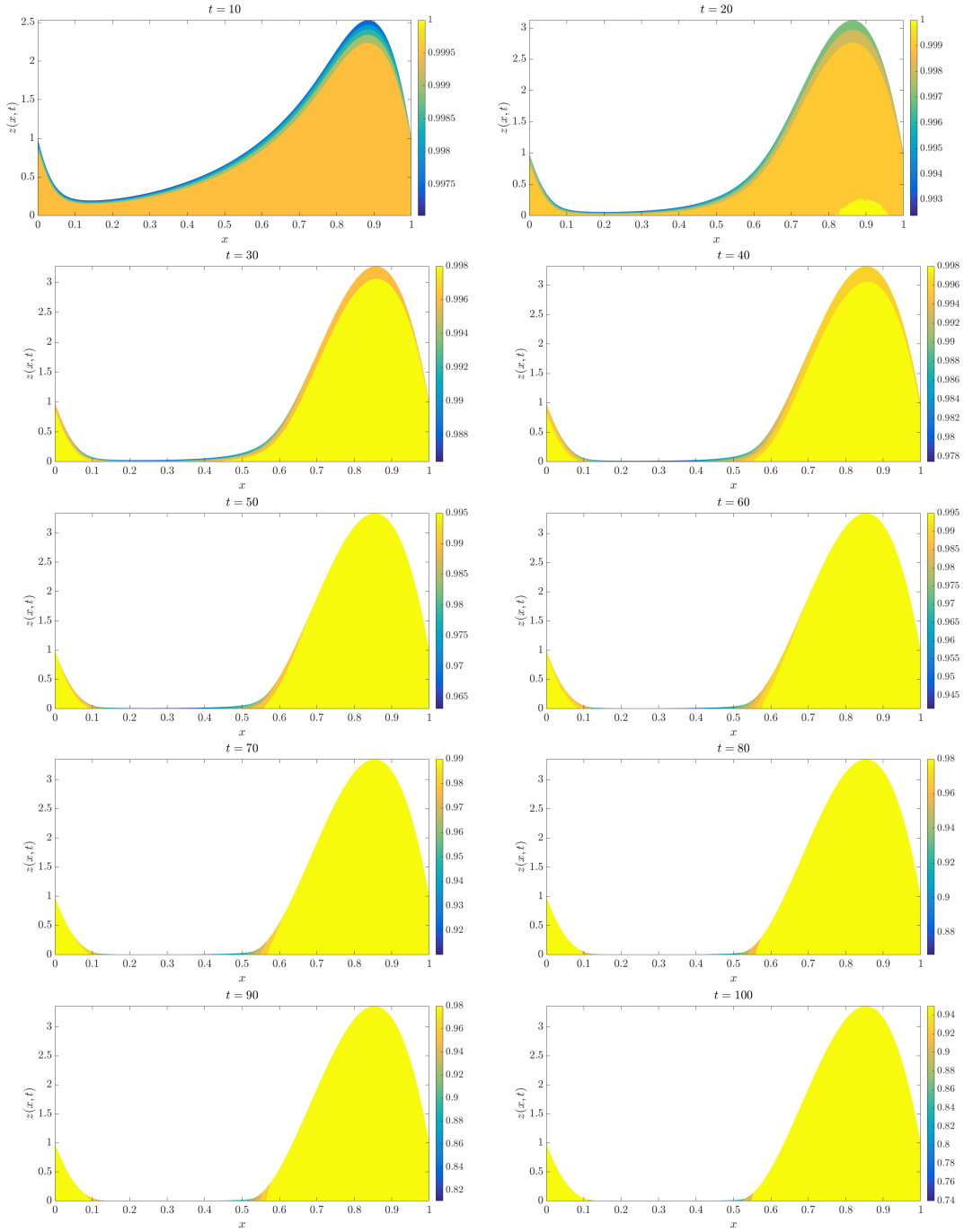


Figure 5.5: The contour plot for (a) $\theta(x, z, t = 10)$, (b) $\theta(x, z, t = 20)$, (c) $\theta(x, z, t = 30)$, (d) $\theta(x, z, t = 40)$, (e) $\theta(x, z, t = 50)$, (f) $\theta(x, z, t = 60)$, (g) $\theta(x, z, t = 70)$, (h) $\theta(x, z, t = 80)$, (i) $\theta(x, z, t = 90)$, and (j) $\theta(x, z, t = 100)$ (the temperature profiles are superimposed on the corresponding free surface shape h), with $Pe_r = 10^3$, $a = 0.02$, $\alpha = 2$, $\theta_s = 0$.

global minimum in $h(x, t)$), respectively. Figure 5.6(d) shows the influence of varying Pe_r on the rupture time, t_{rupt} . We define t_{rupt} as the time taken for the film to drain to a prescribed thickness. In practise, we estimate t_{rupt} to be the time taken until h_{min} reduces to 10^{-2} of its initial thickness. We observe that the film thins more rapidly as

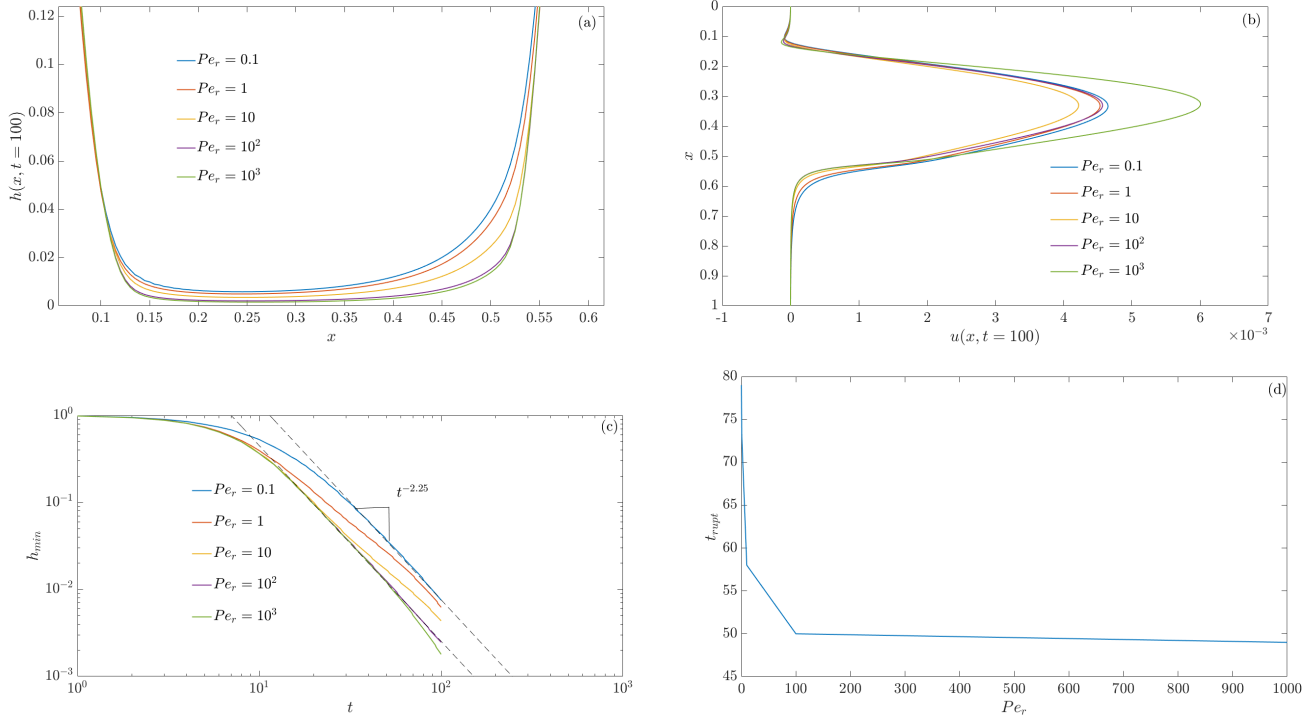


Figure 5.6: (a) Film thickness $h(x, t = 50)$, (b) extensional flow speed $u(x, t = 50)$, and (c) the global minimum $h_{min}(t)$, for varying $Pe_r = 0.1, 1, 10^2, 10^3$ the rupture time t_{rupt} as a function of Pe_r . The parameter values are: $\alpha = 2$, $a = 0.2$ and $\beta = 0$.

Pe_r increases (Fig. 5.6(a)) due to the faster extensional flow speed as Pe_r increases (Fig. 5.6(b)). Note that Fig. 5.6(a) only shows the central regions as the upper and lower parts of the film are not significantly affected by varying Pe_r . The faster flow speed at larger Pe_r is due to the slower and non-uniform cooling of the free surface (see Figs. 5.4, 5.5, for example), resulting in lower viscosities. This is in comparison to smaller Pe_r where the cooling is more rapid and uniform (see Fig. 5.1-5.3, for exam-

ple), resulting in larger viscosities, hence slowing down the flow. Figure 5.6(c) shows the increased thinning of the minimum film thickness, $h_{min}(t)$, as Pe_r increases. We observe isothermal thinning, i.e., approximately $t^{-2.25}$ thinning rate, when Pe_r is either very large or very small. Figure 5.6(d) shows that as Pe_r increases the fluid drains more quickly which causes the middle section to become thinner sooner, therefore more likely to rupture at earlier times.

In Figs. 5.7-5.10, we investigate the influence of varying the heat transfer coefficient a , for fixed $Pe_r = 10^3$, $\alpha = 2$ and $\theta_s = 0$. For larger values of a , the cooling rate due to heat radiating from the film's surface is relatively quicker across and along the film compared to smaller values of a (compare Figs. 5.9,5.10 for $a = 2, 5$, respectively, to Figs. 5.7,5.8 for $a = 0.2, 1$, respectively). This is due to the rate of heat loss being proportional to a (see second term on the right-hand-side of the boundary condition for θ at $z = h(x, t)$ given by Eq. (5.20d)). Figure 5.11(a, b, c) shows the effect of varying $a = 0.2, 1, 2, 5$, on $h(x, t = 48)$, $u(x, t = 48)$ and $h_{min}(t)$, respectively. Figure 5.11(d) shows the influence of varying a on the rupture time, t_{rupt} . We observe that the the film thins more slowly as a increases (Fig. 5.11(a)) due to the slower extensional flow speed as a increases (Fig. 5.11(b)). The faster flow speed at lower a is due to the slower and non-uniform cooling of the free surface (see Fig. 5.7,5.8, for example), resulting in lower viscosities. This is in comparison to larger a where although the cooling is non-uniform, it is relatively quicker (see Fig. 5.9,5.10, for example), resulting in larger viscosities, hence slowing down the flow. Figure 5.11(c) shows the increased

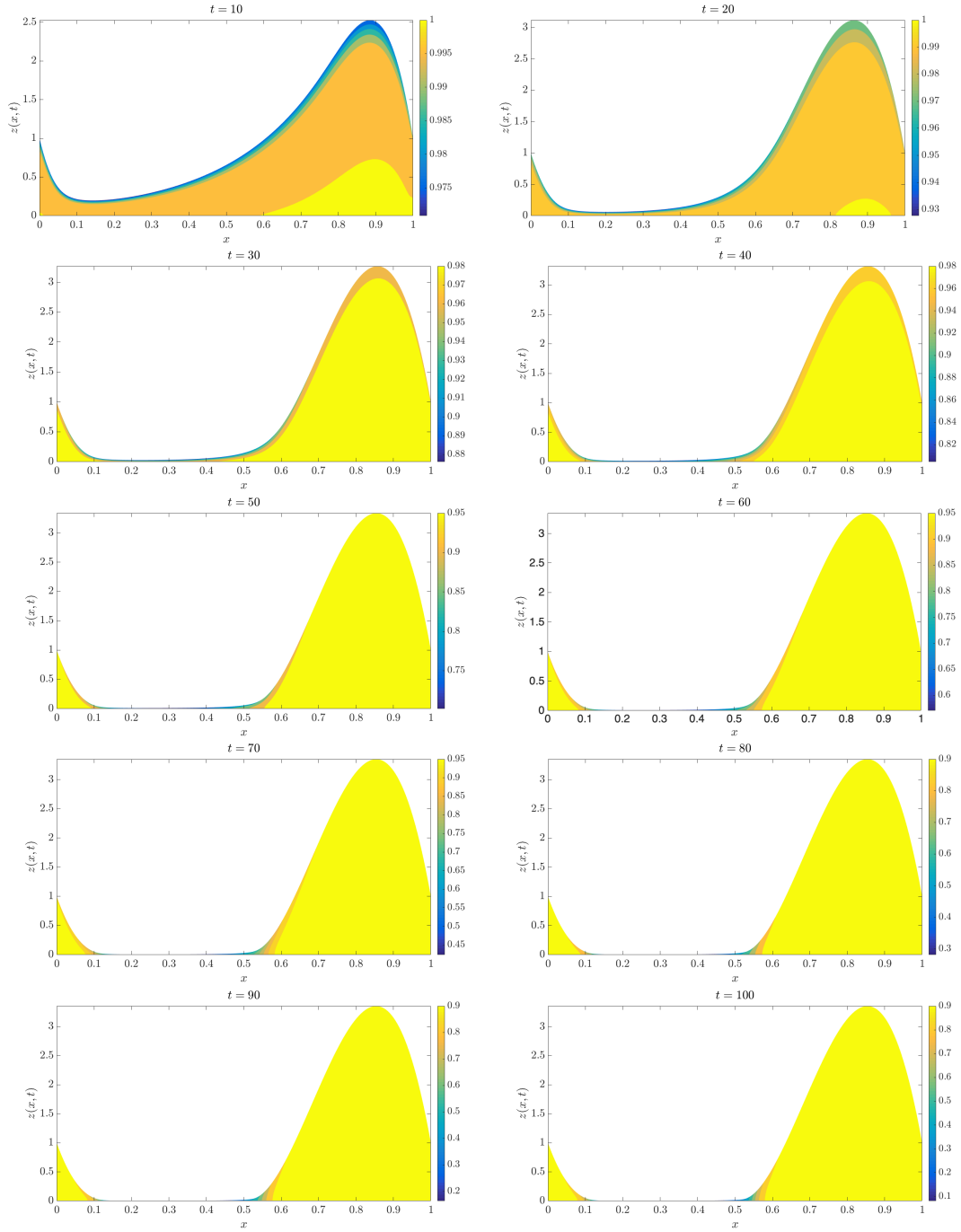


Figure 5.7: The contour plot for (a) $\theta(x, z, t = 10)$, (b) $\theta(x, z, t = 20)$, (c) $\theta(x, z, t = 30)$, (d) $\theta(x, z, t = 40)$, (e) $\theta(x, z, t = 50)$, (f) $\theta(x, z, t = 60)$, (g) $\theta(x, z, t = 70)$, (h) $\theta(x, z, t = 80)$, (i) $\theta(x, z, t = 90)$, and (j) $\theta(x, z, t = 100)$ (the temperature profiles are superimposed on the corresponding free surface shape h), with $Pe_r = 10^3$, $a = 0.2$, $\alpha = 2$, $\theta_s = 0$.

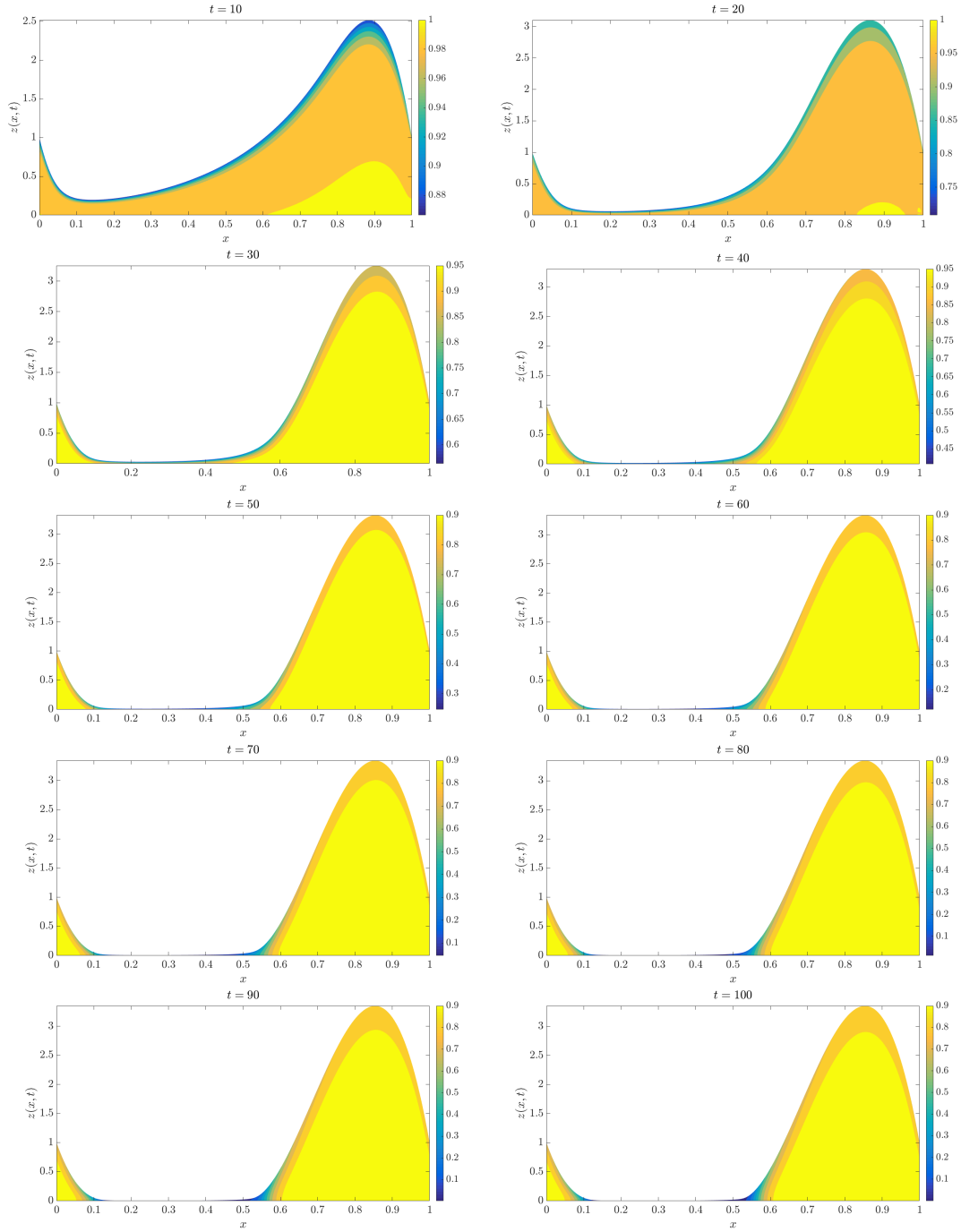


Figure 5.8: The contour plot for (a) $\theta(x, z, t = 10)$, (b) $\theta(x, z, t = 20)$, (c) $\theta(x, z, t = 30)$, (d) $\theta(x, z, t = 40)$, (e) $\theta(x, z, t = 50)$, (f) $\theta(x, z, t = 60)$, (g) $\theta(x, z, t = 70)$, (h) $\theta(x, z, t = 80)$, (i) $\theta(x, z, t = 90)$, and (j) $\theta(x, z, t = 100)$ (the temperature profiles are superimposed on the corresponding free surface shape h), with $Pe_r = 10^3$, $a = 1$, $\alpha = 2$, $\theta_s = 0$.

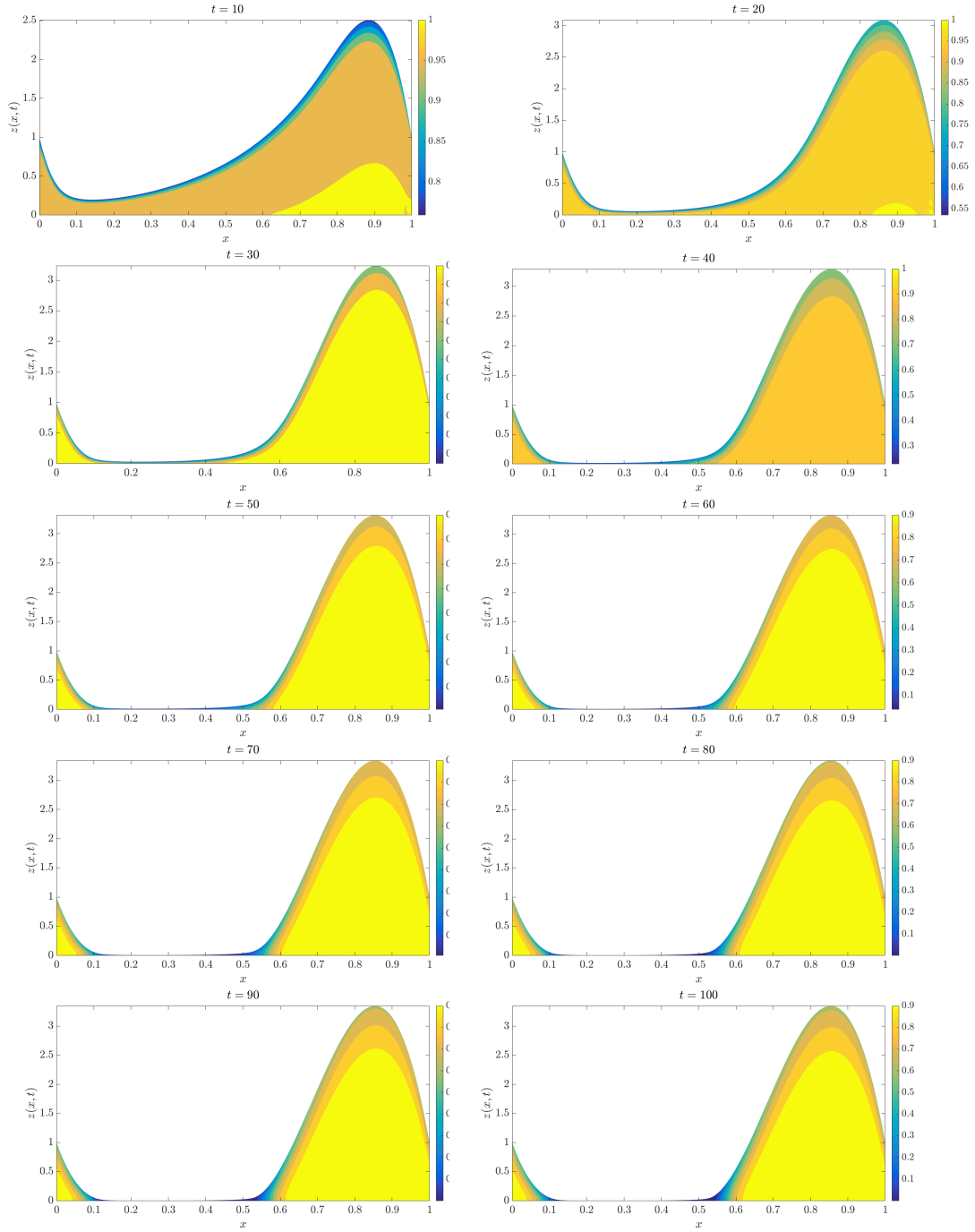


Figure 5.9: The contour plot for (a) $\theta(x, z, t = 10)$, (b) $\theta(x, z, t = 20)$, (c) $\theta(x, z, t = 30)$, (d) $\theta(x, z, t = 40)$, (e) $\theta(x, z, t = 50)$, (f) $\theta(x, z, t = 60)$, (g) $\theta(x, z, t = 70)$, (h) $\theta(x, z, t = 80)$, (i) $\theta(x, z, t = 90)$, and (j) $\theta(x, z, t = 100)$ (the temperature profiles are superimposed on the corresponding free surface shape h), with $Pe_r = 10^3$, $a = 2$, $\alpha = 2$, $\theta_s = 0$.

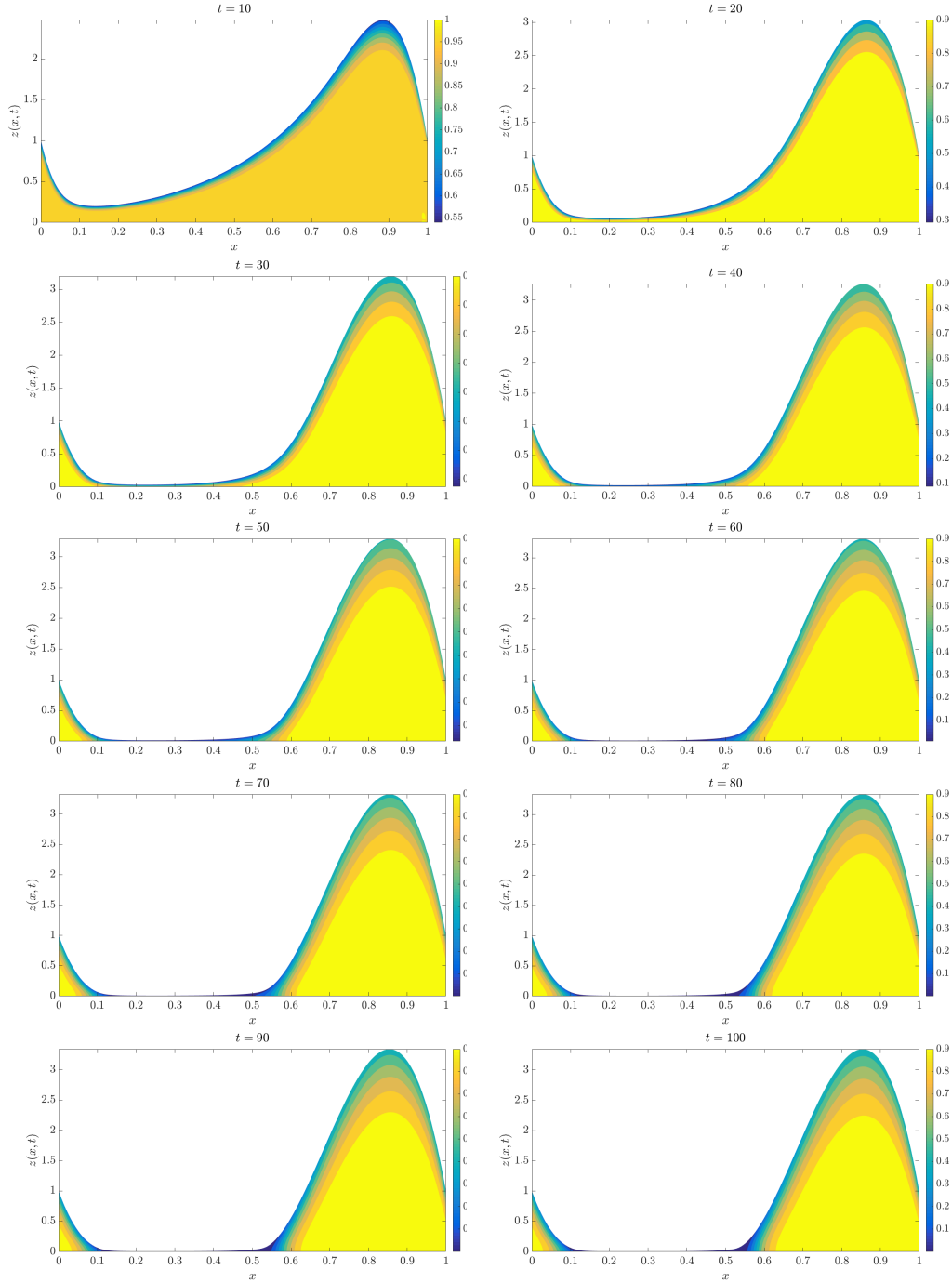


Figure 5.10: The contour plot for (a) $\theta(x, z, t = 10)$, (b) $\theta(x, z, t = 20)$, (c) $\theta(x, z, t = 30)$, (d) $\theta(x, z, t = 40)$, (e) $\theta(x, z, t = 50)$, (f) $\theta(x, z, t = 60)$, (g) $\theta(x, z, t = 70)$, (h) $\theta(x, z, t = 80)$, (i) $\theta(x, z, t = 90)$, and (j) $\theta(x, z, t = 100)$ (the temperature profiles are superimposed on the corresponding free surface shape h), with $Pe_r = 10^3$, $a = 5$, $\alpha = 2$, $\theta_s = 0$.

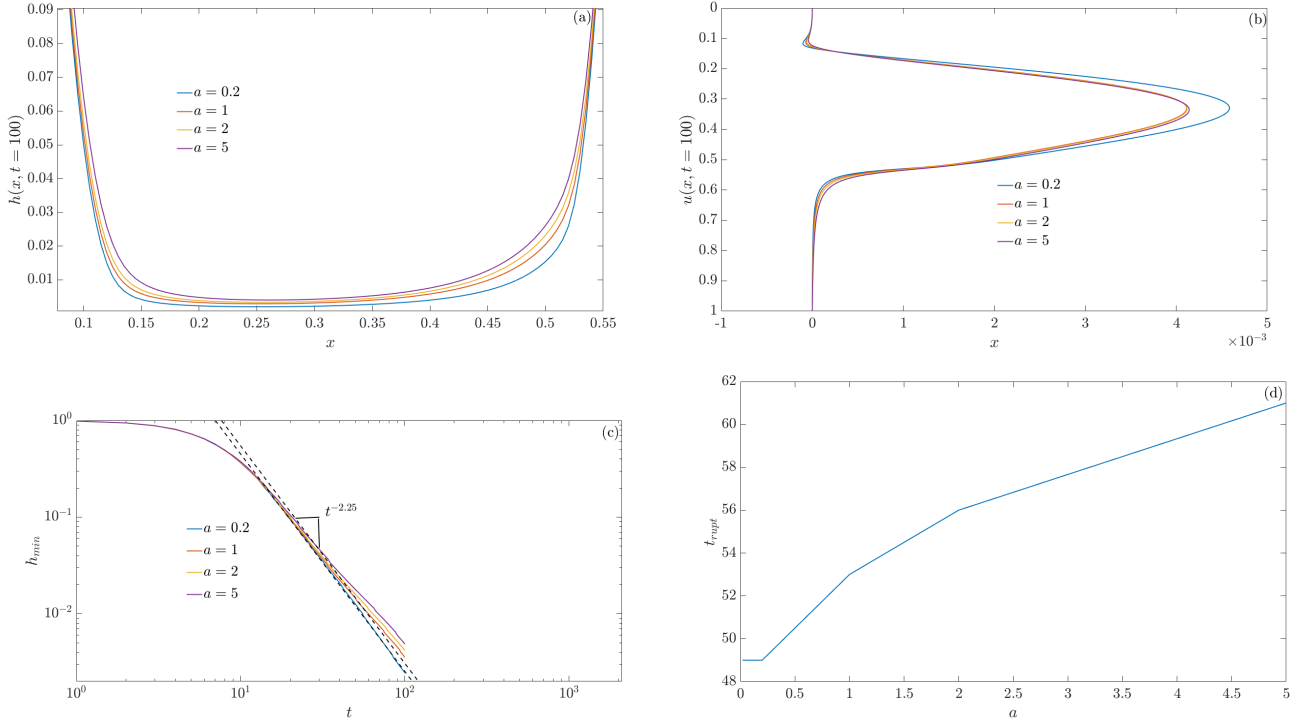


Figure 5.11: (a) Film thickness $h(x, t = 48)$, (b) extensional flow speed $u(x, t = 48)$, and (c) the global minimum $h_{min}(t)$, for varying $a = 0.02, 0.2, 1, 2, 5$ the rupture time t_{rupt} as a function of a . The parameter values are: $\alpha = 2$, $Pe_r = 10^3$ and $\beta = 0$.

thinning of the minimum film thickness, $h_{min}(t)$, as a decreases. We observe isothermal thinning, with $t^{-2.25}$ thinning rate, when a is very small. Figure 5.11(d) shows that as a increases the fluid drains more slowly which slows down the thinning of the middle section, therefore delaying the rupture times.

Figures 5.12-5.14 investigate the influence of varying the viscosity-temperature decay constant $\alpha = 1, 3, 5$, respectively, while keeping $Pe_r = 10^3$, $a = 0.02$, $b = 0$ fixed. Figures 5.12-5.14 show that θ is not very sensitive to variations in α , with the slight reduction in θ observed as α increases. This may be due to convection effects transferring the cooler liquid in the middle region to the bottom pendant drop region. Figure 5.15(a, b, c) shows the effect of varying α , on $h(x, t = 43)$, $u(x, t = 43)$ and $h_{min}(t)$, respectively. Figure 5.15(d) shows the influence of varying α on the rupture time, t_{rupt} . We observe that the the film thins faster as α increases (Fig. 5.15(a)) due to the faster extensional flow speed as α increases (Fig. 5.15(b)). The faster flow speed at higher values of α is due to larger reduction in viscosity as α increases Figure 5.15(c) shows the increased thinning of the minimum film thickness, $h_{min}(t)$, as α increases. Figure 5.15(d) shows that as α increases the fluid drains more rapidly (due to the larger reduction in viscosity) which accelerates the the thinning of the middle section, therefore increasing the rupture times.

In the next set of results presented below, we study the influence of surface tension varying with temperature via the parameter β and take the viscosity to be constant (so, $\alpha = 0$). The temperature profiles are not sensitive to variations in β and behave

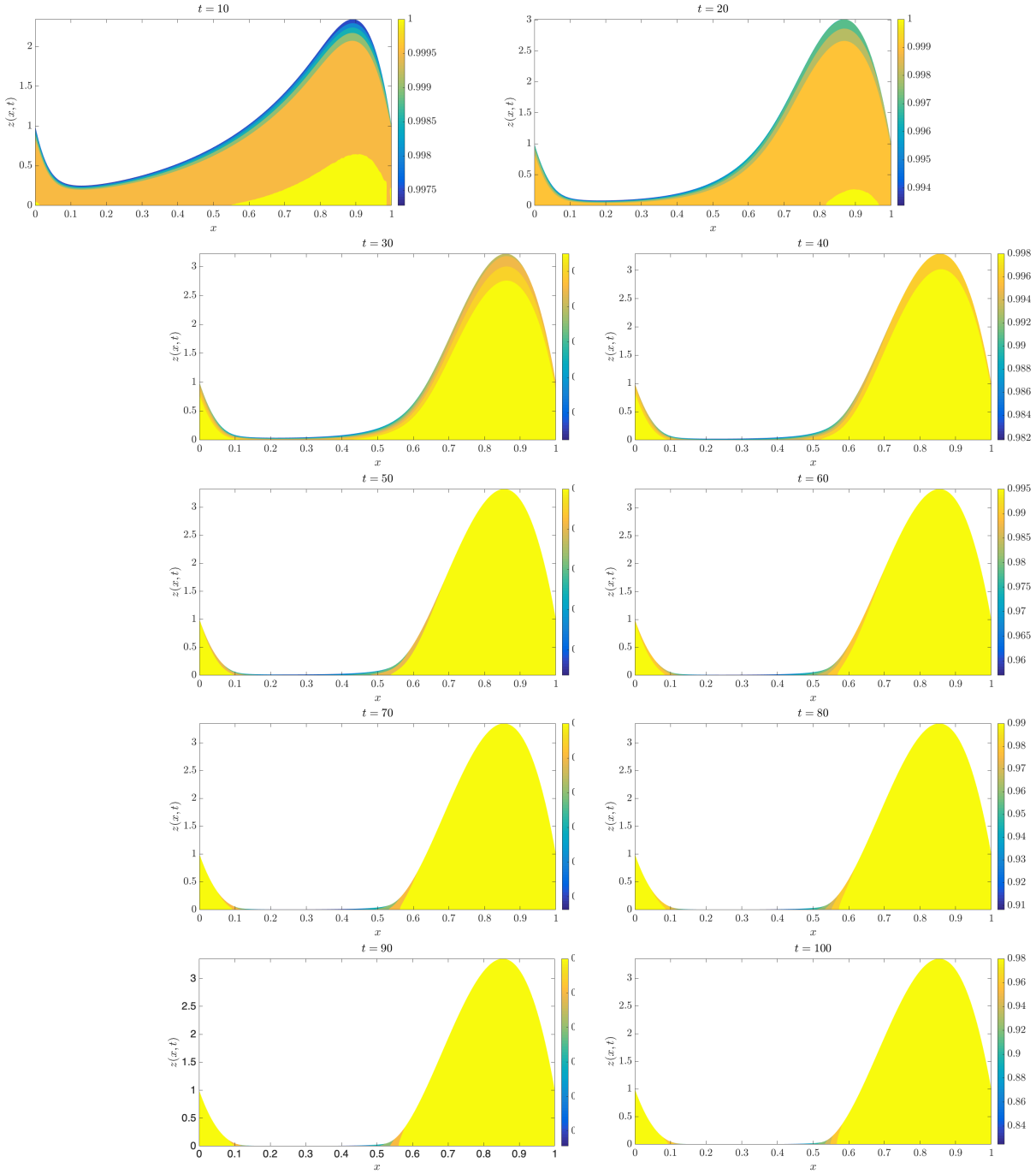


Figure 5.12: The contour plot for (a) $\theta(x, z, t = 10)$, (b) $\theta(x, z, t = 20)$, (c) $\theta(x, z, t = 30)$, (d) $\theta(x, z, t = 40)$, (e) $\theta(x, z, t = 50)$, (f) $\theta(x, z, t = 60)$, (g) $\theta(x, z, t = 70)$, (h) $\theta(x, z, t = 80)$, (i) $\theta(x, z, t = 90)$, and (j) $\theta(x, z, t = 100)$ (the temperature profiles are superimposed on the corresponding free surface shape h), with $Pe_r = 10^3$, $a = 0.02$, $\alpha = 1$, $\theta_s = 0$.)

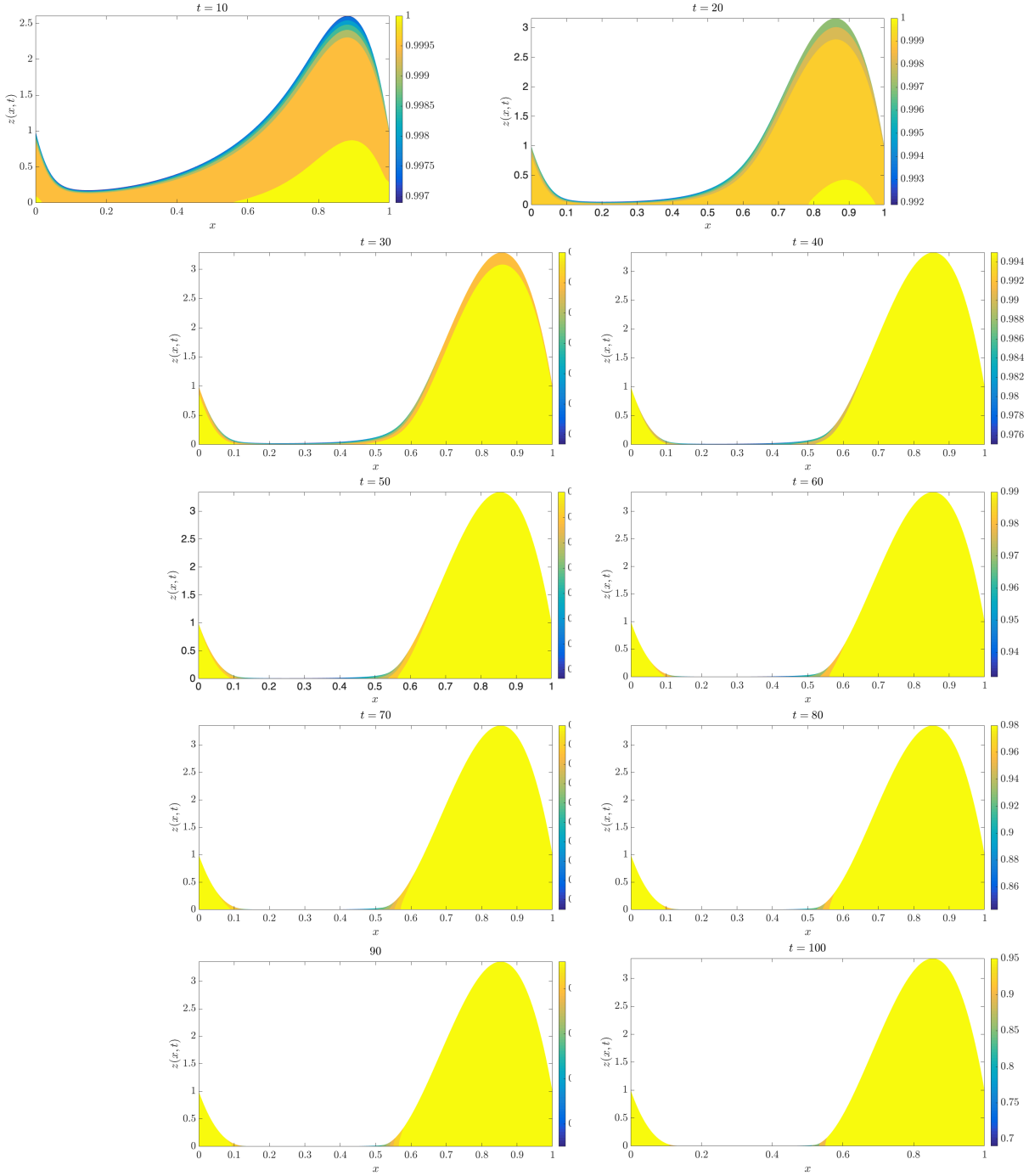


Figure 5.13: The contour plot for (a) $\theta(x, z, t = 10)$, (b) $\theta(x, z, t = 20)$, (c) $\theta(x, z, t = 30)$, (d) $\theta(x, z, t = 40)$, (e) $\theta(x, z, t = 50)$, (f) $\theta(x, z, t = 60)$, (g) $\theta(x, z, t = 70)$, (h) $\theta(x, z, t = 80)$, (i) $\theta(x, z, t = 90)$, and (j) $\theta(x, z, t = 100)$ (the temperature profiles are superimposed on the corresponding free surface shape h), with $Pe_r = 10^3$, $a = 0.02$, $\alpha = 3$, $\theta_s = 0$.

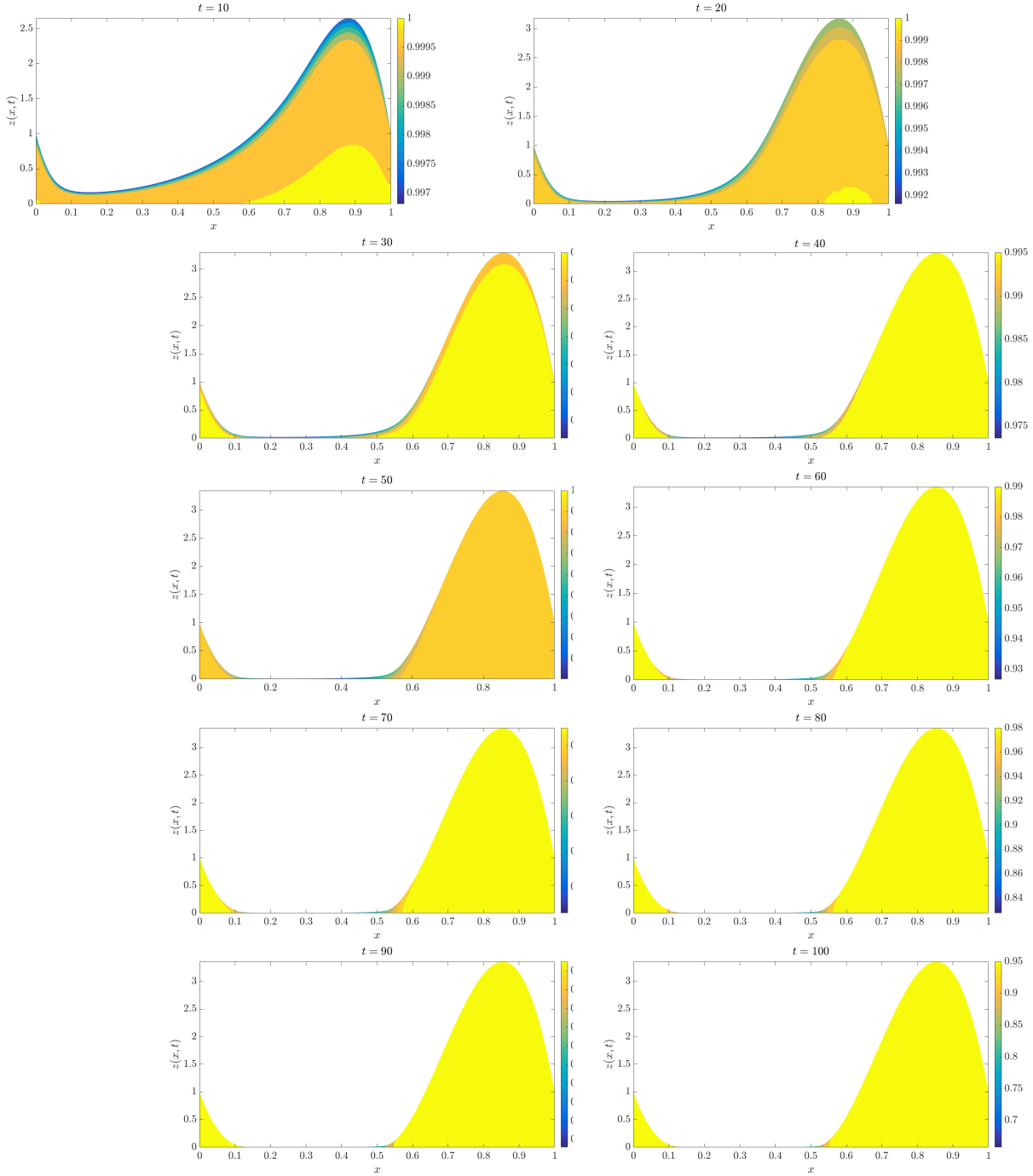


Figure 5.14: The contour plot for (a) $\theta(x, z, t = 10)$, (b) $\theta(x, z, t = 20)$, (c) $\theta(x, z, t = 30)$, (d) $\theta(x, z, t = 40)$, (e) $\theta(x, z, t = 50)$, (f) $\theta(x, z, t = 60)$, (g) $\theta(x, z, t = 70)$, (h) $\theta(x, z, t = 80)$, (i) $\theta(x, z, t = 90)$, and (j) $\theta(x, z, t = 100)$ (the temperature profiles are superimposed on the corresponding free surface shape h), with $Pe_r = 10^3$, $a = 0.02$, $\alpha = 5$, $\theta_s = 0$.

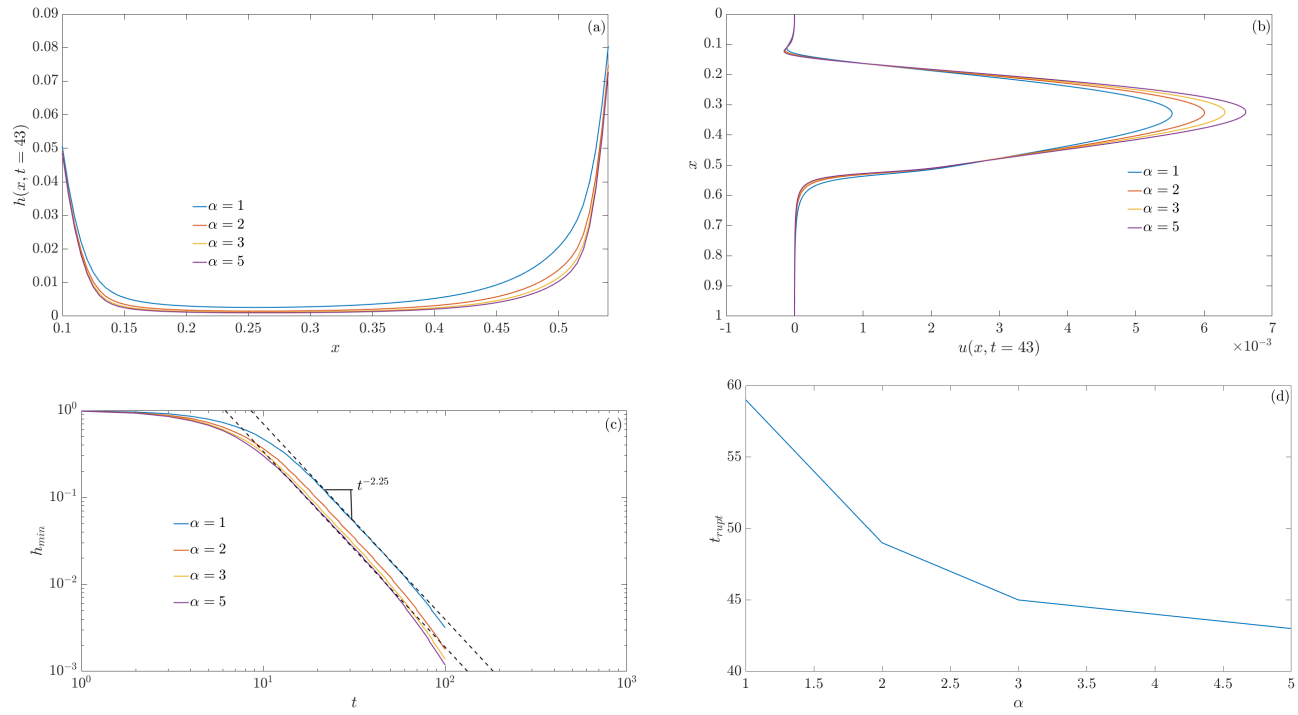


Figure 5.15: (a) Film thickness $h(x, t = 43)$, (b) extensional flow speed $u(x, t = 43)$, and (c) the global minimum $h_{min}(t)$, for varying $\alpha = 1, 2, 3, 5$ the rupture time t_{rupt} as a function of α . The parameter values are: $Pe_r = 10^3$, $a = 0.02$, $\beta = 0$.

similar to the previous results; hence we do not show them in the results to follow. Figure 5.16(a, b, c) show the effect of varying $Pe_r = 10^{-1}, 1, 10, 10^2, 10^3$, respectively, on $h(x, t = 43)$, $u(x, t = 43)$ and $h_{min}(t)$ (the global minimum in $h(x, t)$), respectively. Figure 5.16(d) shows the influence of varying Pe_r on the rupture time, t_{rupt} . For

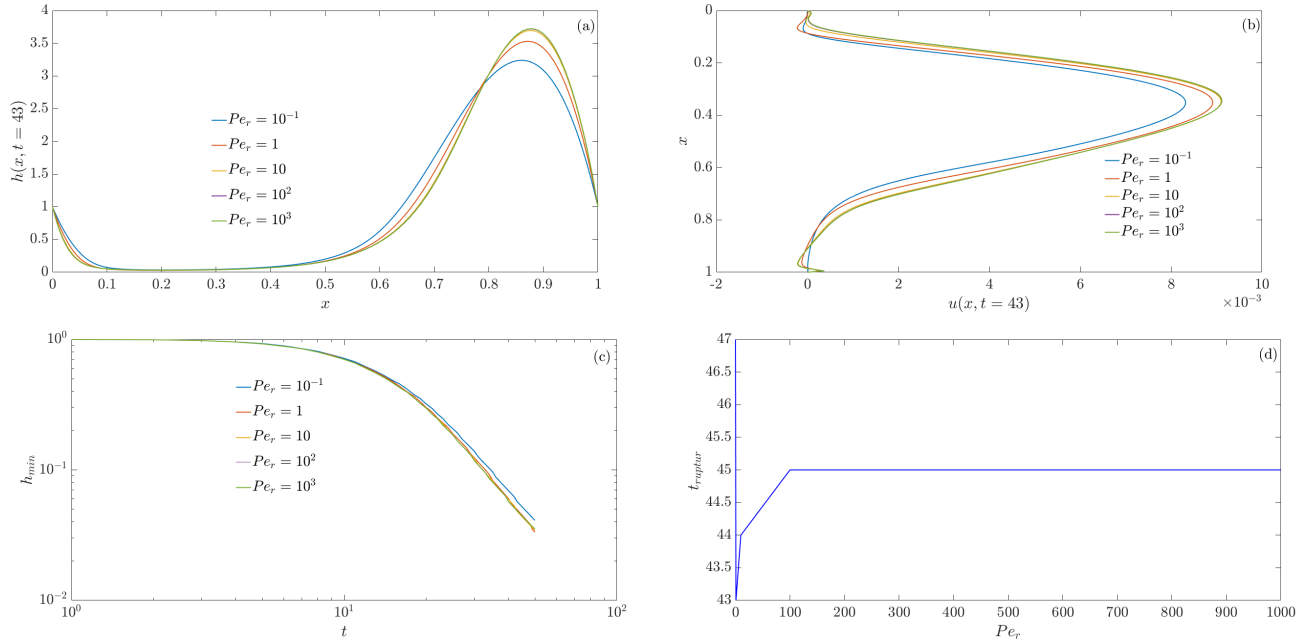


Figure 5.16: (a) Film thickness $h(x, t = 43)$, (b) extensional flow speed $u(x, t = 43)$, and (c) the global minimum $h_{min}(t)$, for varying $Pe_r = 10^{-1}, 1, 10, 10^2, 10^3$ the rupture time t_{rupt} as a function of Pe_r . The parameter values are: $\beta = 0.5$, $a = 0.02$ and $\alpha = 0$.

larger Pe_r , the temperature in the upper capillary meniscus and lower pendant drop regions is much higher compared to that at low Pe_r (similar to Fig. 5.1-5.5). The effect of the elevated temperature is to decrease the surface tension in these regions, which is also where the curvature of the film is most pronounced. As a result, the capillary force acting on the fluid is decreased in comparison to gravity, resulting in a longer and flatter middle section of the film (Fig. 5.16(a)), as well as more liquid collecting in the pendant drop region making it thicker. Since surface tension decreases

with temperature, the effective Capillary number, Ca , increases which results in the lengthening and flattening of the film's middle section (similar to Fig. 3.3 in chapter 3). The extensional flow speed $u(x, t)$ increases as Pe increases (Fig. 5.16(b)), which results in the film draining and thinning faster (Fig. 5.16(c)), consequently rupturing quickly (Fig. 6.7(d)). We note a slight non-monotonicity in t_{rupt} at intermediate Pe , which results in a minimum in the rupture time at $Pe \approx 10$ (Fig. 6.7(d)).

We are not able to show any results for $\alpha, \beta > 0$, corresponding to changes in both viscosity and surface tension with respect to temperature, due to some numerical difficulties and the long computational time taken to simulate such cases. In chapter 6, we investigate the influence of $\alpha, \beta > 0$ in the limit of $Pe_r \ll 1$, which reduces the temperature field from two-dimensional to one-dimensional making it less computationally intensive,

5.5 Conclusions

In this chapter we coupled the thin-film flow equations to a two-dimensional advection-diffusion equation for the temperature field and investigated the draining and thinning of a cooling vertically-aligned hot Newtonian liquid film for the reduced Péclet number, $Pe_r = O(1)$. We considered non-isothermal conditions which included a temperature-dependent viscosity and surface tension, and heat loss due to cooling at the free surface. An extensive parameter study revealed the influence of the system parameters on this

cooling, particularly, the reduced Péclet number, Pe_r , the decay constant in the exponential viscosity-temperature model, α , the heat transfer coefficient, a , and the slope of the surface tension-temperature model, β . The resulting temperature and corresponding viscosity and surface tension contrast arising due to the cooling near the film's free surface significantly influenced the draining and subsequent thinning of the film.

Our results highlighted a very important feature during the draining and thinning process which is the cooling of the film's middle section where the rate of heat loss is maximum due to its much smaller thickness compared to the top and bottom regions of the film. The extent of this cooling was dependent on the parameter values and ranged from

- (i) a draining *collar* of colder liquid sandwiched between two much hotter regions, which were almost insulated from the cooler middle section and a thin cooler boundary layer near the free surface (Fig. 5.5), for intermediate and large Pe_r ,
- (ii) to small Pe_r , where the temperature isotherms became almost vertical across the film and the film cooled uniformly (Fig. 5.1).

We observed that the cooling rate could be enhanced by increasing the heat transfer coefficient a which slowed down the draining and thinning of the film (Fig. 5.11(c)). Moreover, a rapid drop in the viscosity with temperature controlled by the parameter α increased the draining flow and the subsequent thinning of the film (Fig. 5.15(c)). The low Pe_r limit is preferable in polymeric melt films since the hot liquid in the film cools uniformly and rapidly, consequently the liquid viscosity increases uniformly within the

film, resulting in slower drainage and thinning of the film. This can be achieved if the Péclet number, $Pe = U^*L^*/\kappa_d^*$, is small (or the heat diffusivity for the liquid, κ_d^* is large) or the aspect ratio, ϵ is small. Polymeric melts generally have low conductivity (e.g., the thermal conductivity of Polystyrene, $\kappa^* \approx 0.04$), so one would need very thin films for the low Pe_r results to be achieved. Alternatively, one could increase the melt's conductivity, if that is feasible. Another method to sufficiently reduce the drainage so that cooling can occur, is to disperse particles within the melt that can increase its effective viscosity, e.g., alumina particles are dispersed in aluminium foam to increase the viscosity (Yang & Nakae [80]).

While we have extensively investigated the influence of viscosity variation with temperature, we have not fully investigated the influence of temperature variations on surface tension. Our preliminary investigations showed that the reduction in surface tension due to an increase in temperature, controlled by the parameter β , is analogous to increasing the effective Capillary number, Ca . Consequently this increased curvature of the pendant drop region in order to accommodate more liquid accumulating at the bottom due to the relative increase in gravity in comparison to capillary forces (Fig. 5.16(a)). We would need to do further investigations to investigate the combined effect of variations in surface tension and viscosity with temperature. This will be investigated in the next chapter, where we consider a reduced model which will allow us to overcome some of the numerical difficulties and long computational times faced here.

Results for low Pe_r showed that the temperature isotherms became vertical across

the film suggesting the independence of temperature across the film thickness for these values, i.e., $\theta = \theta(x, t)$. This so-called vertical isothermal theory valid in the asymptotic limit of $Pe_r \ll 1$ will be investigated in the next chapter.

Chapter 6

Gravity-driven draining of a vertically-aligned thin Newtonian and non-isothermal liquid free film: the small reduced Péclet number limit

6.1 Introduction

In this chapter, we investigate the asymptotic limit of the reduced Péclet number, $Pe_r = \epsilon^2 Pe \ll 1$, where the Péclet number, $Pe = O(1)$, the so-called diffusion-

dominated scenario of heat transport (also referred to as isothermal or well-mixed heat transport along the thickness of the film). This enables the non-isothermal problem to be reduced from a two-dimensional temperature field $\theta(x, z, t)$ to a one-dimensional evolution equation for the temperature, $\theta(x, t)$, coupled with the evolution of the free surface, $h(x, t)$ via a temperature-dependent viscosity, $\mu(\theta(x, t))$ and temperature-dependent surface tension, $\gamma(\theta(x, t))$.

The outline of this chapter is as follows. In §6.2, the assumption of the reduced Péclet number, $Pe_r \ll 1$, allows simplification of the governing equations and boundary conditions derived in chapter 5 to a system of three coupled PDEs for the evolution of the one-dimensional free surface shape, the extensional flow speed and the temperature field. In §6.3, we perform numerical simulations of the evolution equations to determine the free surface shapes, the extensional flow speeds and temperature fields for a variety of parameter values related to the exponential viscosity-temperature model and a linear surface tension-temperature model. In §6.4, we discuss the main results.

6.2 Asymptotic limit of small reduced reduced Péclet number, $Pe_r = \epsilon^2 Pe \ll 1$

We now consider the asymptotic limit of small reduced reduced Péclet number, $Pe_r = \epsilon^2 Pe \ll 1$, where the Péclet number Pe is assumed to be $O(1)$. This is the so-called diffusion-dominated scenario of heat transport (also referred to as isothermal or well-

mixed heat transport along the thickness of the film). We expand the scaled temperature field $\theta(x, z, t)$ in powers of ϵ^2 . Let $\theta(x, z, t) = \theta_0(x, z, t) + \epsilon^2\theta_1(x, z, t) + \dots$

Substituting into Eq. (5.8) gives to leading order in ϵ :

$$\theta_{0_{zz}} = 0, \quad \theta_{0_z} = 0, \quad \text{at } z = 0, h(x, t), \quad \theta_{0_x} = 0, \quad \text{at } x = 0, 1. \quad (6.1)$$

Integrating and applying the boundary conditions gives $\theta_0(x, z, t) = \theta_0(x, t)$. At $O(\epsilon^2)$, we obtain:

$$\theta_{0_t} + u_0\theta_{0_x} = \frac{1}{Pe} [\theta_{0_{xx}} + \theta_{1_{zz}}], \quad (6.2a)$$

$$\theta_{1_z} = 0, \quad \text{at } z = 0, \quad (6.2b)$$

$$\theta_{1_x} = h_{0_x}\theta_{0_x} - a\theta_0, \quad \text{at } z = h(x, t), \quad (6.2c)$$

$$\theta_{1_x} = b(\theta_0 - \theta_{0_s}), \quad \text{at } x = 0, \quad (6.2d)$$

$$\theta_{1_x} = -b(\theta_0 - \theta_{0_s}) \quad \text{at } x = 1. \quad (6.2e)$$

After rearranging Eq. (6.2a) and integrating with respect to z from $z = 0$ to h , together with the boundary conditions, Eqs.(6.2b,6.2c), we obtain

$$h_{0_x}\theta_{0_x} - a\theta_0 = Pe(h_0\theta_{0_t} + \theta_{0_x}h_0u_0) - h_0\theta_{0_{xx}}, \quad (6.3)$$

where $h_0 u_0 = Q_0$ is the leading order extensional liquid flux, and u_0 is the extensional flow speed. Dropping the subscripts, the leading order temperature field θ is given by

$$\theta_t + \left[u - \frac{h_x}{hPe} \right] \theta_x = \frac{1}{Pe} \theta_{xx} - \frac{a}{hPe} \theta, \quad (6.4a)$$

$$\theta_x = 0, \text{ at } x = 0, 1. \quad (6.4b)$$

Proceeding in the same way as in chapter 5, and noting that the integrals with respect to z in Eqs. (5.13,5.16) can be evaluated analytically when $\theta = \theta(x, t)$, we can write the evolution equations for h_0 , u_0 and θ_0 as (dropping the subscript “0”):

$$h_t + Q_x = 0, \quad Q = uh + \epsilon^2 \frac{h^3}{3} \left[\frac{1}{\mu(\theta)} \left\{ 4(\mu(\theta)u_x)_x + \left(\frac{1}{Ca} \gamma(\theta) h_{xx} \right)_x + 1 \right\} - u_{xx} \right], \quad (6.5a)$$

$$4(h\mu(\theta)u_x)_x + h \left[\left(\frac{1}{Ca} \gamma(\theta) h_{xx} \right)_x + 1 \right] = \frac{1}{Ca} \gamma_x(\theta), \quad (6.5b)$$

$$\theta_t + \left[u - \frac{h_x}{hPe} \right] \theta_x = \frac{1}{Pe} \theta_{xx} - \frac{a}{hPe} \theta, \quad (6.5c)$$

subject to the boundary conditions

$$h(0, t) = h(1, t) = 1, \quad (\gamma(\theta)h_{xx})_x(0, t) = (\gamma(\theta)h_{xx})_x(1, t) = -Ca, \quad u(0, t) = u(1, t) = 0, \\ \theta_x(0, t) = \theta_x(1, t) = 0. \quad (6.5d)$$

The viscosity-temperature relationship, $\mu(\theta)$, and surface tension-temperature relationship, $\gamma(\theta)$, are given in chapter 5, and are represented by Eqs. (5.24,5.25). respectively.

6.3 Numerical results

In this section, we seek the numerical solution of Eq. (6.5) for varying parameters related to the non-isothermal conditions: the Péclet number Pe , the heat transfer coefficient a , the decay constant α in the exponential viscosity-temperature relationship, and β in the surface tension-temperature relationship. In all the results shown below, we choose the heat transfer coefficient at the substrate $b = 0$ and the Reynold's number $Re = 0$. The initial conditions for h , θ and u are chosen as: $h(x, 0) = \theta(x, 0) = 1$ and $u(x, 0) = x(1 - x)/8$.

Equations (6.5) are solved numerically using finite difference method and the method of lines. We use the implicit solver *ode15i* in MATLAB (MATLAB 6.1, The MathWorks Inc., Natick, MA, 2000) for our numerical simulations. The discretisation for the film's thickness (Eq. (6.5a)) and the extensional flow speed (Eq. (6.5b)) are the same as explained in chapter 3. The only difference is the term $(\gamma(\theta)h_{xx})_x$, that appears in Eqs. (6.5a,6.5b,6.5d). We write this term in the form $\gamma'(\theta)\theta_x h_{xx} + \gamma(\theta)h_{xxx}$, and use a second-order centered difference scheme to discretise $\gamma(\theta)_x$, θ_x and h_{xx} . We discretize h_{xxx} in the same way as shown in §3.3. All other terms in Eqs. (6.5) are discretized as previously discussed. We discretize Eq. (6.5c) for $\theta(x, t)$ using second-order centered

differences as follows (keeping the time derivative continuous):

$$\theta_{t,i} + \left[u_i + \frac{1}{Pe h_i} \left(\frac{h_{i+1} - h_{i-1}}{2\Delta x} \right) \right] \left(\frac{\theta_{i+1} - \theta_{i-1}}{2\Delta x} \right) = \frac{1}{Pe} \frac{\theta_{i+1} - 2\theta_i + \theta_{i-1}}{\Delta x^2} - \frac{a}{Pe h_i} \theta_i,$$

$$i = 1, \dots, N + 1. \quad (6.6)$$

We use the boundary conditions at $x = 0, 1$, $\theta_x = 0$ to determine the fictitious points $\theta_0 = \theta_2$ and $\theta_{N+2} = \theta_N$. In all the results shown below, we fix $Ca = 10^3$, and $\Delta x = 5 \times 10^{-4}$ in all the numerical simulations, to achieve convergence within a prescribed tolerance.

In the first set of results shown below, we investigate the influence of viscosity varying with temperature, and take the surface tension to be constant (so, $\beta = 0$). Figure 6.1(a, b, c) shows the evolution of $h(x, t)$, $u(x, t)$ and $\theta(x, t)$, respectively, for $Pe = 10^{-2}$ ($Pe_r = 10^{-4}$), $\alpha = 2$, $a = 0.2$ and $\beta = 0$. The times shown range between $t = 0 - 10^3$. We observe that when Pe is small, the heat loss at the free surface is rapidly diffused along the free surface. Consequently, the free surface cools uniformly to $\theta = 0$ ($T = T_a$) very rapidly from its initial temperature $\theta = 1$ ($T = T_i$) (see Fig. (6.1(c))). The evolution of $h(x, t)$ and $u(x, t)$ shown in Fig. (6.1(a, b)) is similar to the isothermal case with constant viscosity $\mu = 1$ (corresponding to $\theta = 0$ or $T = T_a$).

Figure (6.2)(a–e) shows $\theta(x, t)$ for varying $Pe(Pe_r) = 0.1(10^{-3}), 1(10^{-2}), 10(10^{-1}), 10^2(1), 10^3(10)$, respectively. The times shown range from $t = 0 - 500$, except (e) where $t = 0 - 340$. The parameter values are: $\alpha = 2$, $a = 0.2$ and $\beta = 0$. For small Pe , diffusion of temperature

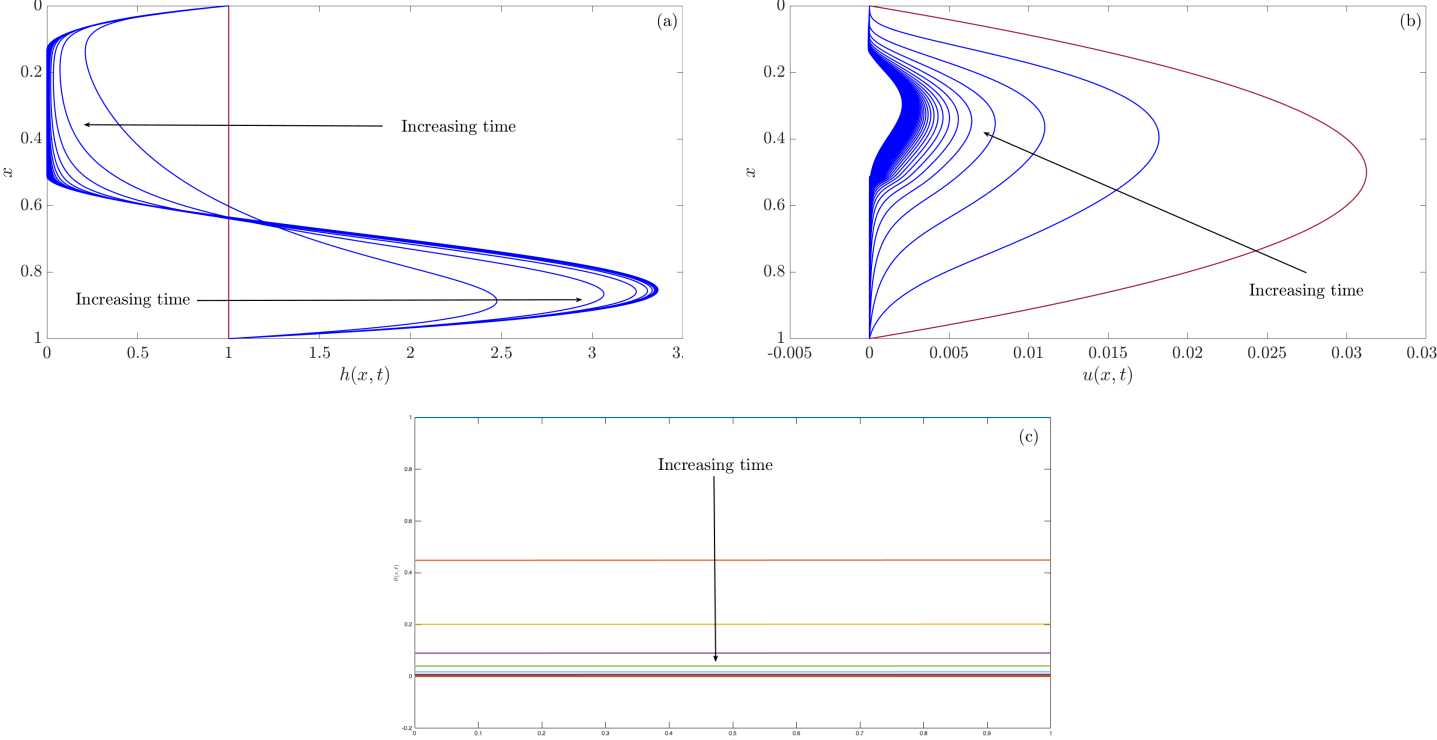


Figure 6.1: (a) The film thickness $h(x, t)$, (b) extensional flow speed $u(x, t)$, and (c) temperature $\theta(x, t)$ for $t = 0 - 10^3$, with $Pe = 10^{-2}$ ($Pe_r = 10^{-4}$), $\alpha = 2$, $a = 0.2$ and $\beta = 0$.

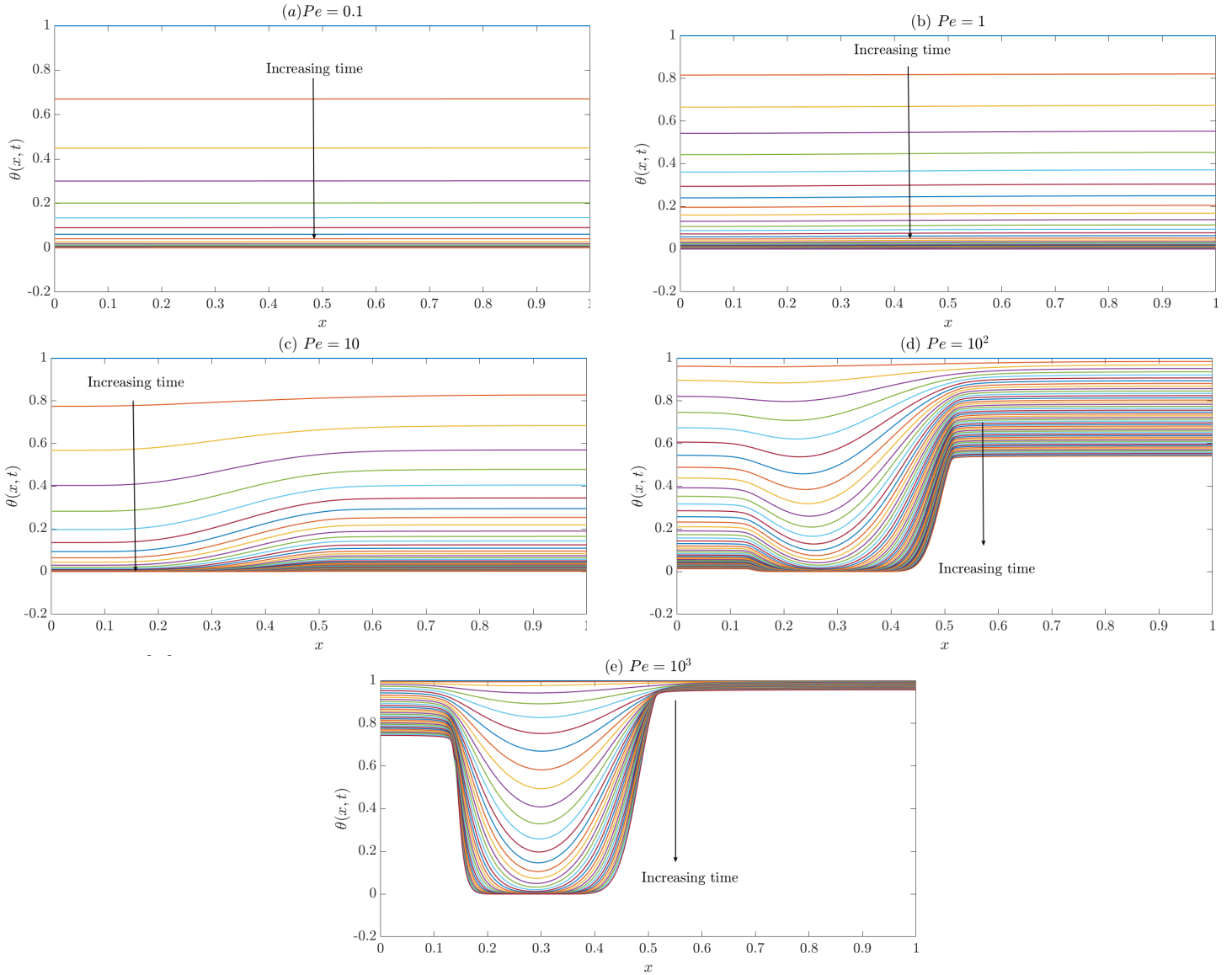


Figure 6.2: The temperature profile $\theta(x, t)$ for varying $Pe(Pe_r) = (a)0.1(10^{-3}), (b)1(10^{-2}), (c)10(10^{-1}), (d)10^2(1), (e)10^3(10)$, and $t = 0 - 500$, except (e) where $t = 0 - 340$. The parameter values are: $\alpha = 2$, $a = 0.2$ and $\beta = 0$.

dominates, suppressing any spatial variations in temperature due to non-uniform cooling, which results in a uniform and rapidly cooling temperature profile, as seen in (Figure 6.2(a) for $Pe = 0.1$). As Pe increases, the slower diffusion rate results in less rapid cooling but still uniform along the free surface (Figure 6.2(b) for $Pe = 1$). For larger Pe , the diffusion rate is even slower, and is less dominant in suppressing spatial variations in temperature due to non-uniform cooling. This results in more pronounced cooling in the middle section of the film where h is much smaller, compared to near the ends where h is comparatively larger (Figs. 6.2(c, d, e)) for $Pe = 10, 10^2, 10^3$, respectively. This non-uniformity in the cooling is due to the rate of heat loss being inversely proportional to h (see second term on the right-hand-side of Eq. (6.5c)). Figure 6.3(a, b, c) show the effect of varying $Pe(Pe_r) = 0.1(10^{-3}), 1(10^{-2}), 10(10^{-1}), 10^2(1), 10^3(10)$, respectively, on $h(x, t = 300)$, $u(x, t = 300)$ and $h_{min}(t)$ (the global minimum in $h(x, t)$), respectively. Figure 6.3(d) shows the influence of varying Pe on the rupture time, t_{rupt} . We define t_{rupt} as the time taken for the film to drain to a prescribed thickness. In practise, we estimate t_{rupt} to be the time taken until h_{min} reduces to 10^{-2} of its initial thickness. We observe that the film thins more rapidly as Pe increases (Fig. 6.3(a)) due to the faster extensional flow speed as Pe increases (Fig. 6.3(b)). Note that Fig. 6.3(a) only shows the central regions as the upper and lower parts of the film are not significantly affected by varying Pe . The faster flow speed at larger Pe is due to the slower and non-uniform cooling of the free surface (see Fig. 6.2(e), for example), resulting in lower viscosities. This is in comparison to smaller Pe where the cooling is more rapid and uniform (see Fig. 6.2(a), for example), resulting in larger viscosities, hence

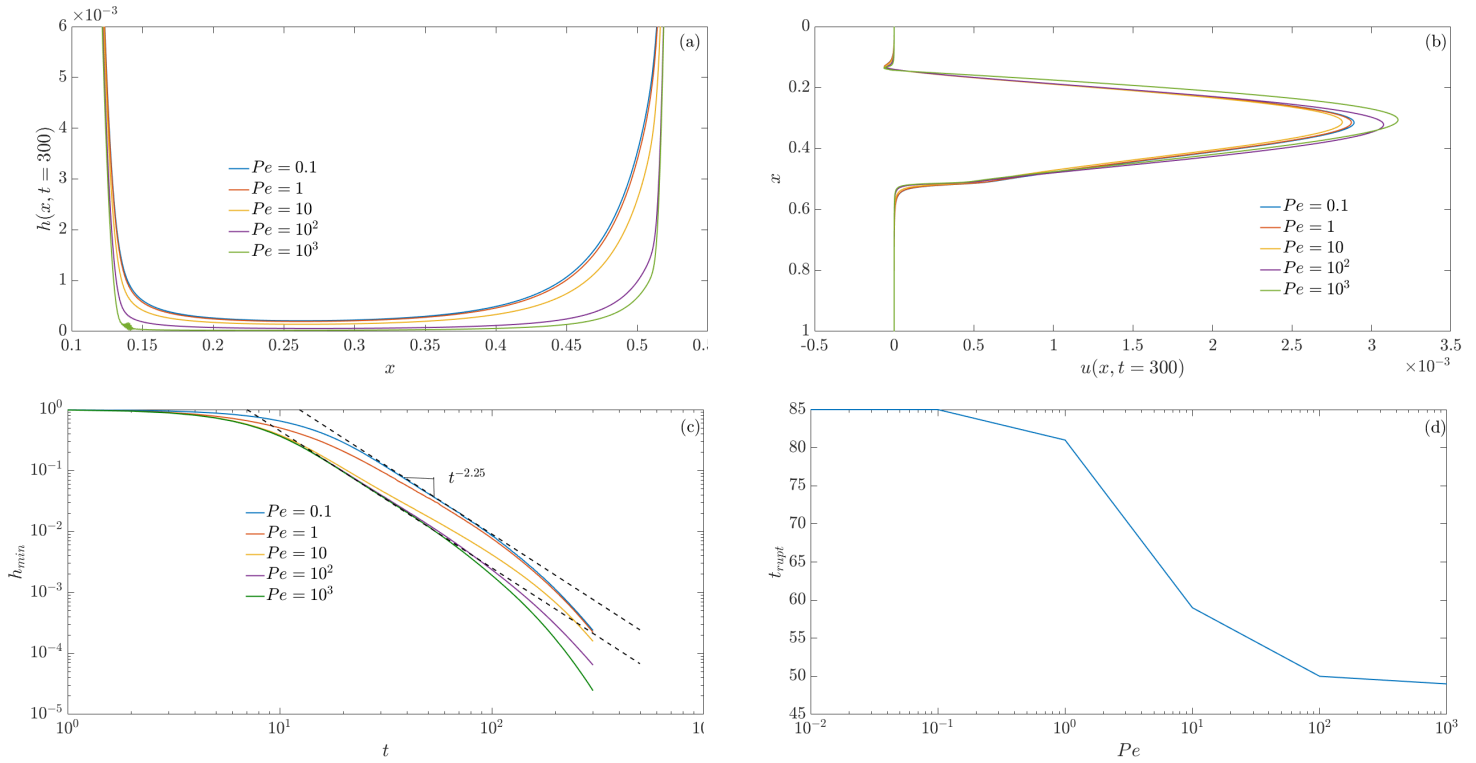


Figure 6.3: (a) Film thickness $h(x, t = 300)$, (b) extensional flow speed $u(x, t = 300)$, and (c) the global minimum $h_{min}(t)$, for varying $Pe(Pe_r) = 0.1(10^{-3}), 1(10^{-2}), 10(10^{-1}), 10^2(1), 10^3(10)$, and (d) the rupture time t_{rupt} as a function of Pe . The parameter values are: $\alpha = 2$, $a = 0.2$ and $\beta = 0$.

slowing down the flow. Figure 6.3(c) shows the increased thinning of the minimum film thickness, $h_{min}(t)$, as Pe increases. We observe isothermal thinning, i.e., approximately $t^{-2.25}$ thinning rate, when Pe is either very large or very small. Figure 6.3(d) shows that as Pe increases the fluid drains more quickly which causes the middle section to become thinner sooner, therefore more likely to rupture at earlier times. Figure 6.4(a – e) shows the effect of varying the heat transfer coefficient $a = 0.1, 0.5, 1.5, 2, 5$, respectively, while keeping $Pe = 10^3$ fixed. For larger values of a , the cooling rate due to heat radiating from the film’s surface is much quicker across the film compared to smaller values of a (compare Figs. 6.4(a, e) for $a = 0.1, 5$, respectively). This is due to the rate of heat loss being proportional to a (see second term on the right-hand-side of Eq. (6.5c)). Figure 6.5(a, b, c) shows the effect of varying $a = 0.1, 0.5, 1.5, 2, 5$, on $h(x, t = 50)$, $u(x, t = 50)$ and $h_{min}(t)$, respectively. Figure 6.5(d) shows the influence of varying a on the rupture time, t_{rupt} . We observe that the the film thins more slowly as a increases (Fig. 6.5(a)) due to the slower extensional flow speed as a increases (Fig. 6.5(b)). The faster flow speed at lower a is due to the slower and non-uniform cooling of the free surface (see Fig. 6.4(a), for example), resulting in lower viscosities. This is in comparison to larger a where although the cooling is non-uniform, it is more rapid (see Fig. 6.2(e), for example), resulting in larger viscosities, hence slowing down the flow. Figure 6.5(c) shows the increased thinning of the minimum film thickness, $h_{min}(t)$, as a decreases. We observe isothermal thinning, i.e., approximately $t^{-2.25}$ thinning rate, when a is either very large or very small. Figure 6.5(d) shows that as a increases the fluid drains more slowly which slows down the thinning of the middle section, therefore

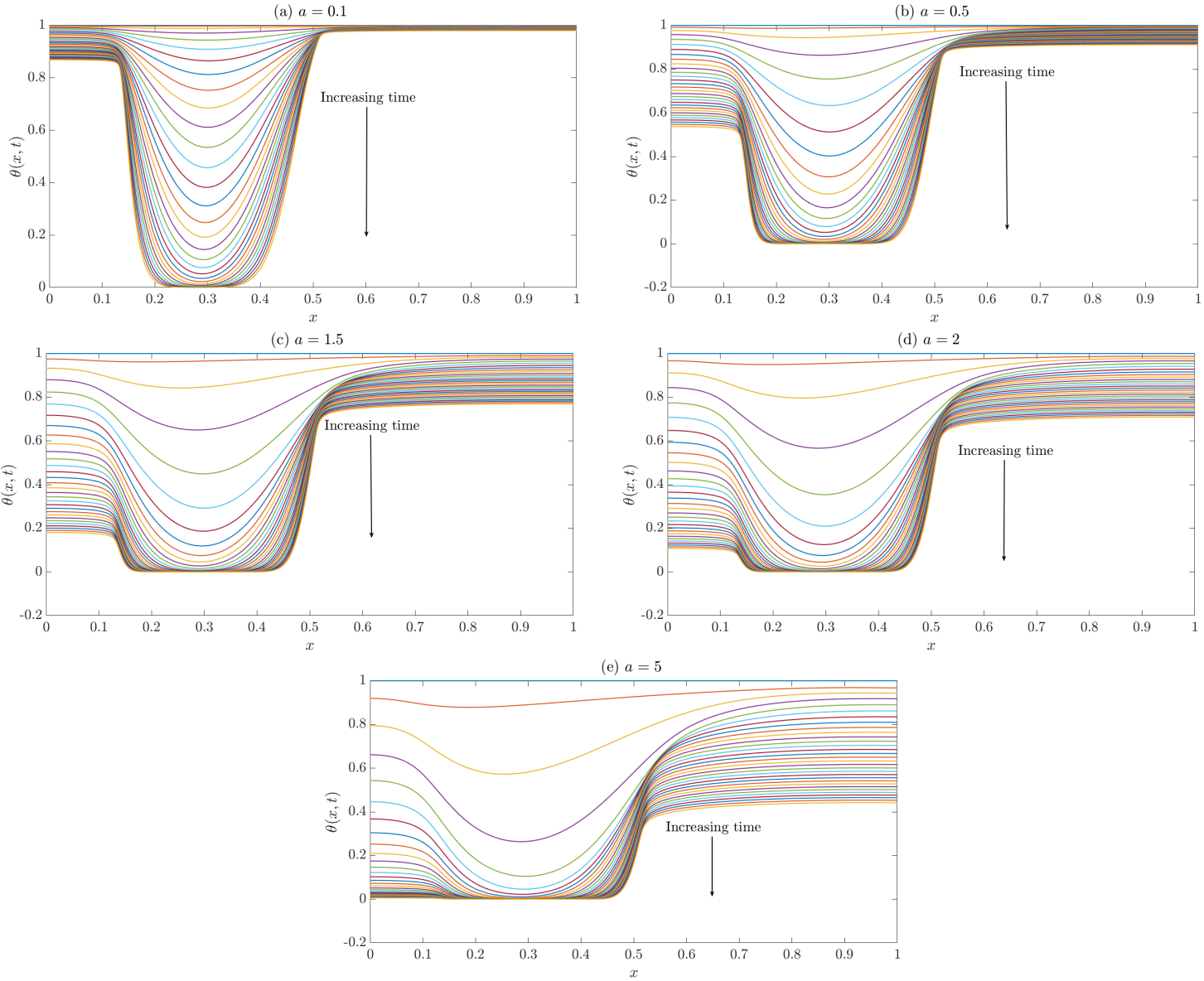


Figure 6.4: The temperature profile $\theta(x, t)$ for varying $a = 0.1, 0.5, 1.5, 2, 5$ and $t = 0 - 300$, respectively. The parameter values are: $Pe = 10^3$ ($Pe_r = 10$), $\alpha = 2$ and $\beta = 0$.

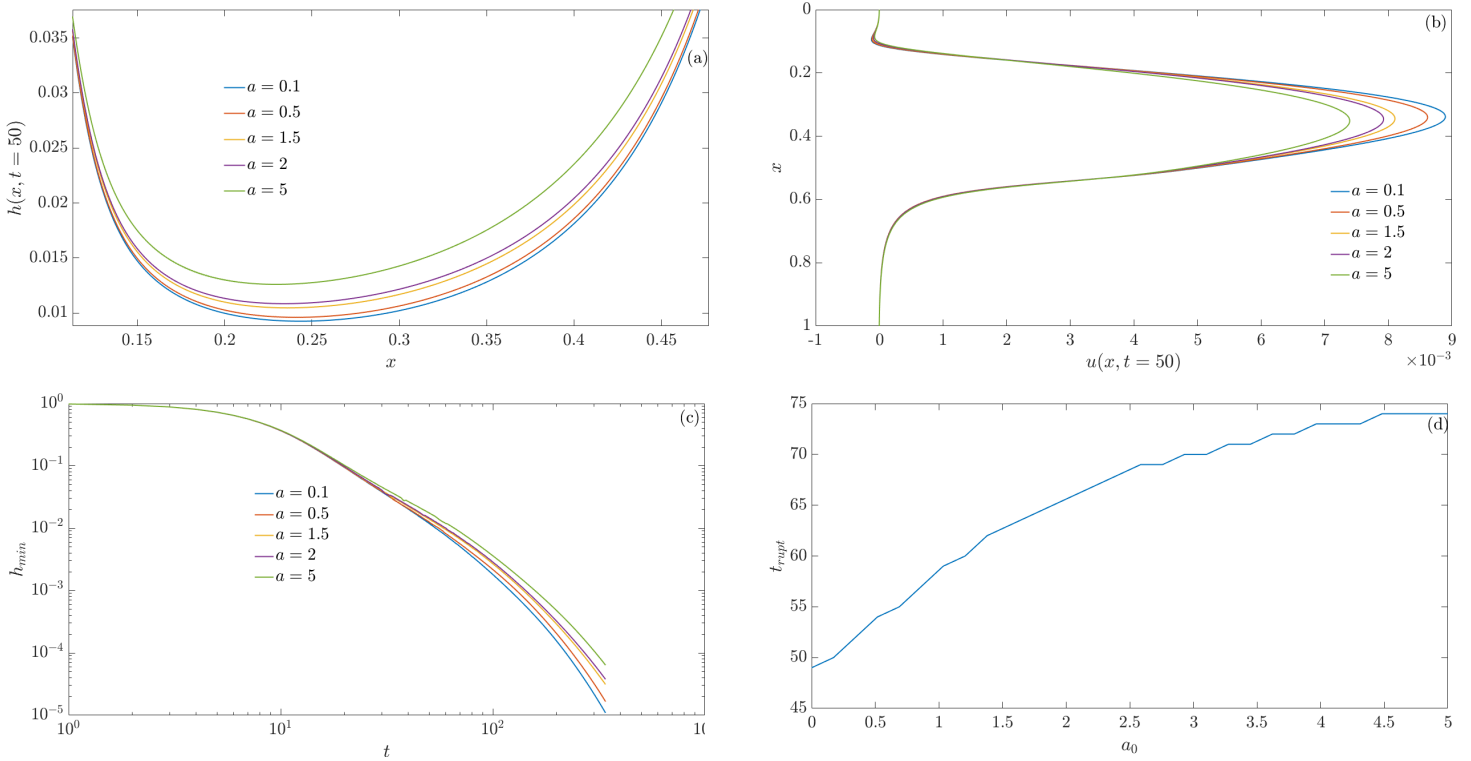


Figure 6.5: (a) Film thickness $h(x, t = 50)$, (b) extensional flow speed $u(x, t = 50)$, and (c) the global minimum $h_{min}(t)$, for varying $a = 0.1, 0.5, 1.5, 2, 5$, and (d) the rupture time t_{rupt} as a function of a . The parameter values are: $Pe(Pe_r) = 10^3(10)$, $\alpha = 2$ and $\beta = 0$.

delaying the rupture times. Figure 6.6(a – d) shows the effect of varying the viscosity-temperature decay constant $\alpha = 0.1, 3, 5, 10$, respectively, while keeping $Pe = 10$ and $a = 0.2$ fixed. We note here that θ is not sensitive to variations in α (results not shown). Equation (6.5c) for θ does not depend on α directly; the influence of α on θ is via convection due the flow, which does not play a significant role in the evolution of the temperature field. Figure 6.6(a, b, c) shows the effect of varying α , on $h(x, t = 45)$, $u(x, t = 45)$ and $h_{min}(t)$, respectively. Figure 6.6(d) shows the influence of varying α on the rupture time, t_{rupt} . We observe that the the film thins faster as α increases

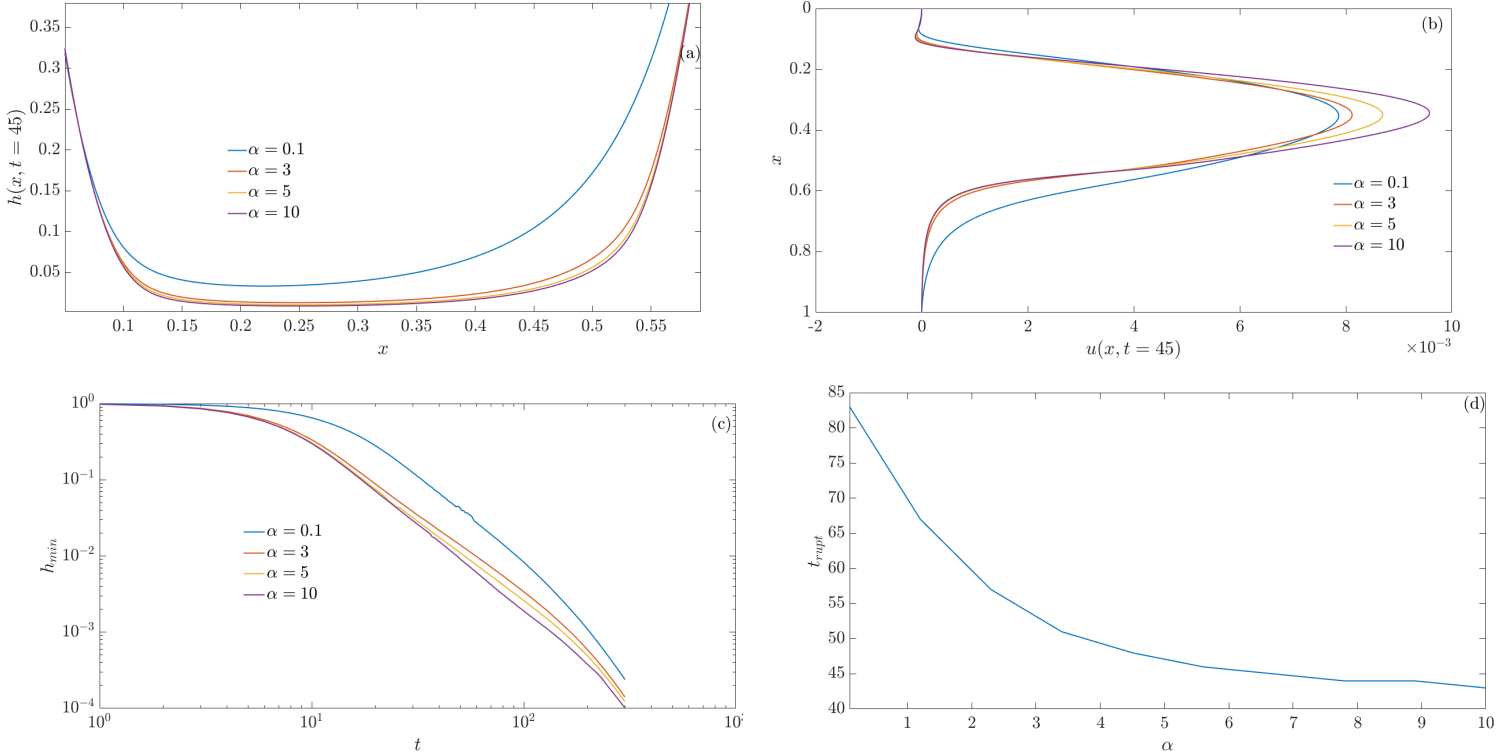


Figure 6.6: (a) Film thickness $h(x, t = 45)$, (b) extensional flow speed $u(x, t = 45)$, and (c) the global minimum $h_{min}(t)$, for varying $\alpha = 0.1, 3, 5, 10$, and (d) the rupture time t_{rupt} as a function of α . The parameter values are: $Pe(Pe_r) = 10(10^{-1})$, $a = 0.2$ and $\beta = 0$.

(Fig. 6.6(a)) due to the faster extensional flow speed as α increases (Fig. 6.6(b)).

The faster flow speed at higher values of α is due to larger reduction in viscosity as α increases. Figure 6.6(c) shows the increased thinning of the minimum film thickness, $h_{min}(t)$, as α increases. Figure 6.6(d) shows that as α increases the fluid drains more rapidly which accelerates the thinning of the middle section, therefore increasing the rupture times.

In the next set of results shown below, we investigate the influence of surface tension varying with temperature via the parameter β , and take the viscosity to be constant (so, $\alpha = 0$). The temperature profiles are not sensitive to variations in β and behave similar to the previous results, hence we do not show them in the results to follow. Figure 6.7(a, b, c) show the effect of varying $Pe(Pe_r) = 10^{-1}(10^{-3}), 1(10^{-2}), 10(10^{-1}), 10^2(1), 10^3(10)$, respectively, on $h(x, t = 68)$, $u(x, t = 68)$ and $h_{min}(t)$ (the global minimum in $h(x, t)$), respectively. Figure 6.7(d) shows the influence of varying Pe on the rupture time, t_{rupt} . For larger Pe , the temperature in the upper capillary meniscus and lower pendant drop regions is much higher compared to that at low Pe (similar to Fig. 6.2). The effect of the elevated temperature is to decrease the surface tension in these regions, which is also where the curvature of the film is most pronounced. As a result, the capillary force acting on the fluid is decreased in comparison to gravity, resulting in a longer and flatter middle section of the film (Fig. 6.7(a)), as well as more liquid collecting in the pendant drop region making it thicker (not shown here). Since surface tension decreases with temperature the Capillary number, Ca , will increase. which results in the lengthening and flattening of the film's middle section. This is analogous to the behaviour observed

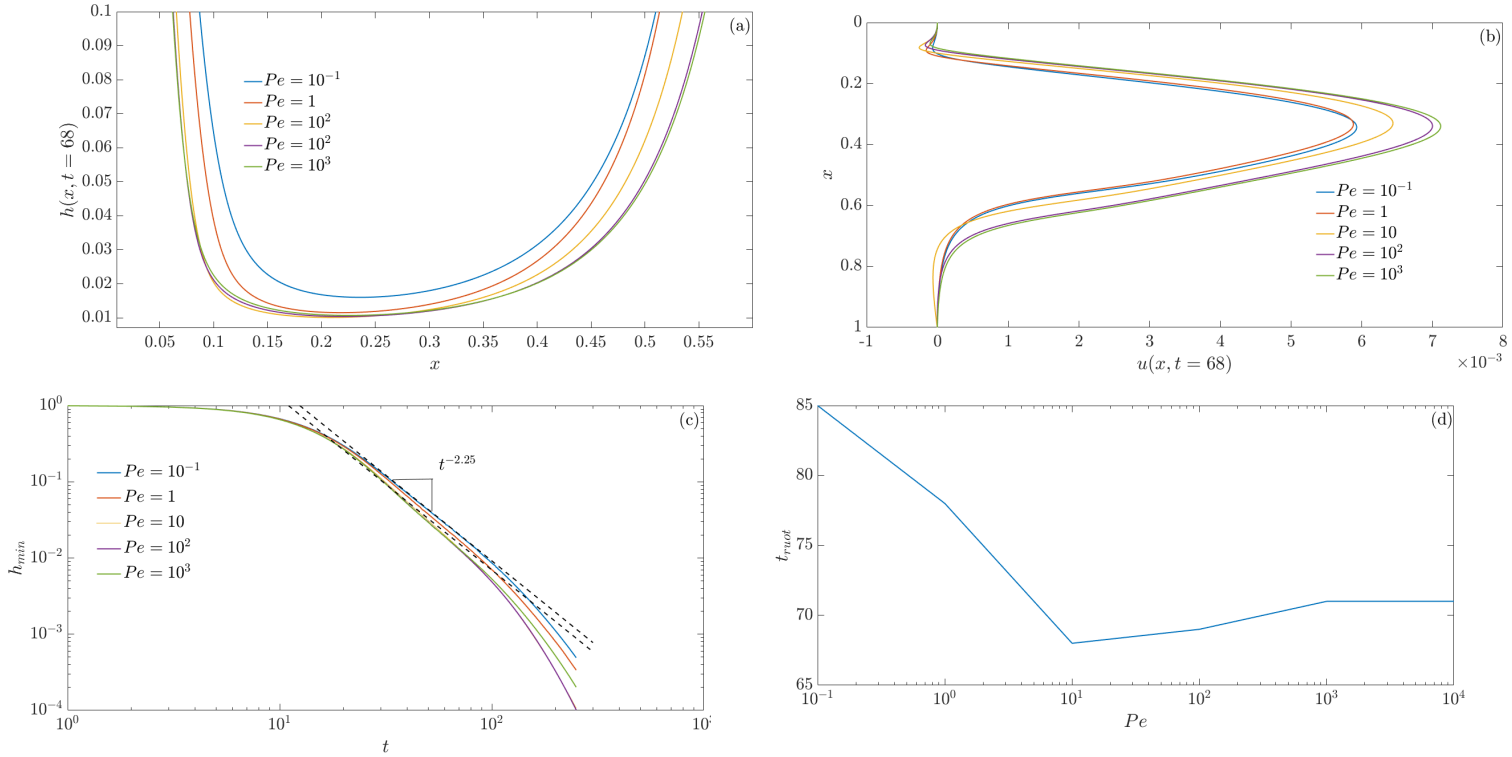


Figure 6.7: (a) Film thickness $h(x, t = 68)$, (b) extensional flow speed $u(x, t = 68)$, and (c) the global minimum $h_{min}(t)$, for varying $Pe(Pe_r) = 10^{-1}(10^{-3}), 1(10^{-2}), 10(10^{-1}), 10^2(1), 10^3(10)$, and (d) the rupture time t_{rupt} as a function of Pe . The parameter values are: $\alpha = 0$, $a = 0.2$ and $\beta = 0.5$.

in chapter 3 (see Fig. 3.2). The extensional flow speed $u(x, t)$ increases as Pe increases, which results in the film draining and thinning faster (Fig. 6.7(d)), consequently rupturing quickly (Fig. 6.7(d)). We note a slight non-monotonicity in the evolution of h and u at intermediate Pe , which results in a minimum in the rupture time at $Pe \approx 10$. In Figure 6.8 we further vary the value of β , for fixed $Pe(Pe_r) = 10^3(10)$, $\alpha = 0$ and $a = 0.2$. Larger values of β increase the sensitivity of surface tension to temperature. Increasing β reduces the surface tension more rapidly, hence increasing Ca . As Ca increases, the film thins more rapidly and the middle section becomes much longer with a corresponding increase in the liquid collecting in the pendant drop at the bottom (Fig. 6.8(a)). As Ca increases, the effect of surface tension decreases in relation to gravity, thereby draining the film further (Fig. 6.8(c)), and reducing rupture times (Fig. 6.8(d)). We also observe that the flow speed increases as β increases (Fig. 6.8(b)), resulting in faster drainage, and hence the film thins rapidly (Fig. 6.8(c, d)). We now consider the combined effect of temperature-dependent viscosity and surface tension, so both α and β positive. We compare this with the previous results of $\alpha > 0$ and $\beta = 0$, and $\beta > 0$ and $\alpha = 0$. We fix $Pe = 10^3$, $\alpha = 2$, $\beta = 0.8$ and $a = 0.2$. We clearly observe that the combined contribution of variable viscosity and surface tension is to drain and thin the film faster (Fig. 6.9(a, c)), due to the increased flow speed (Fig. 6.9(b)). In comparison, at least for the values of α and β chosen here, it appears that the case with surface tension varying with temperature alone ($\beta = 0.8$, $\alpha = 0$) drains and thins slower compared to the case with with viscosity varying with temperature alone ($\alpha = 2$, $\beta = 0.8$). This is due to the bigger decrease in the viscosity with tem-

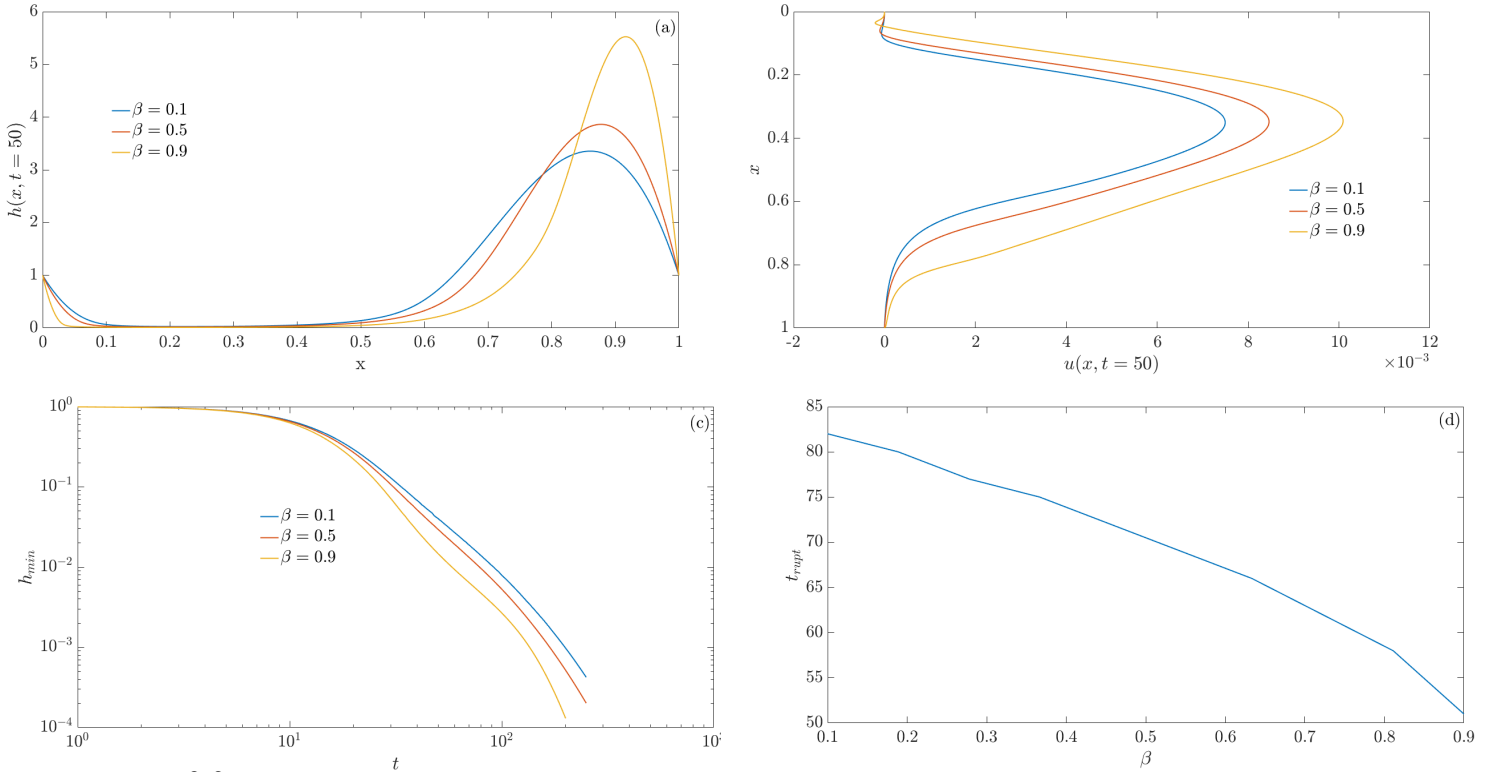


Figure 6.8: (a) Film thickness $h(x, t = 50)$, (b) extensional flow speed $u(x, t = 50)$, and (c) the global minimum $h_{min}(t)$, for varying $\beta = 0.1, 0.5, 0.9$, and (d) the rupture time t_{rupt} as a function of β . The parameter values are: $Pe(Pe_r) = 10^3(10)$, $a = 0.2$ and $\alpha = 0$.

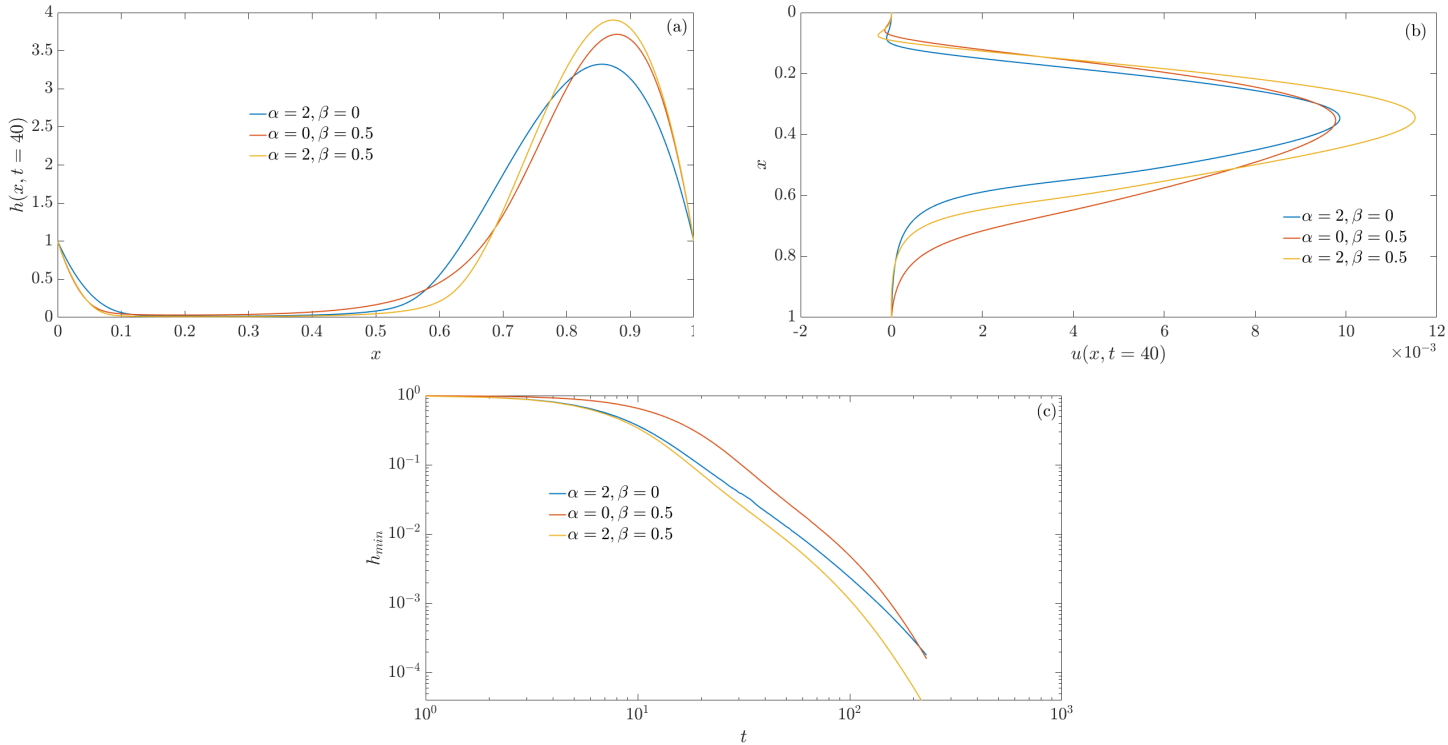


Figure 6.9: (a) Film thickness $h(x, t = 40)$, (b) extensional flow speed $u(x, t = 40)$, and (c) the global minimum $h_{min}(t)$, for varying α and β . The parameters values are: $Pe = 10^3$ and $a = 0.2$.

perature (note that an exponential decay is used to model this variation) compared to the smaller decrease in surface tension with temperature (note that the surface tension is assumed to decrease linearly with temperature). To further investigate the influence of variable viscosity and surface tension with temperature, we map the time taken to rupture, t_{rupt} , in (Pe, β, α) parameter space. Figure 6.10(a – c) shows the colormap of the rupture times for varying $Pe(Pe_r) = 1(10^{-2}), 10(10^{-1}), 10^2(1)$, respectively. The rupture time is based on the minimum film thickness, h_{min} , decreasing to 10^{-2} of its initial thickness. We observe that the rupture time is independent of α and β for

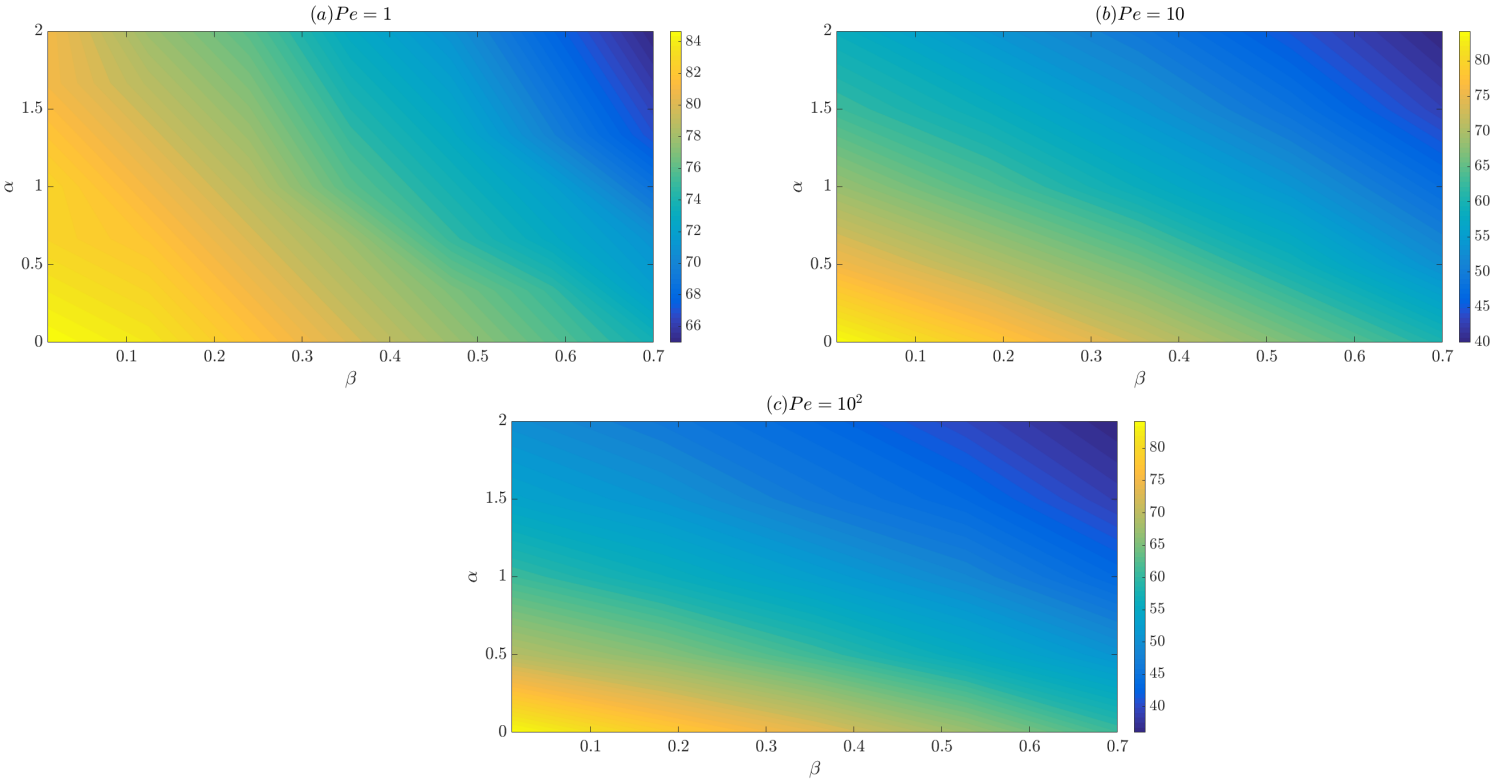


Figure 6.10: Map of the rupture time t_{rupt} as a function of α and β , for $Pe(Pe_r)$ (a) $10^{-2}(10^{-4})$, (b) $1(10^{-2})$, (c) $10(10^{-1})$, and (d) $10^2(1)$. The parameter value $a = 0.2$.

$Pe < 1$. The quicker diffusion timescale in uniformly cooling the film offsets any variations in viscosity or surface tension, so the film evolution behaves almost isothermal for

all (α, β) . As Pe increases, we observe that the range of (α, β) of the highest rupture times shrinks sequentially (Fig. 6.10(b, c)). For large Pe , the highest rupture times are for α and β close to zero (Fig. 6.10(d)). At larger Pe , diffusion is not sufficiently strong to distribute the cooling effects uniformly in the film, hence viscosity and surface tension variations with temperature via α and β have a much stronger influence on the film evolution and rupture time.

6.4 Conclusions

In this chapter we coupled the thin-film flow equations to a one-dimensional advection-diffusion equation for the temperature field and investigated the draining and thinning of a cooling vertically-aligned hot Newtonian liquid film in the asymptotic limit of the reduced Péclet number, $Pe_r \ll 1$. The key flow features related to the draining and thinning of the film, obtained in chapter 5 for small and intermediate values of Pe_r are also reproduced here using the approximate theory valid for $Pe = \epsilon^2 Pe_r \ll 1$, where Pe is the Péclet number. Although we have not made a direct comparison between both sets of results, based on the nearly vertical isotherms observed in the temperature profiles for this parameter range, we can be confident about the validity of the approximate theory.

In this chapter, we have fully investigated the influence of variations in surface tension due to temperature via the parameter β , which we were unable to do in the $Pe_r = O(1)$

theory presented in chapter 5. This allowed us to map the draining and thinning of the film in (Pe_r, α, β, a) parameter space via the rupture times, t_{rupt} , which estimated the time taken by the film to reach a small prescribed thickness of 1% of its initial thickness (Fig. 6.10). This result showed that the optimal operational conditions would be for low Pe_r , where for a large range of (α, β) , the rupture times are almost uniform. However, as mentioned in the §5.5 in chapter 5, polymeric melts generally have a large Péclet number Pe , therefore the low Pe_r regime can be achieved if ϵ is very small. At such small film thickness, other physical effects, such as Van der Waal's forces would need to be taken into account, and the applicability of the current results would be questionable. Nevertheless, the non-isothermal study conducted in this thesis provides a first step towards the understanding of the draining and thinning of free films when the properties of the liquid are dependent on variations in temperature.

Chapter 7

Conclusions and future work

In this thesis, the draining of a vertically-aligned free Newtonian liquid film between two rigid supports due to the combined effects of extensional viscous, gravity and surface tension forces has been modelled. The focus has been on the case where the rescaled Capillary number $Ca = \hat{Ca}/\epsilon \gg 1$, where the Capillary number $\hat{Ca} = \mu^*U^*/\gamma^* = O(1)$. This limit decomposes the liquid domain into a thin lamella (where extensional viscous forces compete with gravity) connecting onto Plateau borders (where surface tension forces balance gravity), with a transition region in between (where surface tension, extensional viscous and gravity forces compete), therefore allowing to replicate the drainage and thinning of the lamella into the Plateau borders in liquid foams [15, 16, 17, 26].

Our model incorporated the effects due to non-Newtonian and viscoplastic behaviour (shear-thinning and a yield stress), a temperature-dependent viscosity and surface ten-

sion, and heat transfer boundary conditions at the film's free surface. These key ingredients are essential to capture the strong coupling between the flow and cooling inherent in metallic, polymeric and ceramic melt flows. A variety of non-Newtonian and viscoplastic constitutive relationships, such as power-law, Carreau and Herschel-Bulkley, are investigated to model the apparent viscosity and the yield stress. An exponential model and a linear model are applied to describe the thermoviscous and thermocapillary coupling, respectively. We used numerical simulations to perform an extensive parameter study on the influence of key parameters on the evolution of the film's free surface and draining and thinning behaviour, such as the apparent viscosity, yield stress, Péclet number, temperature-viscosity coupling constant, slope of the temperature-surface tension constitutive relationship and the free surface heat transfer coefficient.

The influence of non-Newtonian effects, such as shear thinning, in the context of this problem have been previously studied by Brush & Roper [18], without including gravity. They have shown that shear thinning does not change the power-law thinning rate of t^{-2} predicted for a lamella of Newtonian liquid film. However, we showed that the power-law thinning rate of the lamella is weakly dependent on shear thinning, as a consequence of including gravity. To the best of our knowledge, the influence of viscoplastic effects, such as a yield stress, have not been previously investigated in thin liquid film draining flows associated with metallic and polymeric melts using this flow configuration. Our new findings provide the basis to advance the current understanding to a wider class

of liquid film draining flows related to foams.

Our results for the non-isothermal draining of a vertically-aligned free Newtonian liquid film provided some new insights into the important physical mechanisms that are not accessible from previous isothermal studies. Our results highlighted a key feature during the draining and thinning process which was the spatial variability in the cooling, resulting in the lamella losing heat quickly and hence cooling down quickly compared to the Plateau borders. The extent of this cooling was shown to depend strongly on the parameter values. Consequently, the increase in viscosity due to cooling of the lamella reduces the drainage within it and hence its thinning rate. This information could be potentially useful to experimentalists in developing strategies for reducing the drainage and thinning and in delaying the rupture of the liquid melt films.

The work undertaken in this thesis opens up a number of avenues for future research.

These are listed as follows:

1. Extending the framework proposed here to investigate the rupture of thin liquid films in foams. We would need to include long-range attractive molecular forces, such as van der Waals attractions (Sheludko [64]) which are important near rupture.
2. A limitation of the current study is the assumption of a pre-formed liquid film of specified length and thickness (used as an initial condition) before we use the model to investigate its drainage and thinning. In experiments, the film is gradually drawn out of a bath of liquid and whether a film of specified length and

thickness can be reached will depend on the speed at which it is drawn out. This speed also significantly influences the stability of the draining film [22]. We would need to incorporate this into our model by adapting the boundary conditions at the upper boundary via a no-slip boundary condition, so $u(x = 0, t)$ is equal to the speed at which the film is drawn.

3. The fluid flow configuration considered in this thesis involves a thin liquid film supported between wire frames (Figure 2.1). While this setup mimicks the thinning of the lamella in liquid foam films, the supported ends (the bottom end, in particular) are not a true replication of the Plateau borders. We would need to consider another configuration which involves lifting the wire frame completely out of a bath of liquid resulting in a liquid film that connects onto the bath at its lower end (for example, see Champougny *et al.* [22] and Naire *et al* [49, 48, 50, 14]). The bottom end of the film connecting onto the bath's surface is representative of the Plateau border region. The current framework is still applicable, except that one needs to apply the boundary conditions for the film to match onto the bath [49, 48, 50, 14, 22].
4. The theoretical framework proposed in this thesis can be readily adapted to model the drainage and thinning of viscoelastic liquid films, under both isothermal and non-isothermal conditions. Indeed, one can use the form of the evolution equations written in terms of the extensional stresses, τ_{xx} , τ_{zz} and the shear stress τ_{xz} , and use a constitutive model appropriate for a viscoelastic liquid, e.g.,

Oldroyd-B model [2, 3] to relate these stresses to their corresponding shear rates.

5. Incorporating the results from the extensional flows in non-Newtonian, viscoplastic and viscoelastic liquid films to investigate the overall behaviour of the corresponding foam as a network using the framework proposed by Stewart *et al.* [67].

There are limitations to this study which are listed below.

1. One of the key limitations of this study (also mentioned above) is related to the assumption of a pre-formed film of a specified length and thickness used as the initial condition. The existence of this would depend on the speed at which the film is drawn out. This drawing out speed would need to be incorporated and its influence on the drainage and thinning of the film investigated
2. Our non-Newtonian and viscoplastic study is under isothermal conditions. In reality, the yield stress (and to some extent the power law index) strongly depend on temperature. As part of future work, we would need to extend our model to include temperature-dependent non-Newtonian effects and their influence on cooling.
3. Probably more than temperature-dependent non-Newtonian effects, a key ingredient missing in this work is phase transition due to solidification. It is likely that the results reported here might not be applicable when solidification by the formation of a surface crust is taken into account. We would need to include

solidification effects into any future extensions of our model.

4. As in most thin film flow studies one would need to be careful when employing the lubrication approximation, particularly, where there are steep changes in the film thickness. To test the validity of our results full numerical simulations of the Navier-Stokes equations and boundary conditions would need to be undertaken using, for example, boundary element or finite element methods.

In conclusion, the thesis provides new theoretical insight into the influence of non-Newtonian and viscoelastic behaviour in draining flows, and the flow-cooling coupling mechanism that is inherent in draining of hot flows undergoing cooling. This insight would form the basis for future developments of this model to incorporate additional effects mentioned above and to transfer knowledge to experimentalists interested in characterising metallic and polymeric liquid melt films for applications involving foams.

Bibliography

- [1] D.J. Acheson. *Elementary Fluid Dynamics*. Oxford University Press, 1998.
- [2] A. Alhushaybari and J. Uddin. Convective and absolute instability of viscoelastic liquid jets in the presence of gravity. *Physics of Fluids*, 6:044106, 2019.
- [3] A. Alhushaybari and J. Uddin. Absolute instability of free-falling viscoelastic liquid jets with surfactants. *Physics of Fluids*, 32:013102, 2020.
- [4] A.M. Anderson, L.N. Brush, and S.H. Davis. Foam mechanics: spontaneous rupture of thinning liquid films with plateau borders. *Journal Fluid Mechanics*, 658:63–88, 2010.
- [5] G. Ashby. *Cellular Solids: Structure and Properties*. Cambridge University Press, 1999.
- [6] M.F. Ashby, A.G. Evans, N.A. Fleck, L.J. Gibson, J.W. Hutchinson, and H.N.G. Wadley. *Metal foams: A design guide*. Butterworth-Heinemann, 2000.
- [7] N. Balmforth, R. Craster, and R. Sassi. Dynamics of cooling viscoplastic domes. *Journal of Fluid Mechanics*, 499:149–182, 2004.

- [8] N. J. Balmforth, A. S. Burbridge, R. V. Craster, J. Salzig, and A. Shen. Viscoplastic models of isothermal lava domes. *Journal of Fluid Mechanics*, 403, 2000.
- [9] N.J. Balmforth and R.V. Craster. Dynamics of cooling domes of viscoplastic fluid. *J. Fluid Mech.*, 422:225–248, 2000.
- [10] N.J Balmforth and I.J Hewitt. Viscoplastic sheets and threads. *Journal of Non-Newtonian Fluid Mechanics*, 193(C):28–42, 2013.
- [11] J. Banhart. Metal foams: Production and stability. *Advanced Engineering Materials*, 8(9):781–794, 2006.
- [12] Valeria Barra, Shahriar Afkhami, and Lou Kondic. Interfacial dynamics of thin viscoelastic films and drops. *Journal of Non-Newtonian Fluid Mechanics*, 237(C):26–38, 2016.
- [13] M. Bowen and B.S. Tilley. Thermally induced van der waals rupture of thin viscous fluid sheets. *Physics of Fluids*, 24(3):032106, 2012.
- [14] R.J. Braun, S.A. Snow, and S. Naire. Models for gravitationally-driven free-film drainage. *Journal of Engineering Maths.*, 43:281–314, 2002.
- [15] C.J.W. Breward. *The mathematics of foam*. PhD thesis, Oxford University, 1999.
- [16] C.J.W. Breward and P.J. Howell. The drainage of a foam lamella. *Journal Fluid Mechanics*, 458:379–406, 2002.

- [17] L.N. Brush and S.H. Davis. A new law of thinning in foam dynamics. *Journal Fluid Mechanics*, 534:227–236, 2005.
- [18] L.N. Brush and S.M. Roper. The thinning of lamellae in surfactant-free foams with non-newtonian liquid phase. *Journal Fluid Mechanics*, 616:235–262, 2008.
- [19] M. Bunk and J.R. King. Spreading melts with basal solidification. *Z. Angew. Math. Mech.*, 83(12):820–843, 2003.
- [20] I. Cantat, S. Cohen-Addad, F. Elias, F. Graner, R. Hohler, O. Pitois, and A. Rouyer, F. Saint-Jalmes. *Foams – Structure and Dynamics*. Oxford University Press, 2013.
- [21] H.S. Carslaw and J.C. Jaeger. *Conduction of heat in solids*. Oxford University Press, 1980.
- [22] L. Champougny, E. Rio, F. Restagno, and B. Scheid. The break-up of free films pulled out of a pure liquid bath. *J. Fluid Mechanics*, 811:499–524, 2016.
- [23] R. Craster, O. Matar, and D. Papageorgiou. Pinchoff and satellite formation in surfactant covered viscous threads. *Physics of Fluids*, 14:1364–1376, 2002.
- [24] R.V. Craster and O.K. Matar. Dynamics and stability of thin liquid films. *Rev. Mod. Phys.*, 81:1131–1198, 2009.
- [25] S. J. D D’alessio, J. P Pascal, H. A Jasmine, and K. A Ogden. Film flow over heated wavy inclined surfaces. *Journal of Fluid Mechanics*, 665:418–456, 2010.

- [26] M.J. Davis, P.S. Stewart, and S.H. Davis. Local effects of gravity on foams. *J. Fluid Mechanics*, 737:1–18, 2013.
- [27] A. De Wit, D. Gallez, and C.I. Christov. Nonlinear evolution equations for thin liquid films with insoluble surfactants. *Physics of Fluids*, 6:3256–3266, 1994.
- [28] B.V. Deryagin. *J. Colloids*, 17:207, 1955.
- [29] T. Erneux and S.H. Davis. Nonlinear rupture of free films. *Physics Fluids*, 5(5):1117–1122, 1993.
- [30] D. A. Goussis and R. E. Kelly. Effects of viscosity variation on the stability of film flow down heated or cooled inclined surfaces: Long-wavelength analysis. *Physics of Fluids*, 28:3207, 1985.
- [31] D. A. Goussis and R. E. Kelly. Effects of viscosity variation on the stability of a liquid film flow down heated or cooled inclined surfaces: Finite wavelength analysis. *Physics of Fluids*, 30:974, 1987.
- [32] D. A. Goussis and R. E. Kelly. Surface wave and thermocapillary instabilities in a liquid film flow. *Journal of Fluid Mechanics*, 223(1):25–45, 1991.
- [33] R.W. Griffiths. The dynamics of lava flows. *Annu. Rev. Fluid Mech.*, 32:477–518, 2000.
- [34] D. He, J. Wylie, H. Huang, and R. Miura. Extension of a viscous thread with temperature-dependent viscosity and surface tension. *J. Fluid Mechanics*, 800:720–752, 2016.

- [35] P.J. Howell. Models for thin viscous sheets. *Eur. J. Appl. Maths.*, 7:321–343, 1996.
- [36] Yu.O Kabova, V.V Kuznetsov, and O.A Kabov. Temperature dependent viscosity and surface tension effects on deformations of non-isothermal falling liquid film. *International Journal of Heat and Mass Transfer*, 55(4):1271–1278, 2012.
- [37] S. Kalliadasis, A. Kiyashko, and E. Demekhin. Marangoni instability of a thin liquid film heated from below by a local heat source. *Journal of Fluid Mechanics*, 475:377–408, 2003.
- [38] J.R. King, D.S. Riley, and A. Sansom. Gravity currents with temperature-dependent viscosity. *Comput. Assist. Mech. Eng. Sci.*, 7(1):251–277, 2000.
- [39] S. Koehler, H. Stone, M. Brenner, and J. Eggers. Dynamics of foam drainage. *Physical Review E*, 58(2):2097–2106, 1998.
- [40] G. A. Leslie, S. K. Wilson, and B. R. Duffy. Non-isothermal flow of a thin film of fluid with temperature-dependent viscosity on a stationary horizontal cylinder. *Physics of Fluids*, 23(6), 2011.
- [41] G. A. Leslie, S.K. Wilson, and B.R. Duffy. Non-isothermal flow of a thin film of fluid with temperature-dependent viscosity on a stationary horizontal cylinder. *Physics of Fluids*, 6:062101, 2011.
- [42] M.A. Matovich and J.R.A. Pearson. Spinning a molten threadline. steady-state isothermal viscous flows. *J. Fluid Mechanics*, 8:512–520, 1969.

- [43] S. Miladinova, S. Slavtchev, G. Lebon, and Jean-Claude Legros. Long-wave instabilities of non-uniformly heated falling films. *Journal of Fluid Mechanics*, 453:153–175, 2002.
- [44] Faith A. Morrison. *Understanding rheology*. New York: Oxford University Press, 2001.
- [45] T G. Myers. Application of non-newtonian models to thin film flow. *Physical Review E*, 6:066302–066302, 2005.
- [46] T.G. Myers, J. Charpin, and S. J. Chapman. The flow and solidification of a thin fluid film on an arbitrary three-dimensional surface. *Phys. Fluids*, 14:2788–2803, 2002.
- [47] K. J. Mysels, K. Shinoda, and S. Frankel. *Soap Films: Studies of Their Thinning*. Pergamon, 1959.
- [48] S. Naire, R.J. Braun, and S.A. Snow. An insoluble surfactant model for a vertical draining free film. *Journal of Colloid Interface Science*, 230(1):91–106, 2000.
- [49] S. Naire, R.J. Braun, and S.A. Snow. Limiting cases of gravitational drainage of a vertical free film for evaluating surfactants. *SIAM J. Applied Maths.*, 61(3):889–913, 2000.
- [50] S. Naire, R.J. Braun, and S.A. Snow. An insoluble surfactant model for a vertical draining free film with variable surface viscosity. *Physics of Fluids*, 13(9):2492–2502, 2001.

- [51] Paolo A. Netti, editor. *Biomedical Foams for Tissue Engineering Applications*. Woodhead Publishing, 2014.
- [52] H. Ockendon and J.R. Ockendon. *Viscous flows*. Cambridge University Press, 1995.
- [53] A. Oron, S. H. Davis, and S. G. Bankoff. Long-scale evolution of thin liquid films. *Rev. Mod. Phy.*, 69:931–980, 1997.
- [54] J. Plateau. Statique exprimentale at theerique des et th eorique des liquides soumis aux seules forces molecuaires. *Gauthier-Villars Fluids*, 1873.
- [55] M. Prévost and D. Gallez. Nonlinear rupture of thin free liquid films. *J. Chemical Physics*, 84:4043–4049, 1986.
- [56] Douglas A. Reinelt and Andrew M. Kraynik. Simple shearing flow of a dry kelvin soap foam. *Journal of Fluid Mechanics*, 311:327–343, 1996.
- [57] M. Safouane, M. Saint-Jalmes, V. Bergeron, and D. Langevin. Viscosity effects in foam drainage: Newtonian and non-newtonian foaming fluids. *Eur. Phy. J. E*, 19:195–202, 2006.
- [58] A. Samanta. Stability of liquid film falling down a vertical non-uniformly heated wall. *Physica D: Nonlinear Phenomena*, 237(20):2587–2598, 2008.
- [59] M. Scheffler and P. Colombo (Eds), editors. *Cellular Ceramics: Structure, Manufacturing, Properties and Applications*, chapter 1.2. Wiley, 2005.

- [60] B. Scheid, C. Ruyer-Quil, U. Thiele, O. A. Kabov, J. C. Legros, and P. Colinet. Validity domain of the benney equation including the marangoni effect for closed and open flows. *Journal of Fluid Mechanics*, 527:303–335, 2005.
- [61] L.W. Schwartz and H.M. Princen. A theory of extensional viscosity for flowing foams and concentrated emulsions. *J. Colloid Interface Science*, 118:201–211, 1987.
- [62] L.W. Schwartz and R.V Roy. Modeling draining flow in mobile and immobile soap films. *J. Colloid and interface Science*, 218:309–323, 1999.
- [63] M.S. Shah, V. van Steijn, C.R. Kleijn, and M.T. Kreutzer. Thermal fluctuations in capillary thinning of thin liquid films. *J. Fluid Mechanics*, 896:1090–1107, 2013.
- [64] A. Sheludko. Thin liquid films. *Colloid Interface Science*, 1(4):391–464, 1967.
- [65] G. D. Smith. *Numerical Solution of Partial Differential Equations: Finite Difference Methods*. Macmillan, third edition edition, 1985.
- [66] P. Stevenson. *Foam Engineering: Fundamentals and Applications*. Wiley, 2012.
- [67] P.S. Stewart and S.H. Davis. Dynamics and stability of metallic foams: network modelling. *Journal of Rheology*, 56:543–574, 2012.
- [68] P.S. Stewart and S.H. Davis. Self-similar coalescence of clean foams. *Journal of Fluid Mechanics*, 722:645–664, 2013.

- [69] P.S. Stewart, S.H. Davis, and S. Hilgenfeldt. Microstructural effects in aqueous foam fracture. *Journal of Fluid Mechanics*, 785:425–461, 2015.
- [70] F. Suñol and R. González-Cinca. Liquid jet breakup and subsequent droplet dynamics under normal gravity and in microgravity conditions. *Physics of Fluids*, 27:077102, 2015.
- [71] S.S. Thete, C. Anthony, P. Doshi, M.T. Harris, and O.A. Basaran. Self-similarity and scaling transitions during rupture of thin free films of newtonian fluids. *Physics of Fluids*, 28:092101, 2016.
- [72] B.S. Tilley and M. Bowen. Thermocapillary control of rupture in thin viscous fluid sheets. *Journal Fluid Mechanics*, 541:399–408, 2005.
- [73] F.T. Trouton. On the coefficient of viscous traction and its relation to that of viscosity. *Proc. Royal Soc. A*, 77:426–440, 1906.
- [74] S. Wang, P. Austin, and S. Chakrabati-Bell. It’s a maze: The pore structure of bread crumbs. *Journal of Cereal Science*, 54(2):203–210, 2011.
- [75] D. Weaire and S. Hutzler. *The physics of foams*. Clarendon Press, Oxford, 1999.
- [76] D. Weaire, S. Hutzler, S. Cox, N. Kern, M. Alonso, and W. Drenckhan. The fluid dynamics of foams. *J. of Physics: Condensed matter*, 15:S65–S73, 2003.
- [77] S.K. Wilson and B. R. Duffy. On the gravity-driven draining of a rivulet of fluid with temperature-dependent viscosity down a uniformly heated or cooled substrate. *J. Eng. Math.*, 42:349–372, 2002.

- [78] S.K. Wilson and B. R. Duffy. Strong temperature-dependent-viscosity effects on a rivulet draining down a uniformly heated or cooled slowly varying substrate. *Phys. Fluids*, 15:827–840, 2003.
- [79] J. Wylie and H. Huang. Extensional flows with viscous heating. *J. Fluid Mechanics*, 571:359–370, 2007.
- [80] C. C. Yang and H. Nakae. The effects of viscosity and cooling conditions on the foamability of aluminum alloy. *J. Mat. Proc. Tech.*, 141:202–206, 2003.
- [81] A. Zadrazil, F. Stepanek, and O.K. Matar. Droplet spreading, imbibition and solidification on porous media. *J. Fluid Mech.*, 562:1–33, 2006.
- [82] Zhi-Qiang Zhou, Jie Peng, Yang-Jun Zhang, and Wei-Lin Zhuge. Viscoelastic liquid film flowing down a flexible tube. *Journal of Fluid Mechanics*, 802:583–610, 2016.